# Experimental Study of Thermal Degradation of Fire Resisting Compartment Partitions in Fires

by

Matthew Didomizio

A thesis
presented to the University of Waterloo
in fulfillment of the
thesis requirement for the degree of
Doctor of Philosophy
in
Mechanical and Mechatronics Engineering

Waterloo, Ontario, Canada, 2017

**Examining Committee Membership**

The following served on the Examining Committee for this thesis. The decision of the Examining Committee is by majority vote.

| | |
|---|---|
| Supervisor | Elizabeth Weckman<br>Professor, Mechanical and Mechatronics Engineering, University of Waterloo |
| External Examiner | Luke Bisby<br>Professor of Fire and Structures, Civil and Environmental Engineering, The University of Edinburgh |
| Internal Member (1) | Jean-Pierre Hickey<br>Assistant Professor, Mechanical and Mechatronics Engineering, University of Waterloo |
| Internal Member (2) | Kyle Daun<br>Associate Professor, Mechanical and Mechatronics Engineering, University of Waterloo |
| Internal-External Member | John Straube<br>Associate Professor, Civil and Environmental Engineering, University of Waterloo |

I hereby declare that I am the sole author of this thesis. This is a true copy of the thesis, including any required final revisions, as accepted by my examiners.

I understand that my thesis may be made electronically available to the public.

## Abstract

Fire separations in a building (e.g. walls) are often constructed from combustible materials; those containing wood stud framing, mineral wool insulation, and gypsum board wallcoverings are commonplace in Canadian residential buildings. These construction assemblies degrade under fire exposure, a process involving chemical decomposition as well as physical damage. A fire separation's ability to resist the spread of fire is traditionally assessed by means of a fire resistance test, in which a construction assembly is exposed to an intense furnace fire under prescribed conditions. This method of assessment, while standardized and prescribed in the National Building Code of Canada, can be restrictive to the design process. In contrast, a performance-based approach, in which the adequacy of a fire separation is assessed on the basis of its real-world use, can lead to designs with improved safety, efficiency, and flexibility. Such a design approach requires a specific engineering toolset: models capable of predicting the thermal degradation of construction assemblies under specified fire conditions. Development of the next generation of thermal degradation models requires detailed study of the phenomena occurring at the large-scale, in the context of real fires rather than prescribed exposure conditions, and a controlled means by which to conduct this type of study. Also, a diverse set of experimental data is required for the validation of such models. The objective of the present body of work is to develop a novel large-scale experiment tailored specifically for the study of thermal degradation of construction assemblies in real fires, and to demonstrate the utility of the experimental procedure as applied to the detailed study of thermal degradation phenomena. A selection of relevant experimental techniques were identified, and a new apparatus and method of test were developed for this stated purpose. In this new experiment, one wall of a fire compartment was instrumented and monitored as it was subject to a realistic fire exposure. A novel method for measurement of incident heat flux to a large area in a fire compartment was developed, and used to characterize the conditions of the experiment for a wood crib fire. A series tests were conducted on fire resisting compartment partitions that are used in residential buildings in Canada. In the tests, thermal degradation phenomena were observed and assessed relative to temperatures measured in the degrading walls. The utility of this new approach in the experimental study of thermal degradation of construction assemblies subject to real fire exposures was demonstrated. Furthermore, a relevant set of experimental data was generated that may be used for validation of future models of thermal degradation and integrated fire analysis.

**Acknowledgements**

I would like to thank my supervisor, Dr. Elizabeth Weckman, for her advice, wisdom, and patience over the course of my graduate studies. I would also like to express my gratitude to Gord Hitchman, Andy Barber, Rich Gordon, and Dr. Allan Strong for their technical expertise and guidance; to Dr. Kyle Daun for his contributions in the development of the heat flux model; to Patrick Mulherin, Njegos Bijelic, and Noah Ryder for their support in preliminary experiments; and to Kevin Gordon for his significant contributions in the construction and conduct of countless large-scale fire tests.

In addition, I would like to acknowledge the contributions of Richard Roos of ROXUL® Inc., and of the Region of Waterloo and Kitchener fire departments that were present during large-scale fire tests.

# Table of Contents

**List of Tables** **xv**

**List of Figures** **xvii**

**List of Symbols** **xxv**

**1 Introduction** **1**

**2 Background** **5**

2.1 Fire Resistance of Construction Assemblies . . . . . 5

2.2 Thermal Degradation of Construction Assemblies in Fires . . . . . 8

2.3 State of the Art on the Thermal Degradation of Construction Assemblies 14

2.4 Summary . . . . . 24

**3 Preliminary Investigation** **27**

3.1 Construction of the Fire Compartment . . . . . 27

3.2 Instrumentation and Test Methodology . . . . . 31

3.3 Results . . . . . 37

3.4 Discussion and Findings . . . . . 45

**4 Design of Experiment** **49**

4.1 Apparatus . . . . . 51

4.2 Instrumentation . . . . . 58

4.3 Data Acquisition . . . . . 65

**5 Measurement of Heat Flux** **67**

5.1 Steel Wall Heat Flux Sensor . . . . . 68

5.2 The Generalized Thermal Capacitance Model . . . . . 78

5.3 Thermal Capacitance Model for the Steel Wall . . . . . 83

5.4 Model Optimization by Kalman Filter . . . . . 87

5.5 Extension of the Model to Two Dimensions . . . . . 96

5.6 Suitability of Modelling Assumptions . . . . . 100

**6 Characterization of the Experiment** **103**

6.1 Design Fire . . . . . 103

6.2 Test Overview and Data Reduction . . . . . 107

6.3 Results and Discussion . . . . . 110

**7 Assessment of Thermal Degradation of Construction Assemblies** **135**

7.1 Test Overview and Data Reduction . . . . . 135

7.2 Construction and Instrumentation Details . . . . . 138

7.3 Results and Discussion . . . . . 141

**8 Closure** **167**

8.1 Conclusions . . . . . 167

8.2 Recommendations . . . . . 170

**References** **173**

**Appendices**

**A Construction Drawings** **183**

**B Instrumentation** **185**

B.1 Real Wall Thermal Degradation Experiments . . . . . 185

B.2 Steel Wall Characterization Experiments . . . . . 196

**C Fuel Configurations** **203**

C.1 Real Wall Thermal Degradation Experiments . . . . . 203

C.2 Steel Wall Characterization Experiments . . . . . 205

**D Raw Test Data** **211**

**E Raw Test Data Import Procedures — Code Listings** **213**

E.1 Real Wall Thermal Degradation Experiments . . . . . 213

E.2 Steel Wall Characterization Experiments . . . . . 217

**F Computation of Incident Heat Flux — Code Listings** **221**

F.1 Generalized Thermal Capacitance Model . . . . . 221

F.2 Steel Wall Thermal Capacitance Model (0D) . . . . . 225

F.3 Steel Wall Kalman Filter (0D) . . . . . 232

F.4 Steel Wall Kalman Filter (2D) . . . . . 244

**G State Reference Data for the Heat Flux Model** **263**

# List of Tables

3.1 Average sensor heights, in (individual sensor heights are given in braces). 38

6.1 Summary of conditions and events for characterization tests #1–6. . . . . 108

6.2 Summary of conditions and events for characterization tests #7–12. . . . 109

6.3 Summary of design fire statistics. . . . . 132

7.1 Summary of conditions and events for real wall tests #1–5. . . . . 136

# List of Figures


2.1 Furnace temperature curve prescribed in the ASTM E119 fire resistance test. . . . . 6

3.1 Burn house structure at the University of Waterloo Fire Research Facility. 28

3.2 Fire compartment with built-up cement board interior lining. . . . . 29

3.3 Fire compartment with ceramic fibre insulation interior lining. . . . . 30

3.4 Stud wall being constructed, unexposed side of the wall. . . . . 32

3.5 Exposed-side thermocouples hanging in front of the test wall. . . . . 33

3.6 Heat flux rig. . . . . 34

3.7 Velocity rig. . . . . 34

3.8 Overall thermocouple instrumentation plan for the test wall. . . . . 36

3.9 Fire near the end of the test ($t = 44$ minutes). . . . . 37

3.10 Gas temperatures on the exposed side of the wall over all five cavities in the upper/middle region (sensor height = 61 in (155 cm)). . . . . 38

3.11 Gas temperatures on the exposed side of the wall averaged over all five cavities in the upper, middle, and lower regions (min/max). . . . . 39

3.12 Heat flux to the wall in the upper, middle, and lower regions. . . . . 40

3.13 Average in-depth temperatures in the upper region of the wall. . . . . 41

3.14 Temperature contours cavity 3 at $t = 10$, 20, 25, and 30 min. . . . . 42

3.15 Gas velocity out of the compartment at the door in the upper, middle, and lower regions (min/max). . . . . 43

3.16 State of the wall post-fire ($t = 45$ min). . . . . 44

3.17 Depths of charring of the wood studs. . . . . 44

4.1 Section view of the fire test apparatus (refer to Appendix A for details). . 52
4.2 Profile and top views of the wall frame (refer to Appendix A for details). 54
4.3 Fire test apparatus installed on site. . . . . 55
4.4 Insulation panels used in the fire test apparatus. . . . . 56
4.5 Insulation panels installed on the compartment ceiling. . . . . 57
4.6 Insulation panels installed on the compartment walls. . . . . 57
4.7 Fully insulated fire compartment. . . . . 57
4.8 Construction of the fire compartment thermocouple rakes. . . . . 59
4.9 Details of the fire compartment thermocouple rakes. . . . . 59
4.10 Thermocouple rakes on the unexposed-side of the wall. . . . . 61
4.11 Thermocouples on the unexposed-side surroundings. . . . . 61
4.12 Thermocouple locations on a test wall with 24 in (609 mm) stud spacing. 62
4.13 Thermocouple locations on a test wall with 16 in (406 mm) stud spacing. 63
4.14 Data acquisition system in the instrumentation section. . . . . 66

5.1 Thermocouples installed on the unexposed side of the steel wall. . . . . 70
5.2 Thermophysical properties of steel — density. . . . . 70
5.3 Thermophysical properties of steel — specific heat capacity. . . . . 70
5.4 Thermophysical properties of steel — thermal conductivity. . . . . 71
5.5 Thermophysical properties of steel — thermal diffusivity. . . . . 71
5.6 Thermal conductivity of ceramic fibre insulation. . . . . 71
5.7 Steel wall surface preparation (coating). . . . . 72
5.8 Heat transfer schematic for IR camera measurement. . . . . 73
5.9 Spectral blackbody emissive power for various temperatures. . . . . 75
5.10 Blackbody emissive power in the MWIR and LWIR bands. . . . . 76
5.11 Measurement of temperature-dependent emissivity (setup). . . . . 77

5.12 Measurement of temperature-dependent emissivity (IR image). . . . . 77
5.13 Band average emissivity at various temperatures (IR camera tests). . . . 78
5.14 Spectral emissivity at room temperature (reflectometer tests). . . . . 78
5.15 Heat transfer schematic for the generalized thermal capacitance model. . 79
5.16 Results of the forward and inverse generalized thermal capacitance model for the example scenario. . . . . 82
5.17 Effective Biot number for steel for the generalized thermal capacitance model. . . . . 83
5.18 Heat transfer schematic for the generalized thermal capacitance model. . 84
5.19 Normal probability density function for temperature measurement. . . . 88
5.20 Schematic of the Kalman filter with iteration step. . . . . 89
5.21 Results of the steel wall thermal capacitance model for the example scenario (temperature, $\phi = 0.05$). . . . . 93
5.22 Results of the steel wall thermal capacitance model for the example scenario (incident heat flux, $\phi = 0.05$). . . . . 93
5.23 Results of the steel wall thermal capacitance model for the example scenario (temperature, $\phi = 0.01$). . . . . 95
5.24 Results of the steel wall thermal capacitance model for the example scenario (incident heat flux, $\phi = 0.01$). . . . . 95
5.25 Results of the steel wall thermal capacitance model for the example scenario (temperature, $\phi = 0.10$). . . . . 95
5.26 Results of the steel wall thermal capacitance model for the example scenario (incident heat flux, $\phi = 0.10$). . . . . 95
5.27 Discretization schemes used for the two-dimensional model. . . . . 96
5.28 Heat flow schematic for a general 2D element. . . . . 97

6.1 Standard wood crib used in the large-scale experiments. . . . . 105
6.2 Probability density function for wood crib mass. . . . . 106
6.3 Heat release rate for a single wood crib. . . . . 106

6.4 Characterization test #1, temperature line plot. . . . . 112
6.5 Characterization test #1, heat flux line plot. . . . . 112
6.6 Characterization test #1, temperature contour plot, $t = 10$ min. . . . . 112
6.7 Characterization test #1, heat flux contour plot, $t = 10$ min. . . . . 112
6.8 Characterization test #2, temperature line plot. . . . . 113
6.9 Characterization test #2, heat flux line plot. . . . . 113
6.10 Characterization test #2, temperature contour plot, $t = 24$ min. . . . . 113
6.11 Characterization test #2, heat flux contour plot, $t = 24$ min. . . . . 113
6.12 Characterization test #3, temperature line plot. . . . . 114
6.13 Characterization test #3, heat flux line plot. . . . . 114
6.14 Characterization test #3, temperature contour plot, $t = 24$ min. . . . . 115
6.15 Characterization test #3, heat flux contour plot, $t = 24$ min. . . . . 115
6.16 Characterization test #3, fire, $t = 7.5$ min. . . . . 115
6.17 Characterization test #3, fire, $t = 24$ min. . . . . 115
6.18 Characterization test #4, fire, $t = 24$ min. . . . . 117
6.19 Characterization test #4, temperature line plot. . . . . 117
6.20 Characterization test #4, heat flux line plot. . . . . 117
6.21 Characterization test #4, temperature contour plot, $t = 38$ min. . . . . 118
6.22 Characterization test #4, heat flux contour plot, $t = 38$ min. . . . . 118
6.23 Ventilation obstruction panel, fully opened. . . . . 119
6.24 Ventilation obstruction panel, fully closed. . . . . 119
6.25 Characterization test #5, fire, $t = 10$ min. . . . . 119
6.26 Characterization test #5, fire, $t = 21$ min. . . . . 119
6.27 Characterization test #5, temperature line plot. . . . . 120
6.28 Characterization test #5, heat flux line plot. . . . . 120
6.29 Characterization test #5, temperature contour plot, $t = 32$ min. . . . . 120
6.30 Characterization test #5, heat flux contour plot, $t = 32$ min. . . . . 120

6.31 Obstruction panel opening angle measurement. . . . . 121
6.32 Characterization test #6, fire, $t = 12$ min. . . . . 121
6.33 Characterization test #6, temperature line plot. . . . . 122
6.34 Characterization test #6, heat flux line plot. . . . . 122
6.35 Characterization test #6, temperature contour plot, $t = 32$ min. . . . . 122
6.36 Characterization test #6, heat flux contour plot, $t = 32$ min. . . . . 122
6.37 Renovated compartment interior following the test #6 structural failure. 123
6.38 Characterization test #7, temperature line plot. . . . . 124
6.39 Characterization test #7, heat flux line plot. . . . . 124
6.40 Characterization test #7, temperature contour plot, $t = 30$ min. . . . . 124
6.41 Characterization test #7, heat flux contour plot, $t = 30$ min. . . . . 124
6.42 Characterization test #8, temperature line plot. . . . . 125
6.43 Characterization test #8, heat flux line plot. . . . . 125
6.44 Characterization test #8, temperature contour plot, $t = 40$ min. . . . . 125
6.45 Characterization test #8, heat flux contour plot, $t = 40$ min. . . . . 125
6.46 Characterization test #9, temperature line plot. . . . . 127
6.47 Characterization test #9, heat flux line plot. . . . . 127
6.48 Characterization test #9, temperature contour plot, $t = 35$ min. . . . . 127
6.49 Characterization test #9, heat flux contour plot, $t = 35$ min. . . . . 127
6.50 Characterization test #10, temperature line plot. . . . . 128
6.51 Characterization test #10, heat flux line plot. . . . . 128
6.52 Characterization test #10, temperature contour plot, $t = 40$ min. . . . . 128
6.53 Characterization test #10, heat flux contour plot, $t = 40$ min. . . . . 128
6.54 Characterization test #11, temperature line plot. . . . . 129
6.55 Characterization test #11, heat flux line plot. . . . . 129
6.56 Characterization test #11, temperature contour plot, $t = 35$ min. . . . . 129
6.57 Characterization test #11, heat flux contour plot, $t = 35$ min. . . . . 129

6.58 Characterization test #12, temperature line plot. . . . . 130
6.59 Characterization test #12, heat flux line plot. . . . . 130
6.60 Characterization test #12, temperature contour plot, $t = 40$ min. . . . . 130
6.61 Characterization test #12, heat flux contour plot, $t = 40$ min. . . . . 130
6.62 Upper layer fire gas temperature, tests #8–12. . . . . 131
6.63 Incident heat flux to the centre of the wall, tests #8–12. . . . . 131
6.64 Average upper layer fire gas temperature and incident heat flux to the centre of the wall over the five repeat characterization tests. . . . . 133

7.1 Wood stud frame mounted in the fire test apparatus. . . . . 139
7.2 Frame insulation and mounting details. . . . . 139
7.3 In-cavity thermocouples, insulated cavities. . . . . 139
7.4 Thermocouple surface attachment details. . . . . 139
7.5 In-cavity thermocouples, uninsulated cavities. . . . . 140
7.6 Insulated pads for surface thermocouples. . . . . 140
7.7 Finished wall, unexposed side, filled bottom gap. . . . . 141
7.8 Finished wall, exposed side, dried and sanded. . . . . 141
7.9 Test #1, fire gas temperatures, slice average. . . . . 142
7.10 Test #1, fire gas temperatures, rake average. . . . . 142
7.11 Real wall test #1, fire-side camera, 66.1 min. . . . . 143
7.12 Real wall test #1, fire-side camera, 79.5 min. . . . . 143
7.13 Test #1, main wall temperatures, cavity averages. . . . . 144
7.14 Test #1, main wall temperatures, height averages. . . . . 144
7.15 Test #1, back wall temperatures, cavity averages. . . . . 145
7.16 Test #1, back wall temperatures, height averages. . . . . 145
7.17 Real wall test #1, unexposed side of the wall, inadequate wallcovering. . 146
7.18 Test #2, fire gas temperatures, slice average. . . . . 147
7.19 Test #2, fire gas temperatures, rake average. . . . . 147

7.20 Test #2, main wall temperatures, cavity averages. . . . . 148
7.21 Test #2, main wall temperatures, height averages. . . . . 148
7.22 Real wall test #2, fire-side camera, 62.1 min. . . . . 149
7.23 Real wall test #2, fire-side camera, 110.3 min. . . . . 150
7.24 Test #2, back wall temperatures, cavity averages. . . . . 150
7.25 Test #2, back wall temperatures, height averages. . . . . 150
7.26 Test #3, fire gas temperatures, slice average. . . . . 151
7.27 Test #3, fire gas temperatures, rake average. . . . . 151
7.28 Real wall test #3, fire-side camera, end-of-test. . . . . 152
7.29 Real wall test #3, cool-side camera, end-of-test. . . . . 152
7.30 Test #3, main wall temperatures, cavity averages. . . . . 153
7.31 Test #3, main wall temperatures, height averages. . . . . 153
7.32 Test #3, back wall temperatures, cavity averages. . . . . 154
7.33 Test #3, back wall temperatures, height averages. . . . . 154
7.34 Test #4, fire gas temperatures, slice average. . . . . 155
7.35 Test #4, fire gas temperatures, rake average. . . . . 155
7.36 Real wall test #4, fire-side camera, 55.6 min. . . . . 155
7.37 Real wall test #4, cool-side camera, 107.8 min. . . . . 156
7.38 Real wall test #4, cool-side camera, end-of-test. . . . . 156
7.39 Test #4, main wall temperatures, cavity averages. . . . . 157
7.40 Test #4, main wall temperatures, height averages. . . . . 157
7.41 Test #4, back wall temperatures, cavity averages. . . . . 158
7.42 Test #4, back wall temperatures, height averages. . . . . 158
7.43 Test #5, fire gas temperatures, slice average. . . . . 159
7.44 Test #5, fire gas temperatures, rake average. . . . . 159
7.45 Real wall test #5, fire-side camera, 27.1 min. . . . . 159
7.46 Real wall test #5, fire-side camera, 68.2 min. . . . . 160

7.47 Real wall test #5, fire-side camera, end-of-test. . . . . 161
7.48 Test #5, wall temperatures, infrared camera, 40.0 min. . . . . 161
7.49 Test #5, fire gas temperatures, infrared camera, 60.0 min. . . . . 161
7.50 Test #5, main wall temperatures, cavity averages. . . . . 162
7.51 Test #5, main wall temperatures, height averages. . . . . 162
7.52 Test #5, back wall temperatures, cavity averages. . . . . 163
7.53 Test #5, back wall temperatures, height averages. . . . . 163
7.54 Condition of the EW1 wall in the furnace test after 60 min of exposure. . 165

# List of Symbols

$A$ surface area of an object.

$\alpha$ lumped heat transfer parameter.

Bi Biot number.

$\beta$ lumped heat transfer parameter.

$c_p$ specific heat capacity of a substance.

$\Delta$ discrete step change in a variable (e.g. time, temperature, position, etc.).

$\delta$ characteristic length (e.g. thickness of a thermally-thin object).

$E_b$ blackbody emissive power.

$E$ emissive power.

$\varepsilon$ emissivity of a surface.

$F$ state transition model.

$\Gamma$ control input model.

$h_c$ heat transfer coefficient for convective heat transfer.

$h_e$ effective heat transfer coefficient for radiation and convection heat transfer.

$h_r$ heat transfer coefficient for radiation heat transfer.

$K$ Kalman gain.

$k$ time step.

$\kappa$ thermal conductivity of a substance.

$\lambda$ wavelength (in the electromagnetic spectrum).

$m$ mass of an object.

$\mu$ mean.

$P$ state variable, covariance.

$\rho$ density of an object.

$\phi$ process covariance gain.

$\varrho$ reflectivity of a surface.

$Q$ process covariance.

$q''_c$ convective heat flux out of a surface.

$q''_{net}$ net heat flux out of a surface (convection and radiation).

$q''_{r,e}$ radiant heat flux emitted from a surface.

$q''_{r,i}$ incident radiant heat flux, the radiative heat flux incoming to a surface.

$q''_{r,net}$ net radiant heat flux out of a surface.

$q''_{r,o}$ radiant heat flux reflected from a surface.

$R$ measurement, covariance.

$\sigma$ contextual — standard deviation or Stefan-Boltzmann constant.

$\sigma^2$ variance.

$T_\infty$ temperature of gases near to a surface.

$T$ temperature variable.

$\tau_{atm}$ transmissivity of a homogenous and isothermal atmosphere.

$t$ time variable.

$u$ control input.

$V$ volume of an object.

$x$ state variable, mean.

$y$ residual between measurement and state estimate.

$z$ measurement, mean.

# Chapter 1

# Introduction

A fire may be described as a physical manifestation of a chemical reaction [1] — an exothermic combustion process resulting in the generation of reaction products and the release of thermal energy. While this definition may be technically suitable, it does not represent the real-world experience of fire fighters and fire scientists. Fire is a generalized term, and can refer to something as simple as a candle flame, or as complex as a fully involved building fire. Furthermore, a fire is a dynamic process, evolving over time with changes both in the fuels involved and in the surrounding environment.

The present body of work is concerned with fires of compartment-scale, i.e. fires occurring in a physical volume that is consistent in size with a small room in a building, and involving solid fuels which may typically be found in a building. The study of compartment fires and the involved dynamics is an important and historically relevant aspect of fire safety engineering [2]. The motivation for research in this field is to better design structures with improved fire safety, both to reduce the likelihood of the occurrence of a building fire, and to mitigate the extent of damages and loss of life in the event of a building fire. As detailed below, the present work contributes to this field by advancing the current understanding of the impact of real fires on structures.

One component of compartment fire dynamics is the relationship between the fire, the gas environment within the compartment, and the solid boundaries of the compartment (walls, floors, and ceilings). As a fire grows within a compartment, gaseous combustion products accumulate and migrate toward the ceiling, and the compartment boundaries are subsequently heated. In many cases compartment boundaries are constructed in

part from combustible materials*, and will undergo thermal degradation (chemical decomposition as well as physical damage) upon exposure to a fire. If a boundary degrades sufficiently, fire can spread into adjoining compartments. One design paradigm for fire safety in buildings is to compartmentalize different regions of a building using partitions that have been demonstrated to be resistant to the spread of fire. To fulfill this objective, a partition must be able to inhibit the transport of heat, flames, and smoke in the event of a fire [3].

Many compartment boundaries are comprised of a number of different materials assembled in a particular configuration; such boundaries can generally be termed "construction assemblies". The materials that comprise construction assemblies are typically non-homogeneous in composition, and many are classified as being combustible. The thermal degradation of these materials is a complex process, and while a great deal of recent research has been directed toward understanding this process (Chapter 2), much work remains to be done on diversifying and generalizing this knowledge for use in fire analyses. Notably, most thermal degradation analyses focus on small-scale scenarios, in which physical damage is not prevalent. The damage that construction assemblies undergo at the large-scale as a result of fire exposure presents an additional layer of complexity. Certainly both decomposition of the materials and the physical stresses induced within the materials are relevant factors, however there is a dearth of knowledge of the underlying mechanisms for various damage phenomena.

Limited understanding of the mechanisms for thermal degradation does not preclude the prescription of fire safety requirements in structures. In Canada, conformance is achieved by an empirical process: the fire resistance of an assembly is evaluated in a standard test [5, 6] and a fire resistance rating is subsequently assigned. An assembly may then be used in a particular type of application within a building according to the prescribed code requirements [3]. This process can result in deficiencies in the identification of fire hazards (e.g. the impact of compartmentalization on fire growth rates), and is restrictive both to novel design (e.g. atypical structures) and to design optimization (i.e. fire safety, structural integrity, sustainability, energy efficiency, etc.). A performance-based approach, wherein the fire safety of a given assembly for a particular end use may be evaluated using engineering analyses, has significant advantages in this regard. Not only would it facilitate the rapid deployment of novel designs, but it could lead to implementations with better optimized fire protection capabilities [7].

*The National Building Code of Canada [3] defines a "combustible material" as any material that fails to meet the non-combustibility conditions of a CAN/ULC-S114 [4] combustibility test.

Predictive modelling might be utilized in a performance-based approach to evaluating the fire safety performance of a construction assembly in a structure, but would require an in-depth understanding of the thermal degradation mechanisms, a reliable set of measured thermophysical properties, and independent testing for validation. While research is ongoing in this area, and the complexity of physical models is ever-increasing, current approaches are not well validated beyond the relatively simplistic case of prediction of thermal penetration into a composite construction assembly exposed to the standard fire resistance exposure. This is troublesome since fire exposures in real building fires can vary greatly from that of the fire resistance furnace; some issues include (but are not limited to): spatial non-uniformity, growth rates and intensity, convective flows, smoke and species interactions, and flashover potential. Perhaps the most significant issue is localized regions of exposure, such as those that occur when a fire is located near a construction assembly, and those that occur on vertical fire separations (walls) as a result of the natural stratification of hot gases that evolves in a compartment fire.

Development of the next generation of thermal degradation models for construction assemblies requires detailed study of the phenomena occurring at the large-scale, and in the context real fires. Controlled experiments specifically tailored for this purpose are required, and a diverse set of experimental results are required for model validation. Therefore, the main objectives of the present work are:

- to design and implement a novel and controlled large-scale experiment tailored specifically for the study of thermal degradation of construction assemblies in real fires; and
- to demonstrate the utility of the experimental procedure in facilitating the detailed study of large-scale thermal degradation phenomena.

The scope of the present work is limited to a particular type of construction assembly, fire resisting compartment partitions (walls), though the experimental method is adaptable to other scenarios. Once developed, the procedure will be applied in the conduct of a series of fire tests on walls that are typically found in residential buildings in Canada. In the tests, the response of the walls to realistic fire exposures will be monitored, and a relevant set of data will be produced from measured results. This data will be of direct use in supporting the development and validation of future models of thermal degradation of construction assemblies.

The structure of the present dissertation is outlined as follows. First, background information related to the fire performance and thermal degradation of construction

assemblies is presented in Chapter 2, along with a clarification of the motivation and intended outcome of the present research endeavour. Chapter 3 details the conduct and findings of a preliminary investigation, for which the purpose was to evaluate the suitability of various experimental techniques for the study of thermal degradation of construction assemblies in real fires. Based on the findings of this preliminary work, a refined experiment was designed (as detailed in Chapter 4) and characterized (as detailed in Chapter 6), the latter necessitating the development of a novel method for measurement of heat flux in a large-scale fire test (which is presented in Chapter 5). Finally, a series of experiments was conducted on various fire resisting compartment partitions, and the results of these tests are presented and discussed, as well as the utility of the experiment for study of thermal degradation of construction assemblies, in Chapter 7. The dissertation concludes with the main findings and contributions of the work (Chapter 8).

# Chapter 2

# Background

This chapter gives an overview of the role of construction assemblies and performance requirements for fire separations in Canadian buildings, with a focus on residential construction, which is the area of interest in the present research. Next, the topic of thermal degradation of construction assemblies, in the context of building fires, is explored. Finally, the state of the art in experimental investigation and modelling of the thermal degradation of construction assemblies is outlined.

## 2.1 Fire Resistance of Construction Assemblies

The National Building Code of Canada (NBC)* [3] outlines the prescriptive requirements for fire safety in Canadian buildings. A subset of those requirements are outlined here for residential buildings to provide context to discussions that follow.

A typical fire occurring in a building is, at least initially, confined to a single room or compartment. One of the design paradigms in building science is referred to as "compartmentalization"; as it pertains to fire safety, the idea is to design a building with appropriate fire separations to confine a fire to its compartment of origin. The NBC defines a fire separation as a construction assembly (e.g. wall, ceiling, floor) that acts as a barrier against the spread of fire, and has a specified fire resistance rating {NBC:B-3.1.8.1}. The prescribed condition for thermal failure of a fire separation is contingent upon the hazard level of adjoining compartments. A compartment containing a large

*In-text references to the National Building Code of Canada in this section use the following format: {NBC:<*Division*>-<*Section*>}.

quantity of flammable materials (e.g. a large fire load[†]) represents a greater hazard than one containing fewer flammable materials. Accordingly, the NBC defines high-, medium-, and low-hazard occupant spaces by usage {NBC:A-1.4.1.2}, and stipulates the level of fire protection required for separation of occupant spaces {NBC:B-3.1.3.1}. The level of fire protection of a fire separation is quantified by a fire resistance rating: the duration for which a fire separation can withstand a specific controlled fire exposure in a fire resistance test without undergoing thermal or structural failure as defined by the test. Fire resistance ratings in Canada are determined using a fire resistance test such as ASTM E119 [5] or CAN/ULC-S101 [6].

In a fire resistance test, a construction assembly is subjected to exposure from a furnace enclosure, which is heated by a series of gas burners. For walls, thermocouples located 6 in (152 mm) from the exposed face of the wall record the furnace temperature, and the gas flow rate to the burners is adjusted with time to equate the measured furnace temperature to that prescribed in the relevant test standard; the temperature-time curve prescribed in ASTM E119 [5] is shown in Figure 2.1. Failure of the separation occurs when an average temperature rise of more than 140°C is measured on the unexposed side of the construction assembly, or when a maximum temperature rise of more than 180°C is measured at any one point on the unexposed side, or when flames or gases hot enough to ignite cotton are observed to pass through the separation at any location.

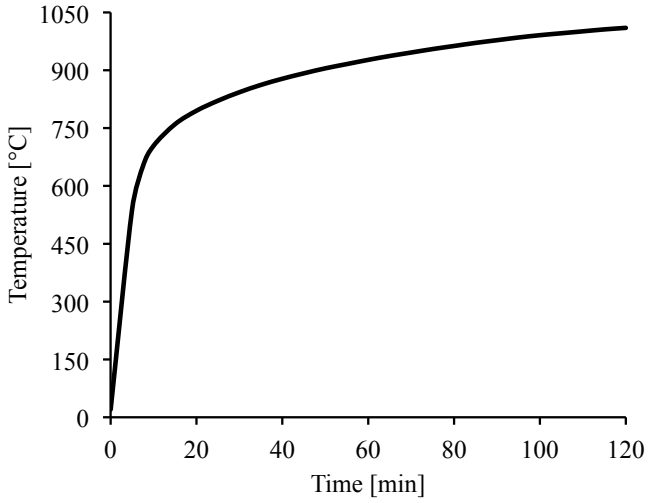


Figure 2.1: Furnace temperature curve prescribed in the ASTM E119 fire resistance test.

[†]A fire load represents the potential severity of a hypothetical fire, calculated from the products of the calorific values of the materials present and their mass, divided by the compartment floor area ($kJ \cdot m^{-2}$).

A typical residential house (referred to as a "single dwelling unit residence" in the NBC) does not contain occupant spaces other than residential and therefore does not required fire separations. An exception to this is the common scenario of a single dwelling unit residence with an attached garage. Since these spaces represent different major occupancies, it might be argued that a fire separation should exist between a garage and adjoining residence. This would be a reasonable argument considering the potential hazards that might exist in a garage space, for example: vehicles, combustible storage, and flammable liquids. This situation warrants a special exception in the NBC: no fire separation is required provided that the garage serves only a single dwelling unit, contains no more than 5 vehicles, and the construction between the storage garage and the dwelling unit provides an effective barrier to gas and exhaust fumes {NBC:B-3.3.4.2}. This requirement is satisfied by the installation of an air barrier system between the garage an the remainder of the building {NBC:B-9.10.9.16}.

As the number of dwelling units in a single residence increases, so too do the fire protection requirements. Multiple dwelling unit residences usually require that adjacent suites be separated by a 45 minute fire separation, or 1 hour for multiple-storey suites. For example, a Group C occupancy building (residential) of no more than 3 stories in height generally requires 45 minute fire resistance ratings on floors, mezzanines, and load bearing walls {NBC:B-3.2.2.52}. Walls in a house with multiple suites which separate dwelling units from each other need not comply with this requirement provided they are protected by a continuous smoke-tight barrier with a minimum of 1/2 in (12.7 mm) thick gypsum board installed on both sides of walls {NBC:B-9.10.9.14}. A requirement does exist, however, for sound control — walls must provide a sound transmission class rating[‡] of at least 43 {NBC:B-9.11.2.1}. The NBC contains a number of reference construction assemblies with listed fire resistance and sound transmission ratings. It is observed that the majority of these rated wall assemblies with sound transmission class of 43 also have fire resistance ratings of 45 minutes or more {NBC:B-A.9.10.3.1}. So even though a fire separation is not prescribed in this scenario, it is likely that some level of inherent fire resistance does exist in walls separating multiple suites in such a structure.

Fire resistance ratings for a number of NBC reference assemblies have been developed from information gathered from fire resistance tests, and by extrapolation in some cases {NBC:B-A.9.10.3.1}. Assemblies not included in the NBC, for example those incorporating new materials, must be tested by the manufacturer or designer to determine

[‡]Sound transmission class is a rating of sound attenuation performance of construction assemblies; tests are conducted according to ASTM E90 [8] and classified according to ASTM E413 [9].

their fire resistance rating. For example, a particular brand of R12 insulation may have been tested by its manufacturer in a given wall configuration and found to provide 45 minutes of fire resistance. Builders could then select this insulation knowing that it would adhere to the NBC for a given scenario. If a change occurs in performance requirements, such as Supplementary Standard SB-12 of the Ontario Building Code mandating a thermal efficiency of R14 in the same scenario [10], the manufacturer would be required to develop a new material that conforms to the new requirements. Furthermore, this material would have to be tested for conformance to the fire resistance requirements of the NBC, even if the new design were based upon the identical material as that already rated. With the constantly evolving nature of building codes, the development of new building materials, and the costs of large-scale fire resistance testing, it is clear that the combined use of experimental investigation and predictive modelling for the estimation of real-world fire performance would provide a great benefit to the industry. This type of modelling requires an in-depth understanding of thermal degradation mechanisms of construction assemblies and their constituent materials when subject to realistic fire exposures; these topics discussed in the following sections.

## 2.2 Thermal Degradation of Construction Assemblies in Fires

Thermal degradation refers to the process by which a material or structure breaks down as its temperature becomes elevated. In the context of construction assemblies which undergo heating by exposure to fire, thermal degradation is an exceptionally complex process occurring simultaneously in multiple non-homogeneous materials, involving changes both at the chemical and structural levels, and driven by complex boundary conditions (multi-mode heat transfer, convective flow, and chemical reactions). The motivation for the study of thermal degradation in this context is to better understand the ability of a construction assembly to prevent the spread of fire within a structure. As described in Section 2.1, typically this is assessed experimentally in a fire resistance test, and expressed by a fire resistance rating. While the fire resistance rating is certainly a pertinent design parameter, it does not provide adequate information to support detailed fire safety analyses, e.g. fire spread between compartments, on a case-by-case basis. With better understanding of the underlying physics of thermal degradation, it becomes possible to develop predictive models capable of supporting such analyses.

Much work has been done to date on the study of thermal degradation at the material level. For combustible construction (in the context of residential walls), the most commonly used materials can be divided into three categories based on their usage: studs, insulation, and wall coverings.

### 2.2.1 Wall Studs

Both metal and wood studs are used in the fabrication of construction assemblies. While metal studs will not degrade in the traditional thermochemical sense, they will lose structural integrity at fire temperatures; the critical temperature[§] of lightweight steel studs is often taken to be 350–400°C [11]. Wood studs, on the other hand, will actively decompose as they are exposed to fire, with significant mass loss beginning at approximately 280°C, and 80% mass loss occurring by 400°C [11]. A great deal of literature exists on the thermal degradation of wood; Dietenberger and Hasburgh [12] provide an excellent background on this topic. Wood studs will contract and char as they burn, but retain much of their initial load capacity even with the reduced cross sectional area. Steel studs, on the other hand, undergo thermal expansion and lose much of their load capacity; for non-loadbearing walls, this typically does not present an issue from a fire resistance perspective. A comparison of the two options is provided by Sultan et al. [13, 14], who conducted full scale fire resistance tests on non-load bearing wall assemblies, and found that wood studs provided better fire resistance than steel studs in non-load-bearing walls with a double layer of gypsum on each side. One attributing factor was the delayed thermal penetration in the case of the wood studs, due to the lower thermal diffusivity of wood relative to steel. Notably, no particular benefits were noticed for walls with staggered or double-row stud frames.

Wood framing is the focus of this work, as it is currently the most prevalent framing type for residential construction in Canada, and there is recent demand to use wood in larger commercial and residential structures [15]. Typically these frames are built using 2×4 or 2×6 SPF lumber (high grade timber produced from various Canadian spruce, pine, and fir species). Studs may be installed in single-row, staggered, or double-row configurations, depending on the desired fire resistance (single-row having the least fire resistance). Studs may be spaced 16 in (406 mm) or 24 in (609 mm) on centres, although stud spacing does not tend to affect the fire resistance of the construction assembly [3].

[§]Critical temperature in this case is the temperature at which a steel member no longer meets its designed level of structural support in a given loading scenario.

In the case of wood studs, thermal degradation analyses must consider not only the thermochemical decomposition (charring) of the material, but also the resulting effect on the structural integrity of the construction assembly.

### 2.2.2 Insulation

Common insulation types used in construction assemblies include: batts (e.g. mineral wool), foam boards (e.g. polystyrene), loose-fill (e.g. cellulose), sprayed foam (e.g. polyurethane), and more. Primarily insulation is used to maintain the thermal environment and noise within a building at levels suitable for human comfort, but insulation also impacts a structure's ability to withstand a fire exposure. Many insulation materials are combustible and release toxic combustion products when heated and burned, causing a greater hazard for building occupants and emergency responders even in the early stages of a building fire. Mineral wool insulations are known to yield low levels of toxic combustion products [16], in general, and are most prevalent in modern residential constructions; these are are the focus of the present work. Mineral wool insulations may be divided into three categories: glass wool or fibreglass (manufactured from glass fibres), stone wool (manufactured from natural rock), and slag wool (manufactured from slag, which is a byproduct of various industrial processes, and may include components such as steel, copper, lead, and ceramics).

Mineral wool insulations are manufactured by melting the glass/rock/slag, and spinning the molten material to produce fibres, which are then formed into batts using organic binders (the exact composition of which is unique to the manufacturer and the product). The mass percent of binder is generally greater in fibreglass insulations (3–8%) compared to stone/slag wool insulations (0.5–3.5%) [17]. Both materials can achieve a non-combustible rating in the ASTM E136 [18] "tube furnace" test, and a flame spread rating of 15 in the ASTM E84 [19] "Steiner tunnel" test [20]. Despite the non-combustibility rating of the materials, both are known to burn under the right conditions. Upon exposure to direct flame, fibreglass insulation will melt, burn, and release smoke, earning it a Euroclass[¶] A2 rating; this degradation is caused first by the binder burn-off beginning at 250–350°C, followed by melting at 700–800°C [11, 22]. In contrast, stone/slag wool has a Euroclass A1 rating since it only experiences a mass loss consistent with burning of the binder content between 200°C and 550°C [23]. In

[¶]Euroclass is the European fire classification system for materials, construction products, and building elements; see BS EN 13501-1 [21].

accordance with the Euroclass system, the maximum services temperatures for fibreglass and stone/slag wool insulations are 450°C and 900°C, respectively [17].

Given its greater susceptibility for thermal degradation, construction assemblies using fibreglass insulation typically have lower fire resistance ratings than those using stone/slag wool. For example, Sultan et al. [13, 14] conducted full scale fire resistance tests on non-load bearing wall assemblies, and found that the fire resistance ratings of walls insulated with stone wool were 54% greater than those insulated with fibreglass.

### 2.2.3 Gypsum Board Wall Coverings

Aside from niche applications, gypsum board is by far the most prevalent form of wall covering used in fire resistant compartment partitions in Canada. Gypsum board is comprised of a core of calcium sulphate dihydrate sandwiched between layers of paper backing. As part of a construction assembly, gypsum board coverings can protect underlying components from direct fire exposure — in a fire resistance test, this delays thermal penetration, and is an important factor in achieving good fire resistance ratings. Additionally, some types of gypsum board use special additives such as glass fibres, which further enhance the fire resistance of construction assemblies in which they are used (e.g. "type X" or "firecode" gypsum board) [11].

As the material undergoes heating in a fire scenario, a dehydration/calcification reaction occurs at approximately 120°C [24]. This reaction absorbs thermal energy and produces a heat barrier effect at the surface of the material. As the material is heated, crystallized water is released and transformed into vapour, which is transported through the porous gypsum material by pressure and by molecular diffusion. When migrating into colder regions, the vapour can condense. This vapour transport and phase change are mechanisms for heat transport within the material, along with heat conduction. As the material continues to heat, a secondary reaction occurs between 210°C (Andersson and Jansson [25]) and 300°C (Groves [26]), completing the dehydration process. Finally, a third reaction has been observed to occur at temperatures in excess of 650°C (Groves [27]) for type X gypsum board, presumably due to the breakdown of the additives.

### 2.2.4 Construction Assemblies

In the previous sections, the thermal degradation of constituent wall components is described in terms of critical temperatures at which reaction phenomena occur. Typically

these are assessed by means of thermogravimetric analysis, which is a bench-scale experimental method for measuring the relative change in the mass of a material as a function of increasing temperature. Using this data, it is common to model the mass reduction of a material as its temperature increases by an Arrhenius equation [11]. At larger scales, however, these models must account for much more than single-component homogeneous reaction kinetics. Complicating the issue is that the temperature of the materials is not uniform, and is usually not known, therefore the drive for the thermal degradation must be specified in terms of a fire exposure. When multiple materials are involved, as is the case with a construction assembly, the complexity of the coupled heat and mass transport problem increases significantly. Engineering analyses of the thermal degradation ultimately adopt simplified models for these complex physics.

In the typical case, the problem is simplified to one of heat conduction within a solid material, and solved by a conservation of energy approach. One example of this is the Advanced Calculation Methods provision (Annex B) of Eurocode 5, Parts 12 [28], which provides a practical means by which to estimate the temperature rise and mass loss of a material, and is suitable for many engineering analyses. Effective temperature-dependent thermophysical properties of materials may be deduced by experimental methods: density (e.g. thermogravimetric analysis), specific heat capacity (e.g. differential scanning calorimetry), and thermal conductivity (e.g. heat transfer experiment[‖]); Sultan [30] provides an excellent listing of such properties relevant to the materials of interest here. These curves implicitly represent some thermal degradation phenomena; for example, Bénichou and Sultan [31] showed that the effective density of gypsum board decreases and the effective specific heat capacity increases at 120°C, corresponding to the occurence of the dehydration reaction. Such models can reproduce good estimates of some experimentally observed details; for example, Takeda and Mehaffey [32] used effective thermophysical properties to predict the temperature rise in layered gypsum board, and achieved excellent predictions of in-depth temperature rise, precisely capturing the inflection corresponding to the dehydration reaction at 120°C.

Beyond the basic energy conservation approach, mass transport and reaction kinetics can also be included in a model. Rigorous mathematical formulations have been

[‖]Since combustible materials decompose at elevated temperatures, it is difficult to measure thermal conductivity independent of other parameters. One approach is to use a custom heat transfer experiment to deduce thermal conductivity of a material using measurements of temperature, control of boundary conditions, and an energy conservation model. For example, Park et al. [29] used a slug calorimeter and heat conduction model to deduce the thermal conductivity of gypsum board up to 700°C.

produced (see Weber [24] and Manzello et al. [33] for two clear examples of such formulations). First, chemical reactions (e.g. wood decomposition, gypsum dehydration, insulation binder decomposition) must be represented by gas-phase and liquid-phase mass conservation, as well as energy conservation (typically these reactions are exothermic). This requires knowledge of:

- the porosity of each material;
- the density of each material;
- the initial moisture content each material;
- the fraction of the pore space in each material occupied by gas and liquid phases;
- the molar concentration of water vapour in the gas mixture;
- the amount of water condensed and adsorbed into the solid; and
- the temperature of all involved species.

Gas momentum must also be conserved, which is typically treated using Darcy's law for mass transport through a porous material. In addition to the above stated parameters, this requires knowledge of:

- the convective velocity of the gases;
- the diffusivity of the gases;
- the permeability of each material; and
- the viscosity of the gases.

Finally, energy conservation cannot be neglected. In addition to the above stated parameters, this requires knowledge of:

- the specific heat capacities of the solids and the condensed and adsorbed vapours;
- the thermal conductivities of each solid-phase material; and
- the enthalpies of state and phase change, not only for exothermic combustion reactions, but also for evaporation/condensation and adsorption/desorption.

Although more complex thermal degradation models are a better representation of the underlying physics, the reality is that model uncertainty increases with model complexity due to the uncertainty in many of the necessary input parameters. For example, Bal et al. [34] applied five different models of varying complexity, which used between 3 and 30 input parameters depending on the model, to the problem of computational

pyrolysis of polymethylmethacrylate (a process similar in theory to decomposition of wood, insulation, or gypsum board). They found that the predicted results of all models achieved similar levels of accuracy, due to the additional uncertainty introduced in the more complex models. This work highlights an important issue with complex models of decomposition: there is a very real possibility that compensation effects will exist between the implemented mechanisms.

Regardless of the complexity of the model used to represent thermal degradation, it is clear that the process is fundamentally dependent on the temperature of the involved materials (which is, in turn, driven by the fire exposure). To properly investigate the thermal degradation of construction assemblies, it is crucial to have information on the temperature of the materials over time. Therefore, in any experiment tailored for studying thermal degradation phenomena, temperature of the involved materials must be considered a required measurement. With this in mind, the following section outlines the state of the art in the experimental study, and modelling, of the thermal degradation of construction assemblies in fires.

## 2.3 State of the Art on the Thermal Degradation of Construction Assemblies

The previous section outlined some of the criteria for experimental investigation and modelling of thermal degradation. As applied to construction assemblies subjected to a fire, such models may be termed "fire endurance" models. In this context, the term fire endurance is used to describe the ability of a construction assembly to withstand a fire exposure; there is no implied performance requirement. Fire endurance models simply aim to predict the thermal degradation of a construction assembly in terms of its temperature, decomposition (mass loss), and structural integrity. fire resistance models are a subset of fire endurance models with the specific requirement that the fire exposure corresponds to that of a fire resistance test, and the intent is to predict failure of construction assemblies according to the performance criteria of the test.

Fire endurance is an important concept in fire safety engineering because real building fires will never produce exposure conditions consistent with a fire resistance test (i.e. uniform spatially and consistent with a prescribed temperature-time relationship), yet analyses of real-world problems are necessary. For example, a fire safety engineer

might need to analyze how a code-compliant fire separation would hold up to low-intensity high-probability fires in order to assess the potential for long-term damage to that separation in the event of a small fire. Alternately, during a fire investigation, it might be necessary to estimate the failure of a given wall in order to ascertain when and how the fire spread to adjacent rooms. This latter calculation, when based simply on the assumption that the wall failed completely after the time specified as its fire resistance rating, will not result in a sensible re-creation of the fire scenario.

The basic form of a fire endurance model is a solution to the transient thermal degradation problem of a construction assembly subject to a fire exposure on one side, with some other conditions (typically an ambient environment) on the unexposed side. The boundary conditions that evolve on both sides of the construction assembly consist of convective and radiative heat exchange with the exposed- and unexposed-side environments, as well as mass transport of vapours due to the interactions between fire/ambient gases and the reacting solid boundary materials. Heat conduction and in-cavity convection and radiation occur within the construction assembly, as well as mass transport through any porous materials (driven by temperature and pressure gradients); heat generation from the typically exothermic decomposition reactions of the constituent materials also occurs. Analytic solutions of this problem are generally not possible, unless gross assumptions are used. Numerical solutions may be adopted, which use spatial and transient discretization and a solution methodology that can incorporate physics sub-models and temperature-dependent material properties. The desired outputs of such models include temperature, mass loss, and structural integrity. This third parameter, which describes large-scale degradation phenomena (e.g. gypsum board paper burn-off, shrinkage, cracking, joint separation, and ablation/sloughing), is as yet very difficult to quantify and model.

### 2.3.1 Early Development of Fire Endurance Models

An early fire resistance model was developed by Fischl in the 1950s [35]. He derived an expression for the rate of temperature rise on the unexposed side of a wall that was subjected, on the exposed side, to the standard fire conditions specified by the BS 476 furnace test (ostensibly the same fire curve as ASTM E119 [5]). The model was essentially an approximate analytical solution to a one-dimensional thermal resistance network. A uniform heat flux boundary condition was assumed on the exposed side of the wall, which was treated as a semi-infinite slab (no side boundary interactions) made

of a single material with constant thermophysical properties. Thermal degradation, multi-component characteristics of the wall, and structural failure mechanisms were not considered. With these simplifications, the model was found to be unsuitable for prediction of wall response to conditions of high thermal exposure as in a fire, although it was found to be well suited to situations where the wall was exposed to lower temperatures, such as home heating and cooling applications. Nonetheless, this type of fundamental analysis was a starting point for more in depth models in the future.

By the 1960s, Tjoan [36] had built upon the simplified one dimensional wall model of the type described above by accounting for the change in thermal conductivity of the wall materials with increasing temperature. Experiments were conducted on concrete and clay brick walls between 5 cm and 17 cm thick using the standard fire resistance exposure on one face, and measuring the temperature of the walls. A power law relationship between thermal conductivity and temperature was assumed and coefficients were determined to facilitate agreement between experimental and calculated results. This work demonstrated that the use of temperature-dependent thermophysical properties, which in this case were essentially a representation of un-modelled physics, could yield better temperature predictions in a fire resistance model. This work also highlights an important problem that even modern thermal degradation and pyrolysis models can suffer from [34] — the derived "properties" are not properties at all, but are tuning parameters used to minimize the differences between modelled and experimental results. The implication of this is that these properties cannot be universally applied, for example, to a scenario with a non-standard fire exposure. It is crucial that the thermophysical properties of each material involved, as outlined previously in Section 2.2.4, be determined and validated by independent experiment.

Improvements to the one dimensional models for conductive heat transfer through walls continued through the 1990s. As computing resources facilitated ever-increasing complexity of numerical analyses, the semi-infinite slab assumption was no longer necessary — the thermal resistance network could be discretized in both time and space. In addition to basic principles of heat transfer, models began to incorporate the effects of heat generation and mass transport within the wall materials. For example, in 1997 Harada [37] investigated the behaviour of concrete walls subjected to a uniform thermal exposure similar to that of the CAN/ULC S101 [6] furnace. Both heat and mass transport (water vapour only) were modelled in one dimension for a solid wall of a single material with constant thermophysical properties. Harada was able to demonstrate and model the phenomenon of rapid temperature rise around 100°C and delayed temperature rise

from 100°C to 150°C as a result of water vapour transport within the concrete. This phenomenon is relevant for all porous building materials, including gypsum board as outlined in Section 2.2.

### 2.3.2 Prediction of Fire Resistance of Construction Assemblies

A significant breakthrough in the development of fire endurance models for walls came in 1998 when Takeda and Mehaffey [32] released the `WALL2D` model. `WALL2D` was a two-dimensional (depth and height) model for predicting heat transfer through uninsulated wood-stud walls with gypsum board wall coverings. The model used temperature dependent properties for gypsum board with the input values of material density, specific heat, and thermal conductivity determined via independent experiments. The combined effects of gypsum board shrinkage and paper burn-off were accounted for by adopting an experimentally-derived relationship between the the net shrinkage (depth, into the wall) and the wall temperature. Combustion of the wood studs was also modelled, assuming that water vapourization and pyrolysis (single-stage reaction) followed the 100°C and 288°C isotherms, respectively. Cavity gases were assumed to be non-participating, and in-cavity radiation was calculated using surface-to-surface view factors. In-cavity convection was accounted for by assuming a constant convection coefficient of 9 $\mathrm{W{\cdot}m^{-2}{\cdot}K^{-1}}$.

`WALL2D` model results were consistent with those of small-scale experiments conducted in an electrical furnace, and with full-scale fire resistance tests. In these, the walls were instrumented with thermocouples and moisture probes to track temperature evolution and vapour transport. The radiative exposures used in both of the experiments were spatially uniform over the entire wall, so any vertical thermal gradients predicted by the model were solely a consequence of buoyancy effects within the wall cavity itself. The model was found to be capable of making excellent predictions of temperature rise at the small-scale, capturing temperature inflections corresponding to the onset of calcination as well as temperature rise up to 800°C through as many as four layers of gypsum board over two hours of exposure. Furthermore, it was able to predict the onset of charring of the wood studs in a furnace test to within 1.3%, and demonstrate good overall consistency with temperature measurements around the studs over a 60 min ASTM E-119 [5] test. A notable shortcoming of the model was its omission of damage mechanisms for the exposed-side gypsum board (cracking, ablation, etc.), and consequently, any secondary thermal effects that might have resulted from such phenomena. This is a threshold that must be overcome if such models are to be used to reliably predict wall degradation and

fire spread once damage has occurred.

In 1997, during the development of the previously-described WALL2D model, Lin and Mehaffey [38] used a combination of a zone fire model, CFAST [39, 40], and fire endurance model, WALL2D (a version pre-dating the 1998 release), to demonstrate a proof-of-concept of how to integrate a fire model with an independent model for heat transfer through a wall. CFAST was used to model a compartment fire environment for some prescribed fire. The thermal boundary condition on the compartment walls (note that all walls are treated as a single effective wall by a zone fire model [41]) was determined by the zone model predictions: height of the developing hot gas layer over time, average temperatures of the upper (hot) and lower (cool) gas layers, and the average heat flux to the walls in the upper and lower gas layer regions. Using the CFAST results as the boundary conditions, WALL2D was then used to model the resulting temperature profile within the wall. Six compartment fire scenarios were considered; the construction assembly selected was an uninsulated wood-stud wall with 1/2 in (12.7 mm) type X gypsum board wall coverings on both sides. No experimental validation was performed in conjunction with these scenarios as the study was meant only to demonstrate how an integrated fire and boundary analysis might be utilized to predict thermal failure of fire separations under a non-uniform fire exposure that is more typical of a realistic fire. Notable shortcomings were that the analysis was uncoupled (the impact of the degrading wall on the fire development was not considered), and that the vertical exposure domain consisted of only two regions.

Despite Lin and Mehaffey's [38] proof-of-concept, in 2001 fire endurance models were still predominantly used for the determination of fire performance in accordance with performance-based building requirements [42]. Although it had been shown that custom fire exposures could be specified and the ensuing boundary conditions applied, these models were still primarily used with the uniform fire resistance test exposure. This also meant that validation experiments were limited to furnace exposures. Instead of pursuing coupled analysis, researchers chose instead to extend fire endurance models to account for additional phenomena such as non-constant wall geometry, re-entrant corners and gaps, radiation within the wall cavity, mass transport through wall materials, and certain details of thermal degradation of gypsum board such as cracking and ablation.

Of relevance to the present research, Clancy [42] found that for uninsulated partitions, in-cavity radiation into the studs was the dominant mode of heat transfer at high temperatures. Structural weakness of studs became apparent when the majority of a given stud reached 100°C due to vapours expanding through the wood pores and distributing heat.

Further, Clancy compared model predictions using material properties for wood and gypsum board determined by other researchers and found that independently obtained material properties could be used in a fire endurance model, with careful consideration to match the methods of determination of those properties to their use in predicting the phenomena of interest. An example of this is the use of temperature-dependent specific heat capacity and density to account for heat generation and mass loss associated with phase change and thermo-chemical reactions in the gypsum board [43]. The assumption of gypsum board cracking occurring at a critical temperature had been adopted, but gypsum board from different manufacturers was found to crack at very different temperatures [42] — the damage model was clearly an oversimplification. Furthermore, since multi-layered gypsum board construction was quite common, it was noted that fire endurance models should be extended to account for sequential sloughing of the sheets.

Later research by Takeda [32] focused on other areas of improvement to `WALL2D`. These included modifications that allowed prediction of heat transfer through in-cavity fibreglass or stone wool insulation [44], as well as polystyrene and polyurethane foam insulation [45]. Simplified models for the opening of joints between gypsum sheets (over studs), and sloughing of gypsum layers, were also incorporated [44]. Finally, `WALL2D` was expanded to model heat transfer through wood-framed exterior walls with various types of external siding [46, 47]. During this period as well, Takeda [48] re-branded his version of the `WALL2D` model as `HTwall`, after which there appears to be no further development. It must be noted here that these advanced three-dimensional thermal degradation phenomena were represented using simplified relationships based on experimental data — `WALL2D` and `HTwall` were two-dimensional models only. Predictions in the context of a fire resistance furnace exposure were improved, but these relationships will not apply universally.

At around the same time, Clancy and Young [49] conducted full-scale furnace experiments to validate models for evaluating the fire resistance of uninsulated wood framed walls. Their approach differed from models that focused solely on thermal failure in that they considered the structural components. They designed an experiment to measure the applied structural load on wall members, and determined the structural load capacity of the assembly, which was then used in a fire resistance model to predict the time to failure by structural collapse. Two key shortcomings of the existing research into the fire endurance of walls were identified. These were: 1) limitations in understanding of the mechanisms contributing to structural failure of construction assemblies beyond simply the applied loads; and 2) a lack of consistency in the published values of the thermal properties for wood and gypsum across the literature. Further, based in part on Clancy's

previous work [42], they stressed the importance of using independent material property data rather than data tailored to ensure a fit between model and experiment. Clancy and Young further noted that for the uniform temperature exposures experienced during fire resistance tests, the use of two dimensional models was justified since variations in temperatures inside the wall cavity were mainly due to in-wall convection and changed primarily with height above the floor, while variations in temperature over the width of the wall were less significant. In a real fire however, the wall exposure is not uniform and thus, as is investigated in the present work, any two-dimensional simplification is likely not suitable.

### 2.3.3 Fire Endurance For Realistic Fire Exposures

Manzello et al. [50] in 2005 published one of the first detailed investigations into the response of partition walls to realistic compartment fires. In this work, a wall assembly was exposed to an intense compartment fire, with a total burn time of 45 min and a peak net heat flux to the wall of about 150 $kW \cdot m^{-2}$ after 13.5 min. This study is very pertinent to the present research, and therefore is reviewed in detail here.

The compartment used measured 10.7×7.0 m, and 3.4 m in height, with a single opening on one of the 7.0 m walls. The test wall, located opposite the compartment opening, measured 2.44×2.44 m (8×8 ft). The test wall was non-load bearing, and consisted of steel studs spaced 609 mm (24 in) on centres, with 15.9 mm (5/8 in) thick type X gypsum board (USG Firecode®) attached vertically to the studs using drywall screws, spaced at 305 mm (12 in). No insulation was used in these walls. All drywall joints were taped.

Water-cooled Schmidt-Boelter heat flux gauges were mounted flush to the exposed face of the gypsum board panels at four locations. It is apparent (from images present in the article [50]) that the post-test condition of the panels was different near the gauges locations. This speaks to a clear influence of the gauges on the decomposition of the gypsum board panels — not surprising considering that the gauges were maintained below 75°C with water cooling during the tests.

K-type, 22 gauge, bead-welded thermocouples were attached to the exposed side of the panels (methodology not indicated) and the unexposed sides of the panels (using insulating pads per ASTM E119 [5]) at 30 locations. During the fire, several exposed-side thermocouples failed (perhaps due to becoming detached from the wall). This points

to an important practical consideration of this type of fire test — instrumentation failure in the fire compartment must be accounted for in the experimental design.

In the tests, the temperature of the panel peaked at 750°C on the exposed face and 500°C on the unexposed face. Perhaps most interesting of these presented results are the observations of the post-test condition of the wall. Paper burn-off had occurred, both vertical cracks and transverse cracks were observed to have formed between the screw locations, and the vertical joint had opened and expanded. These damage events were likely caused by the contraction of the panels brought on by temperature increase and calcification of the material, and the resulting stresses which developed between fixture locations; ablation likely also played a role. While the post-test condition was certainly interesting, much insight would be gained if damage events could be observed in realtime.

Manzello et al. [33] in 2007 extended his experimental testing to compare the fire response of standard gypsum board to that of type X fire resistant gypsum board in the same compartment fire conditions. Despite its improved thermal properties, type X was found to be more prone than regular gypsum board to shrinkage and cracking at the mounting points at elevated temperatures; consequently, the overall fire performance (gauged in terms of thermal penetration to the unexposed side of the wall) of the two materials was found to be similar. The model did not capture this result because, although it took in-depth shrinkage into account, it did not capture the phenomena of shrinkage, cracking, and failure of the gypsum board propagating from fixture locations. The work of Manzello et al. [33, 50] confirmed that damage events occurring on a wall involved in a real fire can relate the dynamic response of the wall to the conditions of the fire compartment. The next step is to apply this knowledge to fire safety analyses. This requires the development of advanced models of thermal degradation, likely in three dimensions, and potentially with coupling of the dynamic fire environment to the degrading structures.

### 2.3.4 Recent Refinements to Fire Endurance Models

Based on the research of Manzello et al. outlined above, Kukuck [51] continued investigation of heat and mass transfer through uninsulated steel stud, gypsum covered partitions by incorporating simplified in-cavity radiation (transparent gas assumption), yielding incremental improvements in the accuracy of predictions.

In different research, Craft [52] developed a two-dimensional finite element model for

heat and mass transfer in uninsulated gypsum and wood frame floor assemblies. Craft used similar methods to Takeda et al. [45] for representing heat transfer processes, and focused in particular on mass transport. In `WALL2D`, a modified thermal conductivity and specific heat were used to model vapour transport and heat from evaporation and pyrolysis respectively in each material. In Craft's model, reaction volatiles and vaporization of moisture were considered in a mass transfer function. The rate of thermal degradation of wood and gypsum materials was modelled by Arrhenius expressions reliant on element temperature, and temperature-dependent material properties were used.

Craft's work culminated with development of `CUWoodFrame`, a model for simulating heat and mass transfer in gypsum and wood assemblies in order to predict the thermal response of a wood-frame floor assembly under fire exposure. Full-scale fire resistance tests (CAN/ULC-S101 [6]) were conducted using both the standard fire resistance test exposure, and an experimental curve that was designed to be representative of a house fire (different temperature-time curve, but still uniform spatially). In the tests, thermocouples were installed at various locations within the floor assembly: on the joists, between gypsum layers, on the inside surface of the gypsum board (in-cavity), and between gypsum board and joists. The model yielded good temperature predictions compared to experimental measurements for the standard furnace curve up to the point at which sloughing of gypsum board layers began. This is to be expected, considering that the model did not incorporate any mechanisms for gypsum sloughing. For the non-standard furnace curve, which was a significantly greater fire exposure, sloughing of gypsum layers began after only a few minutes of exposure, after which model predictions were unsuitable. This work highlights the importance of accounting for damage phenomena in a complex model of thermal degradation of construction assemblies.

Craft's [53] work reaffirmed the recommendation of Clancy [42]; almost a decade later, there was still a lack of robust and trustworthy thermophysical property data for the construction materials used. Craft et al. [54] attempted to address this by using the cone calorimeter to study the thermal degradation of wood and gypsum board (the same used in his earlier work) under the well-defined boundary conditions of the apparatus in order to obtain more representative thermophysical properties. While the results showed some improvement, it was concluded that significantly more work still needed to be done in terms of generating appropriate material property data for use in fire endurance models. This issue was further investigated by Saidu [55], who in 2011 reported on the spread in physical and thermal properties of wood and gypsum at elevated temperatures as published by researchers across the industry. This is to be expected to some degree

since some variability should be expected for manufactured materials such as gypsum or stone wool insulation, which may vary in composition over different manufacturers and even over different product lines from the same manufacturer. Similarly, raw materials such as dimensional lumber can vary in composition even from the same mill year-to-year. The determination of robust material data for specific materials continues to be an important area of research required to support thermal degradation modelling.

Building upon Craft's approach of using small-scale fire tests to study the thermal degradation of constituent materials, Aire et al. [56, 57] conducted a series of small-scale experiments on construction assembly mock-ups. Mock-ups were assembled in layers consisting of gypsum board, insulation, and SPF wood. The specimens were instrumented with thermocouples, placed in an insulated sample holder, and exposed to constant irradiation from the electric resistance heater of a cone calorimeter. Many of the same phenomena described previously, such as the representative reaction temperatures of each material, were reproduced at the small-scale. Furthermore, the results were used to validate a simple thermal degradation model (one dimensional in-depth conduction heat transfer using effective thermophysical properties); given the temperature measurements and well-defined boundary conditions, this data would also be useful for validation of more complex models in the future. Where the small-scale mock-up experiments fell short was in the reproduction of large-scale degradation phenomena, such as gypsum board shrinkage, cracking, joint separation, and ablation. Such effects cannot be reproduced at the small scale.

More recently Lu [58] developed a three-dimensional finite element model for uninsulated solid wood floor joist assemblies. Model setup was similar to that of Craft [52] with the exception of the inclusion of mass transport, which was represented as a percent reduction in density (a common simplification [43]). Arrhenius functions were used to determine the rates of chemical reaction (single-stage) for pyrolysis of wood joists and calcination of gypsum board, and moisture evaporation was assumed to occur locally along the 100°C isotherm (represented by an effective specific heat; mass transport was neglected). In-cavity radiation was simplified to surface-to-surface (no gas radiation, and no gas accumulation in-cavity due to the mass transport simplification). Gypsum board falloff was assumed to occur locally at joist interfaces when the temperatures between the wood joist and the gypsum board reached 300°C (a gross simplification). The solution methodology utilized a commercial finite element package (`ABAQUS`) and submodels for time-varying distributed heat flux on the exposed face (a simulated fire exposure), and a subroutine for internal heat generation from reactions and phase change.

Lu's model was used to predict failure (critical temperature criterion) of floor assemblies under exposure to a uniformly distributed furnace exposure. Predicted temperatures were compared to CAN/ULC-S101 [6] test results using the standard thermocouple placements, and to results obtained using Craft's [52] model. In all cases, temperature predictions were very good up to the point of gypsum falloff. Lu's research is encouraging in that it demonstrated that with modern computing resources it was possible to extend fire endurance models to three dimensions; it remains to be seen whether this level of modelling detail is necessary for fire endurance modelling of wall separations in realistic fire environments. Further investigation into the thermal failure mechanisms of covering materials is also necessary to advance the state of the art in this regard.

This section has outlined the development of fire endurance models over the past 60 years to their present state. The key points here are summarized in the following section, where the motivation and intended outcome of the present research is put into perspective.

## 2.4 Summary

Thermal degradation models for construction assemblies subject to a fire resistance test exposure have evolved to the point of being suitable for predicting the failure of some types of construction assemblies, up to the point of occurrence of significant damage events. These models have not been demonstrated to be suitable for all types of constructions and materials, and are not well validated for realistic fire exposures. The complexity (and utility) of these models is limited by the current understanding of thermal degradation phenomena, and the methods for representing these phenomena in a model. At the present time the most advanced models adopt a numerical solution of the heat and mass transfer equations over a three-dimensional finite element domain, typically incorporating basic reaction kinetics for the decomposition of constituent materials. These models are lacking in the capability to predict the occurrence of large-scale damage phenomena, as well as the impact of these events on further degradation of the assembly. Furthermore, models developed to date treat the fire exposure as a uniform boundary condition — incorporation of multidimensional exposure conditions or coupled analysis has not yet been fully realized (beyond one-dimensional treatments [59]).

Development of the next generation of thermal degradation models requires detailed study of the phenomena occurring at the large-scale, and in the context of a real fire. This

can only be accomplished by experimental methods. Experiments to date have mostly been limited to those that use uniform furnace exposures (e.g. the fire resistance curve), with very few exceptions. There is a need not only to conduct additional experiments tailored to the above stated purpose, but also to develop a methodology that will facilitate the generation of a diverse array of experimental data in a consistent and controlled manner. Given these requirements, the main objective of the present research is to design and implement a novel experimental method for the study of thermal degradation of construction assemblies, in particular fire resistant compartment partitions, in real fires.

As identified earlier in this chapter, it is crucial that the experimental method will incorporate measurements of the temperature of the construction assembly in multiple locations, as well as realtime observation of large-scale damage phenomena. Also, sufficient information must be gathered about the fire conditions in order to reproduce the exposure directly (e.g. as a boundary condition in a model of thermal degradation), or indirectly (e.g. as a set of field conditions which define the coupled relationship between a fire dynamics model and a thermal degradation model). The intended outcome is that the experiment to be implemented will include such measurements, and that the fire conditions will be characterized accordingly. Furthermore, it is expected that a contribution of this research will be the generation of a relevant set of experimental data from experiments involving construction assemblies that are used in residential buildings in Canada exposed to realistic fires.

To begin, a preliminary investigation was conducted for the purpose of evaluating the suitability of various experimental techniques for the study of thermal degradation of construction assemblies in real fires; this is the focus of the following chapter.

# Chapter 3

# Preliminary Investigation

A preliminary investigation of the thermal degradation of construction assemblies in large-scale fires was conducted in August of 2014. The main objectives for this phase of the research were to gain some insight into the damage and thermal penetration that a wall would experience when involved in a realistic building fire, and to assess various experimental methods for the study of these phenomena. To this end, a one-off compartment fire experiment was conducted in which a compartment was constructed of non-combustible materials except for a single wall, hereinafter referred to as the "test wall", which was a typical residential construction assembly. The test wall was then exposed to a compartment fire environment. A visual assessment of the post-fire damage to the wall was made, thermal penetration into the wall was measured, and the effectiveness of the experimental procedures adopted were evaluated.

This chapter details the findings of this preliminary investigation, which provided a foundation up which future work was based. The following section is concerned with the construction of the fire compartment; subsequent sections detail the test methodology, results, and findings of this phase of the research.

## 3.1 Construction of the Fire Compartment

A compartment was needed to house the test wall; at the University of Waterloo Fire Research Facility, the two-storey steel burn house structure shown in Figure 3.1 was both suitable and available for use in the study of large-scale building fires. The south-east corner of the building was selected as the location for the fire compartment. This location

was used in previous work for large-scale fires in other configurations, and a method for fire protection of the structure itself* had already been established [60].

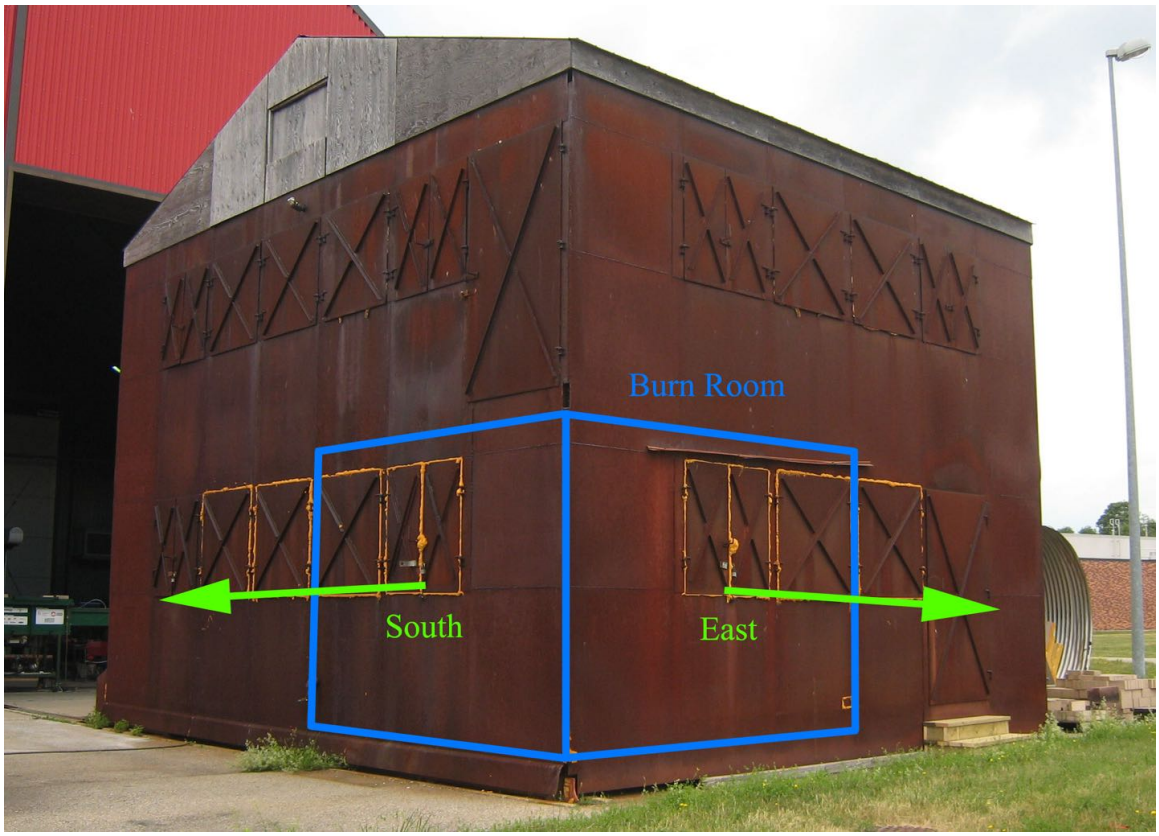


Figure 3.1: Burn house structure at the University of Waterloo Fire Research Facility.

The southeast corner of the structure is configured with a window on each of the east and south building faces, and an interior door on the west wall. It was decided to use this door as the sole source of compartment ventilation, therefore the windows were sealed with spray foam insulation, as is apparent in Figure 3.1. Given this layout, the north wall of the compartment was selected as the test wall.

The burn house structure is constructed of welded steel plate with I-beam supports. In order to retain heat within the fire compartment, the ceiling and walls of the compartment (aside from the designated test wall) were lined with insulating materials. From outside to inside, the compartment lining on the walls and ceiling consisted of [60]:

*The University of Waterloo steel burn house structure is used for various fire and smoke movement experiments. In these, direct fire exposure to the steel structure must be avoided due to the potential for thermal expansion, warping, and failure of welds.

- 3/4 in (19.1 mm) Radiant Barrier Sheathing (RBS) plywood attached to I-beam structural supports using high-strength beam clamps, 2 in (50.8 mm) cap screws, and 3/8 in (9.5 mm) washers;
- 1×4 spruce strappings attached to the underlying plywood using 2 in (50.8 mm) wood screws and 1/4 in (6.4 mm) washers; and
- 1/2 in (12.7 mm) Durock® cement board attached to the underlying strappings using 3-1/4 in (82.5 mm) Tapcon® concrete screws and 1 in (25.4 mm) fender washers.

Figure 3.2 shows the interior lining of the fire compartment at the time of the installation of cement board. Once the cement board was installed, joints were faced with mortar. Vertical studs were affixed at the location of the test wall, with the intention that the wall be mounted on these. A steel burn pad was also present in the room, a remnant of previous work [60], as shown in Figure 3.2.

Figure 3.2: Fire compartment with built-up cement board interior lining.

Fiberfrax Durablanket S® is a high temperature refractory ceramic fibre blanket designed for use in high temperature insulation applications such as furnace linings, gas turbines, and fire protection. Capable of withstanding temperatures up to 1430°C,

the material is lightweight, has low thermal conductivity and heat storage, high heat reflectance, and is extremely resilient to high temperature loading [61]. The compartment interior was lined with this material, and was held in place using 20 gauge 1 in (25.4 mm) hexagonal galvanized steel netting, which was affixed to the underlying cement board using 3-1/4 in (82.5 mm) Tapcon® concrete screws and 1 in (25.4 mm) fender washers. Figure 3.3 shows the fully insulated fire compartment.

Figure 3.3: Fire compartment with ceramic fibre insulation interior lining.

The insulated compartment had a footprint measuring 122×122 in (3.10×3.10 m), and was 92 in (2.34 m) high; the door measured 34 in (0.86 m) wide and 78 in (1.98 m) high. The steel burn pad was centred in the compartment, re-bricked with high temperature refractory bricks, and insulated underneath with Fiberfrax scraps.

With the construction of the fire compartment completed, the next step was to develop a test protocol and instrumentation scheme to support the investigation of thermal penetration into the test wall during a fire. The following section addresses this topic.

## 3.2 Instrumentation and Test Methodology

For this investigative study, the wall of interest was constructed to the "W1c" specification as defined in the NBC [3]. This type of residential construction assembly is often used for interior walls which separate a dwelling unit and an attached garage. It has a fire resistance rating of 30 min provided that the room is tight fitting. A wall with a low fire resistance rating was selected for this investigation in order to cause significant thermal penetration and damage to the wall with a fire of moderate intensity and duration. The NBC stipulates that this type of wall be constructed as follows:

- 1.5×3.5 in (38.1×88.9 mm) wood studs spaced 16 in (406 mm) on centres;
- 3.5 in (88.9 mm) thick absorptive material (insulation) in cavities;
- a layer of 1/2 in (12.7 mm) gypsum board on the inside (exposed) face; and
- a layer of 1/2 in (12.7 mm) gypsum on the outside (unexposed) face.

The options for absorptive materials in this assembly include fibre processed from rock, slag, glass, or cellulose, filling at least 90% of the cavity depth, and not overfilling the cavity to the point of producing significant outward pressure on the finishes. Note that the gypsum board barrier on the outside face of a W1c wall is optional, and other sheathing materials may be substituted provided they satisfy the tight fitting requirement (e.g. plywood, oriented strand board (OSB), or wafer board).

Based on these specifications, the test wall in this experiment was constructed using CGC Sheetrock® lightweight gypsum board, Roxul ComfortBatt® R14 stone wool insulation, and spruce studs and OSB sheathing from an Ontario mill. The exposed side of the wall was faced in gypsum board, while the unexposed side was faced in OSB. The wall measured 122 in (3.10 m) wide by 92 in (2.34 m) tall, with eight studs spaced 16 in (406 mm) on centres and a single stud spaced at 7 in (178 mm); this resulted in a total of seven full-width stud cavities. Figure 3.4 shows the wall as it was being constructed, with the stud frame and exposed-side gypsum board mounted in place. The photograph was taken from the unexposed side of the wall, such that the front of the compartment (with the door) was located on the right in the photograph. The small cavity was therefore located at the rear of the compartment.

It was necessary to instrument the wall with thermocouples (for measuring thermal penetration) before insulating and attaching wallcoverings to the unexposed side. The thermocouple budget was dictated by the data acquisition system (DAQ) used, which was

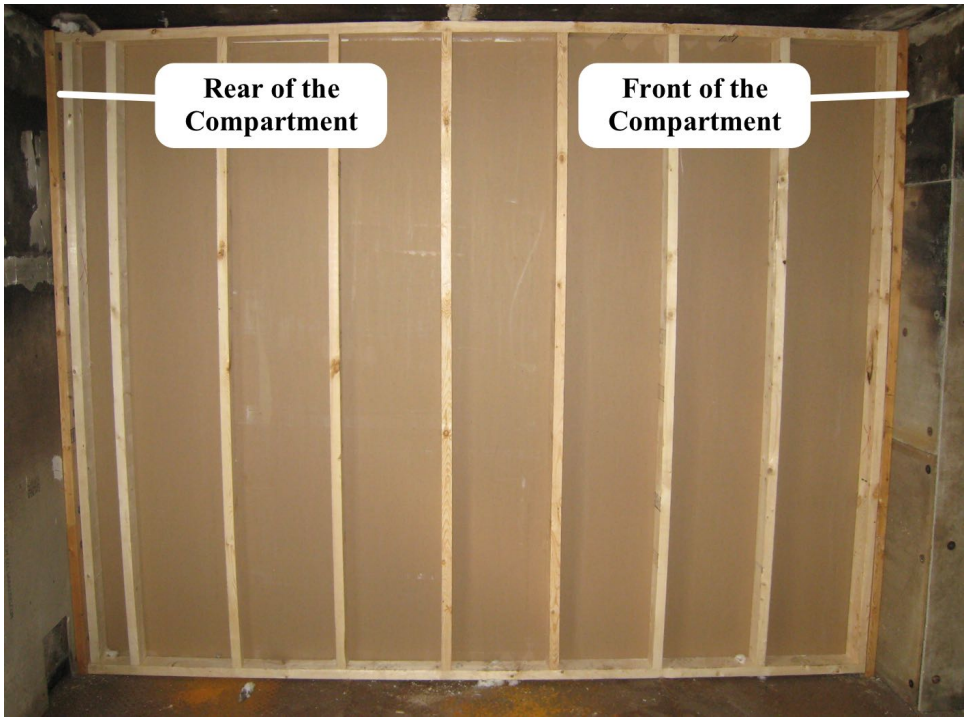


Figure 3.4: Stud wall being constructed, unexposed side of the wall.

a flexible and expandable Compact FieldPoint data acquisition system manufactured by National Instruments. The DAQ was comprised of a set of modular backplanes (NI cFP-1808 [62]), each of which is capable of supporting up to 8 Compact FieldPoint modules. Each module supports up to eight measurements of temperature (NI cFP-TC-125 [63]), or analog voltage or current (NI cFP-AI-110 [64]). Both types of module have 16-bit resolution, built-in calibration and scaling, and signal conditioning via a 50/60 Hz noise rejection filter. Two backplanes were used:

- the first backplane contained eight temperature modules devoted to measurements of wall temperatures (64 channels); and
- the second backplane contained four temperature modules devoted to measurement of wall temperatures (32 channels), one analog module devoted to measurement of heat flux (8 channels), and one each of analog and temperature modules devoted to measurement of velocity at the door (8 channels each).

Since 96 sensors were available for measurements of wall temperature, it was decided to limit instrumentation to only five of the seven cavities, and to use a large number of the sensors in the centre cavity in order to obtain detailed measurements of the in-depth

thermal gradient at that location. The thermocouple layout schematic is provided in Figure 3.8, at the end of this section.

K-type, bead-welded, exposed junction, Inconel sheathed thermocouples were installed at each position in the wall, as shown in Figure 3.8. For cavities 1, 3, and 5, eight thermocouples per cavity were located on the exposed (a) and unexposed (e) sides of the wall. The top row of sensors was located 6 in (152 mm) below the top of the wall, the top three rows of sensors were spaced 6 in (152 mm) apart, the remaining five rows were spaced 12 in (305 mm) apart. For cavities 2 and 4, four thermocouples per cavity were located on the exposed (a) side of the wall, spaced 24 in (609 mm) apart. For cavity 3, additional thermocouples were positioned on both sides of the insulation batts as well as in the middle of the insulation (b, c, d). Thermocouples were also placed on studs 4, 5, 6, and 7 at several locations in the upper region.

Thermocouples on the exposed side were not affixed to the wall, since fire exposure would cause them to detach regardless. Instead, they were hung from the ceiling so as to be positioned within 1 in (25.4 mm) of the wall (refer to Figure 3.5).

Figure 3.5: Exposed-side thermocouples hanging in front of the test wall.

In-cavity thermocouples (cavity 3) were pushed into the insulation to the correct depths from the back, and then bent 90 degrees such that the leads extended along the back of the batts (location d) to the floor, exiting the wall at the bottom. Unexposed-side thermocouples were affixed to the wall using masking tape, which pressed the junction firmly onto the material; the unexposed side OSB was not expected to reach temperatures high enough to cause the tape to detach.

In addition to the temperature measurements outlined above, heat flux was measured at three heights on the side of the compartment opposite the test wall (aligned with the centre of Cavity 3) using water-cooled Gardon gauges. The gauges were spaced 24 in (61 cm) apart vertically (corresponding to heights of 32 in (81 cm), 56 in (142 cm), and 80 in (203 cm) above the floor). An insulated rig was constructed within which heat flux gauges were positioned, and data and water cooling lines were contained, as shown in Figure 3.6.

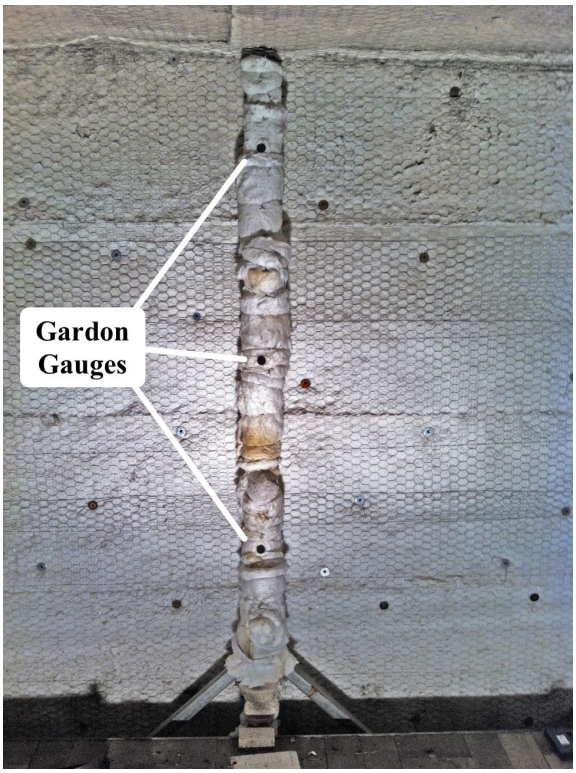


Figure 3.6: Heat flux rig.


Figure 3.7: Velocity rig.

Gas velocities at the doorway were measured at eight different heights using a rig (shown in Figure 3.7) comprised of bi-directional probes attached to differential pressure transducers, and corresponding thermocouples. Bi-directional probes were connected to

the pressure transducers using a combination of stainless steel and high temperature silicone tubing; the upper region of the rig was insulated with ceramic fibre insulation prior to the test. This rig was repurposed from previous work by Obach [65]; construction and calibration details may be found in that work.

The fire exposure was created by stacking two softwood cribs, each weighing approximately 15 kg, side-by-side in the centre of the burn pad. Cribs were ignited using 200 ml of heptane in a foil pan located below each crib. The fuel type and ignition procedure were adapted from previous work by Obach [65]. This same fuel source was later used in future experiments; additional details are provided in Section 6.1. To prolong the burning duration, firefighting personnel entered the compartment at regular intervals to add additional cribs to the fuel bed. The timing for these events was determined on-the-fly based on the monitored gas temperatures. Results of the experiment are presented in the following section.

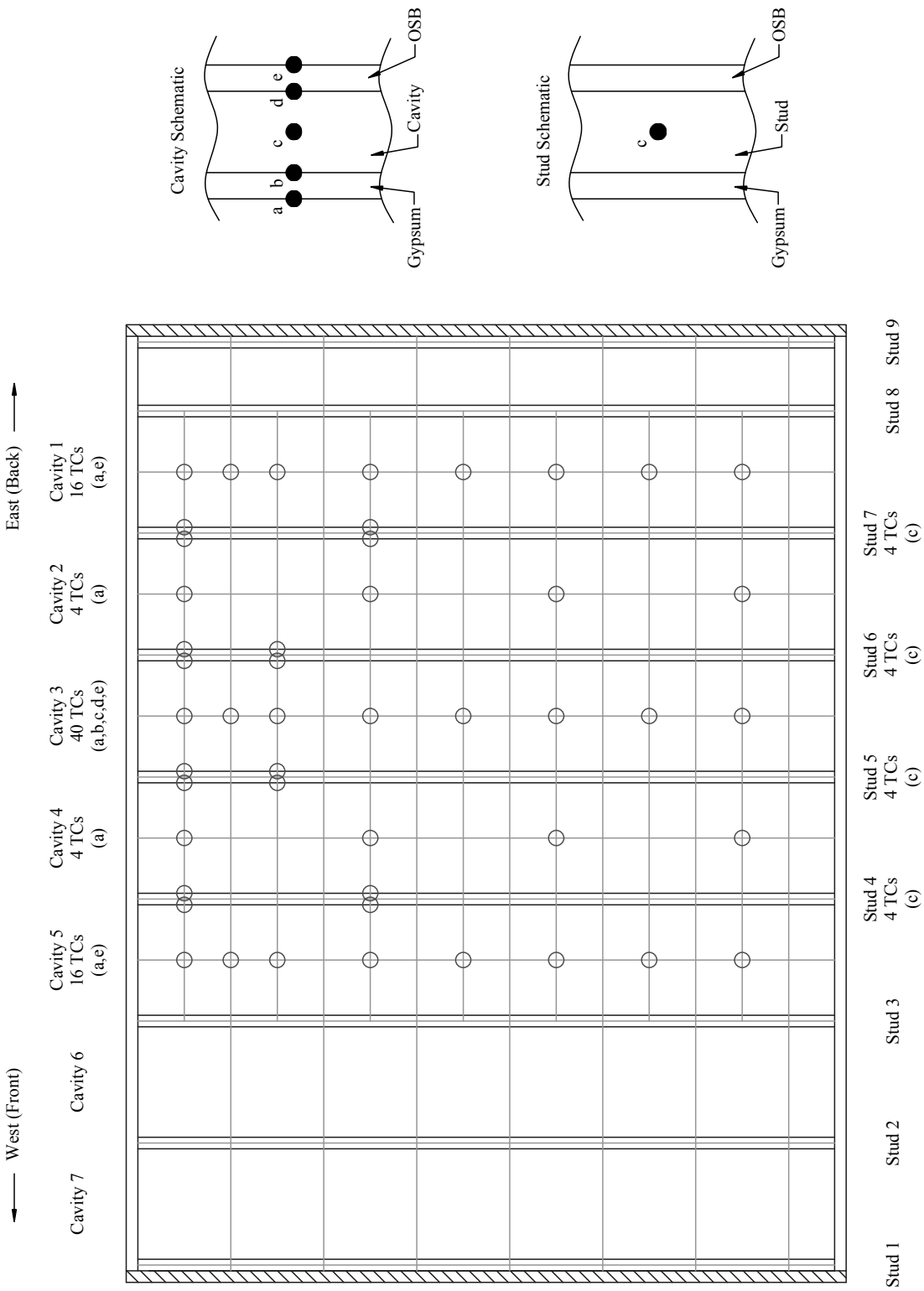


Figure 3.8: Overall thermocouple instrumentation plan for the test wall.

## 3.3 Results

Following ignition ($t = 0$), the door to the compartment was closed to an opening angle of 30 degrees after 1.9 min in order to better contain heat within the compartment. At $t = 11.3$ min the door to the compartment was opened, a third crib was added, and the door closed again to 30 degrees. The same procedure was followed for the fourth and fifth cribs, which were added at $t = 18.9$ min and 24.6 min, respectively. After 43.8 min the door was fully opened, and the test concluded; data was recorded for a few minutes following this final event. Figure 3.9 shows the state of the fire near the end of the test, as the final crib burned.

Figure 3.9: Fire near the end of the test ($t = 44$ minutes).

| Region | Height of Sensor Above Compartment Floor (in) | | |
|---|---|---|---|
| | Heat Flux | Velocity at Door | Gas Temperature at Wall |
| Upper | 80 | 74 {77, 71} | 74.5 {85, 79, 73, 61} |
| Middle | 56 | 50 {65, 55, 45, 35} | 43 {49, 37} |
| Lower | 32 | 20 {25, 15} | 19 {25, 13} |

Table 3.1: Average sensor heights, in (individual sensor heights are given in braces).

The main results of interest here were the gas temperatures near the wall, the thermal penetration into the wall, the heat flux to the wall, and the gas velocity profile at the door. For purposes of clarity in the identification of trends in the measured data, the presented results are divided into three regions based on the height of the sensors above the compartment floor. Results are presented in terms of average values in the "upper", "middle", and "lower" regions of the compartment, as defined in Table 3.1.

Figure 3.10 shows the gas temperatures near the wall measured by sensors located at a height of 61 in (155 cm) above the floor (the upper-middle region of the compartment, given that the compartment height was 92 in (234 cm)). Over all five cavities, the temperatures measured were remarkably similar, which is a clear indication that gas temperatures were fairly uniform in the horizontal dimension near to the wall.

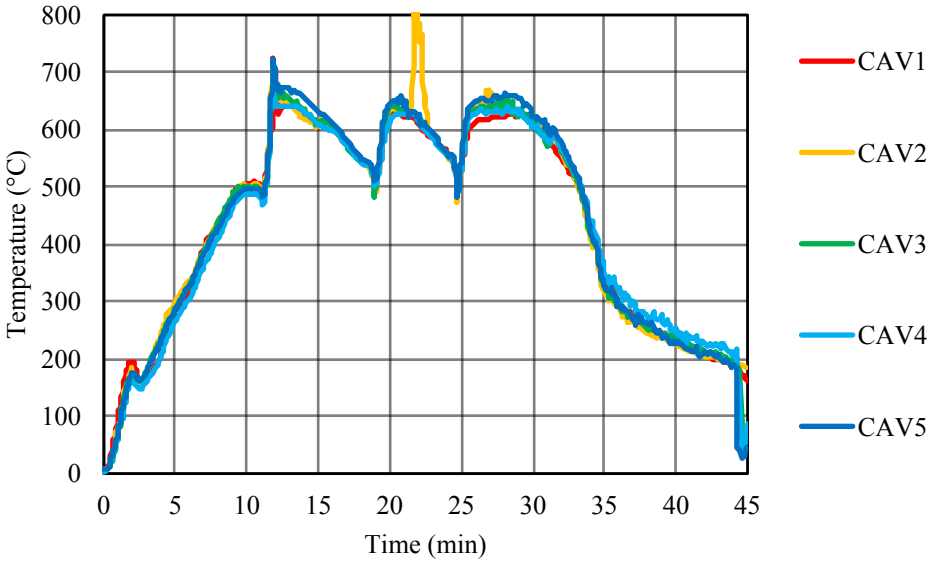


Figure 3.10: Gas temperatures on the exposed side of the wall over all five cavities in the upper/middle region (sensor height = 61 in (155 cm)).

Figure 3.11 shows the gas temperatures near the wall, averaged over cavities 1–5 at each height, and divided into the three regions based on height above the compartment floor. Minimum and maximum temperatures measured in each region are also represented in the figure (lightweight lines with corresponding colours). The "upper" and "lower" regions are representative of the upper and lower layer gas temperatures in the compartment for the majority of the test (the min/max range is greater for the upper region after about 35 min as the final crib was consumed and the hot gas layer dissipated). Upper layer gas temperatures peaked at approximately 650°C each time a new crib was added, and averaged around 600°C during the "steady burning" period from 12–32 min; lower layer temperatures averaged approximately 260°C during this same period. Based on these gas temperatures and the controlled fuel load, this fire can be classified as a pre-flashover fire (i.e. not fully-developed). For comparison, the furnace temperature in a fire resistance test, which is not representative of a fuel-controlled fire, reaches approximately 650°C after 10 min, and 850°C after 30 min (see Figure 2.1).

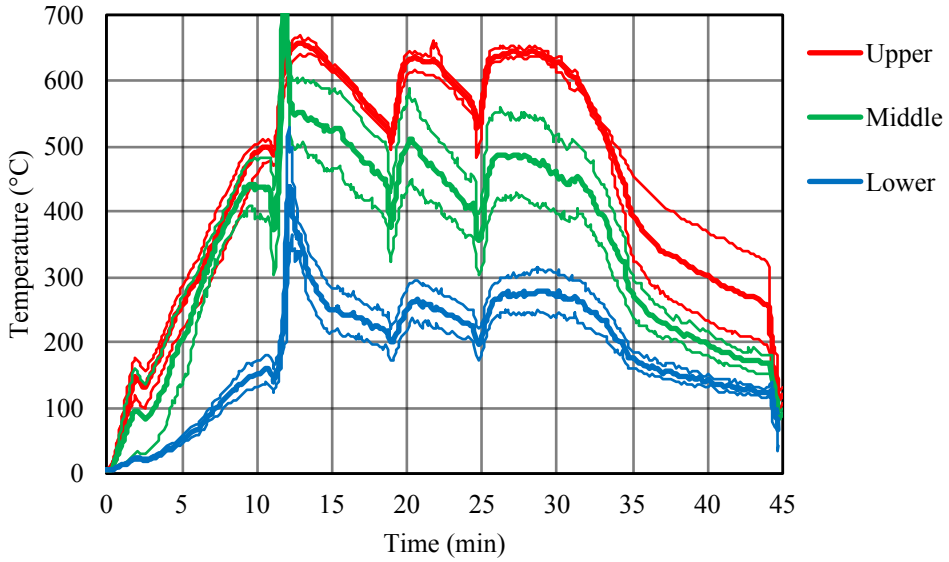


Figure 3.11: Gas temperatures on the exposed side of the wall averaged over all five cavities in the upper, middle, and lower regions (min/max).

Figure 3.12 shows the heat flux measured at three heights opposite the test wall. At the upper position of 80 in (203 cm), which is 12 in (30 cm) below the ceiling, the maximum heat flux measured was 70 kW·m$^{-2}$, and the average heat flux over the steady burning period was about 50 kW·m$^{-2}$. In comparison, irradiation from a blackbody adjacent to the sensor at 600°C would be about 33 kW·m$^{-2}$; considering the influence of

the fire plume and fuel bed, the measured values are reasonable. This level of exposure is also consistent with that used in concurrent work, in which thermal penetration through small-scale assembly mockups was measured using a cone calorimeter [57, 66, 67]. The middle and lower heat flux probes were located at heights of 56 and 32 in (142 and 81 cm) respectively, so the average height of the two gauges was 44 in (112 cm). This is approximately equal to the middle height of the compartment, 46 in (117 cm), so these two gauges give an idea of the exposure levels above and below the middle of the wall. Interestingly the lower gauge measured a slightly greater heat flux, which can likely be attributed to the influence of the fire plume and fuel bed, as mentioned above. Regardless, the results confirm that the exposure to the wall was greatest in the upper region.

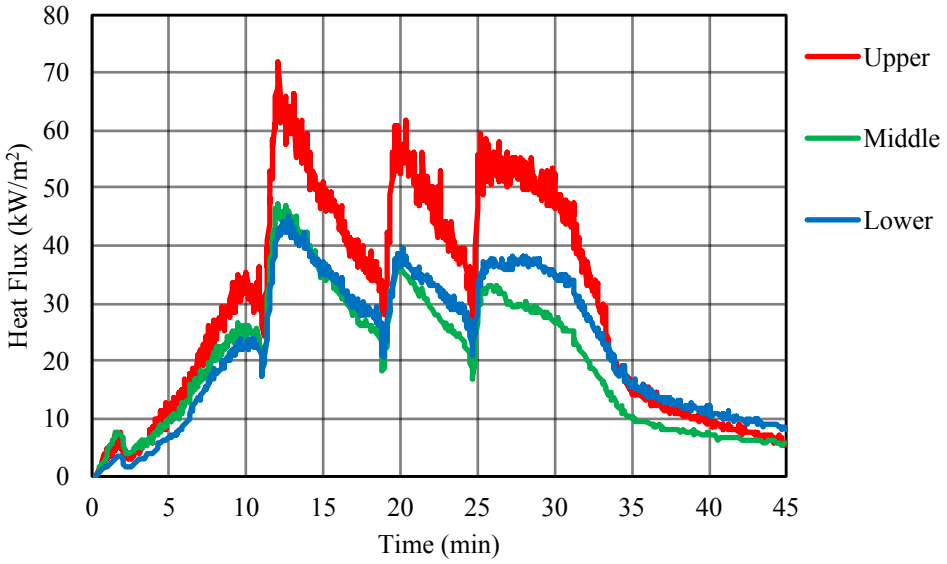


Figure 3.12: Heat flux to the wall in the upper, middle, and lower regions.

Thermal penetration, in terms of the temperature rise on the unexposed side of the wall, is measured and reported in a fire resistance test. It was of interest in this test, however, to investigate the temperature gradient through the multiple layers of the wall. Temperatures in the middle cavity were measured at five positions into the depth of the wall, "a" through "e", as detailed previously. The upper four temperature measurements were averaged at each depth position to produce an average in-depth temperature measurement in the upper region of the wall over time; results are plotted in Figure 3.13. Similar plots were produced for the middle and lower regions, but are not presented here for brevity — this discussion focuses on thermal penetration through the more severely exposed upper region of the wall.

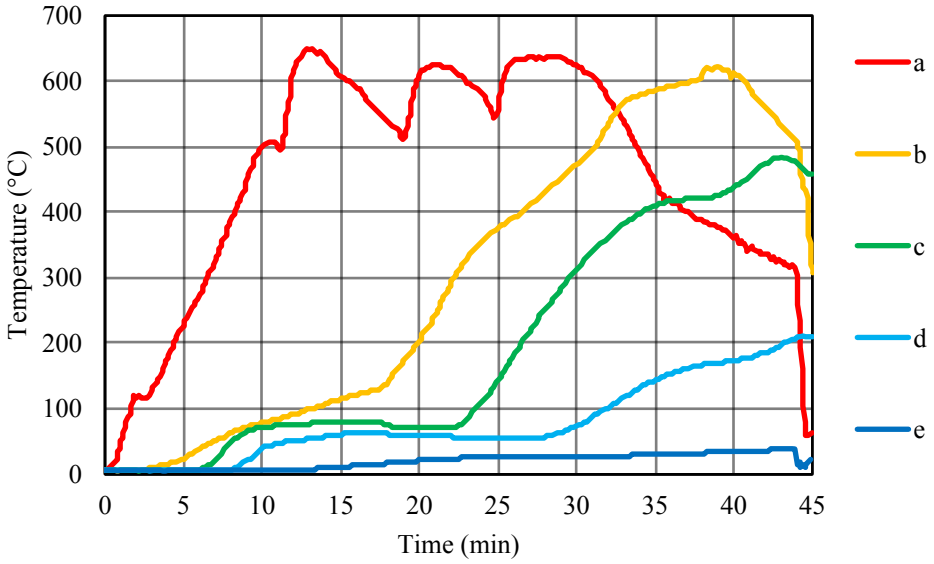


Figure 3.13: Average in-depth temperatures in the upper region of the wall.

Temperatures on the back of the exposed-side gypsum board (b) did not rise appreciably until approximately 2 min. The rate of temperature rise increased notably after 18 min, when the temperature on the unexposed side of the gypsum board reached about 120°C. This behaviour is consistent with the expected behaviour of gypsum board in this temperature range (Section 2.2.3), as the first stage of calcination occurs. Similar behaviour is seen in the insulation, where the rate of temperature rise increased at 23 min at location "c" and 27 min at location "d". These measurements are consistent with those of Aire [56], who subject small-scale assembly mockups a constant irradiance, and found a similar increase in the rate of temperature rise in the insulation material in this temperature range. Likely this can be attributed to combined heat mass transport of water vapour from the exposed gypsum board through the material, as decomposition of the binder in the insulation does not occur until approximately 150°C [23].

In addition to the time evolution of temperature within the wall assembly, it is also of interest to visualize the two dimensional variation into the depth of the wall. Figure 3.14 shows a sequence of temperature contours into the depth of the wall after 10, 20, 25, and 30 min of exposure. The figure confirms that thermal penetration in the upper region of the wall was greatest. It also shows that thermal penetration was fairly linear into the depth of the wall in the upper region. In contrast, in the middle and lower regions, the temperature gradient varied both with height above the floor and depth into the wall, as evidenced in Figure 3.14.

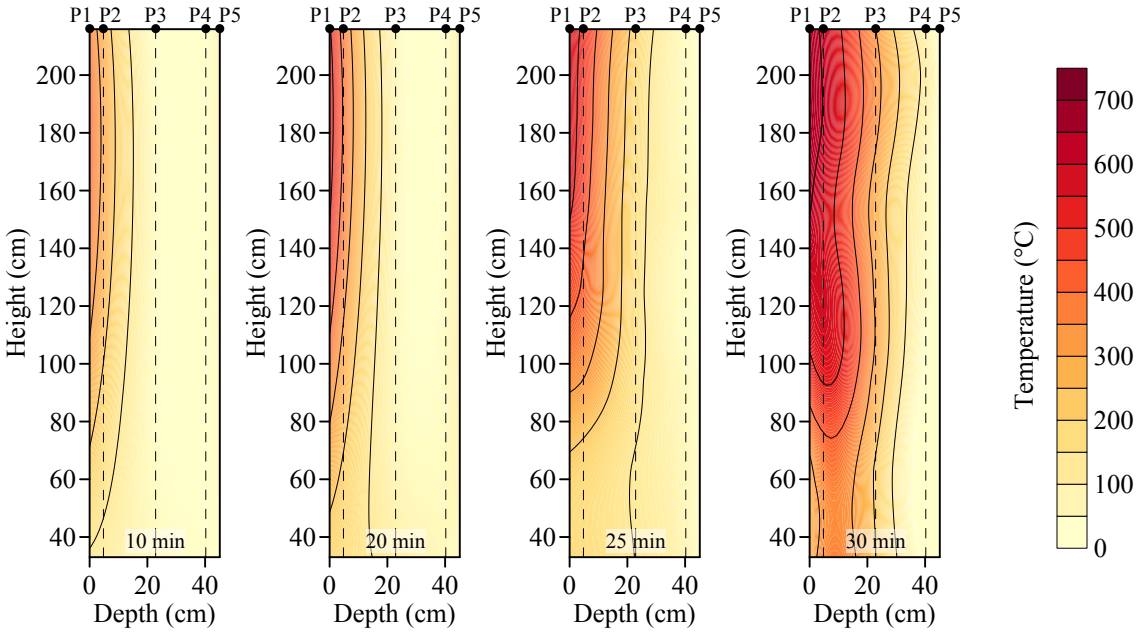


Figure 3.14: Temperature contours cavity 3 at $t$ = 10, 20, 25, and 30 min.

Measurements of average gas velocity out of the compartment door are shown in Figure 3.15 for the upper, middle, and lower regions. Near the top of the door the gas velocity was positive throughout the test as hot fire gases exited the compartment, and was negative in the lower region as fresh air was drawn into the compartment. These results are very typical for a compartment fire [68], and speak to their validity. While not directly pertinent to the present analysis, this gas velocity data is useful for validation of fire models for this scenario, which might be implemented in the future.

Real-time observations of the state of the degrading wall were not possible in this experiment due to the orientation of the test wall relative to the compartment door, and because no video cameras were installed inside the compartment. Consequently, only a post-fire assessment of the damage to the wall was made. Figure 3.16 shows the state of the wall at the end of the test ($t$ = 45 min). Significant cracking is visible between fixtures (drywall screws). Also, large chunks of gypsum board fell off in the upper region, causing the underlying insulation and wood studs to be directly exposed to the fire environment. Damage to the gypsum board wallcovering was significant, despite the exposure level being relatively moderate (an average of about 50 kW·m$^{-2}$ over 30 min). The most significant damage was observed in the upper region, which is consistent with the measured heat flux and temperatures being greater in the upper region.

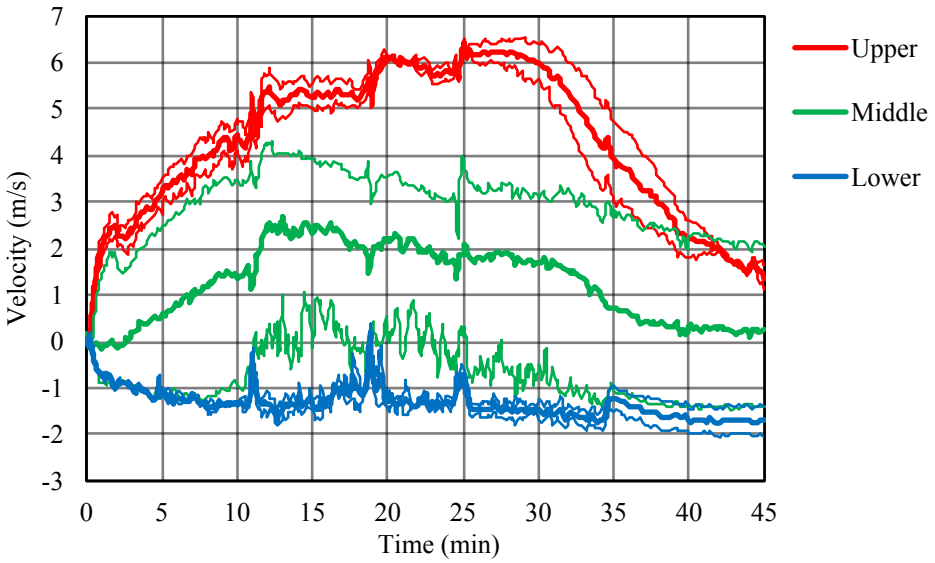


Figure 3.15: Gas velocity out of the compartment at the door in the upper, middle, and lower regions (min/max).

Despite failure of the thermal barrier, temperatures measured on the unexposed side of the wall did not exceed about 45°C. As is apparent in Figure 3.16, the rock wool insulation remained intact through the fire exposure, with some brownish discolouration and reduction in integrity (batts were brittle due to the binder burning off). It is apparent that the insulation acted as a secondary level of fire protection to the underlying OSB sheathing, as evidenced by the low measured temperatures. This explains how such a wall is able to achieve a 30 min fire resistance rating under CAN/ULC S101 furnace exposure, which is of much greater intensity than the fire exposure used here (gas temperatures of 900°C and heat flux of 90 kW·m$^{-2}$ after 30 min) [69].

Figure 3.17 shows the post-test remains of the wood stud frame. The studs had a "carved out" appearance, with about 10% of the stud thickness burned away in the lower regions of the wall, and about 60% of the stud thickness burned away in the upper regions. In areas where the gypsum board had fallen off, some studs were charred through 90% of the original depth. Again, despite this level of degradation, the unexposed OSB showed no visual signs of charring or vapour penetration. These observations further support the thermal penetration results presented in Figure 3.14 above.

Measured and observed results from the preliminary investigation have been presented above. The following section provides further discussion with respect to the stated objectives of this investigation, and summarizes the findings.

Figure 3.16: State of the wall post-fire ($t = 45$ min).

Figure 3.17: Depths of charring of the wood studs.

## 3.4 Discussion and Findings

The preliminary investigation confirmed the expected outcome that a wall exposed to a realistic fire would preferentially degrade in the upper region. This was demonstrated by measurements of thermal penetration through the depth of the wall, and confirmed by observation of damage. Furthermore, temperature measurements into the depth of the wall were consistent with those measured experimentally in small-scale mockups of the same construction assembly, subject to a heat exposure of similar intensity. Despite this similarity, conduct of large-scale experiments with real fire exposures is required in order to investigate real-scale phenomena such as cracking of gypsum board and the interaction of fire gases with the test wall. Future experiments should be of sufficient scale to make such phenomena observable.

Thermal penetration into the depth of the wall was measured at several heights in a single wall cavity, and a distinct vertical gradient was identified. Post-test observations of the remaining stud wall frame (Figure 3.17) clearly show that this vertical gradient was not the same in all cavities, varying strongly in three dimensions within the wall. These results point to a fire exposure that varied not only in the vertical dimension, as indicated by the measured heat flux, but also in the horizontal dimension. From this, it is concluded that the fire exposure to a wall in a compartment fire must be specified in two dimensions (over the entire surface of the wall) in order to adequately model thermal degradation phenomena of interest. This brings to light a complication in the design and conduct of this type of experiment — a single vertical probe rake of heat flux gauges is not sufficient to measure the two-dimensional fire exposure to the required level of detail. This difficulty must be addressed in future experiments.

The idea of using a compartment fire exposure (as opposed to a uniform furnace exposure) to represent realistic fire conditions was demonstrated to be a success. Further refinement to the experimental technique is required, particularly as pertaining to the fire. Wood cribs are a useful fuel source for this type of experiment, but the burn time is unsatisfactory for analyses demanding long-duration exposures. The idea to extend the burn duration by having firefighters add additional fuel to the fire at regular increments proved fruitful, however this process of entry and fuel addition had a significant impact on the fire dynamics. The discontinuities seen in the gas temperature and heat flux curves (which correspond to the re-fuelling events) are not representative of a realistic fire environment. Therefore, future experiments must address this issue in the design of a fire exposure.

Although the fire exposure was non-uniform over the surface of the wall in both horizontal and vertical dimensions, the gas temperature field adjacent to the wall varied predominantly only in the vertical dimension. Certainly this would not have been the case closer to the fire plume — the approximate fire area was 1150 $in^2$ (7420 $cm^2$), for two cribs side-by-side, and the fire centreline was 69 in (175 cm) from the wall. However the results indicate that when fire is not too close to the wall, the gas temperatures near the wall do not appear to be significantly influenced by the non-uniform radiation from the fire and compartment surroundings, but rather by the natural stratification of gases which occurs in a compartment fire environment. This will of course depend on the proximity of the fire to the wall and on fluid dynamics in the compartment; asymmetric ventilation or fuel configurations will impact the uniformity of gas stratification.

The implication of this finding is that the two-dimensional gas temperature field adjacent to the wall can be approximated by a one-dimensional (vertical) temperature field. Furthermore, assuming that the gas layer stratification is uniform across the entire compartment area (except near the fire plume of course), the temperature field near the wall may actually be approximated by the global stratified gas layer temperature, or "slice" temperature. The slice temperatures in a rectangular compartment can be measured experimentally with vertical probe rakes, usually installed symmetrically through the compartment (e.g. in the four corners). An advantage of approximating the gas temperature field near the wall using the compartment slice temperature is that no thermocouple instrumentation is required near the exposed side of the wall. If possible, future experiments should avoid the use of exposed-side instrumentation for four reasons:

- sensors obscure the line-of-sight from the fire to the test wall, having a direct (and difficult to quantify) influence on the exposure;
- the presence of permanent sensors adjacent to the test wall complicates construction, assembly, and post-test cleanup;
- the use of replaceable sensors adjacent to the test wall negates the previous point, but adds significant preparation time and increases the infrastructure cost of each test; and
- failure of instrumentation in a compartment fire environment is likely to occur over time, therefore it is preferred to use robust, well protected, permanent probe rakes that are positioned such that they don't obstruct the test wall.

A practical observation of relevance from this investigation was that the time to construct the compartment and test wall, instrument the wall, run the experiment, repair sensors after an experiment had been conducted, and prepare the compartment for the next test was very long. Future experiments should optimize this procedure to minimize the time taken to conduct a single experiment, facilitating the conduct of multiple experiments in a short time frame. A significant issue in this investigation was the limitations imposed by the selected medium — the steel burn house structure presented multiple difficulties in being a confined space with configuration restrictions. Future experiments should adopt a refined apparatus with accommodations for cable routing, video recording, line-of-sight to the test wall, access to both sides of the test wall, and a simple means of in-place construction of the test wall.

The findings of this preliminary investigation were the foundation upon which the large-scale experiment developed in the present work was built. The following chapter outlines the design of this experiment.

# Chapter 4

# Design of Experiment

The experiment adopted in the present work is intended to be used to study the thermal degradation of construction assemblies (specifically walls), involved in real fires. Given this objective, and taking into account the findings of the preliminary work, several design criteria were developed.

First, the experiment was to be capable of accommodating a wall of realistic size and as-built construction. The minimum wall size was to be three standard wall cavities in width (with stud spacing of up to 24 in (609 mm) on centres); the intent of this criteria was to ensure that there will always be at least one cavity that is not directly subject to the boundary conditions that will develop at the sides of the wall. The experiment was also to accommodate a diverse range of wall types suitable for use in Canadian construction; for example, offset studs, multilayered gypsum board, various types of insulations, exterior wall assemblies, etc. Common residential construction opts for the used of 2×4 or 2×6 stud walls; combining this with options such as offset studs, the thickness of walls being studied was anticipated to be as large as perhaps 8 in (203 mm).

The second criterion was that the experiment must expose a wall to realistic fire exposure conditions. This implies some degree of "non-uniformity" in the mixed-mode thermal boundary condition, as opposed to a fire resistance test, as is expected in a real pre-flashover fire. Furthermore, it was required that the experiment facilitate realistic interactions between the fire gases and decomposing wall, as is typical in a fire environment, and in contrast to a purely heat-based exposure such as that from a radiant panel, for example. These first two criteria are both related to the realism of the fire exposure, relative to that of an actual building fire. Therefore, a compartment

fire style of experiment was adopted, which can produce fires of the desired realism (i.e. compartment-scale fire plume and development of a distinct hot gas layer) when appropriate fuels (i.e. solid materials typically found in structures, such as wood, plastics, and textiles) are used, and is of an adequate scale to accommodate large walls (i.e. at least three stud cavities wide, and height of a typical compartment). To keep the scope of the experiment manageable, a single boundary of the compartment, designated the "test wall", is the focus of the thermal degradation assessment.

Next, the experiment was to produce repeatable results, such that the measured and observed thermal degradation phenomena for a particular construction assembly and fire exposure will be consistent test-to-test. A well-controlled compartment fire experiment addressees this criteria to some extent. Due to the nature of large-scale fires, in particular those utilizing solid fuels and natural ventilation, some test-to-test variability must be accepted. For example, Fang [70] conducted a series of four compartment fire experiments utilizing an upholstered furniture fuel load, and quantified variability in measured results (heat flux, temperatures, event times, etc.) by a coefficient of variation, which was as high as 13.3%. Nonetheless, good repeatability can be promoted by adequate control of the relevant experimental variables (e.g. initial conditions, ambient conditions, ventilation, and fuel load). Repeatability of the experiment is discussed in Chapter 6.

For practical reasons, the experiment was to facilitate the rapid preparation of specimens, and the timely conduct of successive tests. A wall of compartment fire scale can be constructed in a few hours, however instrumentation can add significantly to specimen preparation time. Furthermore, any test involving a wall with gypsum board tape lines must be afforded time for the joint compound to cure, typically two days under controlled temperature and humidity conditions. For these reasons, it was decided that the in-place construction of the test wall within a rigid mounting frame (taking cues from the CAN/ULC S101 [6] and ASTM E119 [5] fire resistance tests) will best facilitate rapid specimen preparation. The present work is concerned with non-loaded wall partitions, but future work may consider loaded partitions. In this case, the experiment should be able to incorporate some means for application of mechanical stress, e.g. hydraulic press. Once a wall is constructed in-place, the compartment and test wall are conditioned for two days prior to the start of a test. With regards to successive testing, the most time-consuming factors are post-test cleanup (a compartment fire environment will retain heat long after the test has been completed) and replacement of damaged instrumentation. Affording these tasks two days, plus one day for conduct of a test, the expectation was that successive tests may be conducted within a five-day timeframe.

The apparatus was to be instrumented with sensors, and measurements be recorded via a data acquisition system, in order to support both present engineering analyses and future detailed modelling endeavours. This involved characterization of the compartment fire environment, wall exposure, and thermal degradation process. Primarily this necessitates the measurement of temperature, the primary variable in fire analyses; and heat flux, the most useful parameter for investigating the thermal interaction between a fire and a solid boundary. Furthermore, visual observations are a crucial component of the experimental assessment. The instrumentation selected for this experiment is discussed in detail in Section 4.2 below.

Finally, there were practical and budgetary constraints to be considered. Experimental design began in the late summer of 2015, and available resources delayed completion of the apparatus until spring 2016. A finite budget existed for materials and contracting, therefore in-house construction and on-hand materials were used whenever possible. The budgetary constraint extended to instrumentation, which was designed to be robust and survive multiple tests where possible. The most significant practical constraint was physical accommodation on the University of Waterloo Fire Lab site. An indoor installation of the desired scale was not possible, therefore it was required to construct an apparatus outdoors. Given this constraint, and the cool winter temperatures in Waterloo, Ontario, it was required that characterization and the first series of experiments be completed by the autumn of 2016.

Taking into consideration the criteria and constraints outlined above, the following sections detail the design and instrumentation of the large-scale experiment.

## 4.1 Apparatus

While there is no single configuration that is used universally for compartment fire experiments, a historically relevant option is the ISO 9705 Room Corner Test [71] configuration. While this test is often used for the study of post-flashover fires, the configuration is universal and may be readily adopted to other work. This test standard specifies a compartment measuring 3.6 m long, 2.4 m wide, and 2.4 m tall. The compartment has a single vent (a doorway) measuring 0.8 m wide 2.0 m tall, located on one of the short sides of the compartment. This configuration was used as the starting point for the apparatus design in the present work. To build a compartment of this size that is capable of withstanding fire exposures, some degree of non-combustible

construction or fire resistant insulation was required. Since the location of the apparatus in the present work was constrained to be outdoors, weatherproofing was also necessary. The solution adopted here was to retrofit a standard 20 ft (6.1 m) sea container with an integrated fire test area and instrumentation room. By consolidating the apparatus into a single self-contained unit, flexibility in location was afforded, and weatherproofing would not be a concern. Design drawings were produced in August 2015 (Appendix A), and the modified container was fabricated by Secure Container Solutions Inc. and delivered to the University of Waterloo Fire Lab site in November 2015.

The sea container, which has nominal dimensions of 6.1 m long, 2.4 m wide, and 2.4 m tall, was divided into three distinct sections: the "fire compartment", "transition section", and "instrumentation section". Sections were separated by frames fabricated from 10 ga steel sheet and 3/16 in (4.8 mm) structural steel square tube, which were welded directly to the steel interior of the the container. Figure 4.1 is an excerpt from the construction drawings, and shows a section view along the length of the apparatus. In the figure, the fire compartment is visible on the left and the instrumentation section on the right. This drawing may be viewed in full detail in Appendix A, along with the remainder of the construction drawings.

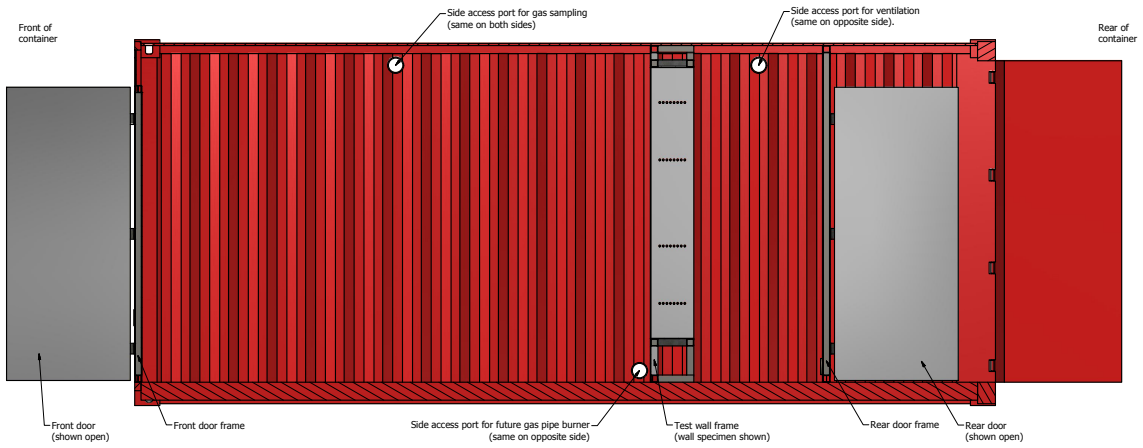


Figure 4.1: Section view of the fire test apparatus (refer to Appendix A for details).

The frame separating the fire compartment from the transition section is termed the "wall frame", in which the test wall is mounted. The wall frame was designed to fulfill the minimum wall size criterion (three 24 in (61 cm) stud cavities in width), which amounts to a total width of 73.5 in (187 cm) on wood studs (and similar for steel studs). Furthermore, it was decided to insulate the interior of the wall frame with 1 in (25.4 mm) of ceramic fibre insulation on all four sides, in order to insulate and

better quantify the heat loss boundary conditions at those locations; given this design consideration, the total width of the wall frame opening is 75.5 in (192 cm). Since the height and width of the room are identical, it was decided to use a wall of identical height and width, therefore the height of the wall frame opening is also 75.5 in (192 cm). Note that this wall size is smaller than that of a fire resistance test (for which width and height are at least 270 cm [5]), but still large enough to represent a compartment boundary. The depth of the frame opening is 12 in (305 mm), thus accommodating a large variety of different types of walls. The preliminary investigation demonstrated that thermal penetration (Figure 3.14) and degradation (Figure 3.17) in a compartment wall are least significant near the compartment floor, and most significant in the upper regions. Given the intention of the experiment, it was decided to elevate the bottom edge of the wall frame 12 in (305 mm) above floor level. This positioned a test wall such that the spacing between the top of the wall and the ceiling of the compartment is identical to the spacing between the sides of the wall and the sides of the compartment (once insulated, as described below). The wall frame is shown in Figure 4.2; refer to Appendix A for complete details.

The fire test apparatus was installed on site at the University of Waterloo Fire Research Lab as shown in Figure 4.3. The rear of the container (instrumentation section) faces the fire lab (the red building), while the front of the container (fire compartment) faces the roadway. The container was oriented in this manner so as to prevent fire gases from venting into the lab space, and to afford greater access to the fire compartment in the event that suppression is required.

Once installed on site, the interior floor of the container was lined with 2.5 in (63.5 mm) fire bricks to provide stability, thermal insulation, and fire protection to the floor. The interior walls and ceiling of the fire compartment were insulated with panels constructed from 1/2 in (12.7 mm) cement board and 1 in (25.4 mm) Fiberfrax Durablanket S® refractory ceramic fibre blanket. This insulation system provides fire protection to the steel container, prolonging the life expectancy of the apparatus, and retains heat within the compartment as traditional building construction would. Lining the compartment with gypsum board was another option, however this would necessitate replacement each test, and could potentially break down mid-test, whereas the insulation panels will survive multiple tests. Panels were assembled using machine screws (8-32 UNC, 2 in (50.8 mm) length), nuts (8-32 UNC, 5/16 in (7.9 mm) drive), and fender washers (3/16 in (4.8 mm) inner diameter, 1 1/8 in (28.6 mm) outer diameter). After a 25% compression of the insulation at the screw attachment locations, the screws extended

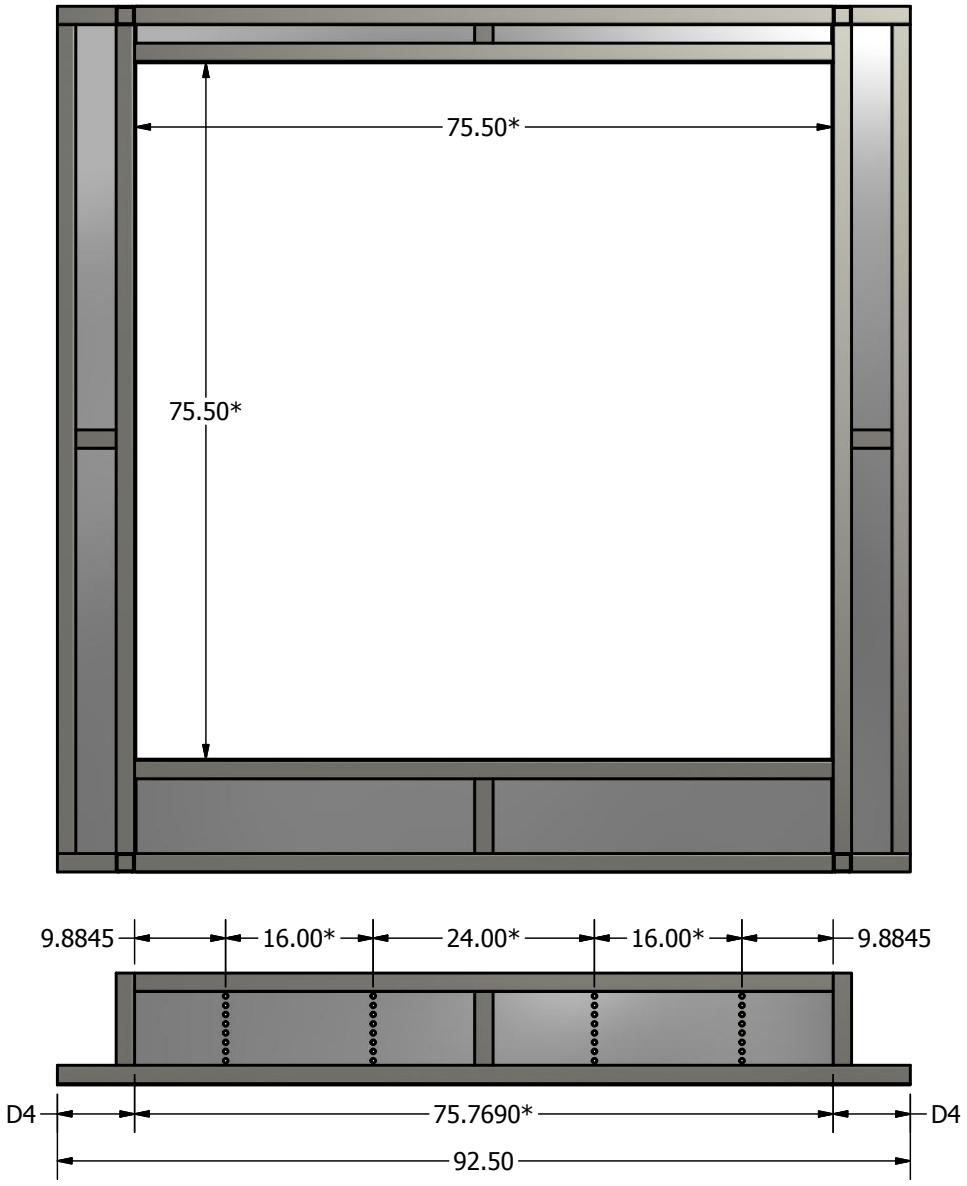


Figure 4.2: Profile and top views of the wall frame (refer to Appendix A for details).


Figure 4.3: Fire test apparatus installed on site.

through the back side of the panels by approximately 1/2 in (12.7 mm); this was done to create an air gap between the back of the panels and the steel container surfaces. Figure 4.4 shows the front (fibre) and back (cement board) sides of a constructed insulation panel.

(a) Front side. (b) Back side.

Figure 4.4: Insulation panels used in the fire test apparatus.

Ceiling panels were suspended on beams of 1 5/8 in (41.3 mm) Unistrut channel spaced 24 in (61 cm) apart, as shown in Figure 4.5. Note that the wall frame is also visible in the figure, with steel sheet covering the opening; this is described in Section 5.1. Next, wall panels were prepared, held in place by the rigidity of the cement board and a friction fit under the ceiling; refer to Figure 4.6. The fully insulated compartment is shown in Figure 4.7. The interior dimensions of the insulated compartment are reduced to 138 in (351 cm) long, 90 in (229 cm) wide, and 90 in (229 cm) high. The bottom of the wall frame is 12 in (31 cm) above the brick floor, and the top of the wall frame is 87.5 in (222 cm) above the brick floor, 2.5 in (63.5 mm) below the ceiling. Note that the insulation along the top of the wall frame in Figure 4.7 had not yet been trimmed. The two vertical steel channels in the figure contain temperature sensors, and are detailed in the following section.

Figure 4.5: Insulation panels installed on the compartment ceiling.

Figure 4.6: Insulation panels installed on the compartment walls.

Figure 4.7: Fully insulated fire compartment.

## 4.2 Instrumentation

With the fire compartment constructed, the next step was to instrument the fire test apparatus. The intended purpose of this experiment is to study the thermal degradation of a test wall subjected to a realistic compartment fire exposure, as well as the interaction between a compartment fire environment and its surroundings. Therefore it was necessary to install sensors to monitor both the fire compartment and the test wall. While any number of sensor types might be selected, and certainly the apparatus should be flexible in its accommodation of a broad range of sensor types, the most important measurements for the present work are gas temperatures, surface temperatures, heat flux at surfaces, and visual observations. A complete overview of the instrumentation used in the experiment may be found in Appendix B.1.

Measurement of gas temperatures in the fire compartment is crucial in order to adequately describe the fire, and invaluable for purposes of fire model validation. Given that gases will stratify vertically in a fire compartment, it is important to measure the vertical temperature gradient at several locations; this was accomplished by use of vertical probe rakes, which distribute sensors from the floor to the ceiling of the compartment. Probe rakes were assembled by lining 1 5/8 in (41.3 mm) Unistrut channels with k-type thermocouple cables (20 ga solid wires, glass fibre and Inconel sheathed, one duplex pair per cable) and ceramic fibre insulation. Bead-welded exposed junction thermocouples were extended 1/2 in (12.7 mm) from the channel at regular increments along its length, as shown in Figure 4.8. This type of rake construction has been used in previous work [65], and was demonstrated to be robust, capable of surviving multiple repeat fires.

Four rakes were assembled, and placed in each of the four corners of the fire compartment; these are denoted T1, T2, T3, and T4 (refer to Figure B.6). Seven thermocouples were used in each rake, plus an additional thermocouple extending from the top of the rake to the ceiling of the compartment. The heights of the seven thermocouples within the rakes ranged from 12 in (31 cm) to 84 in (213 cm) above the floor, such that the top thermocouple was 6 in (152 mm) below the ceiling. The eighth thermocouple in each rake was located 2-1/2 in (63.5 mm) below the ceiling, extending 1/2 in (12.7 mm) below the ceiling channels.

Gas temperatures adjacent to the wall, as well as measurements of wall surface temperature, would be excellent for purposes of model validation. However, the difficulty in measuring the surface temperature of a decomposing material is well known [72], and only exacerbated in the context of a harsh fire environment. Furthermore, it is critical

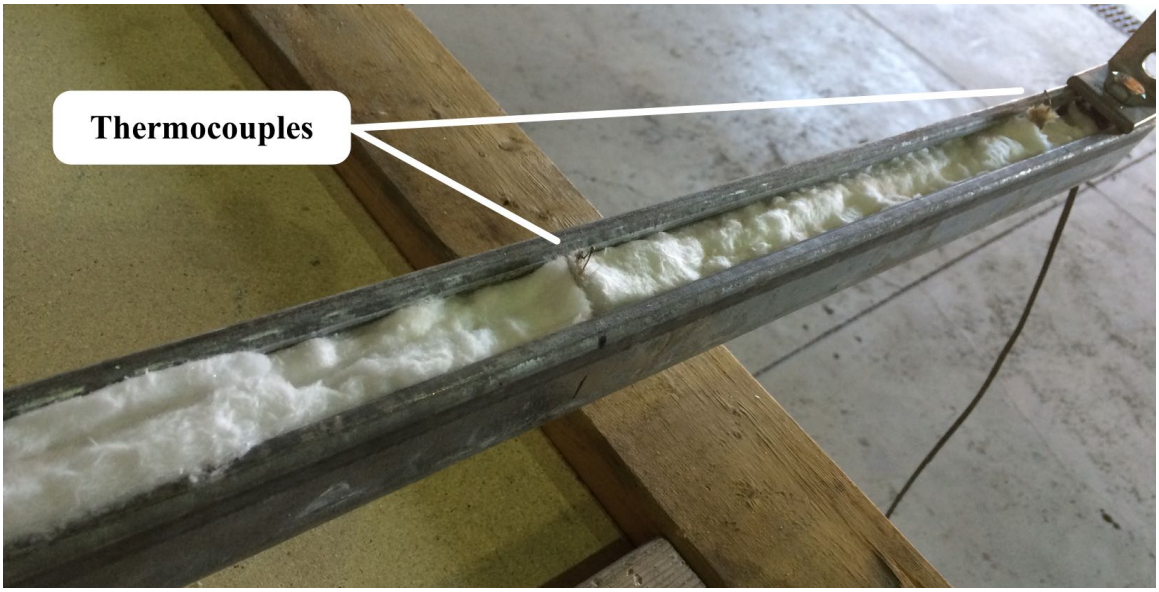


Figure 4.8: Construction of the fire compartment thermocouple rakes.

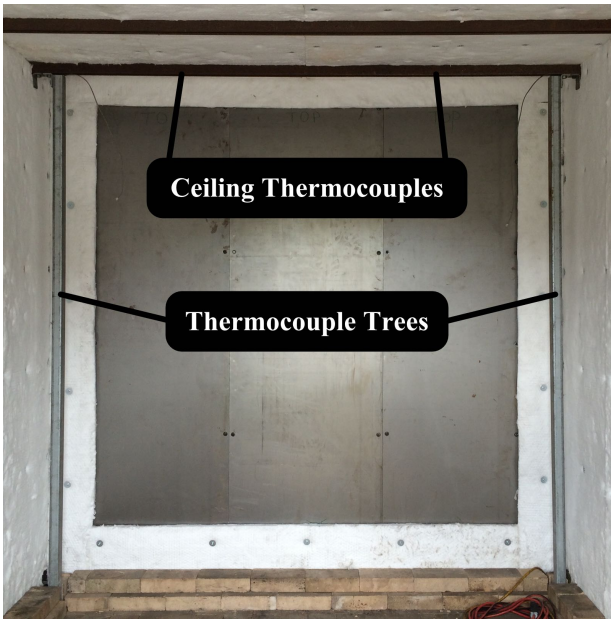


(a) Positions in the compartment.

(b) Extension from the channels.

Figure 4.9: Details of the fire compartment thermocouple rakes.

that any type of fire-side instrumentation not interfere with the interaction between fire and wall. As discovered in the preliminary investigation, temperature sensors positioned directly adjacent to the test wall had a high rate of failure, necessitating frequent replacements. This is undesirable for the permanent sensors outlined here; however, several channels in the data acquisition system were set aside for future expansion which can accommodate additional sensors of this nature, if desired.

Gas thermocouples were also installed in the transition section in order to monitor the conditions on the unexposed side of the wall. The gas environment will be relatively quiescent in this section, therefore a coarse measurement of the floor-to-ceiling temperature gradient was all that was required. Thermocouple rakes were assembled by looping Inconel-sheathed K-type thermocouples into vertically-hanging chains on the left and right sides of the wall frame, with three sensors per chain; these are denoted TR and TL (refer to Figure B.6). The top and bottom thermocouples in these chains were at the same height as the top and bottom of the wall frame, and the middle thermocouples were at the mid-way height of the wall frame. Note that the height of the transition section is 93.5 in (238 mm), as opposed to the height of the fire compartment at 90 in (229 mm), since it is uninsulated. The unexposed-side thermocouple rakes can be seen in Figure 4.10 below.

In addition to the gas temperatures, the temperature of the steel frame adjacent to the wall it is of interest from a heat transfer perspective (since the primary mode of radiative heat exchange on the unexposed side of the wall will involve this steel frame). Due to the high thermal conductivity and expected low temperatures of the steel frame, a single sensor was placed on each side of the frame (at the same height as the middle thermocouple in the unexposed side rakes). These two thermocouples were welded directly to the steel frame, and are denoted BR and BL (refer to Figure B.6). Figure 4.11 shows these sensors as-installed.

The temperature of the wall frame itself is critical in assessing heat losses. Eight thermocouples were welded directly to the inside of the wall frame, two per side, 25 in (63.5 cm) from the corners of the wall frame. As mentioned previously, the test walls were surrounded by ceramic fibre insulation as-installed. These wall frame temperature measurements may be used to quantify the heat losses through the border insulation, providing a boundary condition specification which may be used in future models. These thermocouples are denoted FL and FR (refer to Figure B.6).

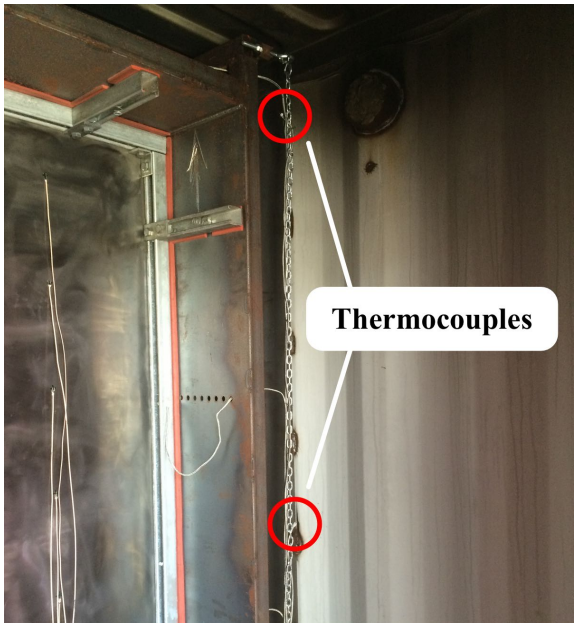


Figure 4.10: Thermocouple rakes on the unexposed-side of the wall.

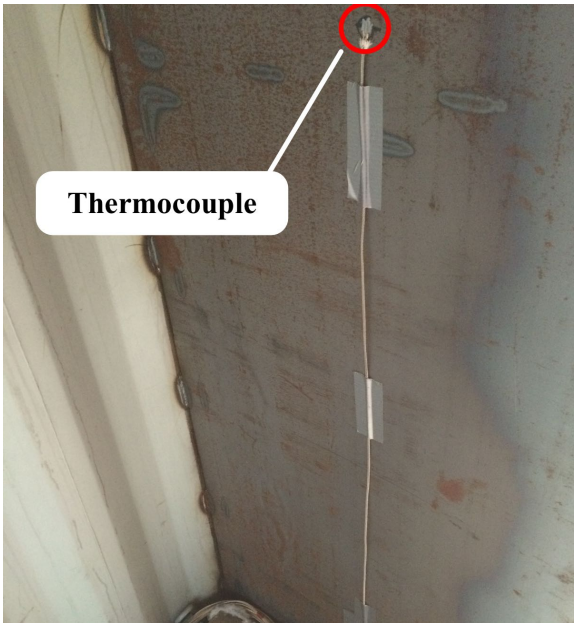


Figure 4.11: Thermocouples on the unexposed-side surroundings.

As mentioned previously, the apparatus is designed to accommodate a stud wall consisting of 3 cavities with studs 24 in (609 mm) on centres. Given this, 36 thermocouples were allocated for use in measuring temperatures within a wall specimen. Eight thermocouples were allocated for each wall cavity on the back side of the exposed thermal barrier (Location 1), and four per wall cavity on the back side of the unexposed thermal barrier (Location 2), as shown in Figure 4.12. This thermocouple allotment can easily be adapted for a stud wall consisting of 4 cavities with studs 16 in (406 mm) on centres, as shown in Figure 4.13. Additional details, including dimensions, are provided in Figure B.7.

In addition to temperature measurements, events were monitored and recorded using video cameras; hardware details are provided in Section 4.3 below. It was of interest to monitor both the exposed and unexposed sides of the decomposing wall, in order to aid assessment of the thermal degradation. Therefore two cameras were allocated for this purpose. The front camera is positioned at the compartment door, but not mounted permanently, so that it may be removed if thermal failure becomes eminent during a test. The rear camera was positioned so as to maximize the view of the unexposed side of the wall (on the floor at the base of the door in the rear wall frame, oriented up toward the wall).

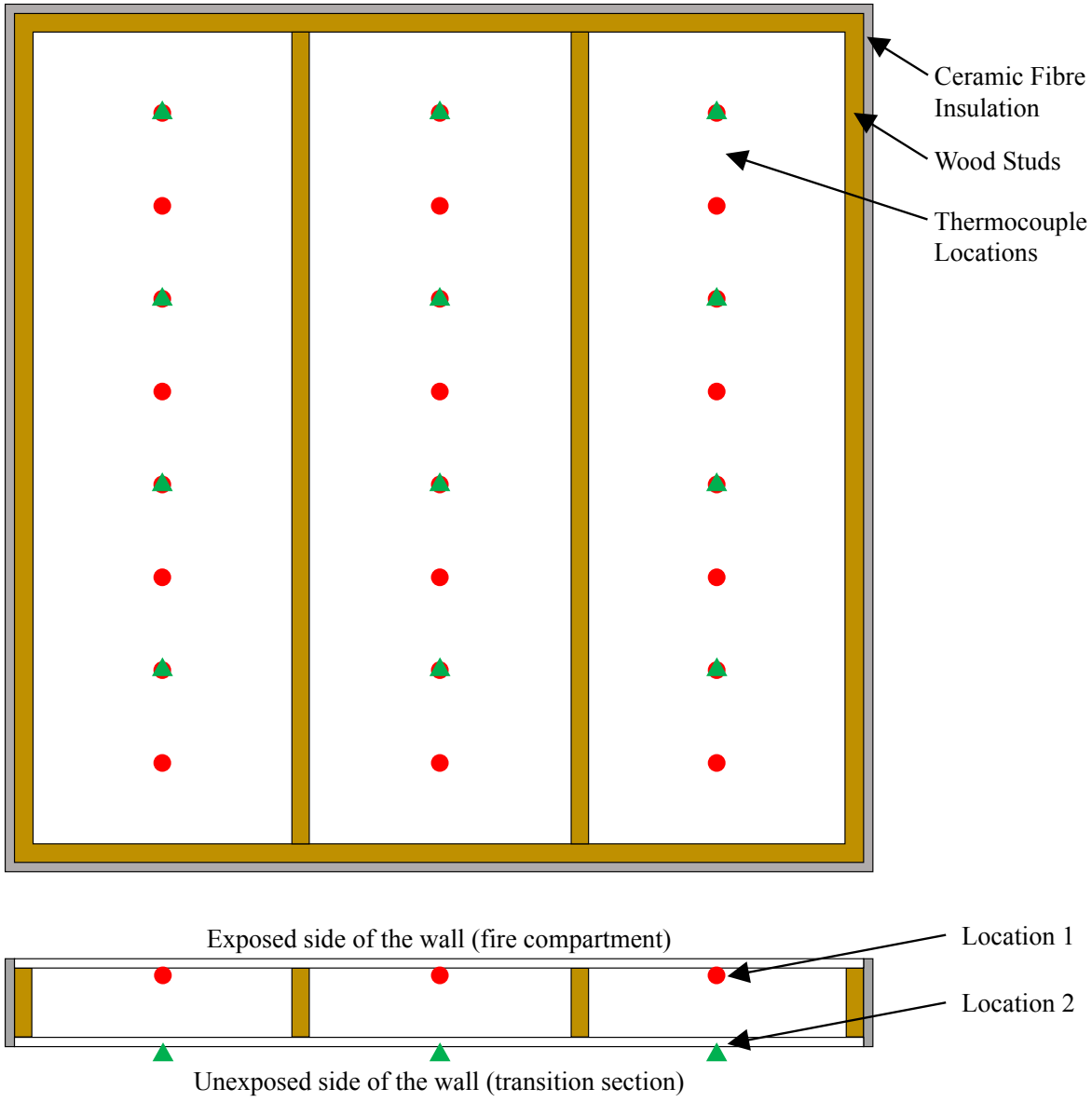


Figure 4.12: Thermocouple locations on a test wall with 24 in (609 mm) stud spacing.

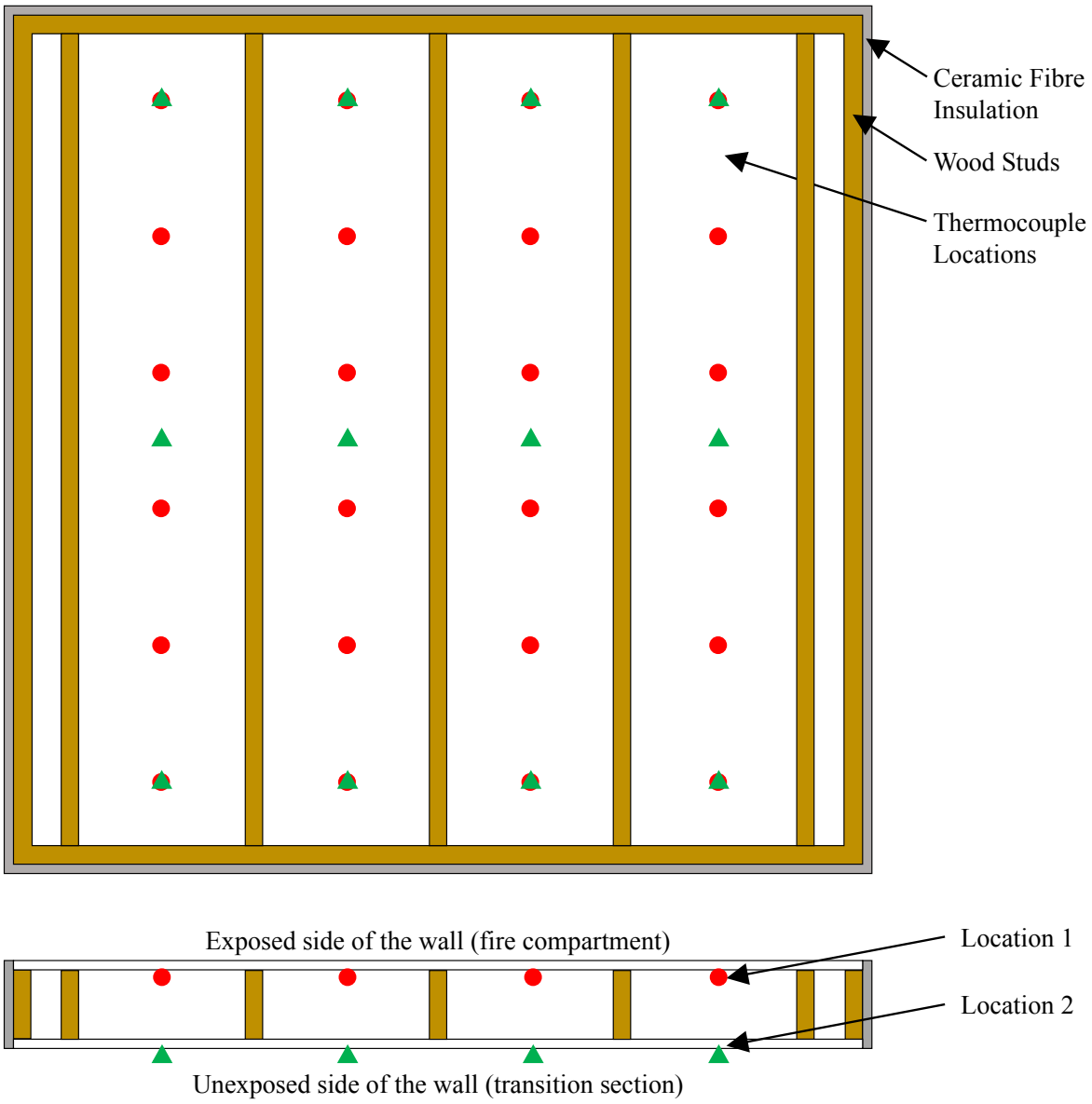


Figure 4.13: Thermocouple locations on a test wall with 16 in (406 mm) stud spacing.

The final consideration was to measure the exposure boundary condition (incident heat flux) on the test wall during a test. In a compartment fire, the exposure is described by the complex interaction of surface radiation (from the compartment walls), gas radiation (fire plume, upper gas layer, lower gas layer), and convection heat transfer [73]. Given sufficient knowledge of the primary variables (temperature), it is possible to deduce the exposure boundary condition on the wall; in fact, this would be the goal of a coupled model of thermal degradation and fire dynamics. However it is desired in this experiment to use heat flux sensors to measure the derived variable (incident heat flux) directly. Since the distinguishing characteristic of this experiment is the realistic or "non-uniform" fire exposure imposed upon the test wall, the primary consideration for sensor selection was that heat flux over the entire surface of the wall needed to be measured, to a resolution sufficient for quantification of the non-uniformity of the exposure field. Using traditional "point source" sensors, this would necessitate multiple sensors installed over the wall area.

The most useful types of heat flux sensors for a large-scale fire experiment are the Gardon gauge, the thin-skin or slug calorimeter, and the directional flame thermometer (DFT) [73]. Gardon gauges would have to be installed within the wall, with the measurement face mounted flush with the wall surface, necessitating holes to be drilled into the exposed-side thermal barrier at each gauge location. In addition to compromising the structural integrity of the thermal barrier, the water-cooled gauges require cooling lines to be installed, introducing undesired temperature differentials throughout the construction assembly. On the other hand, calorimeter and DFT gauges could be suspended in front of the wall rather than within it, but this poses problems similar to those of mounting thermocouple probes or plate thermometers near to the wall. Therefore, rather than measuring heat flux to the wall during each test, it was decided instead to first design a well controlled compartment fire; to then characterize the exposure condition to the wall for that design fire using a novel measurement procedure; and finally to reproduce that design fire for subsequent fire tests. The measurement procedure and apparatus used are outlined in Chapter 5, with results subsequently presented and discussed in Chapter 6. First, an overview of the data acquisition procedure is provided in the following section.

## 4.3 Data Acquisition

As outlined in the previous section, the apparatus was outfitted with a total of 84 temperature sensors, 36 of which were specific to the test wall, plus additional (as yet unspecified) heat flux sensors and video cameras. The same data acquisition system used in the preliminary investigation was used here (refer to Section 3.1 for details). As before, two backplanes were used:

- the first backplane contained eight temperature modules, and was devoted to measurements of compartment and boundary temperatures (48 active signals, 16 open channels for future expansion); and
- the second backplane contained six temperature modules, devoted to measurement of wall temperatures (36 active signals, 12 open channels for future expansion), and two modules dedicated to generic voltage measurements.

The two backplanes were connected to a network switch using gigabit ethernet, and the switch connected to a computer running a custom LabVIEW virtual interface. Data were sampled at a rate of approximately 0.9 Hz (sampling increment of 1.1 seconds), and saved to Comma Separated Value (CSV) datafiles. Column headings in the datafiles used the following naming convention: "`MmCc (DAQb Mm)`", where:

- "`b`" is the backplane number, [1,2];
- "`m`" is the module number, [1,2,3,4,5,6,7,8]; and
- "`c`" is the channel number, [0,1,2,3,4,5,6,7].

Sensor locations and the corresponding DAQ channels are detailed in Chapters 6 and 7.

Video cameras were connected to a QSee high definition analog video recorder capable of supporting up to eight simultaneous camera inputs. Video was recorded in real time to SD flash, so that in the event of camera failures resulting from fire exposure, the recorded video would not be compromised.

The data acquisition system and computer were located in the instrumentation section of the apparatus (Figure 4.14). K-type thermocouple extension cables (20 ga solid wires, polyvinyl sheathed, with 20 duplex pairs per cable) were used to connect thermocouples in the fire compartment to the instrumentation section; cable routing is shown in Figure B.5. Electronics were placed in enclosures in order to protect the equipment from heating, as well as from water in the event of rainy conditions during a test.

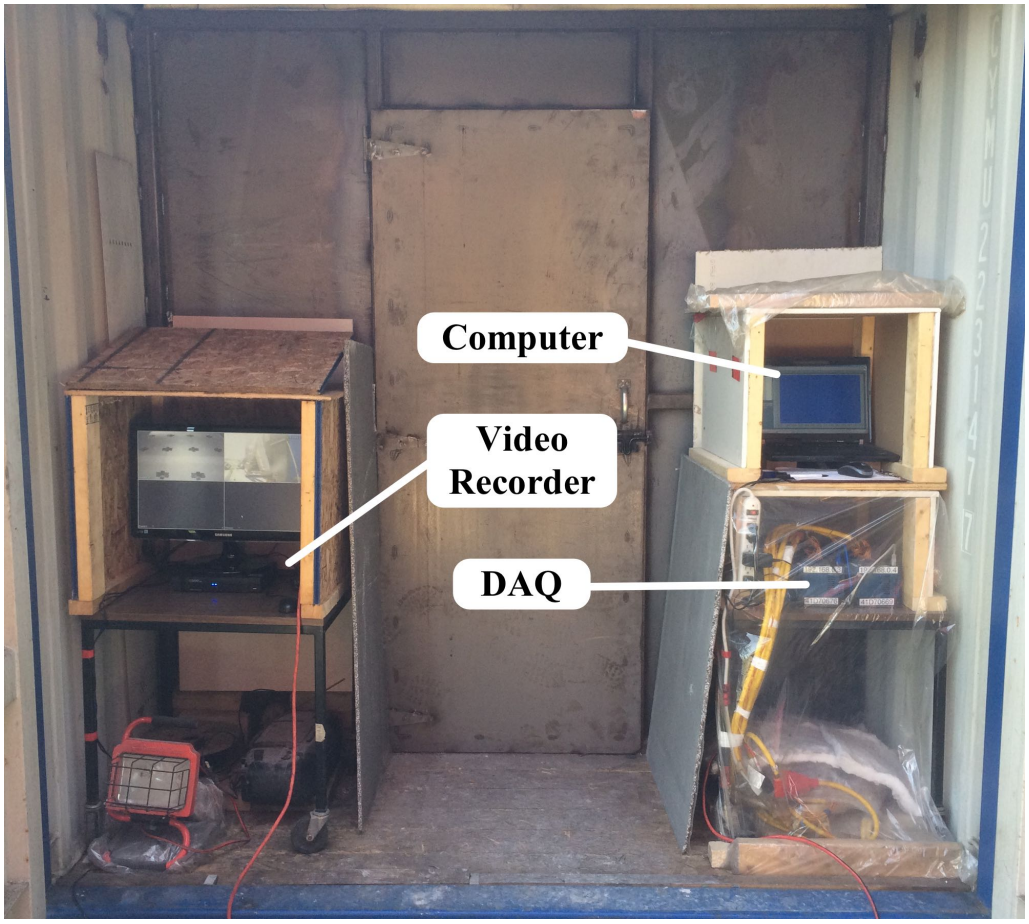


Figure 4.14: Data acquisition system in the instrumentation section.

This chapter has outlined the design of the experiment, but some details of the experimental methods have been purposely omitted. Two types of experiments were conducted in the present work: "steel wall tests" (characterization of the experiment — Chapter 6) and "real wall tests" (assessment of thermal degradation of construction assemblies — Chapter 7). Additional details of the experimental methods specific for each of these types of experiments are provided in the respective chapters. First, however, the following chapter outlines the procedures used for measurement of heat flux.

# Chapter 5

# Measurement of Heat Flux

As outlined in Section 4.2, a novel apparatus and procedure for measurement of the two-dimensional fire exposure on a wall was required to characterize the thermal boundary condition that develops during a specified fire scenario. The concept for the apparatus developed here is based on a thermal capacitance calorimeter sensor, similar to those described in ASTM 457 [74] (slug calorimeter) and ASTM E459 [75] (thin-skin calorimeter). In short, the sensor is comprised of a highly conductive object of which the temperature is measured, and the net heat flux to the exposed area of the object is deduced using a model of thermal energy storage.

At this point it is useful to clarify some terms, for posterity:

- incident radiative heat flux, or irradiance ($q''_{r,i}$), is the radiative heat flux incoming to a surface;
- radiosity is the radiant heat flux outgoing from a surface, consisting of the reflected incident heat flux ($q''_{r,o}$ and the surface emission ($q''_{r,e}$);
- net radiative heat flux ($q''_{r,net}$) is the difference between the irradiance and radiosity at a surface (outgoing, by convention);
- net heat flux ($q''_{net}$) is the combined net radiative heat flux and convective heat flux ($q''_c$) at a surface (outgoing, by convention).

The present work requires a measurement of the incident radiative heat flux distribution over the entire wall, therefore the exposed area of the sensor is equal to the exposed area of a test wall. The sensor developed here, denoted the "steel wall sensor", is mounted into the wall frame in place of a real wall, and the incident radiant heat

flux to the sensor during a fire exposure is deduced via measurements of temperature and use of a thermal capacitance heat transfer model. The following section details the design and construction of the sensor, and subsequent sections outline the development and implementation of the heat transfer model.

## 5.1 Steel Wall Heat Flux Sensor

Given the limitations of a thermal capacitance heat transfer model*, it was decided to adopt a "thin-skin" design for this sensor. Accordingly, 18 gauge (1.27 mm) sheet steel was used for the primary sensing surface. As shown in the construction drawings (Appendix A), the opening size of the wall frame is 75-1/2×75-1/2 in (192×192 cm). A 1/4 in (6.35 mm) thick high-temperature silicone rubber gasket was used to insulate the steel wall sensor from the wall frame, therefore the total exposure area of the steel wall was 75×75 in (190×190 cm). Steel sheet is difficult to obtain in the widths required here, therefore the wall was assembled in three sections, each being 25 in (64 cm) wide.

Next, a frame was designed to support the steel sheets, while remaining rigid during the inevitable thermal expansion of the steel. Taking the linear thermal expansion coefficient for steel to be 12E-6 $K^{-1}$ [28], and assuming that the wall would experience a temperature rise of 800 K, a linear expansion of about 3/4 in (19.1 mm) was expected. Therefore it was decided to build a "floating" frame using 1-5/8 in (41.3 mm) Unistrut steel channels. Details of the frame construction are provided in Appendix A. In summary, each frame component was under-sized by 1/4 in (6.4 mm), and the frame was assembled using standard Unistrut fittings and 1/2 in (12.7 mm) bolts (finger-tight). With the frame in-place, 1/2 in (12.7 mm) holes were drilled into the frame and the steel sheet. The sheet was then affixed to the frame using 1/4 in (6.4 mm) bolts (finger-tight) and fender washers to distribute the load. The end result was a structure that was both rigid and free to expand under fire exposure without buckling.

The main consequence of using such a rigid frame was an increased mass — the total mass of the steel wall sensor including fittings was calculated to be approximately 128 kg using AutoDesk Inventor 2016, assuming a steel density of 7850 kg·$m^{-3}$ for all components. Also, this mass was not evenly distributed over the 2D wall area due to the frame geometry. As detailed in the following sections, the heat transfer model for this

*ASTM test standards for slug [74] and thin-skin [75] calorimeters provide an excellent overview of the development, history, limitations, sensitivity, and accuracy of these types of sensors.

steel wall adopts a simplified geometry, taking the volume of the wall to be simply the product of the exposure area ($A$) and the depth ($\delta$). Given the large thermal mass of the frame, the effective wall thickness was calculated to be 4.5 mm:

$$\delta = \frac{m}{\rho A} \quad , \tag{5.1}$$

where $m = 128$ kg, $A = 3.63$ m$^2$, and $\rho = 7850$ kg·m$^{-3}$. Compared to the actual thickness of the 18 gauge steel sheet (1.27 mm), this represents an increase in thickness of 3.5 times, which is approximately equivalent to 8 gauge steel sheet.

A total of 24 channels on the data acquisition system were allocated for measurement of the steel wall temperature. Sensors were distributed in three columns (corresponding to each section of the steel wall), each with eight sensors distributed vertically; refer to Appendix B.2 for specifics. 24 gauge K-type glass fibre sheathed thermocouple wire was used; leads were welded directly to the steel with a 1–2 mm gap. The sheathed thermocouple cable has a profile measuring 1.4 mm × 2.3 mm, and is rated to a maximum temperature of 871°C. Figure 5.1 shows the unexposed side of the steel wall with thermocouples welded in place. All cable leads were routed neatly into the steel channel below the wall, and into the instrumentation room (to the right in the photo).

In order to implement the aforementioned heat transfer model, knowledge of the thermophysical properties of the constituent materials is required. The properties that are relevant to a solid phase non-reactive heat transfer analysis are: density ($\rho$), specific heat capacity ($c_p$), and thermal conductivity ($\kappa$). In addition to temperature dependence, these properties can vary widely depending on the composition and crystallographic structure of the material, which themselves can change under fire exposure. The material used in the present work was AISI 1020 cold-rolled carbon steel. Constant thermophysical properties were assumed based on values for steel used in fire-specific applications [28, 76, 77] over the temperature range of 0–800°C; refer to Figures 5.2–5.5 for more information. The suitability and consequences of this simplification are discussed where relevant.

The model also requires the thermal conductivity of the silicone insulation to be known (refer to Sections 5.2–5.5 below), which was taken to be 0.24 W·m$^{-1}$·K$^{-1}$ based on the manufacturer's specification [78]. The ceramic fibre insulation used elsewhere in the apparatus is not involved directly in the heat transfer analysis, but it is beneficial to list the thermophysical properties here. The insulation used here, "Fiberfrax Durablanket S® refractory ceramic fibre blanket", has a nominal density of 128 kg·m$^{-3}$ and thickness of 25.4 mm. The manufacturer's specification [79, 80] gives a specific heat capacity of 1130 J·kg$^{-1}$·K$^{-1}$, and a thermal conductivity as detailed in Figure 5.6.

Figure 5.1: Thermocouples installed on the unexposed side of the steel wall.

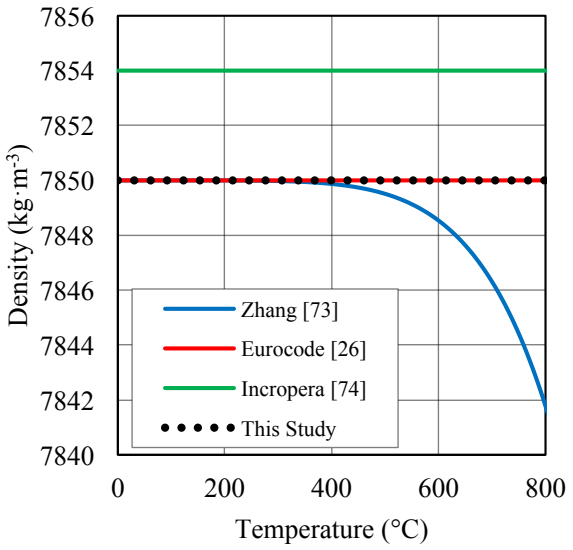


Figure 5.2: Thermophysical properties of steel — density.

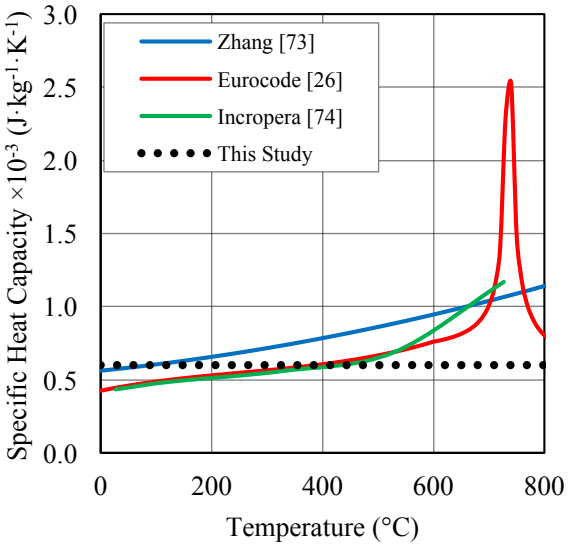


Figure 5.3: Thermophysical properties of steel — specific heat capacity.

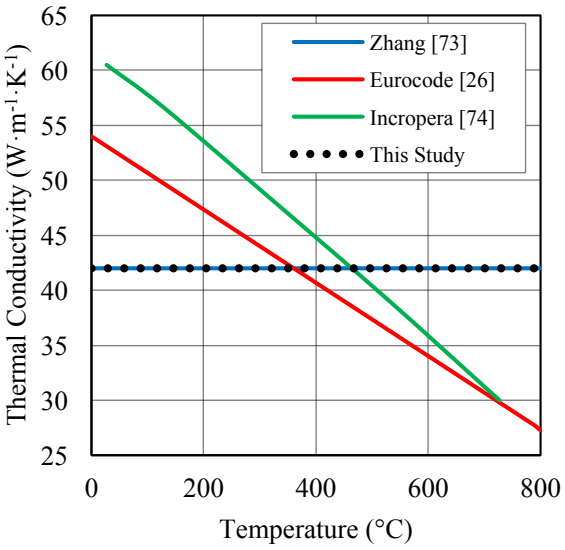


Figure 5.4: Thermophysical properties of steel — thermal conductivity.

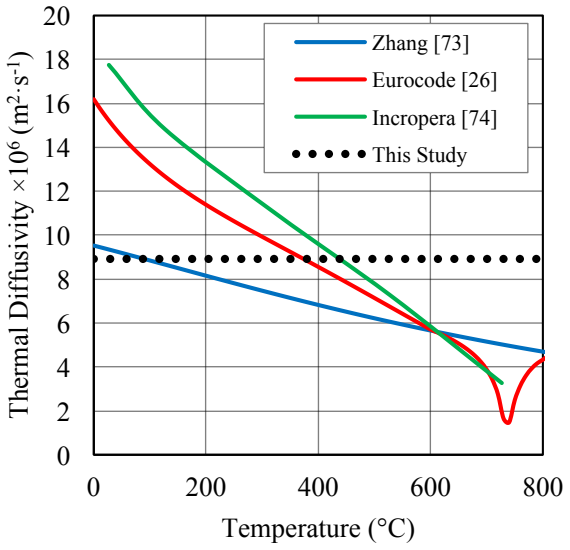


Figure 5.5: Thermophysical properties of steel — thermal diffusivity.

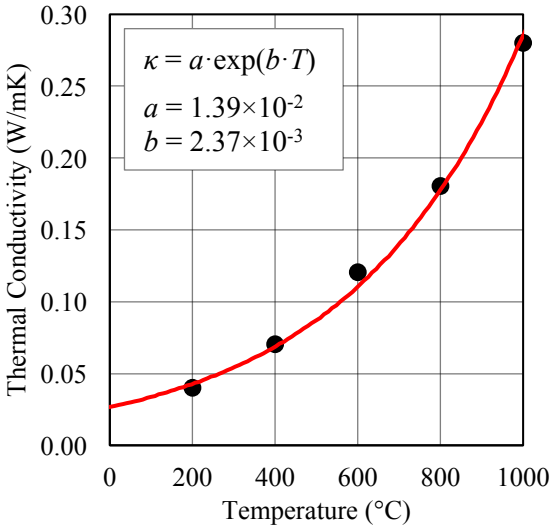


Figure 5.6: Thermal conductivity of ceramic fibre insulation.

Finally, it is required to know the surface emissivity of the steel wall to deduce the incident heat flux. The steel sheet used was flat and rust-free, however given sufficient exposure the carbon steel would surely rust in time, greatly changing the radiative surface properties. Therefore to achieve a consistent and well-characterized surface, a high temperature coating was applied to the wall. Both sides of the steel wall were first ground and polished in-place using an angle grinder and 80-grit flap disk; this also had the benefit of removing any surface oils from the steel. At this point thermocouples were welded to the wall as described above. Next, the entire wall (including the Unistrut frame) was coated in matte black VHT Flameproof® paint, which is rated for continuous operation up to 704°C. The paint was applied in four light coats, alternating the angle of application by 90° for each coat. The polished and painted steel wall is shown in Figure 5.7.

Figure 5.7: Steel wall surface preparation (coating).

With the steel wall prepared, the next step was to characterize the radiative surface properties. This was done by conducting a series of small-scale tests on steel surrogates. Four specimens were prepared from 1/4 in (6.4 mm) thick AISI 1020 stock cut into squares with side lengths of 4-1/2 in (114 mm). The specimen surfaces were prepared in an identical manner as the steel wall, including polishing and coating.

Steel specimens A and B had a K-type thermocouple welded to the top surface prior to paint application (thermocouple leads were separated by a 1–2 mm gap). These two specimens were used in conjunction with a hotplate and infrared (IR) camera (manufactured by FLIR Systems, model T650sc) to estimate the emissivity of the surface; thermocouple temperature was monitored using a Fluke 50 Series digital thermometer.

An IR camera works by measuring the radiant heat flux from emitting surfaces, and deducing the temperature of those surfaces. Figure 5.8 shows schematically the radiative heat exchange between an object, the IR camera, and the surrounding surfaces and atmosphere. The total radiation received by the camera, $E_{tot}$, is:

$$E_{tot} = \tau_{atm}\varepsilon E_{b,obj} + \tau_{atm}\left(1-\varepsilon\right)E_{b,sur} + \left(1-\tau_{atm}\right)E_{b,atm} \quad , \tag{5.2}$$

where $\tau_{atm}$ is the transmissivity of the atmosphere (assumed to be homogeneous and isothermal), $\varepsilon$ is the total emissivity of the object, $\varrho$ is the reflectivity of the object, and it is assumed that the object's surface is diffuse and grey over the entire electromagnetic spectrum from $\lambda = 0$ to $\lambda = \infty$.

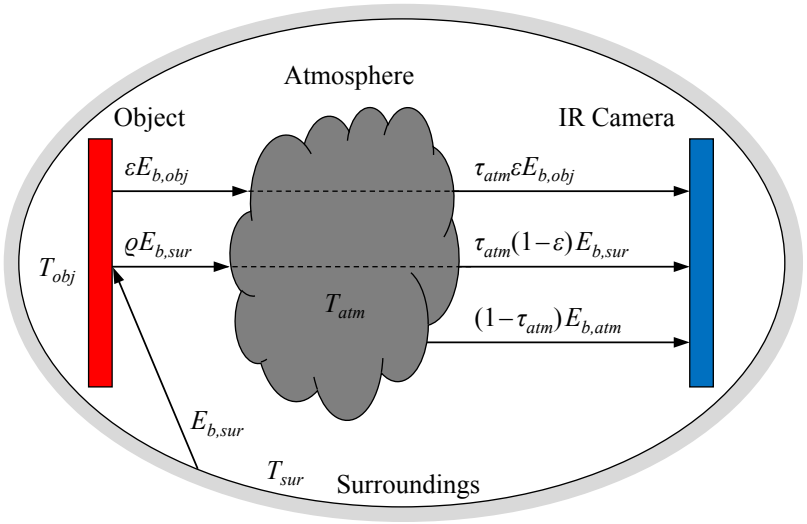


Figure 5.8: Heat transfer schematic for IR camera measurement.

In reality, not only is the surface of an object unlikely to be grey, but the IR camera's sensor is limited to a finite band of the IR spectrum. Typically IR cameras are designed to operate in the mid-wavelength infrared (MWIR) band, from 2 µm to 5 µm, or the long-wavelength infrared (LWIR) band, from 7.5 µm to 14 µm; the FLIR T650sc operates in the LWIR band. Spectral blackbody emissive power, $E_{b,\lambda}$, is given by Planck's law:

$$E_{b,\lambda} = \frac{2\pi h c_0^2}{n^2 \lambda^5 \left[\exp\left(hc_0/n\lambda kT\right) - 1\right]} \quad , \tag{5.3}$$

where $h$ is Planck's constant ($6.626\times10^{-34}$ J·s), $c_0$ is the speed of light in a vacuum ($2.998\times10^{8}$ m·s$^{-1}$), $k$ is Boltzmann's constant ($1.381\times10^{-23}$ J·K$^{-1}$), and $n$ is the refractive index of the transmission medium (assumed to be constant, and approximately equal to 1 for room temperature air) [81]. From this, total blackbody emissive power is:

$$E_b = \int_0^\infty E_{b,\lambda} \mathrm{d}\lambda = n^2 \sigma T^4 \quad , \tag{5.4}$$

where $\sigma$ is the Stefan–Boltzmann constant ($5.670\times10^{-8}$ W·m$^{-2}$·K$^{-4}$). Similarly, the band blackbody emissive power, which is the total blackbody emissive power within a specific spectral band $\lambda_1$–$\lambda_2$, is:

$$E_{b,\lambda_1-\lambda_2} = \int_{\lambda_1}^{\lambda_2} E_{b,\lambda} \mathrm{d}\lambda = \left[f\left(n\lambda_2 T\right) - f\left(n\lambda_1 T\right)\right] n^2 \sigma T^4 \quad , \tag{5.5}$$

where $f\left(n\lambda_1 T\right)$ represents the fraction of blackbody emissive power contained between 0 and $n\lambda_1 T$. This parameter, which is evaluated as a complex integral, may be calculated in practice by an infinite series expansion:

$$f\left(n\lambda_1 T\right) = \frac{15}{\pi^4} \sum_{m=1}^{\infty} \frac{\exp\left(-m\zeta\right)}{m^4} \left(6 + 6(m\zeta) + 3(m\zeta)^2 + (m\zeta)^3\right) \quad , \tag{5.6}$$

where:

$$\zeta = \frac{hc_0/k}{n\lambda T} \quad .$$

Spectral blackbody emissive power is plotted in Figure 5.9 for various temperatures, and the MWIR and LWIR bands are indicated. It is apparent that the band blackbody emissive power depends strongly on temperature. As shown in Figure 5.10 (solid line traces), the band blackbody emissive power is greater in the LWIR band than the MWIR band at temperatures less than 350°C, and conversely is greater in the MWIR band than

the LWIR band at temperatures greater than 350°C. Figure 5.10 also shows (dotted line traces), that the blackbody emissive power in the LWIR band represents approximately 40–45% of the total emissive power at room temperature, and only 20% at 500°C†. This means that, at greater temperatures in particular, the thermal radiation seen by the IR camera only represents a fraction of the actual thermal radiation.

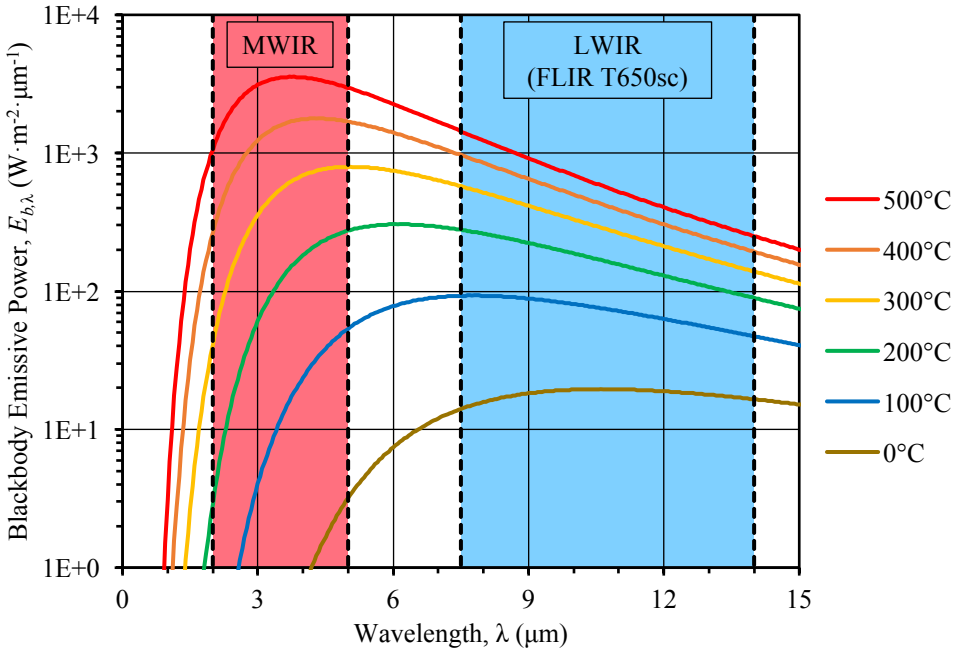


Figure 5.9: Spectral blackbody emissive power for various temperatures.

In consideration of the spectral limitations of the IR camera, care must be taken in applying energy calculations based on its measurements. FLIR has implemented a number of hardware and software corrections in its application of Equation 5.2. First, rather than assuming that the surface of the object is grey (over the entire spectrum), it is assumed that the surface of the object may be treated as being grey over the band of interest (LWIR). This means that the emissivity of the surface represents a band-averaged value; in other words, it is the ratio of the actual emissive power of the surface (in the LWIR band) and the blackbody emissive power of the surface (in the LWIR band). Temperature of the surroundings, temperature and relative humidity of the atmosphere, and distance between the camera and the object are used to calculate the atmospheric transmission and emissive power attributed to the surroundings and atmosphere.

†The ratio of total blackbody emissive power was calculated by dividing the band blackbody emissive power (Equation 5.5) by the total blackbody emissive power (Equation 5.4) for a given temperature.

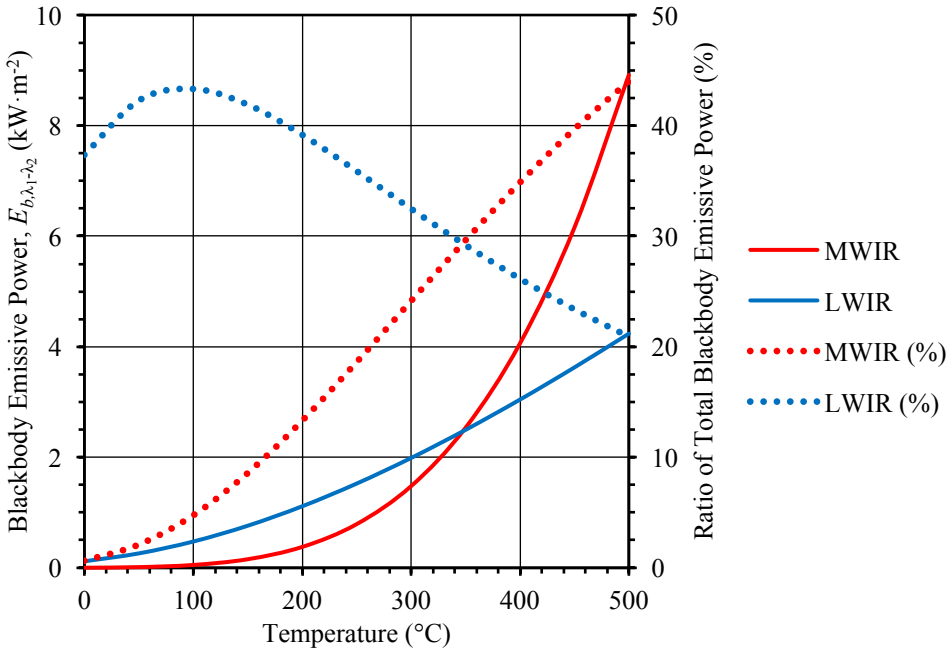


Figure 5.10: Blackbody emissive power in the MWIR and LWIR bands.

In the present work, the IR camera was oriented above and perpendicular to the steel specimen (Figure 5.11), and the average temperature in an elliptical region centred on the thermocouple junction was measured using the IR camera (Figure 5.12). The specimen was the heated until it reached a steady temperature, at which time the hotplate was turned off, the lights in the room were turned off, and temperature measurements were recorded as the steel cooled over time using both the IR camera and the thermocouple. Two experiments were conducted, one each for specimen A and B.

After the experiments were conducted, FLIR ResearchIR 4 software was used to adjust the emissivity parameter until the temperature measured by the IR camera was equal to the thermocouple measurement at each measurement time. In consideration of the aforementioned assumptions, emissivity deduced in this manner is representative of the average hemispherical emissivity of the painted surface in the LWIR band (i.e. the spectral hemispherical emissivity averaged over the LWIR band). The results are shown in Figure 5.13, which shows the relation between band average emissivity and surface temperature. While LWIR average emissivity increases with temperature, it should be cautioned to presume that the total emissivity has the same dependence, as this may partially be an artifact of the reduced blackbody emissive power within the LWIR band at temperatures above approximately 100°C — refer to Figure 5.10.


Figure 5.11: Measurement of temperature-dependent emissivity (setup).

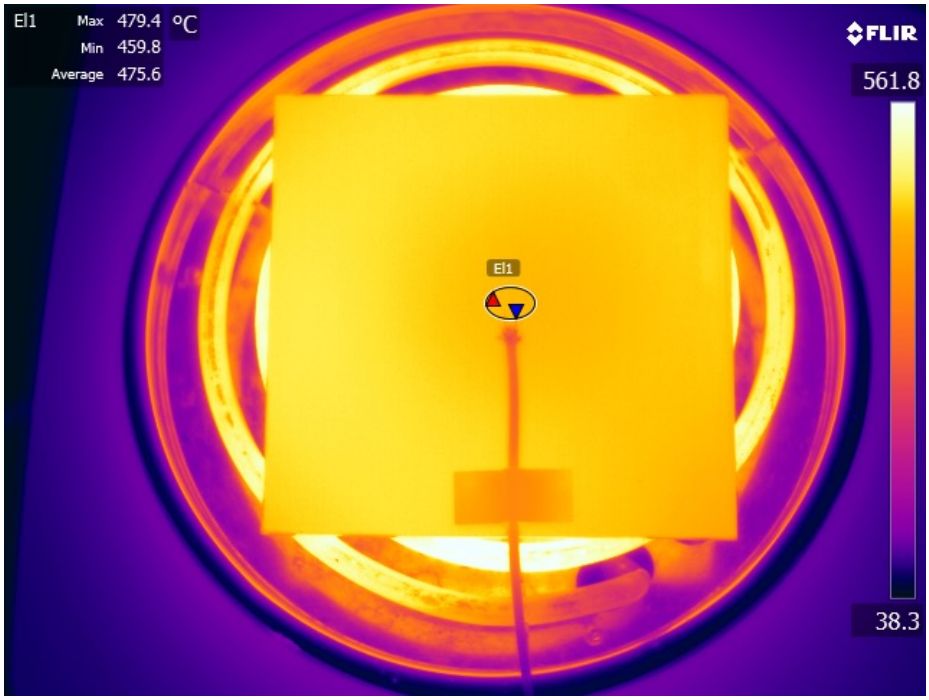


Figure 5.12: Measurement of temperature-dependent emissivity (IR image).

In addition, spectral emissivity was measured at 21°C using a SOC-400T reflectometer (manufactured by Surface Optics Corp.) for the remaining two square specimens. The device was calibrated relative to a gold reference prior to the tests; refer to Kotey [82] for more information. The results are plotted in Figure 5.14, which shows that the painted surface is, in fact, very near-black. The average value of spectral emissivity in the LWIR band was 0.932; this measurement is consistent with the LWIR band emissivity measured using the IR camera at room temperature. Based on these findings, $\varepsilon$ was taken to be constant value of 0.93 in the present work.

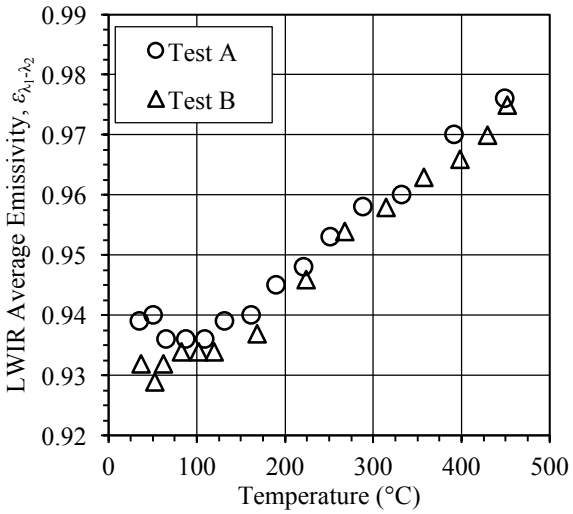


Figure 5.13: Band average emissivity at various temperatures (IR camera tests).

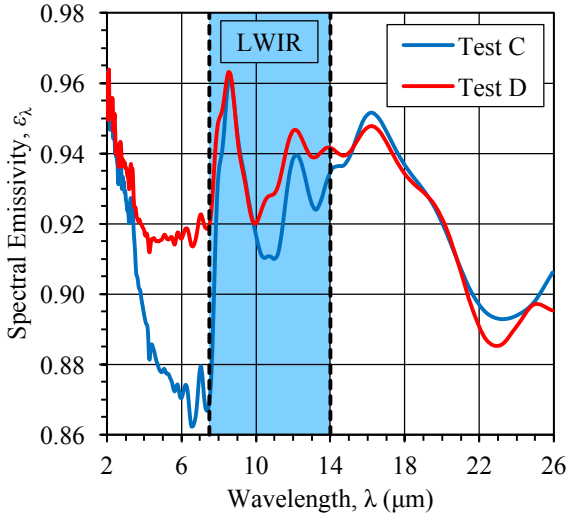


Figure 5.14: Spectral emissivity at room temperature (reflectometer tests).

This steel wall sensor was designed to measure temperature at multiple locations over its surface, with the intent to deduce heat flux from these measurements. As mentioned previously, a thermal capacitance model is used for calculation of this derived variable. The following section outlines the derivation and application of this type of model for a generalized situation (a zero-dimensional slug); subsequent sections refine the model for the specific steel wall sensor application.

## 5.2 The Generalized Thermal Capacitance Model

Consider some generic and thermochemically inert object, described here as a "slug". Presuming that the density and specific heat capacity of the slug are known, and

presuming that the slug may be treated as isothermal throughout its entire volume under a given heating scenario, then the exposure condition on the surface of the slug may be inferred given the measured temperature history. This is the generalized thermal capacitance method, as represented schematically in Figure 5.15, in which an object is exposed to some form of a heat transfer boundary condition (e.g. a combined radiative and convective heat flux). The derivation of the thermal model follows.

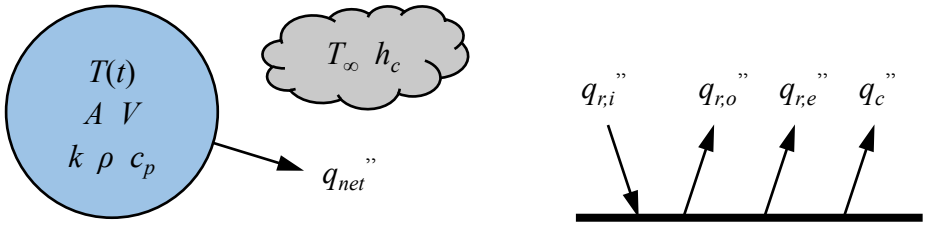


Figure 5.15: Heat transfer schematic for the generalized thermal capacitance model.

By conservation of energy, the rate of temperature change of the slug is given by:

$$\rho V c_p \frac{\mathrm{d}T}{\mathrm{d}t} = -A q''_{net} \quad , \tag{5.7}$$

where $q''_{net}$ is the net rate of heat transfer out of the slug per unit surface area $A$ at time $t$, $V$ is the volume of the slug, $\rho$ is the density of the slug material, and $c_p$ is the specific heat capacity of the slug material. For some irradiance $q''_{r,i}$, the net heat flux is:

$$q''_{net}(t) = q''_{r,o}(t) - q''_{r,i}(t) + q''_{r,e}(t) + q''_{c}(t) \quad ,$$

where $q''_{r,o}$ is the reflected irradiance (equal to $\varrho q''_{r,i}$, where $\varrho$ is the reflectivity of the surface), $q''_{r,e}$ is the emitted heat flux (equal to $\varepsilon E_b$, where $E_b$ is the total emissive power of the surface), and $q''_c$ is the convective heat flux out of the surface:

$$q''_{c}(t) = h_c(t)\left[T(t) - T_\infty(t)\right] \quad ,$$

where $h_c$ is a convection heat transfer coefficient and $T_\infty$ is the gas temperature near the slug. From an energy balance at the surface:

$$q''_{r,i}(t) - \varrho q''_{r,i}(t) = \alpha q''_{r,i}(t) \quad ,$$

where $\alpha$ is the absorptivity of the surface, assuming that the surface is opaque ($\varrho = 1-\alpha$). Combining terms, the net heat flux out of the slug is:

$$q''_{net}(t) = -\alpha q''_{r,i}(t) + \varepsilon E_b(t) + h_c(t)\left[T(t) - T_\infty(t)\right] \quad .$$

Finally, making the assumption that the surface is diffuse gray ($\alpha = \varepsilon$), and representing the total emissive power of the surface in terms of its temperature ($E_b = \sigma T^4$), the net heat flux out of the slug is:

$$q''_{net}(t) = -\varepsilon q''_{r,i}(t) + \varepsilon\sigma T(t)^4 + h_c(t)\left[T(t) - T_\infty(t)\right] \quad . \tag{5.8}$$

Working from Equations 5.7 and 5.8, the system model is reduced to:

$$\frac{\rho V c_p}{A}\frac{\mathrm{d}T(t)}{\mathrm{d}t} = \varepsilon q''_{r,i}(t) - \varepsilon\sigma T(t)^4 - h_c(t)\left[T(t) - T_\infty(t)\right] \quad . \tag{5.9}$$

A numerical solution to this non-linear differential equation was adopted. Representing the temporal derivative using a first order backward difference approximation, the finite difference form of the differential equation is:

$$\frac{\rho V c_p}{A}\frac{T_k - T_{k-1}}{\Delta t} = \varepsilon q''_{r,i_k} - \varepsilon\sigma T_k^4 - h_{ck}\left(T_k - T_{\infty k}\right) \quad , \tag{5.10}$$

where $k$ is the time step and $\Delta t = t_k - t_{k-1}$. By linearizing the dependent variable ($T$), a tractable solution is developed in which $T_k$ is implicitly represented; let:

$$h_{rk} = \varepsilon\sigma T_k^3 \quad ,$$

where $h_{rk}$ is a radiation heat transfer coefficient. This presents a problem of approximating the heat transfer coefficient using the unknown value of $T$ at the current time step. This is addressed by simply evaluating the heat transfer coefficient using the value of $T$ at the previous time step:

$$h_{rk} \approx h_{rk-1} = \varepsilon\sigma T_{k-1}^3 \quad .$$

This assumption is reasonable for a small $\Delta t$, or for a very slow rate of temperature change. However, the error associated with this assumption can be effectively negated by iterative computation; refer to Appendix F (Section F.1, `s_general_model.m`, lines 65–84) for the implementation used here. By introducing the lumped heat transfer coefficients $\alpha_k$ and $\beta_k$, Equation 5.10 reduces to:

$$\frac{T_k - T_{k-1}}{\Delta t} + \beta_k T_k = \alpha_k \quad , \tag{5.11}$$

where

$$\beta_k = \frac{A}{\rho V c_p}\left(h_{rk} + h_{ck}\right) \quad ,$$

and

$$\alpha_k = \frac{A}{\rho V c_p}\left(\varepsilon q''_{r,i_k} + h_{ck} T_{\infty k}\right) \quad .$$

This model can be run in two modes. The first, referred to as "forward" mode, is used to compute the temperature of the slug given a known irradiance:

$$T_k = \gamma_k T_{k-1} + \gamma_k \Delta t \alpha_k \quad , \tag{5.12}$$

where

$$\gamma_k = \frac{1}{1 + \beta_k \Delta t} \quad .$$

The second, referred to as the "inverse" mode, is used to compute the irradiance given the known temperature history of the slug:

$$q''_{r,i_k} = \alpha^*_k \frac{\rho V c_p}{A\varepsilon} - \frac{h_{ck}}{\varepsilon} T_{\infty k} \quad , \tag{5.13}$$

where

$$\alpha^*_k = \left( \frac{1}{\Delta t} + \beta_k \right) T_k - \frac{1}{\Delta t} T_{k-1} \quad .$$

It should be noted that iterative computation of $h_{rk}$ is not required in the inverse model, since the temperature at the current time step is known.

It is useful to demonstrate implementation of this model by means of example. Consider the following scenario: a spherical steel slug with diameter of 1 cm is initially at 300 K and at thermal equilibrium with its environment. At $t$=0, external heating is applied; the irradiance increases at a rate proportional to $t^2$ to a peak value of 50 kW·m$^{-2}$ after 10 minutes. The fluid temperature is constant at 300 K, and the convection heat transfer coefficient is constant at 10 W·m$^{-2}$·K$^{-1}$. The density, specific heat capacity, and emissivity of the steel are taken to be 7850 kg·m$^{-3}$, 600 J·kg$^{-1}$·K$^{-1}$, and 0.9, respectively. The model was first run in forward mode to predict the temperature of the slug given the known exposure, and subsequently run in inverse mode to predict the incident heat flux given the known slug temperature.

As shown in Figure 5.16, in forward mode the model predicts that the slug temperature will increase to approximately 600°C after 10 minutes of exposure. A large time step of 10 seconds was used (61 steps total) and the model completed a total of 161 iterations. This means that for each time step it took an average of 2.64 iterations for $h_r$ to converge. When run in inverse mode, the model predicts exactly the irradiance that was originally input to the forward model. This result is not meaningful in the context of the example, but is simply a verification that the inverse equations have been implemented correctly in the code. In reality, if noisy temperature data is used as the model input, there will likely be issues with determining a convergent solution, due to the ill-posed nature of the

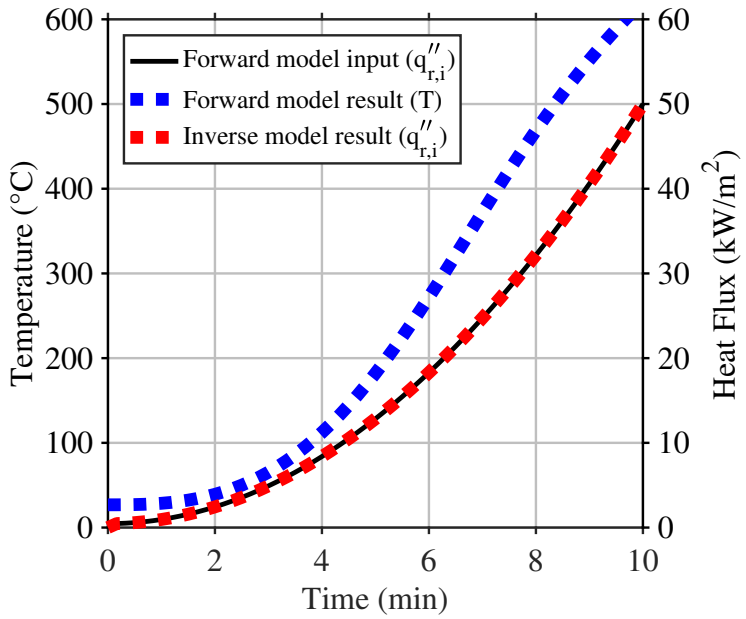


Figure 5.16: Results of the forward and inverse generalized thermal capacitance model for the example scenario.

problem. This issue is addressed in subsequent sections, below. The code listing for the model implementation used here may be found in Appendix F (Section F.1).

The "thermally thin" assumption is critical in the formulation of the thermal capacitance model; in other words, at any given time the temperature of the object is the same through it's entire volume. This condition can be evaluated by lumping the effective radiation and convection heat transfer coefficients and calculating an effective Biot number — the thermally thin assumption is generally acceptable for Bi $< 0.1$ [77]. For this example, it is assumed that the irradiance may be represented by the following expression:

$$q''_{r,i} \approx \sigma T_{\infty}^{4} \quad ,$$

then, from Equation 5.8, the net heat flux out of the object is:

$$q''_{net} = h_e \left(T - T_{\infty}\right) \quad ,$$

where $h_e$ is an effective heat transfer coefficient defined as follows:

$$h_e = h_c + \varepsilon\sigma \left(T + T_{\infty}\right)\left(T^2 + T_{\infty}^2\right) \quad . \tag{5.14}$$

The Biot number may be calculated by:

$$\mathrm{Bi} = \frac{h\delta}{\kappa} \quad ,$$

where $h = h_e$, $\kappa$ is the thermal conductivity (taken to be 42 $\mathrm{W{\cdot}m^{-1}{\cdot}K^{-1}}$ for steel), and $\delta$ is the characteristic length, typically taken to be the volume of the object divided by its surface area ($\delta = D/6$ for the spherical slug, where $D$ is the diameter of the sphere). Figure 5.17 shows the effective Biot number calculated for various different characteristic lengths for surface temperatures up to 600°C, assuming a fluid temperature of 600°C and a convective heat transfer coefficient of 10 $\mathrm{W{\cdot}m^{-2}{\cdot}K^{-1}}$ (a conservative estimate). Greater values of either $T_\infty$ or $h_c$, as might be expected in a compartment fire, will increase the effective Biot number for a given characteristic length.

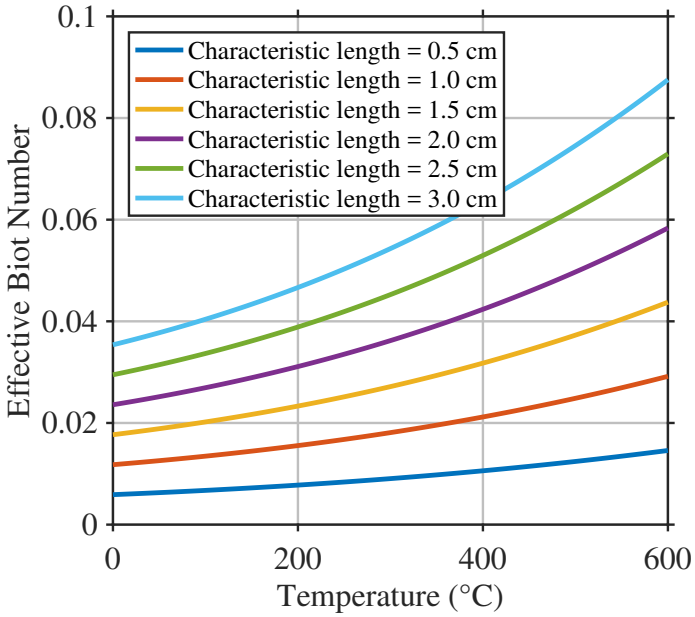


Figure 5.17: Effective Biot number for steel for the generalized thermal capacitance model.

Building upon the generalized method for calculation of irradiance by thermal capacitance, the technique is applied to the steel wall sensor of interest in the present work in the following section.

## 5.3 Thermal Capacitance Model for the Steel Wall

The steel wall sensor is essentially a thin, highly-conductive barrier separating the compartment fire section from the intermediate section of the fire test apparatus. It is assumed that the steel is thermally thin, such that the temperature on either side of

the sheet is identical at a given time, for a given heat exposure; the suitability of this assumption is addressed in Section 5.6. Furthermore, it is assumed that the radiative heat transfer on either side of the steel wall may simply be treated as surface-to-surface radiation within an enclosed volume. In practice this is a very poor assumption on the exposed side of the wall, since it completely negates flame radiation as well as the participation of gases in the transport medium. A consequence of this assumption is that model uncertainty is quite high — this shortcoming will be addressed in the following sections. On the unexposed side of the wall, where there is no flame radiation or accumulation of fire gases, the assumption is reasonable. A schematic for this model is provided in Figure 5.18 below, where the "$f$" subscript represents the exposed "fire" side of the wall, and the "$c$" subscript represents the unexposed "cool" side of the wall.

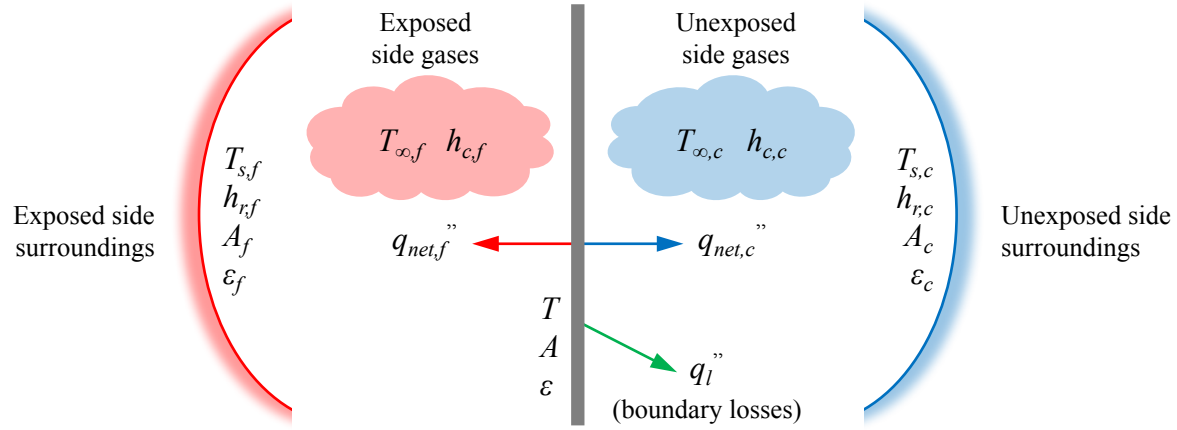


Figure 5.18: Heat transfer schematic for the generalized thermal capacitance model.

For this "two surface enclosure" [77] it is convenient to formulate the model in terms of net heat flux rather than incident heat flux due to the interaction between the wall surfaces and the surrounding surfaces on both sides. Assuming that both surfaces are diffuse gray and that the wall is flat, the net radiative heat flux out of the wall on side "$x$" (representing either the fire side or the cool side) is:

$$q''_{r,net,x}(t) = \frac{\sigma}{r_x}\left[T(t)^4 - T_{s,x}(t)^4\right] \quad , \tag{5.15}$$

where

$$r_x = \frac{1}{\varepsilon} + \frac{A}{A_x}\left(\frac{1}{\varepsilon_x} - 1\right) \quad .$$

It is noted that for an enclosure in which the surroundings are much larger than the surface of the wall ($A_x >> A$), the expression for net heat flux reduces to:

$$q''_{r,net,x}(t) = \varepsilon\sigma \left[T(t)^4 - T_{s,x}(t)^4\right] \quad .$$

In this case, the ratio of wall area to surroundings area is 0.10 on the fire side and 0.25 on the cool side, so the assumption that $A_x >> A$ is not well justified; however, if the emissivity of the surroundings is similar to that of the wall, the correction is minor.

The total net heat flux out of the wall on side $x$, including convection, is:

$$q''_{net,x}(t) = \frac{\sigma}{r_x}\left[T(t)^4 - T_{s,x}(t)^4\right] + h_{c,x}(t)\left[T(t) - T_{\infty,x}(t)\right] \quad . \tag{5.16}$$

Introducing an effective heat transfer coefficient for radiation, $h_{r,x}$, the expression for net heat flux reduces to:

$$q''_{net,x}(t) = h_{r,x}(t)\left[T(t) - T_{s,x}(t)\right] + h_{c,x}(t)\left[T(t) - T_{\infty,x}(t)\right] \quad , \tag{5.17}$$

where

$$h_{r,x}(t) = \frac{\sigma}{r_x}\left[T(t) + T_{s,x}(t)\right]\left[T(t)^2 + T_{s,x}(t)^2\right] \quad .$$

It is convenient to isolate the dependent variable $T$ in Equation 5.17:

$$q''_{net,x}(t) = \left[h_{r,s}(t) + h_{c,s}(t)\right]T(t) - h_{r,x}(t)T_{s,x}(t) - h_{c,x}(t)T_{\infty,x}(t) \quad . \tag{5.18}$$

Given this formulation, the incident heat flux may be calculated using the following expression (derived from Equation 5.8):

$$q''_{r,i,x}(t) = -\frac{1}{\varepsilon}q''_{net,x}(t) + \sigma T(t)^4 + \frac{h_{c,x}(t)}{\varepsilon}\left[T(t) - T_{\infty,x}(t)\right] \quad . \tag{5.19}$$

As was the case for the generalized thermal capacitance model, conservation of energy is applied about the steel wall:

$$\frac{\rho V c_p}{A}\frac{\mathrm{d}T(t)}{\mathrm{d}t} = -q''_{net,f}(t) - q''_{net,c}(t) - \frac{A_l}{A}q''_l(t) \quad , \tag{5.20}$$

where $A_l$ is the contact area around the four sides of the wall and $q''_l(t)$ is the net rate of conductive heat transfer out of the wall over the contact area. Discretizing the differential equation in time and adopting a form that is consistent with the generalized model, the model reduces to:

$$\frac{T_k - T_{k-1}}{\Delta t} + \beta_k T_k = \alpha_k \quad , \tag{5.21}$$

where

$$\beta_k = \frac{A}{\rho V c_p}\left(h_{r,f_k} + h_{c,f_k} + h_{r,c_k} + h_{c,c_k} + h_{lk}\right) \quad ,$$

$$\alpha_k = \frac{A}{\rho V c_p}\left(h_{r,f_k} T_{s,f_k} + h_{c,f_k} T_{\infty,f_k} + h_{r,c_k} T_{s,c_k} + h_{c,c_k} T_{\infty,c_k} + h_{lk} T_{lk}\right) \quad ,$$

$$h_{r,x_k} \approx h_{r,x_{k-1}} = \frac{\sigma}{r_x}\left[T_{k-1} + T_{s,x_{k-1}}\right]\left[T_{k-1}^2 + T_{s,x_{k-1}}^2\right] \quad ,$$

and

$$h_l = \frac{A_l}{A}\frac{\kappa_l}{\delta_l} \quad .$$

Implicit in this formulation is the discretization of the boundary heat losses in the spatial dimension (denoted here by $l$). By Fourier's law:

$$q_l''(t) = -\kappa_l \frac{\partial T(l,t)}{\partial l} \quad ,$$

where $\partial T/\partial l$ is the spatial temperature gradient at the edge of the steel wall. Discretizing this expression over the thickness of the insulation surrounding the wall ($\delta_l$) gives:

$$q_{l\,k}'' = \frac{\kappa_l}{\delta_l}\left(T_{lk} - T_k\right) \quad ,$$

where $T_l$ is the temperature on the opposite side of the insulation.

Running the model in forward mode, the temperature of the wall can be predicted given known temperatures of the fire-side gases and surroundings:

$$T_k = \gamma_k T_{k-1} + \gamma_k \Delta t \alpha_k \quad , \tag{5.22}$$

where

$$\gamma_k = \frac{1}{1 + \beta_k \Delta t} \quad .$$

Running the model in inverse mode, the net heat flux out of the wall on the fire-side can be predicted given known temperature of the wall:

$$q_{net,f_k}'' = -\alpha_k^* \frac{\rho V c_p}{A} + h_{r,c_k} T_{s,c_k} + h_{c,c_k} T_{\infty,c_k} + h_{lk} T_{lk} \quad , \tag{5.23}$$

where:

$$\beta_k^* = \frac{A}{\rho V c_p}\left(h_{r,c_k} + h_{c,c_k} + h_{lk}\right) \quad ,$$

and

$$\alpha_k^* = \left(\frac{1}{\Delta t} + \beta_k\right) T_k - \frac{1}{\Delta t} T_{k-1} \quad .$$

Finally, the incident heat flux on the fire-side can be calculated by the following expression (the discretized form of Equation 5.19):

$$q''_{r,i,f_k} = -\frac{1}{\varepsilon} q''_{net,f_k} + \sigma T_k^4 + \frac{h_{c,f_k}}{\varepsilon} \left[ T_k - T_{\infty,f_k} \right] \quad . \tag{5.24}$$

The code listing for the heat transfer model as implemented here may be found in Appendix F (Section F.2).

The forward application of this model for prediction of the steel wall temperature will not be particularly accurate, due to the gross simplification of a complex fire exposure to that of a simple 2-surface enclosure. However, the inverse application of this model, presuming that the steel wall temperature is known with good accuracy, should be expected to yield a good approximation of incident heat flux using Equations 5.23–5.24. The issue with this approach is that the problem is inherently ill-posed — small perturbations in measurement noise and model error will be amplified into large perturbations in the recovered heat flux measurements. Recall that the irradiance is essentially proportional to the rate of change of the wall temperature — even if the measurement noise is very small, each fluctuation in the measured T will lead to a magnified fluctuation in the calculated $\partial T/\partial t$. In fact, this is a problem with all heat flux sensors that work by deducing a derived variable (heat flux) from a primary variable (temperature) by means of a thermal energy storage model. One might be tempted, then, to simply apply a curve-fit or smoothing filter to the measured temperature before substitution to the inverse model. If the objective is to present heat flux predictions in a "nice" format, then perhaps this approach would be suitable. However, this would eliminate any quantification of uncertainty in the predicted heat flux. What is needed is a way to incorporate both the temperature measurements and the forward application of the heat transfer model to produce the best possible estimate of heat flux, including a quantification of uncertainty. The Kalman filter was used to address this need. The theory and implementation of the filter to the present application is the focus of the following section.

## 5.4 Model Optimization by Kalman Filter

The theoretical underpinning for the Kalman filter is based on Bayesian probability — the determination of what is likely to be true based on past information. In short, it must be admitted that for any given circumstance knowledge is limited, therefore beliefs

should be altered based on the strength of the evidence available. By incorporating some knowledge about how a system behaves (e.g. a thermal energy storage model) and some uncertain measurements (e.g. thermocouple measurements with inherent noise and measurement error), a Bayesian filter may be used to estimate the most likely value of heat flux. The Kalman filter is an implementation of Bayesian filtering that resolves this problem of limited knowledge in a mathematically optimal way [83].

To begin, all variables in the present analysis are treated as continuous random variables. It is assumed that these variables are Gaussians, which is to say that they have a normal probability density function (PDF) with mean $\mu$ and variance $\sigma^2$; this is denoted N($\mu$,$\sigma^2$). For example, consider a temperature sensor which has a mean value of 20°C and has a sensor variance of of 1°C (given in the manufacturer's specifications); the PDF for this variable is shown in Figure 5.19. In the figure, one, two, and three standard deviations ($\sigma$) about the mean are indicated — these represent a 68%, 95%, and 99.7% (respectively) likelihood that the true value of the variable is within this range. It is important to note that although the true value of the variable can never be determined with 100% certainty, it is possible to estimate the most likely value of the variable given the information available. In this case it is likely that the true value of the temperature is between 19°C and 21°C, and exceptionally likely that the true value of temperature is between 17°C and 23°C.

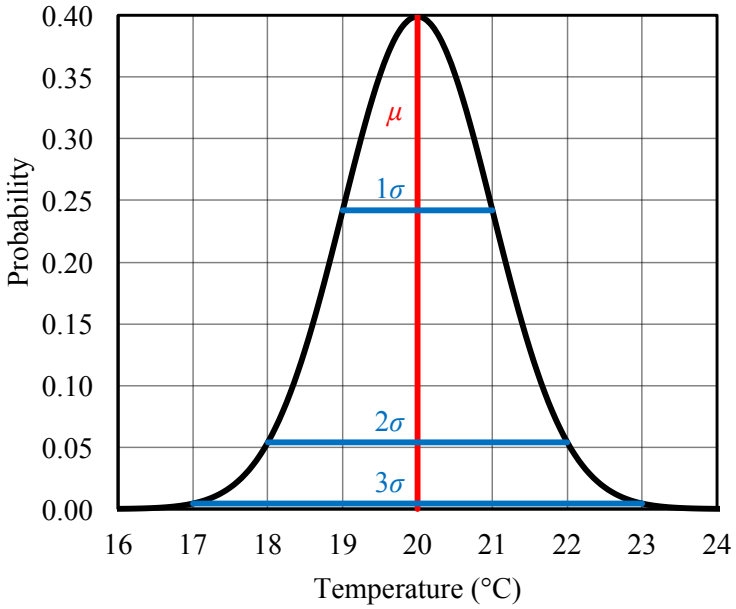


Figure 5.19: Normal probability density function for temperature measurement.

The Kalman filter capitalizes on the assumption of a normal probability distribution for the involved variables — Gaussian arithmetic operations are very straightforward and low-cost computationally. These arithmetic operations are used by the filter to calculate state estimates at a current time step using priors (posterior estimates from the previous time step), as well as the expected values of the states at the current time step based on a process model, and measurement input. Figure 5.20 shows a process diagram of the filter as implemented here.

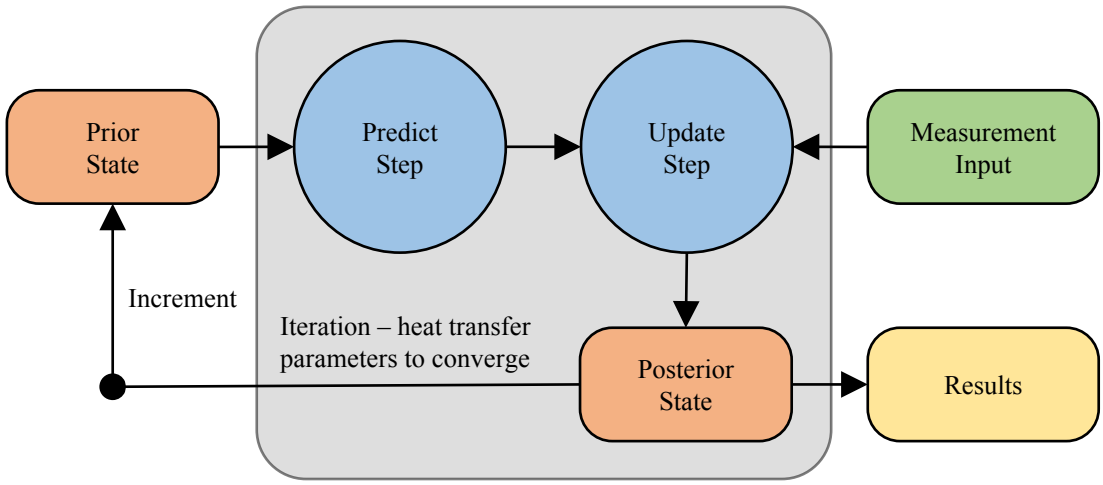


Figure 5.20: Schematic of the Kalman filter with iteration step.

The first step in implementing the filter in the present work is designation of the state variables. Given the thermal energy storage process model, temperature is the primary state variable. The traditional notation used to represent the state is $x$, for the mean, and $P$, for the variance. For $n$ state variables, $x$ is an $n \times 1$ vector and $P$ is an $n \times n$ matrix; when $n > 1$ (e.g. a 2D process) $P$ is the covariance between each state.

The next step is to develop a recursive process model for the predict step of the algorithm. The process model consists of two expressions: one for the state mean (Equation 5.25) and one for the state covariance (Equation 5.26). The process model (state mean) has the following form:

$$\overline{x}_k = F_k x_{k-1} + \Gamma_k u_k \quad , \tag{5.25}$$

where $\overline{x}_k$ is the predicted state estimate at the current time step $k$, $x_{k-1}$ is the prior state estimate, $F_k$ is the state transition model (which governs the state innovation[‡]), $u_k$ is

[‡]Innovation refers to the incremental update to the state variables at each computation step, driven by the state transition model (independent of any influence of control inputs).

the control input (an input to the system of higher order than the innovation), and $\Gamma_k$ is the control input model (which transforms control input to state space).

Referring back to Equation 5.21, the process model (thermal energy storage) is already formulated in a recursive manner, since a backwards difference finite difference expansion of the temporal derivative was used:

$$T_k = \gamma_k T_{k-1} + \Delta t \gamma_k \alpha_k \quad .$$

Comparing this to Equation 5.25, the state mean ($x_k$) is the temperature $T_k$, the state transition model ($F_k$) is the heat transfer parameter $\gamma_k$, the control input mean ($u_k$) is the heat transfer parameter $\alpha_k$, and the control input model ($\Gamma_k$) is equal to $\Delta t \gamma_k$.

The state covariance is given by:

$$\overline{P}_k = F_k P_{k-1} F_k^{\mathrm{T}} \quad , \tag{5.26}$$

where $\overline{P}_k$ is the predicted state covariance estimate at the current time step, $P_{k-1}$ is the prior state covariance estimate, and $^{\mathrm{T}}$ is the matrix transpose operation.

Finally, it must be acknowledged that this process model is imperfect. Recall that $\alpha$ (Equation 5.11) is essentially a representation of the incident heat flux, the "drive" for temperature change, and that the assumed model for $\alpha$ was derived from a very simple two-surface enclosure heat transfer model. Certainly there are higher-order and un-modelled physics involved, and these are represented in the Kalman filter as process noise (associated with the control input, $u_k$). The convention for Kalman filter is to model this error as white noise N($\omega$,$Q$) — a continuous random variable with mean $\omega$ (equal to zero) and covariance $Q$. The complete forms of the state mean and covariance equations that are utilized in the predict step of the Kalman filter are:

$$\overline{x}_k = F_k x_{k-1} + \Gamma_k \left( u_k + w \right) \quad , \tag{5.27}$$

and

$$\overline{P}_k = F_k P_{k-1} F^{\mathrm{T}} + Q \quad . \tag{5.28}$$

The process covariance is represented here using piecewise white noise, which is assumed to be constant over a single time step, but vary step-to-step. Process covariance is related to the control input variance, $\sigma_\alpha^2$. A linear relationship is presumed between the control input standard deviation and the control input mean:

$$\sigma_\alpha = \phi \cdot \alpha \quad , \tag{5.29}$$

where $\phi$ is denoted the process covariance gain. Physically this parameter represents the strength of belief in the adequacy of the process model — setting $\phi = 0$ will force the process covariance to zero. In practice this parameter may be used to tune the model output, as will be explored below. With $\sigma_\alpha$ determined, the process covariance is then:

$$Q = \Gamma \sigma_\alpha^2 \Gamma^{\mathrm{T}} \quad . \tag{5.30}$$

The units for this expression are verified: $\alpha$ has units of $\mathrm{K{\cdot}s^{-1}}$, the covariance on $\alpha$ has units of $\mathrm{K^2{\cdot}s^{-2}}$, $\Gamma$ has units of s, and $Q$ has units of $\mathrm{K^2}$ (state covariance).

Next is the update step, for which measurements of the state variables are used to update the predicted state estimates, resulting in the best possible posterior estimate based on the information available. The posterior state mean and covariance are calculated by:

$$x_k = \overline{x}_k + K_k y_k \quad , \tag{5.31}$$

and

$$P_k = (I - K_k H)\, \overline{P}_k \quad , \tag{5.32}$$

respectively. Measurements are represented by the variables $z$ (mean) and $R$ (covariance). The residual vector $y$ is the difference between the measurement mean $z$ and the state estimate mean $\overline{x}$:

$$y_k = z_k - H\overline{x}_k \quad , \tag{5.33}$$

where $H$ is a function that converts the the state estimate mean to measurement space. For a system with $m$ sensors, $z$ is an $m \times 1$ vector and $R$ is an $m \times m$ matrix. Note that there is no requirement that $m = n$; in other words, fewer sensors may be used than the number of state variables that exist. However, if the number of sensors is equal to the number of states ($m = n$), $H$ is simply equal to the identity matrix $I$ of size $m \times m$.

The Kalman gain, $K$, can be thought of as a weighting factor for the influence of the measurement on the posterior estimate. When $K$ tends toward zero the model will favour the process model predictions, and when $K$ tends toward one the model will favour the measurements. This parameter is calculated on the fly based on knowledge of the state estimate covariance $\overline{P}$ and the measurement covariance $R$:

$$K_k = \overline{P}_k H^{\mathrm{T}} \left[ H \overline{P}_k H^{\mathrm{T}} + R_k \right]^{-1} \quad . \tag{5.34}$$

Upon completion of the predict and update steps, the heat transfer parameter $\alpha^*$ is calculated using the posterior result, and is compared to the value of $\alpha$ used as input to

the predict step. If $\alpha$ and $\alpha^*$ differ significantly (percent difference greater than 0.1% was used here), then the predict and update steps are iterated using $\alpha^*$ as the new input. Once the heat transfer parameters have converged, the posterior state estimates are used to calculate the fire-side incident heat flux (Equations 5.23–5.24). Both mean and covariance of incident heat flux are calculated, based on the posterior state mean covariance — this directly quantifies the strength of belief in the predicted results.

It is useful to demonstrate implementation of this model by means of an example. For this example the actual dimensions of the steel wall and compartment were used, as described previously, and the density, specific heat capacity, and emissivity of the steel were taken to be 7850 kg·m$^{-3}$, 600 J·kg$^{-1}$·K$^{-1}$, and 0.93, respectively. Initially the wall, gases, frame, and surroundings were all at 25°C. At $t = 0$ the fire-side gas temperature and surroundings increased at a rate proportional to $t^2$ to a peak value of 550°C after 10 minutes; the cool-side gases and surroundings, and the wall frame, were maintained at 25°C. In addition, some random noise was added to the fire-side temperatures to provide some realism to the example.

First, the process model was run in the forward mode (Equation 5.22) to provide a prediction of the wall temperature; this is depicted as a blue dotted line in Figure 5.21 below. Next, a set of $t^2$ "measurement" data was generated such that the measured wall temperature after 10 minutes was equal to the process model prediction at that time. A very small amount of noise was added to this data (1/10 of the noise added to the fire gas data). The measurement data is depicted as a red dotted line in Figure 5.21 below. The process model was then run in inverse mode (Equation 5.24) to produce predictions of incident heat flux, as shown in in Figure 5.22 below (using the same colour notation). It is clear from this example that direct substitution of measurement data into the inverse model will result in predictions of incident heat flux with greatly amplified perturbations, even when the measurement noise is barely perceptible. On the other hand, direct substitution of the process model prediction into the inverse model will yield much less noise, but the results cannot necessarily be trusted to be accurate given the uncertainty present in the process model. The code listing for the steel wall thermal capacitance model used here, including the data generation functions, may be found in Appendix F (Section F.2).

Next, the Kalman filter was used to calculate estimates of the wall temperature and incident heat flux. The process covariance gain, $\phi$, was set to a value of 0.05. The error for K-type thermocouple sensors is typically taken to be 2.2 K [84], therefore a

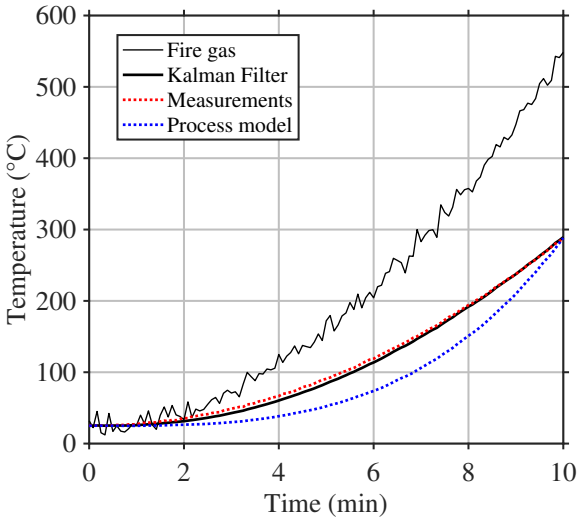


Figure 5.21: Results of the steel wall thermal capacitance model for the example scenario (temperature, $\phi = 0.05$).

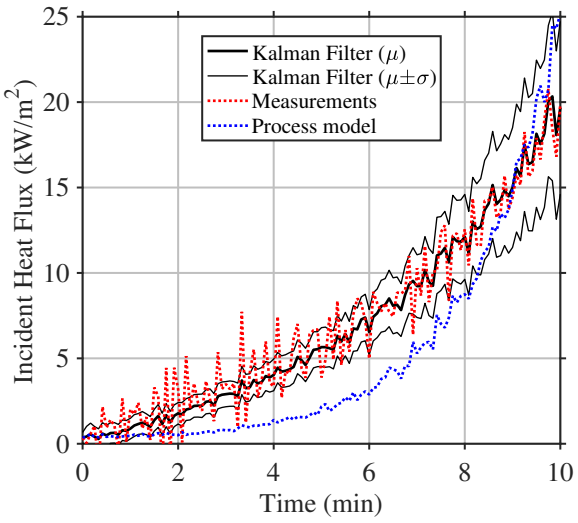


Figure 5.22: Results of the steel wall thermal capacitance model for the example scenario (incident heat flux, $\phi = 0.05$).

measurement variance of 4.8 K was used. The Kalman filter temperature estimates are plotted in Figure 5.21 along with the measurements and the process model estimates. The Kalman filter estimates are much closer to the measurements than to the process model, which is a desired result given the uncertainty present in the process model. The incident heat flux predicted using the Kalman filter approach is shown in Figure 5.22, along with one standard deviation above and below the mean. The Kalman filter result has reduced fluctuations compared to the measurement result. The code listing for the Kalman filter implementation used here may be found in Appendix F (Section F.3).

Figures 5.23–5.24 below show temperature and heat flux predictions when a value of 0.01 is used for the process covariance gain. In this case the filter favours the process model over the measurements, resulting in both temperature and heat flux being under-predicted. At the same time, since the process error is reduced, the fluctuations and overall variance in the predicted incident heat flux are significantly reduced. This is an example of the filter being "over-confident" – it is clear from plot of the primary variable (temperature) that the filter is not producing a good estimate of the measured temperature, therefore the apparent small variance in the derived variable (heat flux) is erroneously small.

Figures 5.25–5.26 below show temperature and heat flux predictions when a value of 0.10 is used for the process covariance gain. In this case the filter very closely favours

the measurements over the process model. This is an example of an "under-confident" model, for which so great an importance is placed on the measurements that the signal noise is over-represented. The consequence is excessively large fluctuations and variance on the predicted heat flux. For any situation a compromise must be attained between the over-confident and under-confident — for this thermal energy balance model, it seems that $\phi = 0.05$ is a good choice.

This example demonstrates some of the advantages of the Kalman filter as applied to the problem of heat flux measurement, however the greatest strength of the Kalman filter lies in its ability to incorporate multiple states and sensors into a tractable algorithm. The following section extends the concepts introduced here to the desired problem — measurement of incident heat flux over the surface of the wall, in two dimensions.

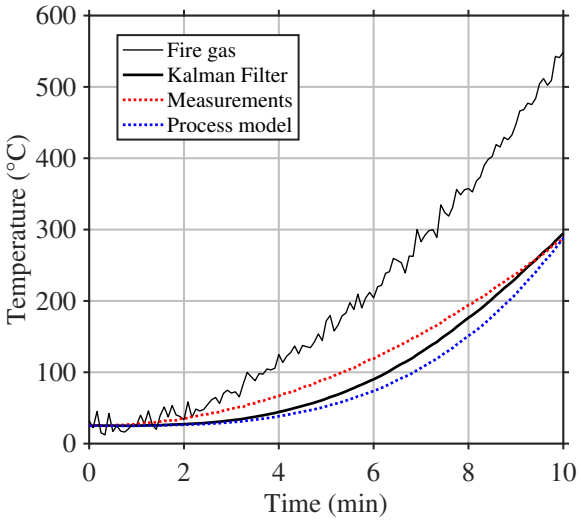


Figure 5.23: Results of the steel wall thermal capacitance model for the example scenario (temperature, $\phi = 0.01$).

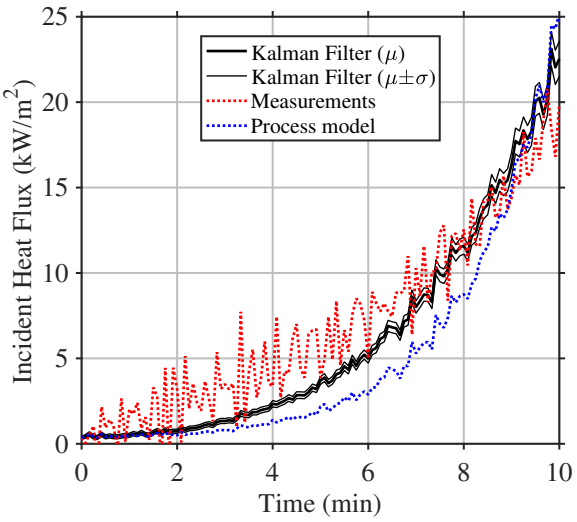


Figure 5.24: Results of the steel wall thermal capacitance model for the example scenario (incident heat flux, $\phi = 0.01$).

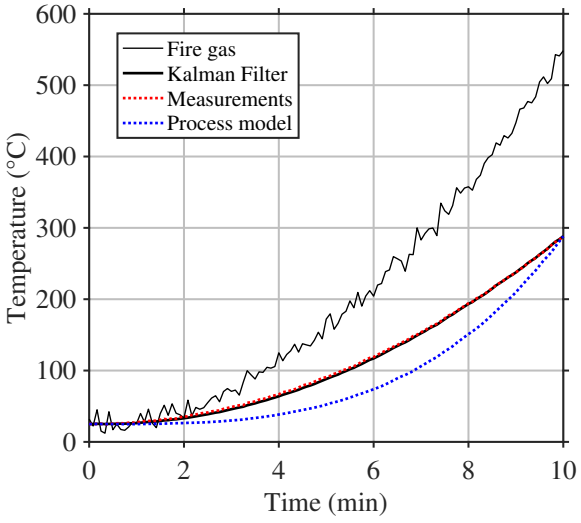


Figure 5.25: Results of the steel wall thermal capacitance model for the example scenario (temperature, $\phi = 0.10$).

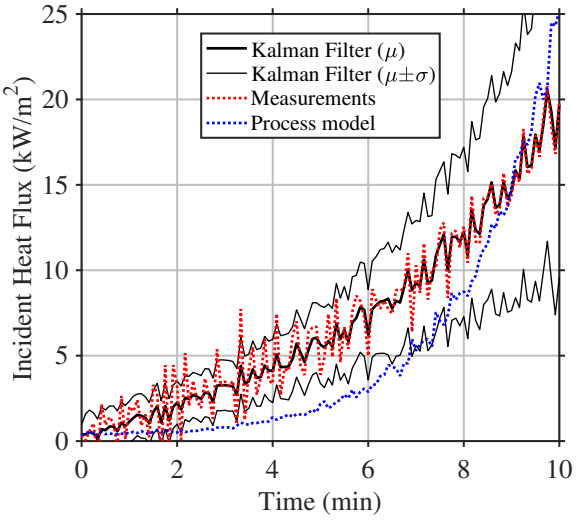


Figure 5.26: Results of the steel wall thermal capacitance model for the example scenario (incident heat flux, $\phi = 0.10$).

## 5.5 Extension of the Model to Two Dimensions

The two-dimensional problem is one of in-plane heat transfer with prescribed conduction losses at the boundaries[§]. The steel wall sensor can be divided into any number of elements, however since 24 sensors (thermocouples) were used, it was convenient to discretize the wall into 24 elements. Furthermore, heat conduction at the edges of the frame needed to be modelled, therefore insulation elements were added on each of the four sides of the wall. Figure 5.27 shows the element discretization used for the 24-state implementation (on the left). Due to the size of the wall and the thermocouple placement, each element is rectangular with an aspect ratio of approximately 8:3. A secondary discretization scheme was also developed using 72 states, and is shown in Figure 5.27 (on the right). For the 72-state implementation the element aspect ratio is approximately 8:9, giving a more consistent finite element grid. In Figure 5.27 sensor locations are depicted by a green highlight (sensors are located in the geometric centre of a given element).

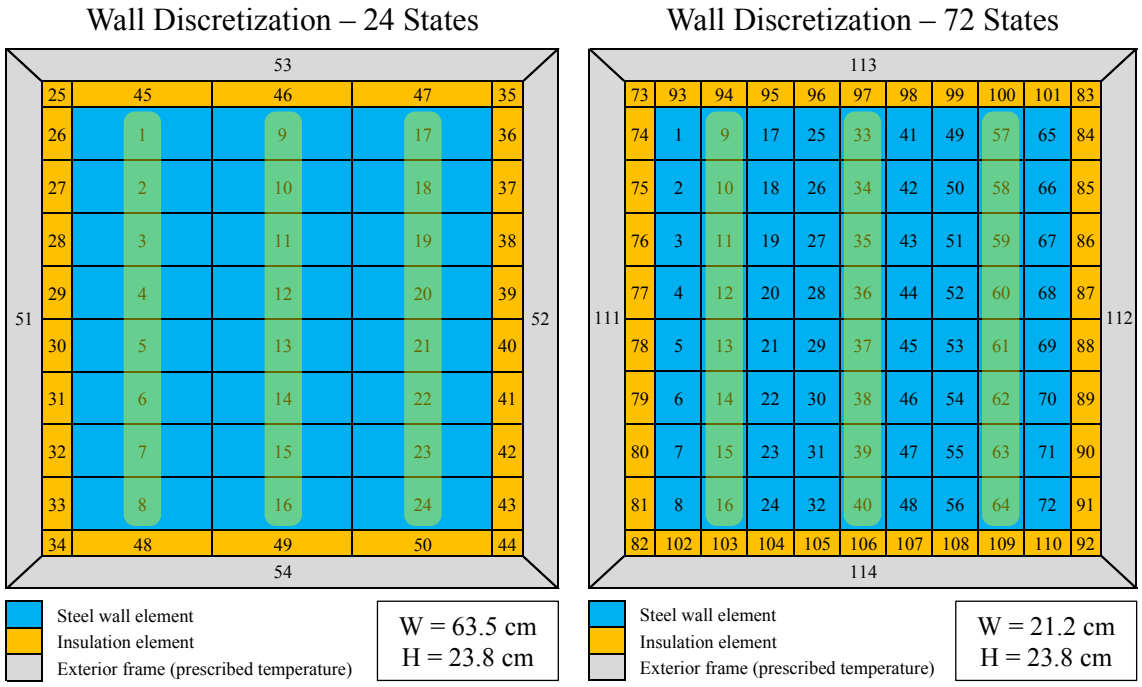


Figure 5.27: Discretization schemes used for the two-dimensional model.

[§]Given that the wall is constructed of a thin and highly conductive material, in-depth heat conduction may be neglected provided the Biot and Fourier numbers are suitable; refer to Section 5.6.

Building upon the 0D thermal capacitance model, conservation of energy is applied about a given element. By convention it is assumed that conduction heat transfer is directed into an element, and in-plane net heat flux directed out of an element on either side of the wall (refer to Figure 5.28). Applying conservation of energy (and a backward difference approximation to the temporal derivative in the energy storage term):

$$\rho V c_p \frac{T_k - T_{k-1}}{\Delta t} = -A q''_{net,f} - A q''_{net,c} + A_{x_1} q''_{x_1} + A_{x_2} q''_{x_2} + A_{y_1} q''_{y_1} + A_{y_2} q''_{y_2} \quad , \tag{5.35}$$

where the conduction heat flux on a given side $i$ of the element is

$$q''_{i\,k} = \frac{\kappa_{ik}}{\Delta i} \left( T_{ik} - T_k \right) \quad ,$$

where $\Delta i$ is the length between the centre of the element and the centre of element $i$. The in-plane heat flux on the fire-side and cool-side of the wall is given by Equation 5.18 as previously derived.

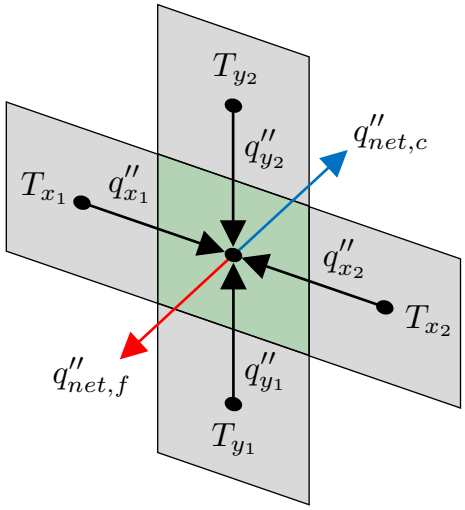


Figure 5.28: Heat flow schematic for a general 2D element.

The 2D model is assembled in the same manner as the 0D model by introducing some effective heat transfer coefficients:

$$T_k = \Delta t \left( \hat{\beta}_k \circ \hat{T}_{k-1} \right) + \Delta t \alpha_k \quad , \tag{5.36}$$

where $\circ$ denotes the Hadamard product binary operation [85], given that:

$$\hat{\beta}_k = \left[ 1/\Delta t - \beta_{tot\,k} \ , \ \beta_{x_1\,k} \ , \ \beta_{x_2\,k} \ , \ \beta_{y_1\,k} \ , \ \beta_{y_2\,k} \right] \quad ,$$

and

$$\hat{T}_{k-1} = \left[T_{k-1}\ ,\ T_{x_1 k-1}\ ,\ T_{x_2 k-1}\ ,\ T_{y_1 k-1}\ ,\ T_{y_2 k-1}\right] \quad .$$

The $\alpha$ and $\beta$ terms are defined as follows:

$$\alpha_k = \beta_{r,f_k} T_{s,f_k} + \beta_{c,f_k} T_{\infty,f_k} + \beta_{r,c_k} T_{s,c_k} + \beta_{c,c_k} T_{\infty,c_k} \quad ,$$

and

$$\beta_{tot_k} = \beta_{x_1 k} + \beta_{x_2 k} + \beta_{y_1 k} + \beta_{y_2 k} + \beta_{r,f_k} + \beta_{c,f_k} + \beta_{r,c_k} + \beta_{c,c_k} \quad .$$

The fire-side exposure coefficients are:

$$\beta_{r,f_k} = \frac{A}{\rho V c_p} h_{r,f} \quad ,$$

and

$$\beta_{c,f_k} = \frac{A}{\rho V c_p} h_{c,f} \quad ,$$

while the cool-side exposure coefficients are:

$$\beta_{r,c_k} = \frac{A}{\rho V c_p} h_{r,c} \quad ,$$

and

$$\beta_{c,c_k} = \frac{A}{\rho V c_p} h_{c,c} \quad .$$

Finally, the conduction coefficients are:

$$\beta_{x_1 k} = \frac{A_{x_1}}{\rho V c_p} \frac{\kappa_{x_1 k}}{\Delta x_1}$$

in the $x_1$ direction,

$$\beta_{x_2 k} = \frac{A_{x_2}}{\rho V c_p} \frac{\kappa_{x_2 k}}{\Delta x_2}$$

in the $x_2$ direction,

$$\beta_{y_1 k} = \frac{A_{y_1}}{\rho V c_p} \frac{\kappa_{y_1 k}}{\Delta y_1}$$

in the $y_1$ direction, and

$$\beta_{y_2 k} = \frac{A_{y_2}}{\rho V c_p} \frac{\kappa_{y_2 k}}{\Delta y_2}$$

in the $y_2$ direction. The areas $A_{x_1}$, etc. represent the conduction pathway areas — these are simply the product of the element dimension ($\Delta x$ or $\Delta y$) by the steel thickness ($\delta$).

The 2D system model (Equation 5.36) may be readily implemented in the Kalman filter (Equation 5.27) by identifying that the state transition function $F_k$ is assembled

from $\Delta t\hat{\beta}_k$, and $\Gamma$ is simply equal to $\Delta t$. Calculation of $F$ was achieved by a custom algorithm:

$$\texttt{algorithm}\left\{\Delta t\left(\hat{\beta}_k \circ \hat{T}_{k-1}\right)\right\} \rightarrow F_k T_{k-1} \quad .$$

First, a state reference array "`n_ref`", which describes the four elements bordering each state, is assembled. For example, in the 24-state model, state 10 has references 2, 18, 11, and 9 for positions $x_1$, $x_2$, $y_1$, and $y_2$, respectively (refer to Figure 5.27). State references were assembled manually and stored in "`state_ref_##.csv`" data files; refer to Appendix G for more details. Next, $\hat{\beta}$ is calculated for each state, and the five elements of $\hat{\beta}$ are assigned to the elements of the state transition matrix $F$ that correspond to the state reference array. For example, for state 10, the five elements of $\hat{\beta}$ are assigned to row [10] columns $[10, 2, 18, 11, 9]$ of $F$. All non-assigned elements of $F$ default to zero (e.g. state 10 does not directly conduct heat to state 14, therefore row [10] column [14] of $F$ will be zero). Complete details of the $F$ matrix assembly may be found in the code listings, Appendix F (Section F.4, `f_import_state_refs.m` and `f_kf_setup.m`).

Calculation of incident heat flux follows the same approach as the 0D model. First, the $\beta$ heat transfer parameters are re-calculated using the posterior state predictions ($\beta_{r,f_k}$ and $\beta_{c,f_k}$ are omitted in this inverse formulation). Then,

$$\beta^*_{totk} = \beta_{x_1 k} + \beta_{x_2 k} + \beta_{y_1 k} + \beta_{y_2 k} + \beta_{r,c_k} + \beta_{c,c_k} \quad ,$$

and the posterior $\hat{\beta}^*_k$ is calculated:

$$\hat{\beta}^*_k = \left[1/\Delta t - \beta^*_{totk} \ , \ \beta_{x_1 k} \ , \ \beta_{x_2 k} \ , \ \beta_{y_1 k} \ , \ \beta_{y_2 k}\right] \quad .$$

The $F$ matrix is re-assembled using $\hat{\beta}^*_k$, and then the posterior $\alpha^*_k$ is calculated by re-arrangement of Equation 5.36:

$$\alpha^*_k = \frac{1}{\Delta t}\left(T_k - F_k T_{k-1}\right) \quad .$$

Net heat flux out of the fire-side is then:

$$q''_{net,f_k} = \frac{\rho V c_p}{A}\left(-\alpha^*_k + \beta_{r,c_k} T_{s,c_k} + \beta_{c,c_k} T_{\infty,c_k}\right) \quad , \tag{5.37}$$

and incident heat flux to the fire-side is:

$$q''_{r,i,f_k} = -\frac{1}{\varepsilon} q''_{net,f_k} + \sigma T_k^4 + \frac{h_{c,f_k}}{\varepsilon}\left[T_k - T_{\infty,f_k}\right] \quad . \tag{5.38}$$

Some important notes about the implementation of this model should be mentioned. First, while the Kalman filter can technically accept any number of state and measurement variables as input, it is up to the designer to select the appropriate state reference

array and measurement space transformation function ($H$). State reference arrays for the 24-state model ($n = 54$ and $m = 24$) and 72-state model ($n = 114$ and $m = 24$) have been developed in the present work, and may be found in Appendix G; for other implementations, these arrays would need to be formulated accordingly.

Second, in the present work, all thermophysical properties were taken to be constant. Steel properties were taken to be: $\kappa = 42$ W·m$^{-1}$·K$^{-1}$, $\rho = 7850$ kg·m$^{-3}$, and $c_p = 600$ J·kg$^{-1}$·K$^{-1}$. The insulation, 1/4 inch (6.4 mm) silicone rubber gasket, was assumed to have a thermal conductivity of 0.24 W·m$^{-1}$·K$^{-1}$. Total emissivity of the wall was assumed to be constant at 0.93. Total emissivity of the surroundings on both fire-side and cool-side was assumed to be 0.75[¶]. The total area of the fire-side surroundings was measured to be 36.4 m$^2$, and the total area of the cool-side surroundings was measured to be 14.3 m$^2$ (the values of $r_f$ and $r_c$ depend on the particular state, per Equation 5.15). The consequences of these simplifying assumptions on the model predictions are discussed in Section 5.6 below.

## 5.6 Suitability of Modelling Assumptions

This solution methodology hinges on the appropriateness of the thermally-thin assumption. The suitability of this assumption can be verified by performing two checks. For one, the lumped approach for thermal energy storage within a solid is generally acceptable when the Biot number is less than 0.1 [77]. Considering a worst-case scenario, when the steel wall temperature is equal to the fire gas temperature and the wall is treated as a blackbody, the effective heat transfer coefficient $h_e$ (Equation 5.14) reduces to:

$$h_e = h_c + 4\sigma T^3 \quad .$$

Taking the fire gas temperature to be 1200 K (a conservative estimate for a pre-flashover compartment fire) and the convective heat transfer coefficient to be 30 W·m$^{-2}$·K$^{-1}$, the effective heat transfer coefficient is calculated to be 400 W·m$^{-2}$·K$^{-1}$.

Recalling from Section 5.2, the expression for Biot number is:

$$\mathrm{Bi} = \frac{h\delta}{\kappa} \quad ,$$

[¶]Typically an emissivity of 0.9 is assumed for ceramic fibre insulation used in furnaces, but in reality the value can range from 0.5 to 0.9 over the relevant temperature and spectral ranges [86].

where $\kappa = 42$ W·m$^{-1}$·K$^{-1}$ for steel.

Two cases are considered:

- when the characteristic length is taken to be the actual thickness of the steel sheet, 1.3 mm, $Bi$ is calculated to be 0.0124; and
- when the characterisic length is taken to be the effective thickness of the steel sheet, 4.5 mm (see Section 5.1), $Bi$ is calculated to be 0.0428.

In both cases, Bi $< 0.1$, therefore the lumped energy storage approach is valid.

A second check of the thermally-thin assumption is to consider the analytical solution for transient heat conduction through a plane wall undergoing convective heat transfer on both sides (again lumping radiation and convection into a single effective heat transfer coefficient). In this case, the temperature on both faces of the plane wall is equal to the temperature at the centre of the plane wall when the Fourier number Fo is greater than 0.2 [77]. The expression for Fourier number is:

$$\text{Fo} = \frac{\alpha}{\delta^2} t \quad ,$$

where $\alpha$ is the thermal diffusivity (9.55 mm$^2$·s$^{-1}$). Again considering two cases:

- when the characteristic length is taken to be the actual thickness of the steel sheet, 1.3 mm, it is found that $Fo = 5.65t$; and
- when the characterisic length is taken to be the effective thickness of the steel sheet, 4.5 mm (see Section 5.1), it is found that $Fo = 0.47t$.

Taking the sampling rate to be 1 sample per second (t = 1 s), it is clear that $Fo > 0.2$ for both cases, again verifying the validity of the thermally-thin assumption.

As mentioned previously, the process model adopted here is relatively simplistic. While the thermal energy balance approach for inverse calculation is quite sound given the thermally-thin nature of the problem, the assumed process model for net heat flux based on a 2-surface enclosure does not adequately represent the relevant physics in a compartment fire. Furthermore the assumption of constant thermophysical properties is unwarranted, since the temperature-dependent properties of the materials used here are readily available (as given in Section 5.1).

Certainly it is possible to derive a more in-depth process model and accordingly implement it via Kalman filter. In theory, such a process model would yield predictions that are in better agreement with the actual (unknown) state values than the process

model used here. This means that the strength of belief in the validity of the process model estimate would be greater; consequently, the Kalman filter would give a greater weighting to the process model in its posterior output. However, since a large number of measurements with relatively low error are available, it is likely that the overall wighting of the filter would remain in favour of the measurements. This means that the filter prediction would not be significantly different if a better process model were used, but the strength of belief in the validity of its predictions would be greater (variance in the predicted heat flux Gaussians would be reduced).

Implementation of a Kalman filter heat transfer model necessitates a cost-benefit analysis to be conducted in order to select an appropriate process model and instrumentation. When multiple states are involved, as is the case for any heat transfer problem with a spatial dimension of 1 or greater, a decision must be made regarding the number of sensors used in addition to the types of sensors and their inherent measurement errors. The decision to adopt the simplified process model here was driven by practical constraints — it was a more productive use of the available resources to use a large number of thermocouple probes on the steel wall than it was to develop a more detailed process model.

Even though the Kalman filter tends to favour measurement input over the process model estimates in this case, the results are much more stable than direct inverse calculation of heat flux based on measurements alone [87]. Use of the filter also provides a quantification of the strength of belief in the predicted heat flux. Furthermore, it allows for more detailed study of the incident heat flux by utilizing more state variables than the number of sensors, thereby refining the discretization grid. The linear algebra involved does not have an excessive computational overhead, therefore the model may be readily expandable to a greater number of states. In this case, 72 states provided meaningful insight into the heat flux distribution over the wall.

With the steel wall sensor designed and an algorithm developed for the calculation of incident heat flux, a number of large-scale experiments were conducted, a fire was designed, and the fire exposure to the wall was characterized. These experiments, and the subsequent characterizations, are detailed in the following chapter.

# Chapter 6

# Characterization of the Experiment

This chapter details the series of steel wall characterization tests conducted in the present work. The objective in conducting these tests was to develop a characterization profile of the experiment, in a particular configuration, which would later be reproduced in subsequent tests. The first step in this endeavour was the design of a fire to be used in this (and future) experiments, which is the focus of the following section. Subsequent sections detail the conduct, result, and findings from this series of testing.

## 6.1 Design Fire

With a system in place for measurement of compartment temperatures (Section 4.2) and heat flux to the wall (Section 5.5), the next step was to design a suitable fire to achieve the target exposure levels. As previously stated, a major design consideration for the experiment is that a wall be subjected to a realistic fire exposure. There are two components to this objective:

- the spatial uniformity of the fire exposure should be representative of that experienced in a real fire (e.g. varying in both horizontal and vertical dimensions); and
- the intensity and duration of the fire exposure should be representative of a fuel-constrained fire (e.g. pre-flashover, and not a fully-developed* fire).

*A fully-developed fire, in this context, describes the post-flashover fire environment. If flashover does not occur, then the transition to a fully-developed fire does not occur [88].

Certainly post-flashover fires are of interest in fire safety analyses, and such fires tend to be well studied in the context of fire resistance tests. In the present work, however, it was decided to start with pre-flashover fuel-constrained fires. One reason for this is that the dynamics of fuel-constrained fires are typically easier to model (i.e. without a transition to flashover), and the results from this experiment are intended to be used to support fire model development and validation. Another reason to select fuel-constrained fires is that the focus of the present work is on investigation of thermal degradation phenomena, many of which are suspected to be directly related to highly non-uniform exposures. The preliminary work established that a localized fire plume and distinct upper gas layer, typical of a fuel-constrained fire, will impart a largely non-uniform exposure.

Given the above-listed constraints, it was decided to use a solid wood fuel source, and to control fire evolution via fuel configuration and ventilation. Wood fuel generates sufficient heat to produce the characteristic separation of "upper" and "lower" gas layers within the compartment, as well as sufficient soot to visually identify the height of the hot layer during an experiment [68]. Furthermore, fire evolution will be dependent on fuel involvement, therefore configuration may be used to control the progression of the "growth", "steady burning", and "decay" phases typical of a compartment fire [88]. Gas burners are another option, and would certainly produce fires with improved repeatability, but would arguably be less representative in terms of natural fire progression and hot layer development. This is an option that may be considered in future work (in fact, the apparatus was designed with burner entry ports at floor level with this in mind).

It is convenient to use modular "cribs" as the wood fuel source in large-scale fire tests. Previous work from the University of Waterloo [65] standardized the construction of a particular type of softwood crib. Cribs were constructed using bulk 2×2 spruce furring strips, available inexpensively in 8 ft (244 cm) lengths from a local wood supplier. Each strip was cut into four 24 in (61 cm) lengths and assembled using 2 3/8 in (60.3 mm) framing nails with six pieces per layer, and six layers total (refer to Figure 6.1).

The same methodology of crib construction was followed in the present work. Cribs were conditioned in a dehumidified room (set to 50% relative humidity) for one week prior to testing in order to reduce the moisture content of the wood. The mass of each crib was measured prior to each test. Based on the 40 cribs used for the characterization experiments, and assuming a Gaussian PDF, the mass of a crib is $\mathrm{N}\left(15.048, 0.214\right)$ kg, as depicted in Figure 6.2.

Figure 6.1: Standard wood crib used in the large-scale experiments.

In his work, Obach [65] measured the effective heat of combustion of a typical crib to be approximately 14.8 MJ·kg$^{-1}$. He also measured the free-burning heat release rate of a single crib and of various configurations of multiple cribs using a large-scale calorimeter. In these tests, a liquid fuel pan located below each crib was ignited by spark to initiate combustion of the crib(s). For a single crib fire, the heat release rate increased to a peak value of 250 kW after 200 s, followed by steady burning for 400 s, and followed by gradual decay for a total burn duration of approximately 30 min. Taking into account the average mass and effective heat of combustion of a crib, as given above, the heat release rate for a single crib may be represented as depicted in Figure 6.3 (presuming $t^2$ growth and decay, total heat release of 222.7 MJ). This curve may readily be adopted as input to a fire model.

Obach [65] also measured the heat release rate of two cribs placed side-by-side, which were ignited simultaneously. He found that the peak heat release rate increased to approximately 500 kW after 200 s, followed by a steady burning period of 400 s, and a total burn duration of approximately 30 min. The resulting heat release rate was almost exactly double those of the single crib. However, if the cribs were spaced further apart or only one was ignited initially, the result was a very different heat release rate curve. In the present work it was desired to achieve a total burn time of 45–60 min and to avoid the transition to a fully-developed fire; this necessitated the determination of a suitable number of cribs, and their configuration.

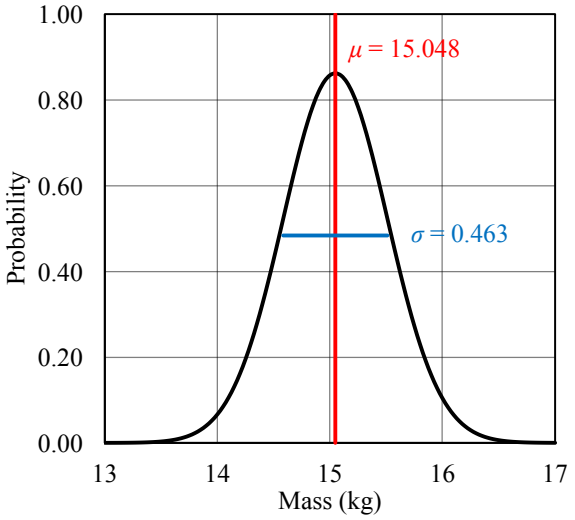


Figure 6.2: Probability density function for wood crib mass.

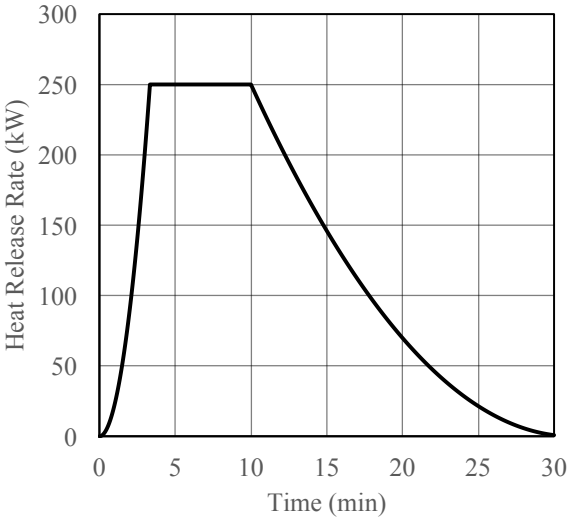


Figure 6.3: Heat release rate for a single wood crib.

To avoid the transition to a fully-developed fire, a limit on the total fuel load needed to be determined. For a single-room compartment fire, the equation of Thomas [89] may be used to estimate the heat release rate required for this transition ($\dot{Q}_F$):

$$\dot{Q}_F = 7.8A_T + 378A_W\sqrt{H_W} \quad , \tag{6.1}$$

where $A_T$ is the interior surface area of the compartment (7.22 m$^2$), $A_W$ is the area of the door (1.59 m$^2$), and $H_W$ is the height of the door (1.99 m). From this, the transition heat release rate was calculated to be approximately 900 kW. A secondary threshold for the transition to a fully-developed fire is when the average gas temperature in the compartment exceeds 600°C [1]. This value does not define a physical threshold for flashover, however it is a sensible reference value used in large-scale fire experiments [90]. Certainly gas temperatures in the lower layer should not exceed this value in the present fire tests, given that flashover is not desired.

Given the results of Obach [65] described above, a 900 kW threshold on fire size would imply that a maximum of four cribs should be used in the experiment. However, heat release rate strongly depends on the surface area of fuel involved; four cribs in a square configuration should be expected to produce a greater heat release rate than four cribs in an in-line configuration. Furthermore, Obach's work demonstrated that increasing the number of cribs will not necessarily increase the burn duration if all cribs are simultaneously involved, and fresh air is in ready supply. In the preliminary

investigation (Chapter 3) the idea of extending the duration of a wood crib fire by intermittently adding additional cribs at regular time increments was explored. While this endeavour was successful in its intent, it required firefighting personnel to actively enter the fire compartment in order to re-fuel the fire, and the resulting temperature-time traces were consequently quite discontinuous. Therefore, the approach adopted for the present characterization tests was to control fire growth by adjusting the number and configuration of cribs, and the spacing between them. In addition, ventilation control was used to influence air supply and exhaust at the compartment door. Details are provided in the following sections.

## 6.2 Test Overview and Data Reduction

Given the large number of variables, and the complexity of modelling large-scale fire dynamics, it is often most practical to design a fire using a combination of engineering correlations (e.g. Equation 6.1 above), intuition, and consecutive experimentation. In the present work a total of 12 characterization experiments were conducted. For the first six experiments, various changes to fuel configuration and ventilation were applied to work toward the design objectives. During the sixth experiment a structural failure of the interior insulation panels occurred, necessitating repair. The seventh test used a reduced fuel load in order to assess the condition of the repaired insulation. The final fuel and ventilation configuration was selected by test #8, and tests #9-12 were repeats of #8 so that variability in the experiment could be assessed. A summary of test conditions and events is provided in Table 6.1 (tests #1–6) and Table 6.2 (tests #7–12). Additional details and results of each test are presented in the following section.

Raw data from each test were saved in the CSV format, and are provided in Appendix D. A script was used to import raw data files to the MATLAB workspace for post-processing and visualization, and the reduced data were saved to the `*.mat` format; refer to Appendix E for details.

For fire gas temperatures, "slice" averages were calculated for each of the eight vertical positions by averaging the measurements from the four probe rakes (in the corners of the compartment) corresponding to each position. Fire gas slice temperatures are stored to the `EXP_FIRE_GAS` variable, which has dimensions of `n_steps`$\times 8$. The second dimension of this array corresponds to the vertical position, from ceiling-to-floor of the compartment.

| Test | Date | Description |
|---|---|---|
| *Preliminary tests.* | | |
| 1 | 08/15/2016 | *Ambient conditions*: 23.5°C, 60% RH, 96.46 kPa.<br>*Fuel*: Small pan (12 in diameter, 2 3/8 in height) filled with 1 L of methanol, located in the centre of the room.<br>*Events*: Door closed for test duration (no ventilation). |
| 2 | 08/16/2016 | *Ambient conditions*: 23.3°C, 90% RH, 97.38 kPa.<br>*Fuel*: Softwood pallet and scraps of red oak, total mass approximately 8 kg, located in the centre of the room.<br>*Events*: Door closed to 1 brick width (2.5 in gap) for test duration. |
| 3 | 08/17/2016 | *Ambient conditions*: 25.4°C, 67% RH, 98.07 kPa.<br>*Fuel*: 3 wood cribs, mass [15.58, 15.17, 15.36] kg, arranged in a "T" with 2 in the back, back row 36 in from wall, fuel pan under front crib with 500 mL methanol.<br>*Events*: Door fully open to start. Fire spread to rear cribs after 9.2 min s. Door closed to 1 brick width (2.5 in gap) after 34.6 min. |
| *Lowered the door soffit from 78.5 in to 53.0 in.* | | |
| 4 | 08/18/2016 | *Ambient conditions*: 25.4°C, 67% RH, 98.07 kPa.<br>*Fuel*: 4 wood cribs, mass [15.81, 15.35, 15.64, 15.39] kg, arranged in a "T" with 3 in the back, back row 36 in from the wall, fuel pan under front crib with 500 mL ethanol.<br>*Events*: Door fully open to start, then closed to 1 brick width after 24.5 min through the end of the test. |
| *Added obstruction panel to front of compartment.* | | |
| 5 | 08/26/2016 | *Ambient conditions*: 25.6°C, 60% RH, 98.15 kPa.<br>*Fuel*: 5 wood cribs, mass [16.33, 15.23, 14.59, 15.56, 15.05] kg, arranged in a 2x2x1 configuration with 2 cribs in the back and middle rows, back row 36 in from the wall, fuel pan under front crib with 500 mL ethanol.<br>*Events*: Closed obstruction panel after 21.2 min, fire went out (rapid temperature drop), opened panel after 23.9 min. |
| 6 | 08/29/2016 | *Ambient conditions*: 24.3°C, 56% RH, 98.70 kPa.<br>*Fuel*: Same 5-crib configuration, mass [14.93, 15.21, 15.97, 15.41, 15.30] kg, fuel pan under fron crib with 500 mL ethanol.<br>*Events*: Obstruction panel angle of 30° to start, then closed to 20° at 19.6 min, then closed to 10° at 21.2 min, then fully closed at 38.4 min, through end of test. As the fire became underventilated pressure fluctuations occurred, and were significant enough to knock down 2 of the side-wall insulation panels. Significant heat retention caused warping of exposed steel members. |

Table 6.1: Summary of conditions and events for characterization tests #1–6.

| Test | Date | Description |
|---|---|---|
| *Re-built side insulation panels and insulated ceiling supports.* | | |
| 7 | 09/14/2016 | *Ambient conditions*: 18.6°C, 60% RH, 98.56 kPa.<br>*Fuel*: 3-cribs in-line configuration (spaced 2 in apart) , mass [14.24, 14.45, 14.77] kg, back crib 24 in from the wall, fuel pan under front crib with 500 mL ethanol.<br>*Events*: Obstruction panel set to a constant 15°. Fire spread to second crib after 14.9 min, and to third crib after 22.3 min. |
| 8 | 09/18/2016 | *Ambient conditions*: 23.5°C, 60% RH, 97.69 kPa.<br>*Fuel*: 4-cribs in-line configuration (spaced 2/4/8 in apart, 8 in spacing closest to the wall), mass [14.61, 14.92, 14.61, 14.57] kg, back crib 12 in from the wall, fuel pan under front crib with 500 mL methanol.<br>*Events*: Obstruction panel set to a constant 15°. Fire spread to second crib after 14.1 min, to third crib after 27.5 min, and to fourth crib after 31.8 min. |
| 9 | 09/19/2016 | *Ambient conditions*: 24.9°C, 47% RH, 97.96 kPa.<br>*Fuel*: 4-cribs in-line configuration (spaced 2/4/8 in apart, 8 in spacing closest to the wall), mass [14.79, 14.64, 14.98, 14.74] kg, back crib 12 in from the wall, fuel pan under front crib with 500 mL methanol.<br>*Events*: Obstruction panel set to a constant 15°. Fire spread to second crib after 15.2 min, to third crib after 23.4 min, and to fourth crib after 26.4 min. |
| 10 | 09/20/2016 | *Ambient conditions*: 24.6°C, 47% RH, 98.21 kPa.<br>*Fuel*: 4-cribs in-line configuration (spaced 2/4/8 in apart, 8 in spacing closest to the wall), mass [14.49, 14.64, 15.55, 14.69] kg, back crib 12 in from the wall, fuel pan under front crib with 500 mL methanol.<br>*Events*: Obstruction panel set to a constant 15°. Fire spread to second crib after 18.4 min, to third crib after 27.0 min, and to fourth crib after 31.1 min. |
| 11 | 09/21/2016 | *Ambient conditions*: 25.2°C, 36% RH, 98.57 kPa.<br>*Fuel*: 4-cribs in-line configuration (spaced 2/4/8 in apart, 8 in spacing closest to the wall), mass [14.82, 15.14, 15.21, 15.07] kg, back crib 12 in from the wall, fuel pan under front crib with 500 mL methanol.<br>*Events*: Obstruction panel set to a constant 15°. Fire spread to second crib after 15.2 min, to third crib after 22.2 min, and to fourth crib after 25.0 min. |
| 12 | 09/23/2016 | *Ambient conditions*: 15.6°C, 86% RH, 98.21 kPa.<br>*Fuel*: 4-cribs in-line configuration (spaced 2/4/8 in apart, 8 in spacing closest to the wall), mass [15.02, 14.86, 14.89, 14.32] kg, back crib 12 in from the wall, fuel pan under front crib with 500 mL methanol.<br>*Events*: Obstruction panel set to a constant 15°. Fire spread to second crib after 17.1 min, to third crib after 28.1 min, and to fourth crib after 30.6 min. |

Table 6.2: Summary of conditions and events for characterization tests #7–12.

Steel wall temperatures were imported to the EXP_WALL variable, which has dimensions of n_steps×8×3. The second dimension of this array corresponds to the vertical position of the thermocouples on the wall, from top-to-bottom. The third dimension of this array corresponds to the horizontal position on the wall, from left-to-right.

For the frame temperatures, average values were calculated for the positions at the top, sides, and bottom of the wall. Frame temperatures were imported to the EXP_FRAME variable, which has dimensions of n_steps×3. The first column corresponds to the average of the two measurements at the top of the wall, the second column is the average of the four measurements at the sides of the wall, and the third column is the average of the two measurements at the bottom of the wall.

The gas temperature on the unexposed side of the wall was imported to the EXP_BACK_GAS variable. There are a total of six measurement locations for this parameter: top, middle, and bottom on both left and right sides of the wall. In the present analysis, gas temperature on the unexposed side of the wall was assumed to be uniform at all locations, therefore all six of these measurements were averaged.

The temperature of the unexposed-side surroundings was measured at two locations, on the left and right side of the door. These two measurements were averaged and stored to the EXP_BACK_SURR variable.

All raw data files may be found in Appendix D. In addition, an extensive set of photographs and digital video were recorded for each experiment; these may be obtained upon request to the fire research group at the University of Waterloo. A subset of measurements is presented in the following section, along with the incident heat flux calculated by the methodology outlined in Section 5.5.

## 6.3 Results and Discussion

In this section the results for the steel wall characterization experiments are presented. For each test, four plots were created:

- a line plot of temperature versus time, which includes the fire-side slice temperatures at the top and bottom positions, as well as temperature measurements at the centre of the wall and the corresponding 72-state Kalman filter predictions of temperature at the centre of the wall (location 36, refer to Figure 5.27);

- a line plot of fire-side incident heat flux versus time, which shows the mean incident heat flux and one standard deviation above and below the mean at the centre of the wall (location 36);
- a contour plot of wall temperatures predicted by the 72-state Kalman filter at a time corresponding to the peak fire-side gas temperature; and
- a contour plot of fire-side incident heat flux to the wall at the same time.

It should be re-stated that the standard deviation shown on the plots of heat flux versus time in this chapter is a representation of the strength of belief in the prediction based on the overall measurement and model error. This belief is strongly influenced by the process covariance gain, $\phi$, which in one sense might be considered a "tuning parameter", leading to a subjective strength of belief in the prediction. With that said, a systematic process was followed in order to deduce a value of $\phi$ that is suitable for this problem, ensuring that the model is neither over-confident (small uncertainty but poor prediction of the overall trend of the primary variable, $T$) nor under-confident (large uncertainty but good prediction of the overall trend of the primary variable, including perturbations). As outlined in Section 5.4, the optimal value of $\phi$ for this problem (0.05) is the smallest value which satisfactorily reproduces the overall trend of the primary variable, the selection of which involves some subjective assessment.

For test #1, a 12 in (31 cm) diameter pan containing 1 L of ethanol was placed in the centre of the room and ignited; the door was subsequently closed and remained closed for the duration of the test. This test is useful for fire model validations since the fuel source, heat release rate, gas velocities, and oxygen availability are all very well controlled. The fuel configuration is shown in Appendix C, Figure C.6. Test results are plotted in Figures 6.4–6.7.

The fire-side gas temperatures for test #1 reached a moderate 140°C roughly 10 min after ignition. By this time, a thermal gradient had developed over the wall with temperatures ranging from about 85°C near the top to 55°C near the bottom. Plume radiation was not overwhelming for this small fire; stratification in compartment gases was likely the primary cause for the measured temperature gradient. Incident heat flux reached a peak of only 1.5 $\text{kW}\cdot\text{m}^{-2}$ at the centre of the wall. There appears to be a localized region of high fire exposure in the upper-right region of the wall, however this amounts to a difference of only 0.3 $\text{kW}\cdot\text{m}^{-2}$ from the centreline value, and is likely not a result of significance considering the overall low levels of irradiance evolved in the test.

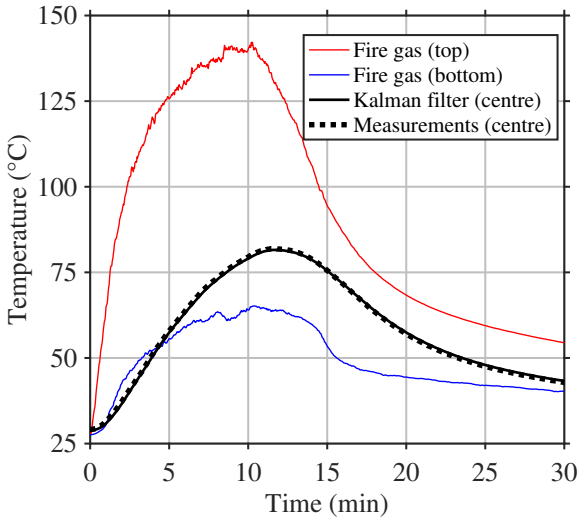


Figure 6.4: Characterization test #1, temperature line plot.

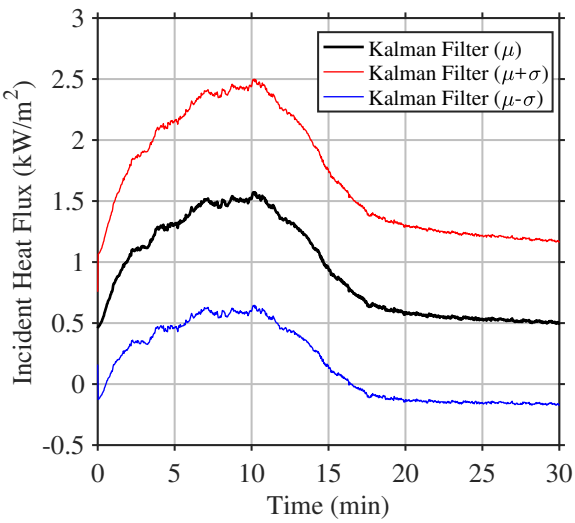


Figure 6.5: Characterization test #1, heat flux line plot.

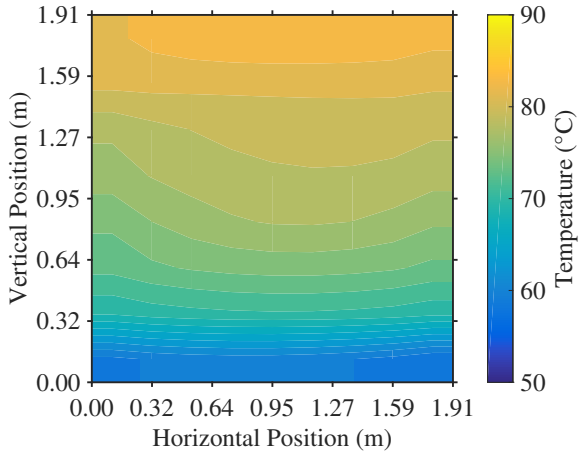


Figure 6.6: Characterization test #1, temperature contour plot, $t = 10$ min.

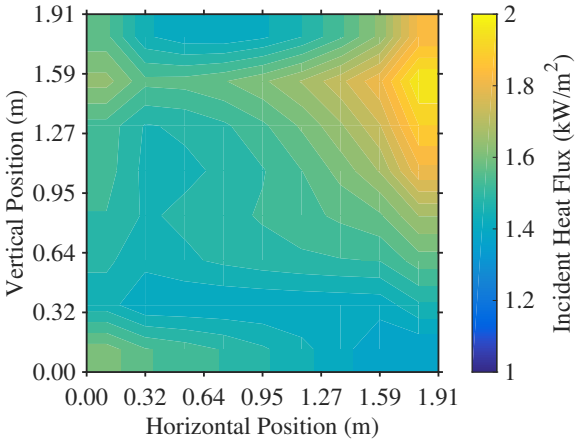


Figure 6.7: Characterization test #1, heat flux contour plot, $t = 10$ min.

For test #2, an impromptu collection of hardwood and softwood was assembled in the centre of the room and ignited using an ethanol-soaked rag. The door was partially closed, propped open by brick such that a 2.5 in (6.4 cm) gap was available for ventilation, for the duration of the test. This test was intended to evaluate the responsiveness of the data acquisition system to the realistic generation of heat and fire gases from solid fuel combustion. The fuel configuration is shown in Appendix C, Figure C.7, and the fuel contents are detailed in Figure C.8. Test results are plotted in Figures 6.8–6.11.

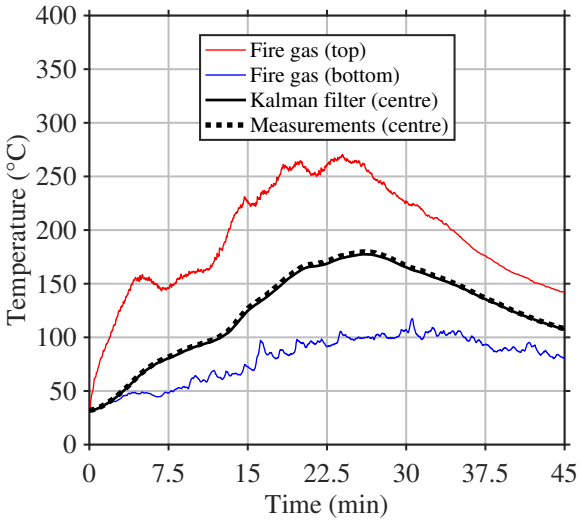


Figure 6.8: Characterization test #2, temperature line plot.

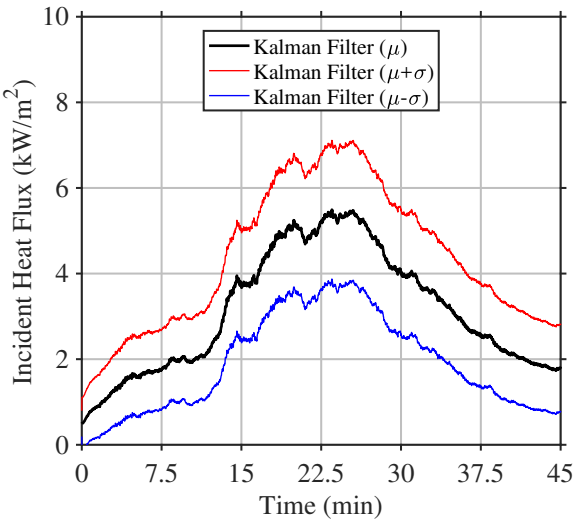


Figure 6.9: Characterization test #2, heat flux line plot.

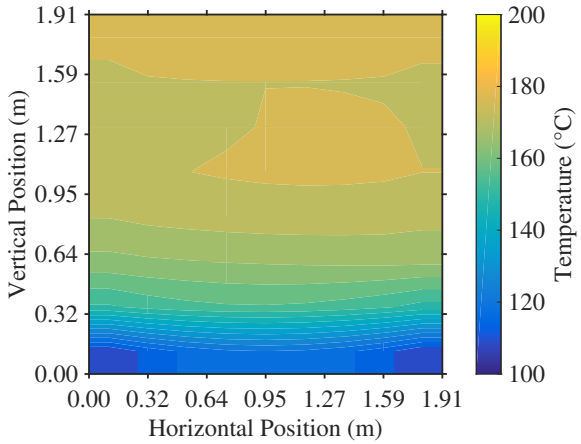


Figure 6.10: Characterization test #2, temperature contour plot, $t = 24$ min.

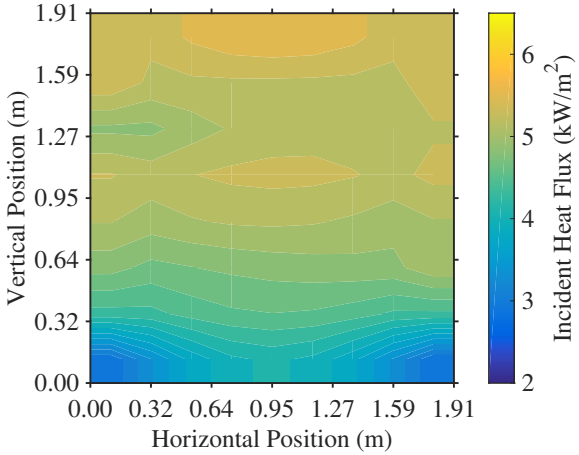


Figure 6.11: Characterization test #2, heat flux contour plot, $t = 24$ min.

The fire-side gas temperatures in test #2 reached a peak value of 270°C roughly 24 minutes after ignition. The fire gas temperature-time curve is notably less continuous than was the case in test #1, attributed to the complexity of the fuel source. Wall temperatures at this time ranged from 190°C near the top of the wall to 110°C near the bottom. While the temperature gradient is predominantly in the vertical dimension, it is notable that even at these moderate temperatures the lower corners of the wall are significantly cooler than adjacent areas; this trend is consistent through all tests.

Incident heat flux ranged from 2.5 kW·m$^{-2}$ at the bottom corners, to 6.0 kW·m$^{-2}$ at the top-centre of the wall; again, the heat flux gradient was predominantly in the vertical dimension. It can be concluded that for small fuel loads, for which a significant fire plume does not develop, no significant horizontal variance of irradiance should be expected.

For test #3, the standard softwood crib fuel bundles were used for the first time. The mass of each crib was measured within 30 min of the start of a test, before any significant amount of moisture could be absorbed by the wood. In this test three cribs were arranged in a "T" shape, with one crib in front (near the door) and two at the rear (near the wall), located 3 ft (91.4 cm) from the wall as shown in Appendix C, Figure C.9. Test results are plotted in Figures 6.12–6.15.

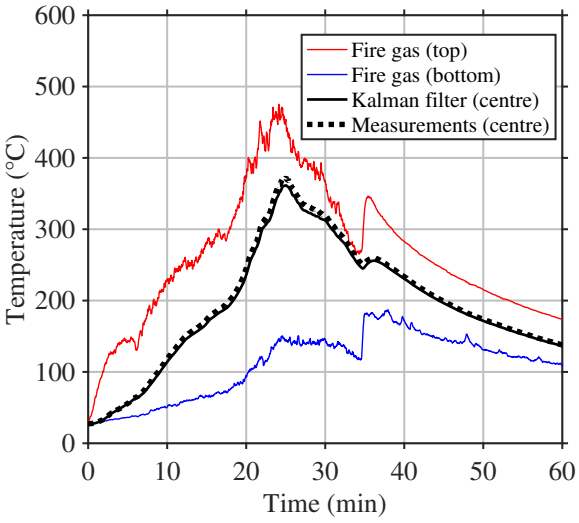


Figure 6.12: Characterization test #3, temperature line plot.

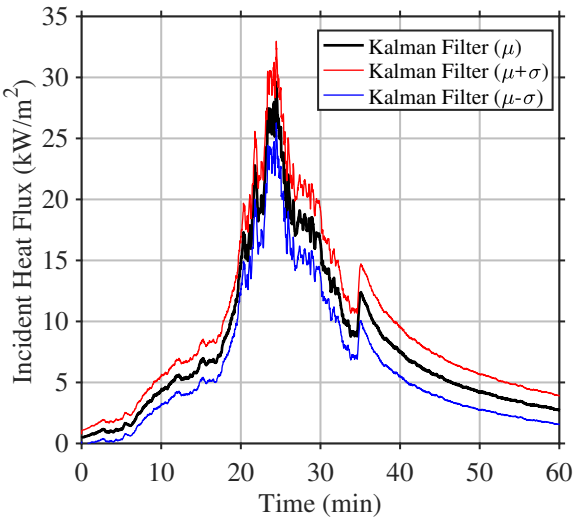


Figure 6.13: Characterization test #3, heat flux line plot.

The cribs in test #3 were elevated 2.5 in (6.4 cm) above the floor prior to testing by placing a fire brick in each corner. At the start of the test, an aluminum foil pan containing 500 ml of methanol was placed under the front crib and ignited. The door was initially left open to support well-ventilated burning of the wood cribs. It was eventually closed once the fire had reached a state of decay in order to contain heat. Figure 6.16 shows the state of the fire after 7.5 min, when the first crib was fully involved. After 12.7 min the fire had spread to the rear cribs, and the entire fuel package became involved. Figure 6.17 shows the state of the fire after 24 min, the time at which fire-side gas temperatures were at a maximum. It is clear from these figures that a well-defined, albeit short in height, fire plume developed in this test.

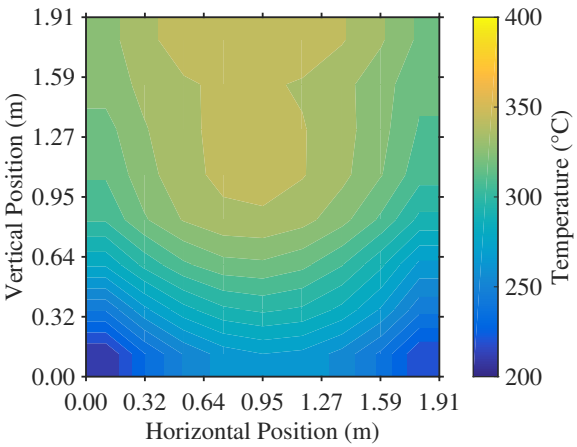


Figure 6.14: Characterization test #3, temperature contour plot, $t = 24$ min.

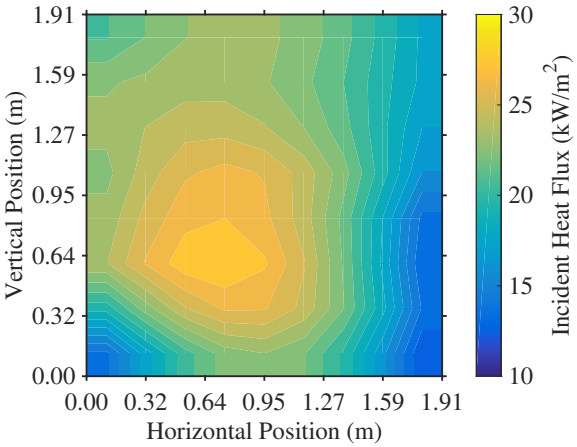


Figure 6.15: Characterization test #3, heat flux contour plot, $t = 24$ min.

Figure 6.16: Characterization test #3, fire, $t = 7.5$ min.

Figure 6.17: Characterization test #3, fire, $t = 24$ min.

Fire-side gas temperatures in test #3 reached as high as 470°C after 24 min. After 36.8 min the compartment door was closed, resulting in an immediate spike in gas temperatures. Following this, the rate of decay of compartment gas temperatures was more gradual, confirming the intended outcome. Sensor fluctuations also decreased as compartment ventilation was eliminated. The wall reached peak temperatures of about 370°C, with significant variation in temperatures in both the horizontal and vertical dimensions. The same can be said for incident heat flux, which ranged from 12–28 kW·m$^{-2}$ over the wall after 24 min of fire exposure. Interestingly the greatest heat

flux was localized in the centre of the wall rather than at the top, which is consistent with the height of the fire plume and its proximity to the wall at that time. This test confirms the hypothesis that thermal exposures on walls in a building fire are highly non-uniform, and consequently that multidimensional thermal degradation phenomena should be accounted for in comprehensive models of wall degradation in building fires.

Test #3 demonstrated that, despite fire growth being slowed by fuel configuration, the burn duration was still too short. The target was to achieve a peak heat flux after about 30 min, and to maintain relatively high exposure levels through 45–60 min. Also the exposure level was below expectations; incident heat flux exceeding 50 $kW \cdot m^{-2}$ was desired. Therefore, it was decided for test #4 to increase the fuel load to four cribs, arranged in a "T" shape, with one crib in front and three at the rear, spaced 3 ft (91 cm) from the steel wall as shown in Appendix C, Figure C.10.

For test #4 the size of the door was reduced in order to restrict ventilation, with the aim to increase fire gas temperatures and prolong burning duration. This was accomplished by installing an insulation panel at the top of the door, lowering the soffit by 1/3 of the initial height, reducing the door height from 78.5 in (199 cm) to 52.5 in (133 cm), and reducing the door area from 1.59 $m^2$ to 1.06 $m^2$. By Equation 6.1, the heat release rate necessary for a transition to a fully-developed fire is about 500 kW in this new configuration. Given that 4 cribs were used, the door was partially closed once the fire began to grow, thereby forcing the fire to become ventilation-limited, and ensuring that the threshold conditions for transition to a fully-developed fire would not be met. Figure 6.18 shows the fire after 24 min, when upper layer gas temperatures approached 600°C. This was an indication that the fire was approaching a fully-developed state, so at 24.5 min the door was closed to the width of a single fire brick (visible in the figure).

Results for test #4 are plotted in Figures 6.19–6.22. Fire-side gas temperatures reached a peak of 615°C before the door was closed, after which gas temperatures sharply decreased. Following this, the fire established a new equilibrium, and upper layer temperatures gradually increased to achieve peak values of 670°C. This test was very promising in that a burn duration of 60 minutes was achieved during which time gas temperatures remained in excess of 300°C. Despite this level of heat retention, however, the incident heat flux only reached approximately 45 $kW \cdot m^{-2}$ at the centre of the wall after 38 min. Inspection of heat flux contours at this time reveals that the fire exposure was relatively uniform in the horizontal dimension, which is consistent with the "wide" configuration of cribs used, and consequently the wide fire plume shown in Figure 6.18.

Figure 6.18: Characterization test #4, fire, $t = 24$ min.

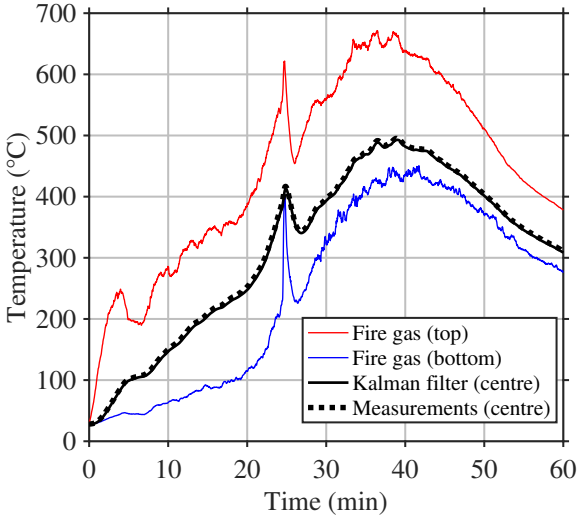


Figure 6.19: Characterization test #4, temperature line plot.

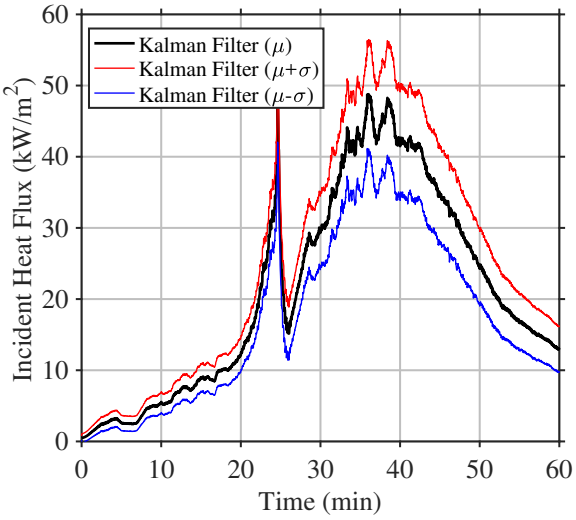


Figure 6.20: Characterization test #4, heat flux line plot.

Contour plots for test #4 show that the wall temperature and irradiance were greater in the upper-right region of the wall. This can be attributed to an asymmetric ventilation restriction at the door. The difference is quite significant, amounting to about 40°C and 8 kW·m$^{-2}$ from left-to-right at the top of the wall after 38 min of exposure.

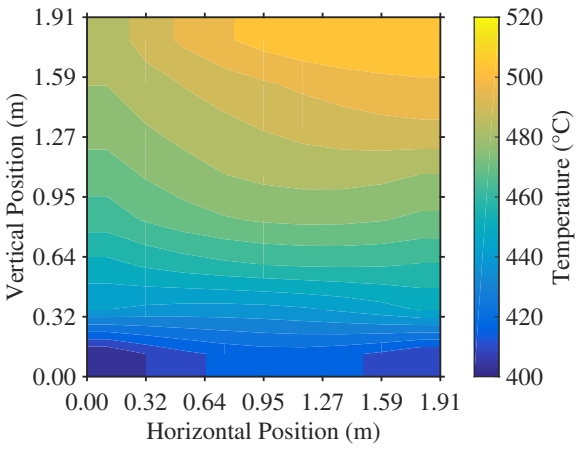


Figure 6.21: Characterization test #4, temperature contour plot, $t = 38$ min.

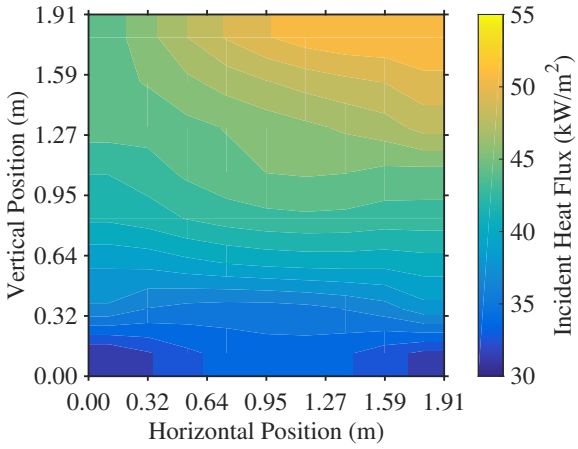


Figure 6.22: Characterization test #4, heat flux contour plot, $t = 38$ min.

To promote a more symmetric airflow in subsequent tests, an adjustable "obstruction panel" was designed, which afforded greater control of compartment ventilation. The panel was constructed from spruce lumber insulated with ceramic fibre insulation. The panel, positioned in front of the compartment door, could be pivoted from the bottom in order to adjust the opening angle. This design preferentially restricted airflow into the compartment versus exhaust of fire gases from the upper layer. A vertical slit was built along the centreline so that the panel could be completely closed, while still allowing a small amount of ventilation to support continued burning. The width of the slit was 2.5 in (61 cm), identical to the opening size used in previous tests (a single brick width). Refer to Figures 6.23–6.24 for details.

For test #5, the number of cribs was increased to five, as shown in Appendix C, Figure C.11. The idea was to further prolong the burning duration by increasing the fuel mass, while limiting the overall fire size via harsh restriction of ventilation. The panel was open at the start of the test, and closed fully after 21.2 min when the upper layer gas temperature began to approach 600°C. Figure 6.25 shows the fire after 10 min, as the second row of cribs became involved, and Figure 6.26 shows the fire after 20 min, as third row of cribs became involved and just prior to the obstruction panel being closed.

Results for test #5 are plotted in Figures 6.27–6.30. The fire-side gas temperatures reached a peak of 550°C before the panel was closed, after which time temperatures sharply decreased. At this point there was a concern that the fire had become excessively under-ventilated as upper layer temperatures dropped to 300°C, therefore it was decided


Figure 6.23: Ventilation obstruction panel, fully opened.

Figure 6.24: Ventilation obstruction panel, fully closed.

Figure 6.25: Characterization test #5, fire, $t = 10$ min.

Figure 6.26: Characterization test #5, fire, $t = 21$ min.

to open the panel back up after 23.9 min. With the introduction of fresh air the fire grew in size rapidly, reaching upper layer temperatures in excess of 750°C. With all four cribs in the back two rows involved, this fire was much more intense than in previous tests, with the peak irradiance at the centre of the wall reaching 75 kW·m$^{-2}$ after 32 min. Heat flux varied by over 30 kW·m$^{-2}$ from top-to-bottom of the wall, a significant gradient.

Test #5 was successful in terms of increasing the intensity of wall exposure to the desired levels, however it was apparent that the fire size was rapidly approaching the

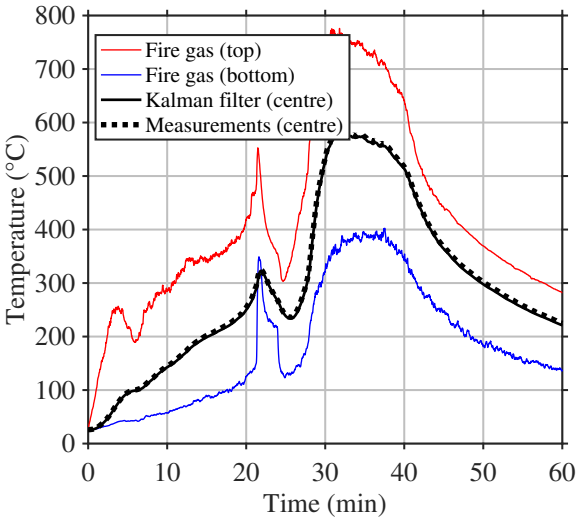


Figure 6.27: Characterization test #5, temperature line plot.

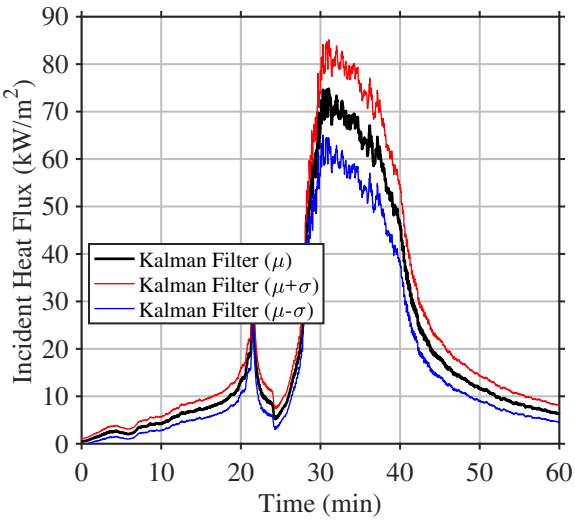


Figure 6.28: Characterization test #5, heat flux line plot.

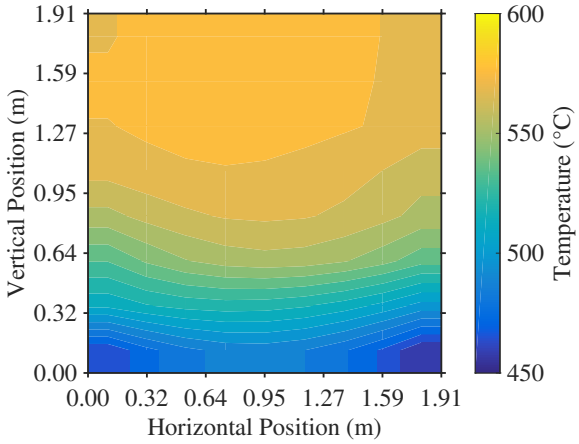


Figure 6.29: Characterization test #5, temperature contour plot, $t = 32$ min.

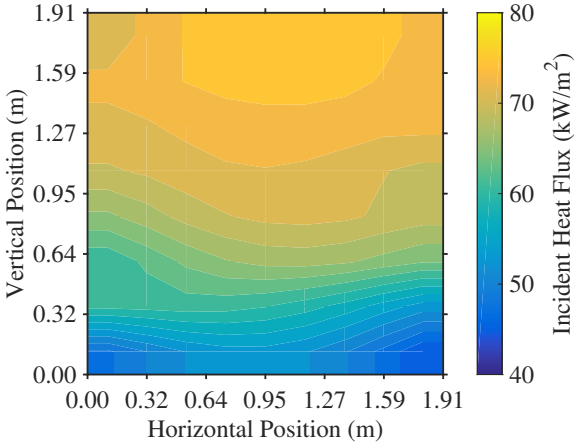


Figure 6.30: Characterization test #5, heat flux contour plot, $t = 32$ min.

threshold criteria for a transition to a fully-developed fire. Furthermore, it was apparent that when the obstruction panel was fully closed, the slit was not quite large enough to allow a fire of the desired size to develop. Therefore, for the next test it was decided to dynamically adjust the angle of the panel in order to fine-tune the fire evolution.

The same fuel configuration was used in test #6 as was in test #5 (refer to Appendix C, Figure C.12). The opening angle of the obstruction panel was initially set to 30° (Figure 6.31). By 12 min the fire fire had spread to the second row of cribs

(Figure 6.32), which was slightly slower than was the case for test #5, as expected. By 19.7 min the fire was beginning to grow rapidly as it spread to the back row of cribs, so the opening angle of the obstruction panel was reduced to 20°. This did not appear to notably slow fire growth, therefore the opening angle was reduced to 10°, after 21.2 min.

Figure 6.31: Obstruction panel opening angle measurement.

Figure 6.32: Characterization test #6, fire, $t = 12$ min.

Results for test #6 are plotted in Figures 6.33–6.36. It is clear that the reduction of the opening angle at 21.2 min initially caused a rapid decrease in gas temperatures, which in turn caused a significant reduction in incident heat flux to the wall. This is an important observation — even small changes to the ventilation had a large impact on the heat flux results. This impact is clearly unnatural (externally imposed), and undesirable, therefore for future tests a constant opening angle was adopted.

The temperature of compartment gases in test #6 reached a peak after 32 min, before decaying. By 38.4 min the upper layer temperature had dropped below 700°C, therefore the obstruction panel was fully closed in an attempt to contain hot gases within the compartment, and prolong the decay period. This approach was successful for a time, however as the fire became oxygen starved intense pressure fluctuations began to occur within the compartment. These were so significant that after approximately 54 min a structural failure occurred within the container — the middle wall insulation panels on both sides of the compartment were knocked down and subsequently destroyed.

An assessment of the compartment interior after the test revealed that, in addition to the structural failure of the insulation panels, some of the exposed steel members (Unistrut supports) were warped. Therefore, as part of the repairs it was decided to also

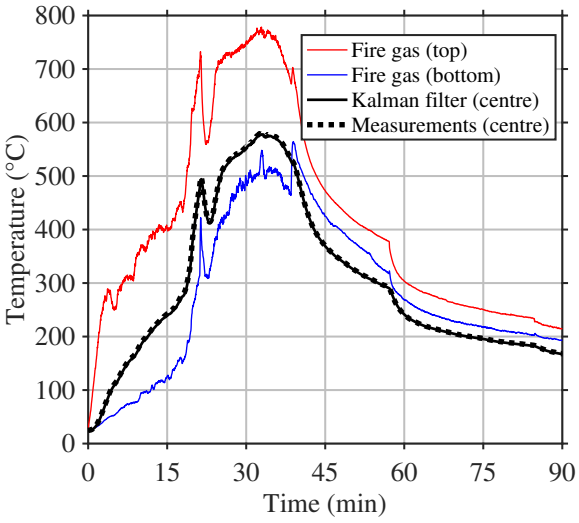


Figure 6.33: Characterization test #6, temperature line plot.

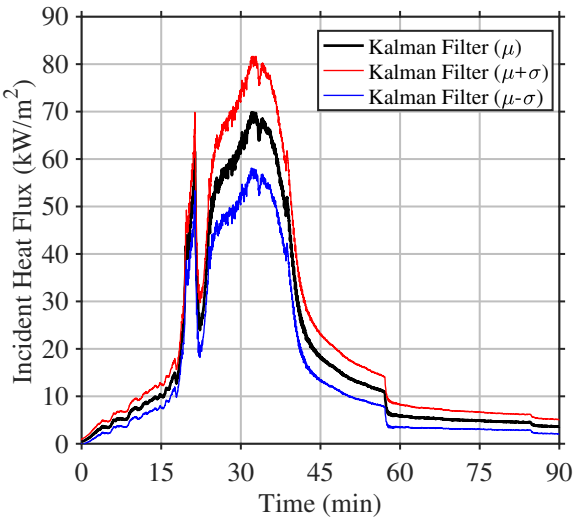


Figure 6.34: Characterization test #6, heat flux line plot.

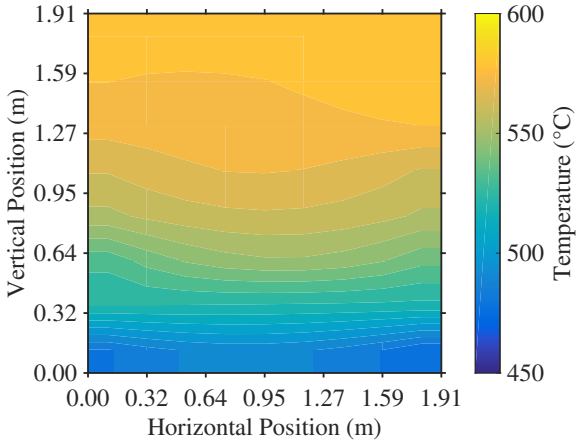


Figure 6.35: Characterization test #6, temperature contour plot, $t = 32$ min.

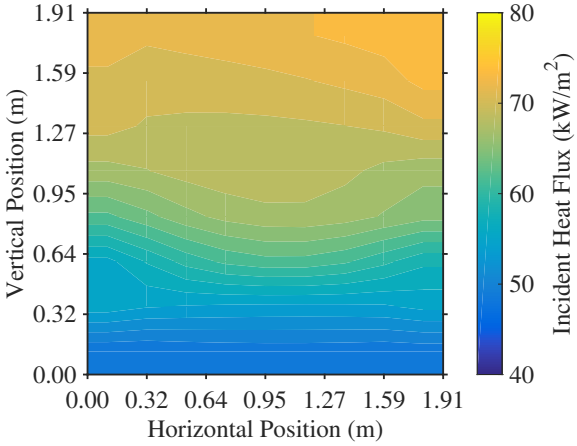


Figure 6.36: Characterization test #6, heat flux contour plot, $t = 32$ min.

fully insulate all previously-exposed steel members, including the ceiling supports and the thermocouple rakes. Also, to help to stabilize the side insulation panels, a horizontal member was added to each side of the compartment. The renovated compartment interior can be seen in Figure 6.37.

In reviewing the results from test #6, it is clear that the ventilation restriction was effective, however the fuel load was greater than strictly necessary. For test #7, it was decided to re-think the approach in consideration of the design objectives. The previous

Figure 6.37: Renovated compartment interior following the test #6 structural failure.

results show that increasing compartment gas temperatures will result in a greater fire exposure; alternatively, a more intense fire exposure could be achieved by moving the fire plume closer to the wall. Therefore, for test #7 a smaller fuel load of three cribs was used, with the rear cribs spaced 24 in (61 cm) from the wall rather than the 36 in (91 cm) used previously (Appendix C, Figure C.13). Furthermore, the cribs were arranged in-line in order to slow fire growth, allowing the compartment boundaries to heat in the early-stage fire, and ultimately increasing the fire exposure during peak burning.

Ventilation restriction was utilized in test #7, setting the obstruction panel opening angle to a constant 15°. Results are plotted in Figures 6.38–6.41. Visual observations confirmed that the rate of fire growth was slower than in the "T" configurations as the fire spread from the first to the second crib after 14.9 min, and to the third crib after 22.3 min. Once the third crib became involved, the fire growth rate became significant, ultimately reaching peak upper layer temperatures of 550°C after 30 min.

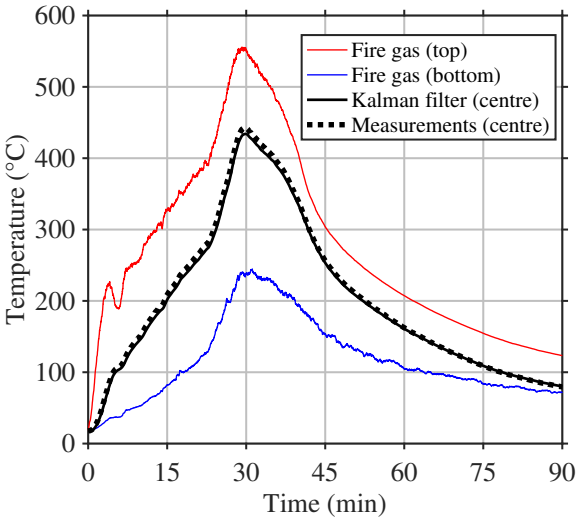


Figure 6.38: Characterization test #7, temperature line plot.

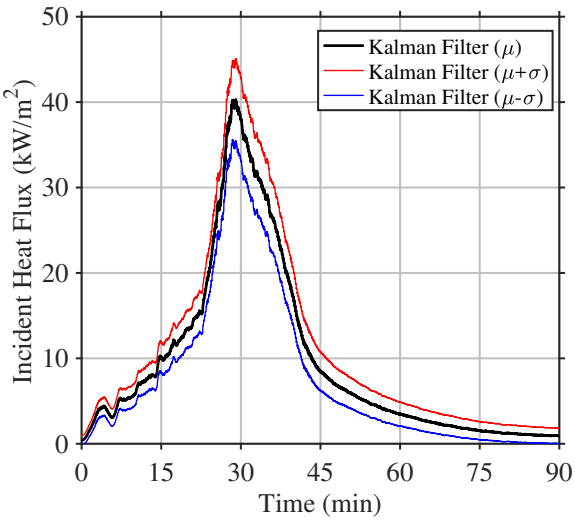


Figure 6.39: Characterization test #7, heat flux line plot.

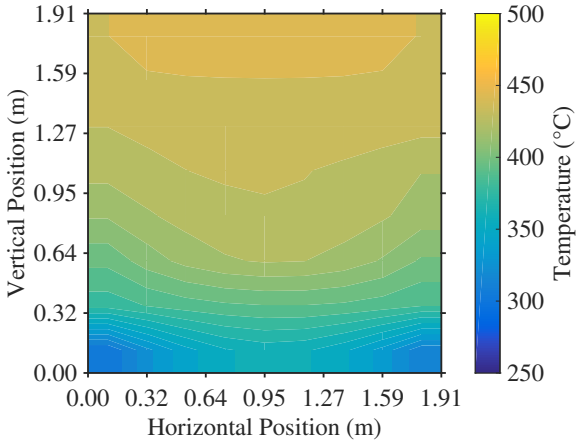


Figure 6.40: Characterization test #7, temperature contour plot, $t = 30$ min.

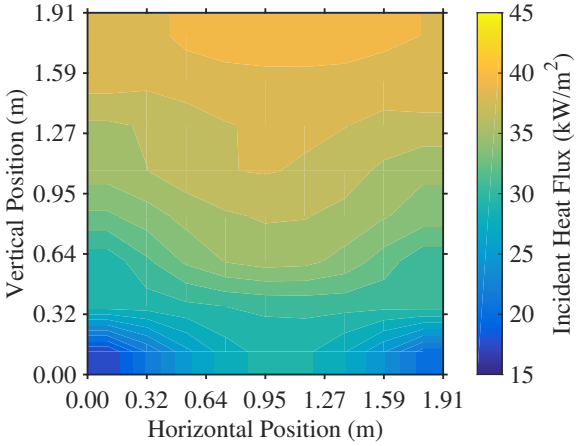


Figure 6.41: Characterization test #7, heat flux contour plot, $t = 30$ min.

After 30 minutes the temperature over the surface of the wall varied from 260–450°C, and the incident heat flux varied from 17–41 kW·m$^{-2}$. Gradients of temperature and heat flux are apparent both in the vertical and horizontal dimensions, clearly attributable to the closer proximity of the fire plume to the wall. These results are much more in line with the design objectives, with the overall fire size being smaller and the fire exposure being very much non-uniform, as would be the case for a single burning item in proximity to wall in a real fire. Still, the exposure levels were slightly lower than the design objectives, therefore for the following test it was decided to increase the fuel load to four cribs.

For test #8 the fuel configuration was increased to four cribs in-line, with greater spacing between cribs nearer to the wall (Appendix C, Figure C.14). The intent with the uneven spacing was to further slow fire growth as the third and fourth cribs became involved. Also, the rear crib was positioned 12 in (31 cm) from the wall, to further increase the intensity of the fire exposure. Results for test #8 are plotted in Figures 6.42–6.45.

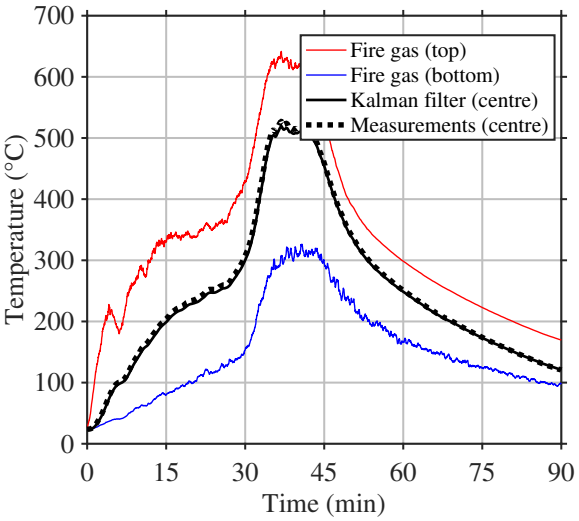


Figure 6.42: Characterization test #8, temperature line plot.

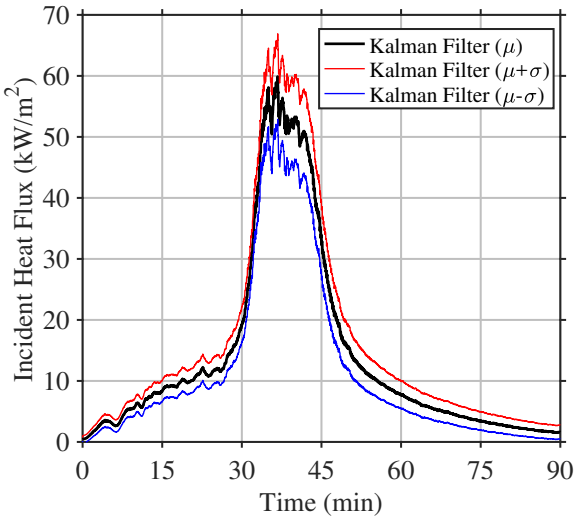


Figure 6.43: Characterization test #8, heat flux line plot.

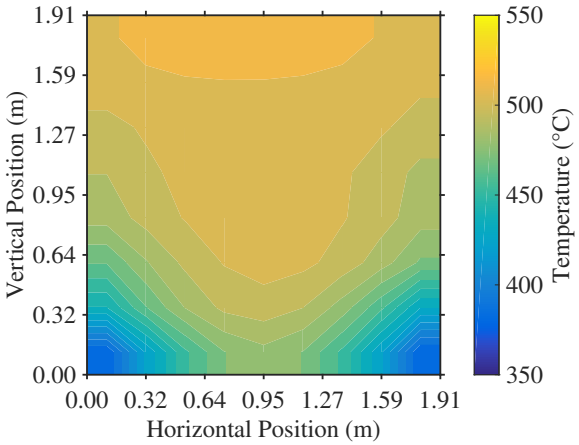


Figure 6.44: Characterization test #8, temperature contour plot, $t = 40$ min.

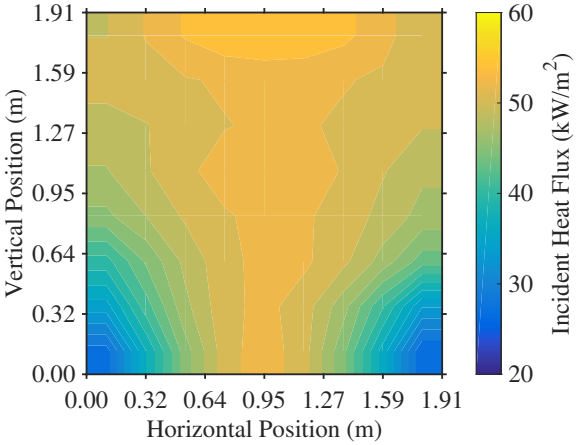


Figure 6.45: Characterization test #8, heat flux contour plot, $t = 40$ min.

Recalling from test #7, the second and third cribs became involved after 14.9 and 22.3 min, respectively. In comparison, the second and third cribs in test #8 became involved after 14.1 and 27.5 min, respectively, and the fourth crib after 31.8 min. From these results it seems that the fire growth rate was successfully slowed.

Fire gases reached an initial temperature plateau at 360°C in the upper layer from about 15–26 min; as the third and subsequently fourth cribs became involved, upper layer temperatures increased to a peak value of 640°C after 35 min. A relatively steady period of burning was maintained through to about 42 min, after which time the fire began to decay.

After 40 min, during the period of steady burning, the temperature gradient over the wall was significant in both horizontal and vertical dimensions. The effect was even more pronounced for the incident heat flux; by 40 min into the test the fire plume was in very close proximity to the wall, and the irradiance pattern closely reflects this fact (Figure 6.45). Incident heat flux at the top-centre of the wall reached about 58 $kW \cdot m^{-2}$, and only decreased to about 52 $kW \cdot m^{-2}$ at the bottom-centre of the wall, a direct consequence of plume radiation. In contrast, heat flux at the bottom corners of the wall was as low as 25 $kW \cdot m^{-2}$ at this time. This is precisely the type of non-uniform exposure that is the goal for the experiment. Given this, fuel load from test #8 was selected as the standard design fire for all subsequent tests.

Tests #9–12 were repeats of test #8, and were used to assess consistency of the fire exposure from test-to-test; fuel configurations for each of the tests are shown in Appendix C, Figures C.15–C.18. The results for tests #9–12 are shown below, in Figures 6.46–6.61. Note that for test #10 data acquisition was terminated prematurely after 75 min of exposure.

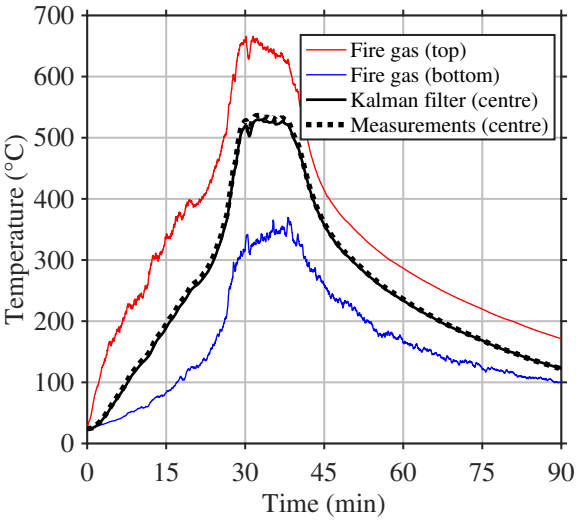


Figure 6.46: Characterization test #9, temperature line plot.

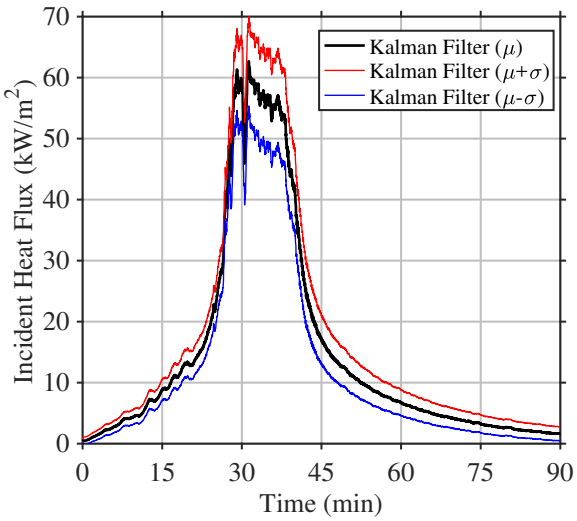


Figure 6.47: Characterization test #9, heat flux line plot.

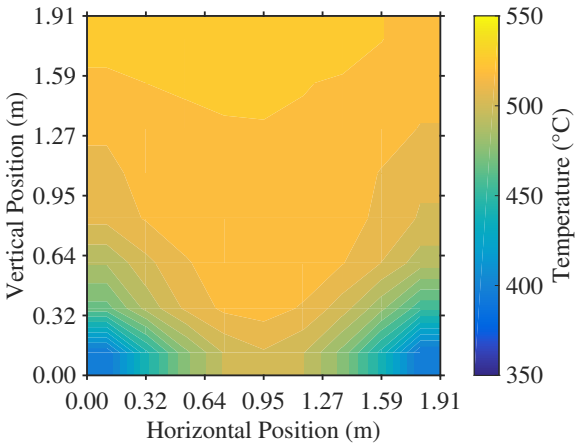


Figure 6.48: Characterization test #9, temperature contour plot, $t = 35$ min.

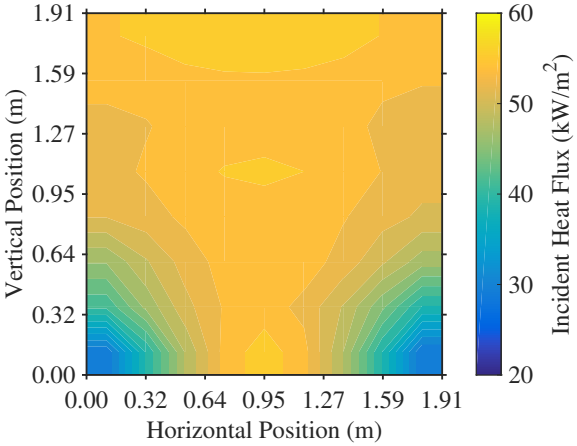


Figure 6.49: Characterization test #9, heat flux contour plot, $t = 35$ min.

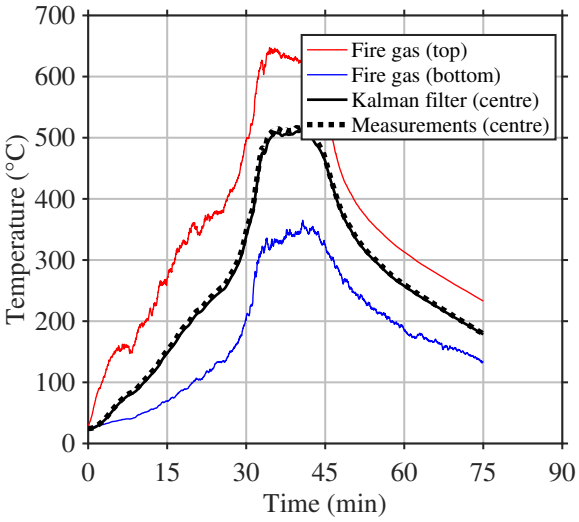


Figure 6.50: Characterization test #10, temperature line plot.

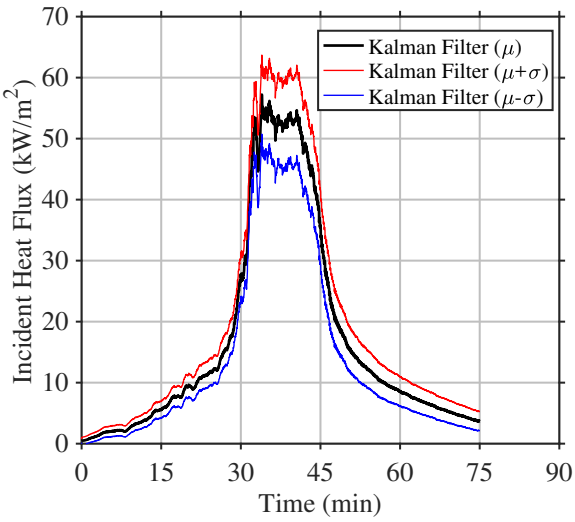


Figure 6.51: Characterization test #10, heat flux line plot.

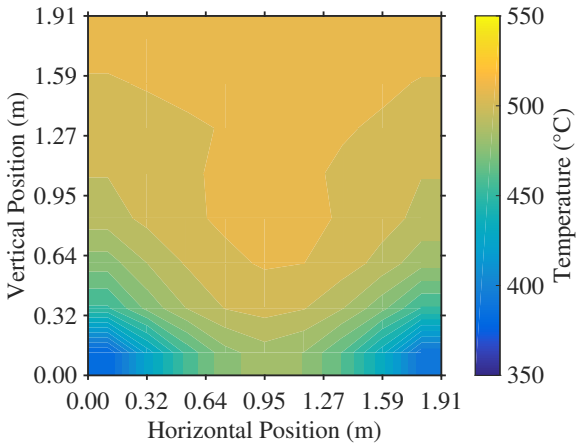


Figure 6.52: Characterization test #10, temperature contour plot, $t = 40$ min.

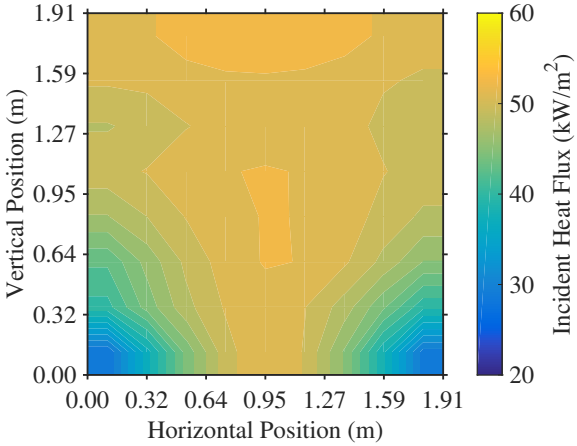


Figure 6.53: Characterization test #10, heat flux contour plot, $t = 40$ min.

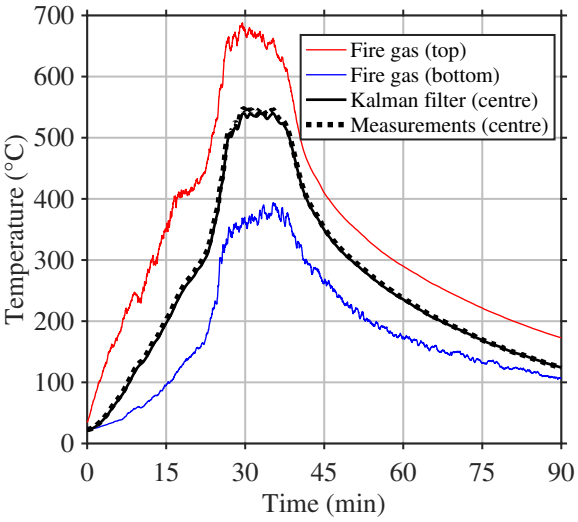


Figure 6.54: Characterization test #11, temperature line plot.

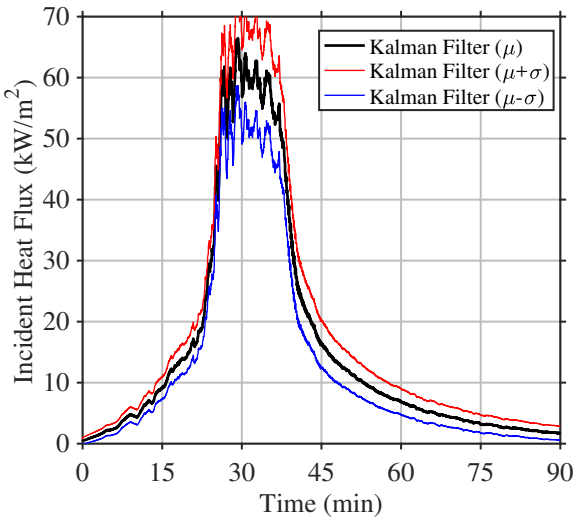


Figure 6.55: Characterization test #11, heat flux line plot.

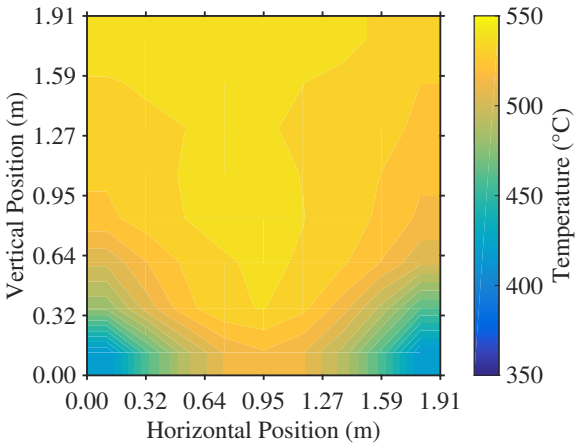


Figure 6.56: Characterization test #11, temperature contour plot, $t = 35$ min.

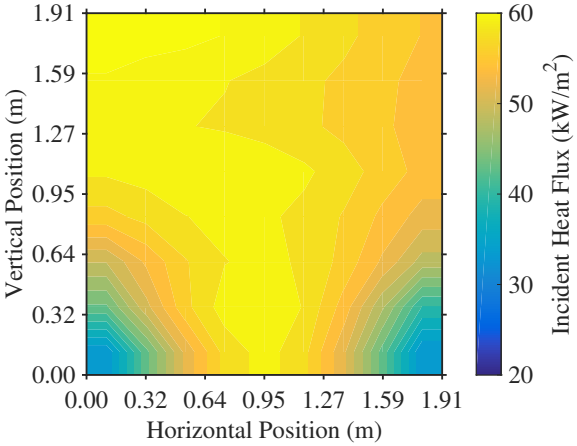


Figure 6.57: Characterization test #11, heat flux contour plot, $t = 35$ min.

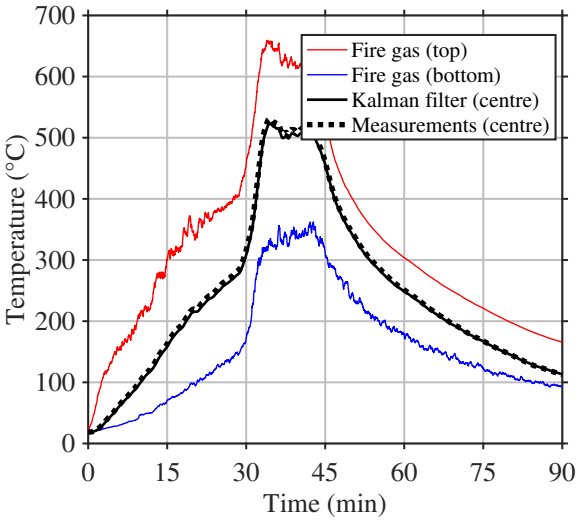


Figure 6.58: Characterization test #12, temperature line plot.

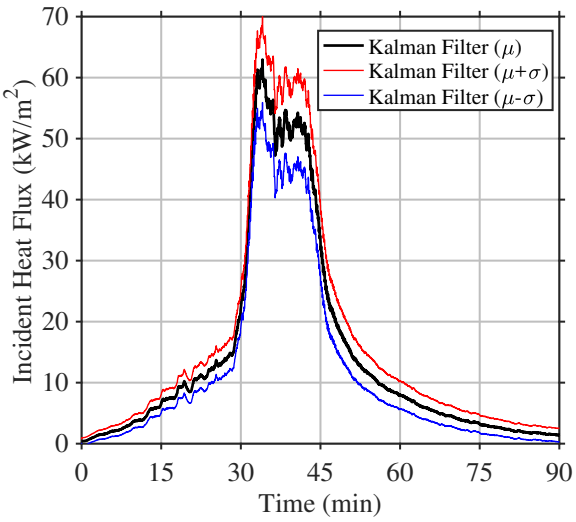


Figure 6.59: Characterization test #12, heat flux line plot.

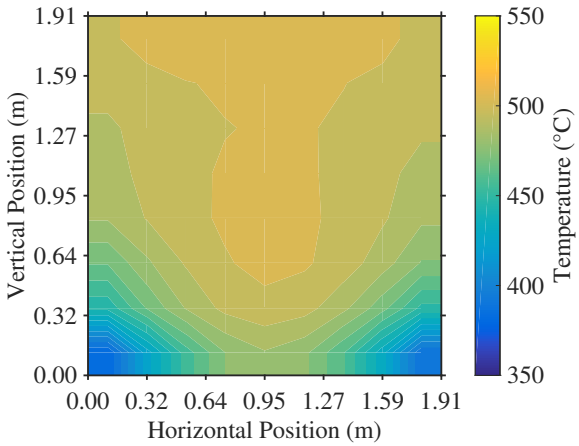


Figure 6.60: Characterization test #12, temperature contour plot, $t = 40$ min.

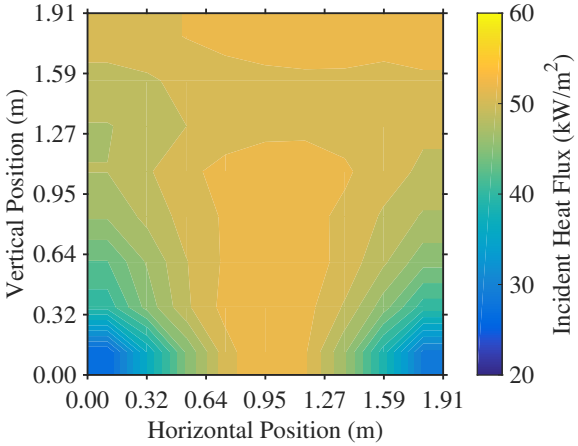


Figure 6.61: Characterization test #12, heat flux contour plot, $t = 40$ min.

### 6.3.1 Summary

With five repeat tests having been conducted, it is possible to make an assessment of the consistency of the experiment, in terms of fire gas temperatures and wall exposures. Figures 6.62–6.63, show the upper layer gas temperatures and the incident heat flux to the centre of the wall for tests #8–12, along with the time-average over the five tests.

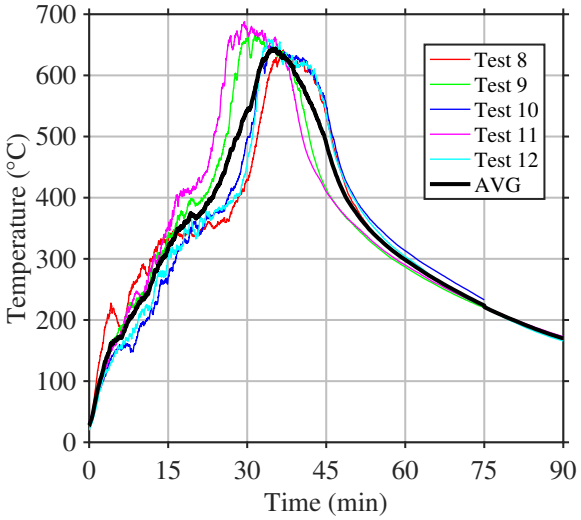


Figure 6.62: Upper layer fire gas temperature, tests #8–12.

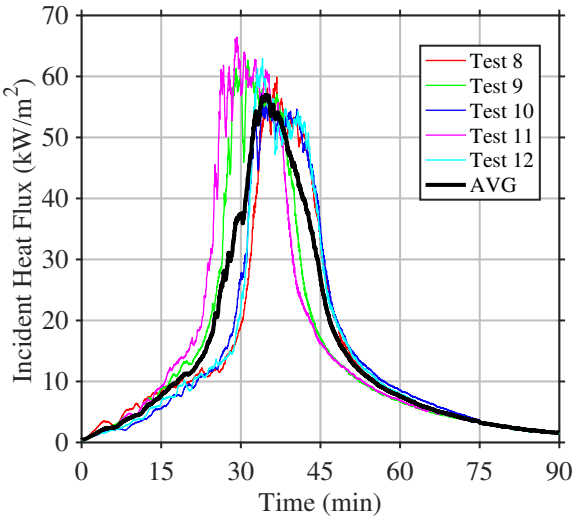


Figure 6.63: Incident heat flux to the centre of the wall, tests #8–12.

A summary of relevant results from these data is given in Table 6.3; these include the times corresponding to the start and end of the steady burning period ($t_1$ and $t_2$, respectively), and the corresponding upper layer temperatures and heat flux to the centre of the wall. The results for tests #8–12 were consistent, with a fire growth period of about 30 min, followed by 10 min of steady burning, and a gradual period of decay through the total exposure duration of 90 min. Over the five tests, the upper layer temperature during the steady burning period was about 635°C on average, and the the heat flux to the centre of the wall was about 55 kW·m$^{-2}$ on average. Tests #9 and #11 had slightly faster growth rates and the peak gas temperatures were slightly greater than the other tests, though no relevant observations were made which could explain this difference in behaviour. These differences can primarily be attributed to non-uniformity in the fuel, coupled with unpredictable airflows into the compartment — realities that must be conceded in large scale fire experiments. Still, both the upper layer gas temperatures and the wall fire exposures are in good agreement over the five tests.

| Test | $t_1$ (s) | $t_2$ (s) | Temperature (°C) AVG | MIN | MAX | Heat Flux (kW·m$^{-2}$) AVG | MIN | MAX |
|---|---|---|---|---|---|---|---|---|
| 8 | 33.5 | 43.5 | 613.4 | 570.6 | 641.7 | 52.05 | 42.28 | 59.89 |
| 9 | 28.5 | 38.5 | 643.5 | 612.2 | 665.7 | 56.32 | 45.91 | 62.67 |
| 10 | 33.5 | 41.5 | 632.3 | 614.5 | 647.4 | 52.96 | 47.94 | 57.22 |
| 11 | 26.5 | 37.0 | 660.1 | 624.7 | 687.8 | 58.56 | 50.09 | 66.47 |
| 12 | 32.5 | 43.0 | 628.2 | 600.3 | 659.0 | 53.53 | 47.00 | 62.96 |
| AVG | 30.9 | 40.7 | 635.5 | 604.5 | 660.3 | 54.69 | 46.64 | 61.84 |

Table 6.3: Summary of design fire statistics.

Figure 6.64 shows the average and standard deviation for upper layer temperature and incident heat flux over the five repeat tests — these were simply computed on a time basis, and the standard deviation here is only an indication of spread over the five tests, rather than a representation of the strength of belief in the accuracy of the results. This plot is a useful reference moving forward as it provides a concise description of the design fire in terms of upper layer temperature and heat flux to the centre of the wall.

It is concluded that the design fire selected here produces the desired fire exposures with sufficient consistency for use in the analysis of thermal degradation of wall assemblies, thereby satisfying the stated objective of characterizing the conditions in the experiment for the selected design fire. In contrast to standardized tests which prescribe a single fire exposure, this experimental methodology allows for any number of different exposures to be created by adjusting fuel and ventilation conditions. Additional characterization tests are only necessary if validation of the exposures is desired. If, on the other hand, the intent is simply to evaluate wall decomposition on the basis of involvement with a compartment fire, which is described by and may be modelled using the aforementioned conditions, then additional characterization tests are not necessary.

With the characterization of the experiment completed, the next step was to move on to tests of real construction assemblies, which are detailed in following chapter.

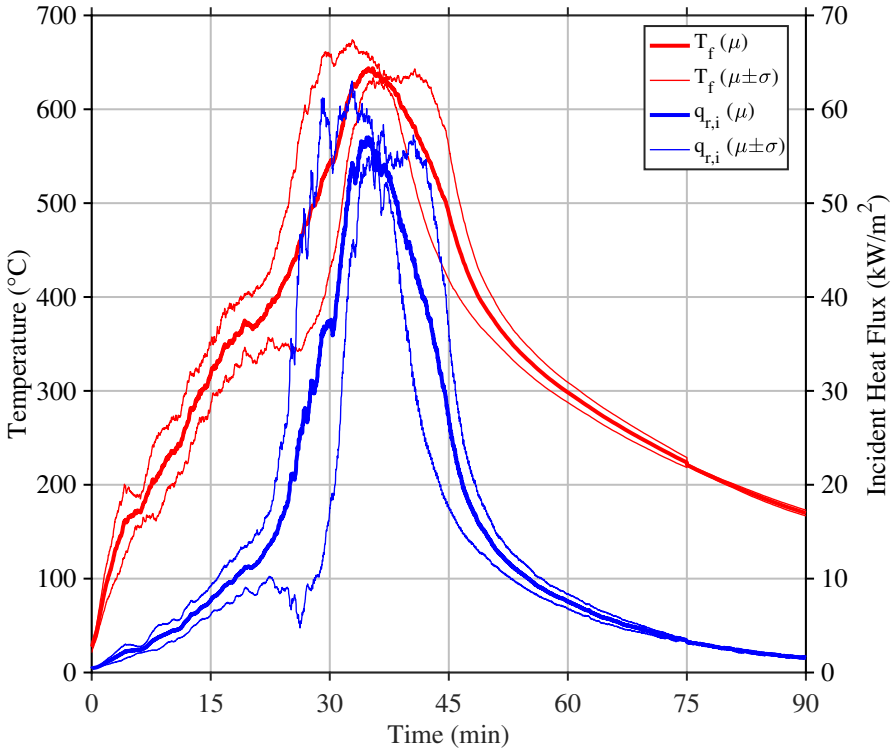


Figure 6.64: Average upper layer fire gas temperature and incident heat flux to the centre of the wall over the five repeat characterization tests.

# Chapter 7

# Assessment of Thermal Degradation of Construction Assemblies

With the conditions of the experiment characterized for the selected design fire, the next step was to demonstrate its utility as applied to the study of thermal degradation of construction assemblies. A series of experiments was conducted, referred to as "real wall" tests as opposed to the "steel wall" tests detailed in the previous chapter. The focus of this chapter is to present the results and findings of these real wall tests, with reference to the objective of demonstrating the utility of the experimental approach in the study of thermal degradation phenomena. The following section provides an overview of the five tests that were conducted in this series.

## 7.1 Test Overview and Data Reduction

The five tests in this series were conducted using the same fuel load and ventilation configuration as was specified for the design fire (Chapter 6). Tests were conducted over a five week period starting in October of 2016. While the fire gas temperatures and heat flux to the wall were expected to be consistent with those given in Figure 6.64, some deviation was expected as a result of the cooling weather conditions. This is one of the shortcomings of locating the apparatus outdoors, which as detailed in Chapter 4 was a compromise driven by practical constraints. Table 7.1 summarizes the conditions and events for each of the tests in this series; detailed results are presented in the following sections.

| Test | Date | Description |
|---|---|---|
| 1 | 10/05/2016 | *Ambient conditions*: 21.7°C, 62% RH, 98.35 kPa.<br>*Wall type*: W1c, 2×4 wood studs spaced 16 in on-centres, Roxul ComfortBatt® R14 stone wool insulation (all cavities), 1/2 in CGC Sheetrock Ultralight® gypsum board (both sides).<br>*Fuel*: 4 cribs in-line configuration, mass [14.13, 14.29, 14.60, 14.32].<br>*Events*: Obstruction panel set to a constant 15°. Fire spread to second crib after 13.6 min, to third crib after 19.9 min, and to fourth crib after 21.7 min. |
| 2 | 10/19/2016 | *Ambient conditions*: 18.8°C, 52% RH, 98.11 kPa.<br>*Wall type*: W1c, 2×4 wood studs spaced 16 in on-centres, CertainTeed Building Insulation® R12 fibre glass insulation (all cavities), 1/2 in CGC Sheetrock Ultralight® gypsum board (both sides).<br>*Fuel*: 4 cribs in-line configuration, mass [17.11, 16.52, 16.66, 16.17].<br>*Events*: Obstruction panel set to a constant 15°. Fire spread to second crib after 26.9 min, to third crib after 42.0 min, and to fourth crib after 47.3 min. |
| 3 | 10/28/2016 | *Ambient conditions*: 8.6°C, 62% RH, 98.58 kPa.<br>*Wall type*: W1d, 2×4 wood studs spaced 16 in on-centres, no insulation, 5/8 in CGC Sheetrock Firecode Core® gypsum board (both sides).<br>*Fuel*: 4 cribs in-line configuration, mass [15.72, 16.03, 16.17, 15.92].<br>*Events*: Obstruction panel set to a constant 15°. Fire spread to second crib after 17.1 min, to third crib after 27.0 min, and to fourth crib after 31.2 min. |
| 4 | 11/01/2016 | *Ambient conditions*: 18.5°C, 73% RH, 97.68 kPa.<br>*Wall type*: W1c, 2×4 wood studs spaced 16 in on-centres, CertainTeed Building Insulation® R12 fibre glass insulation (left cavities, 1-2), Roxul ComfortBatt® R14 stone wool insulation (right cavities, 3-4), 1/2 in CGC Sheetrock Ultralight® gypsum board (both sides).<br>*Fuel*: 4 cribs in-line configuration, mass [16.03, 16.23, 16.41, 15.66].<br>*Events*: Obstruction panel set to a constant 15°. Fire spread to second crib after 18.4 min, to third crib after 26.7 min, and to fourth crib after 28.9 min. |
| 5 | 11/09/2016 | *Ambient conditions*: 7.2°C, 64% RH, 98.05 kPa.<br>*Wall type*: W1c, 2×4 wood studs spaced 16 in on-centres, Thermafiber UltraBatt® R15 mineral wool insulation (left cavities, 1-2), Roxul ComfortBatt® R14 stone wool insulation (right cavities, 3-4), 1/2 in CGC Sheetrock Ultralight® gypsum board (both sides).<br>*Fuel*: 4 cribs in-line configuration, mass [16.03, 16.23, 16.41, 15.66].<br>*Events*: Obstruction panel was removed to accomodate additional video and IR thermography instrumentation. Fire spread to second crib after 14.6 min, to third crib after 21.8 min, and to fourth crib after 24.1 min. |

Table 7.1: Summary of conditions and events for real wall tests #1–5.

Raw test data was saved in the CSV format, and are provided in Appendix D. A script was used to import raw data files to the MATLAB workspace for post-processing,

and the imported data saved to the *.mat format; refer to Appendix E for details.

Fire gas temperatures were stored to the EXP_FIRE_GAS variable, which has dimensions of n_steps×8×4. The second dimension of this array corresponds to the vertical position of thermocouples, while the third dimension corresponds to the rake number. Slice averages were calculated at each of the eight vertical positions by averaging the corresponding measurements at each of the four rake in the corners of the compartment. Slice temperatures were stored to the EXP_FIRE_GAS_V_AVG variable, which has dimensions of n_steps×8. Rake averages were calculated by averaging all eight measurements for each rake. These temperatures were stored to the EXP_FIRE_GAS_H_AVG variable, which has dimensions of n_steps×4.

Wall temperatures were imported to the EXP_WALL_MAIN (temperature measurements on the back of the fire-side gypsum board) and EXP_WALL_REAR (temperature measurements on the back of the cool-side gypsum board) variables; the former variable has dimensions of n_steps×6×4 and the latter variable has dimensions of n_steps×3×4. The second dimension of these arrays corresponds to the vertical position, while the third dimension corresponds to the cavity number. Cavity averages were calculated by averaging all measurements in a given cavity over all heights (EXP_WALL_MAIN_H_AVG and EXP_WALL_REAR_H_AVG), and height averages were calculated by averaging all measurements at a given height over all cavities (EXP_WALL_MAIN_V_AVG and EXP_WALL_REAR_V_AVG).

For the frame temperatures, average values were calculated for the top, upper sides, lower sides, and bottom of the wall. Frame temperatures were imported to the EXP_FRAME variable, which has dimensions of n_steps×8; frame averages were saved to the EXP_FRAME_AVG variable, which has dimensions of n_steps×4.

The gas temperature on the unexposed side of the wall was imported to the EXP_BACK_GAS variable, which has dimensions of n_steps×6. Slice averages were taken at each of the three heights (top, middle, and bottom) based on measurements at the two rakes (left and right), and stored to the EXP_BACK_GAS_AVG variable, which has dimensions of n_steps×3.

The temperature of the unexposed-side surroundings was measured at two locations, on the left and right side of the door. These two measurements were imported to the EXP_BACK_SURR variable (n_steps×2), and the average of the left and right measurements was stored to the EXP_BACK_SURR_AVG variable (n_steps×1).

All raw data files may be found in Appendix D. In addition, an extensive set of photographs and digital video were recorded for each experiment; these may be

obtained upon request to the fire research group at the University of Waterloo. A subset of the measurements is presented in Sections 7.3.1–7.3.5 below; construction and instrumentation details are first discussed in Section 7.2.

## 7.2 Construction and Instrumentation Details

The method of construction and instrumentation of walls tested in this apparatus is unique to each wall type; for example, the mounting of a simple 2×4 wood stud wall would differ from that of a wall with offset steel studs. While Chapter 4 provides an overall description of the apparatus and instrumentation, specific details of the construction and instrumentation of the walls considered here (Table 7.1) are provided below.

All of the walls considered in the present work used 2×4 wood stud frames, which were constructed and mounted in-place in a four-cavity configuration, as shown in Figure 7.1 (refer to Figure 4.13 for more details). Each of the outer four sides of the stud frame was lined with a strip of ceramic fibre insulation; these were cut to a depth of 6 in (152 mm) and pressed flush to the front-facing insulation as shown in Figure 7.2. A 1/2 in (12.7 mm) gap (5/8 in (15.9 mm) for test #3) was left between the front-facing edge of the stud frame and the edge of the front-facing insulation, to accommodate the fire-side gypsum board. Studs were bolted to the steel frame at eight locations (the front-most 1/2 in (12.7 mm) mount holes in the steel frame; refer to Appendix A).

Next, fire-side gypsum board was cut to size and fastened to the stud frame using coarse thread drywall screws (1-1/4 in (31.8 mm) length for 1/2 in (12.7 mm) gypsum board and 1-3/8 in (34.9 mm) length for 5/8 in (15.9 mm) gypsum board) spaced 12 in (305 mm) along the studs. Gypsum board sheets were installed horizontally with the full size sheet at the top, per standard construction practice. The sheets used had nominal dimensions of 48×96 in (122×244 cm); the top sheet was cut to a size of 48×73-1/4 in (122×186 cm) and the bottom sheet to 25-1/4×73-1/4 in (64×186 cm).

With the fire-side gypsum board in place, six K-type bead-welded thermocouples were attached to the back of the exposed-side gypsum board using masking tape (refer to Figure 7.3), located at the centre of each cavity, and spaced 12 in (305 mm) apart. The masking tape was positioned just below the junction so that the bead pressed firmly against the gypsum board (refer to Figure 7.4).

For tests with in-cavity insulation, the batts were then installed in each cavity, pressing the thermocouples tight between the insulation and the gypsum board. For

Figure 7.1: Wood stud frame mounted in the fire test apparatus.

Figure 7.2: Frame insulation and mounting details.

Figure 7.3: In-cavity thermocouples, insulated cavities.

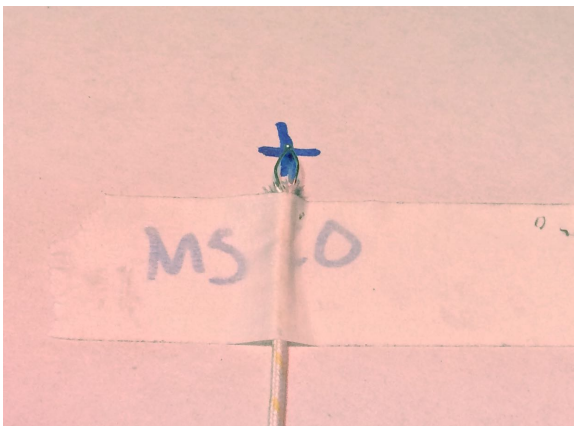

Figure 7.4: Thermocouple surface attachment details.

tests without in-cavity insulation, insulated pads were used to press the thermocouples tightly to the gypsum board. The pads were made of 2×2 in (5.1×5.1 cm) squares of ceramic fibre insulation, 3/8 in (9.5 mm) thick, attached using three 6 in (15.2 cm) strips of duct tape as shown in Figures 7.5 and 7.6

Figure 7.5: In-cavity thermocouples, uninsulated cavities.

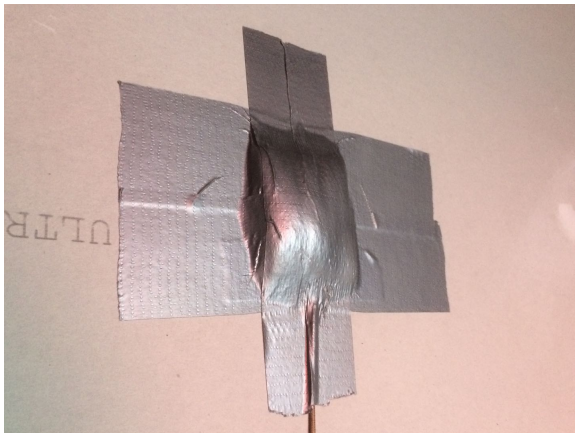

Figure 7.6: Insulated pads for surface thermocouples.

The cool-side gypsum board was installed flush on the wood stud frame in the same manner, with the top sheet cut to a size of 48×73-1/4 in (122×186 cm) and the bottom sheet to 22-3/4×73-1/4 in (58×186 cm) (the cuttoff from the bottom sheet on the fire-side). This left a 2.5 in (6.4 cm) gap at the bottom of the wall, where the in-cavity thermocouples exited. The leads were wrapped in ceramic fibre insulation, and scrap pieces of gypsum board were attached to the bottom of the stud frame to fill in the space at the bottom of the wall. Drywall compound was applied liberally to create a gas seal (refer to Figure 7.7).

The horizontal joints on the fire-side and cool-side gypsum board were sealed using CGC Sheetrock® paper joint tape and CGC Sheetrock® All Purpose drywall compound. Fasteners were tightened to be just below flush with the wall surface, and then sealed with drywall compound. The drywall compound was allowed three days to set, during which time an electric heater was placed on both sides of the wall. Once dry, the surfaces of the wall were sanded smooth. A finished wall mounted in-place in the fire test apparatus is shown in Figure 7.8 from the perspective of the fire-side.

Each test was conducted using the design fire and ignition procedure described previously. In addition to temperature instrumentation, video cameras were positioned to record the state of the wall from both exposed and unexposed sides. Tests were allowed to continue for 3 hours, after which time the observable state of the wall was recorded and the test ended. The following section details the results for the five real wall tests conducted in the present work.

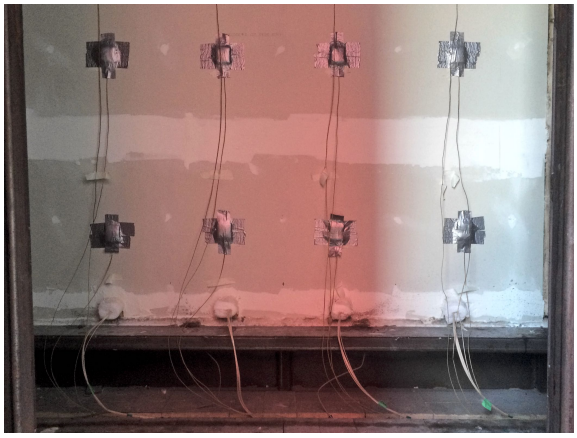

Figure 7.7: Finished wall, unexposed side, filled bottom gap.

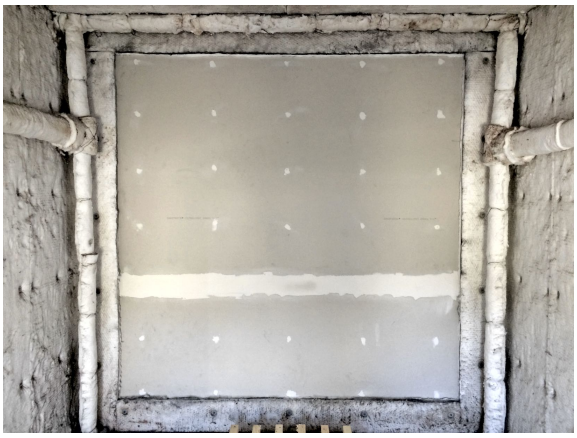

Figure 7.8: Finished wall, exposed side, dried and sanded.

## 7.3 Results and Discussion

### 7.3.1 Test #1 – Stone Wool Insulation

The first test was conducted on a W1c wall with stone wool insulation and lightweight 1/2 in (12.7 mm) gypsum board coverings. Figures 7.9 and 7.10 show the slice and rake averaged fire gas temperatures, respectively. As shown in both figures, the fire initially grew for 22 min before reaching a period of steady burning, which was approximately 9 min sooner than was expected from the design fire. The steady burning duration was about 10 min, and the average temperature near the ceiling was 690°C (compared to the expected 605°C–660°C of the design fire).

It is clear that the fire in test #1 burned more rapidly and more intensely over a shorter duration than the design fire. It is tempting to attribute this solely to heat retention within the compartment, given that the real wall is a much better insulator than the steel wall — for example, the thermal diffusivity of steel is 8.92 $mm^2 \cdot s^{-1}$ (Figure 5.5) compared to that of stone wool insulation, 1.65 $mm^2 \cdot s^{-1}$ [56], and gypsum board, 0.32 $mm^2 \cdot s^{-1}$ [56] (at room temperature). However there was also a significant deviation from the normal methodology for this test that must be considered. The standard method of fuel preparation was to assemble cribs three days prior to a test, and condition the cribs in a room at 50% relative humidity during that time. This method gave a rough control over the moisture content in the wood, resulting in a crib mass of $N(15.05, 0.46)$ kg for the cribs used in the characterization tests. The cribs used for this test, however,

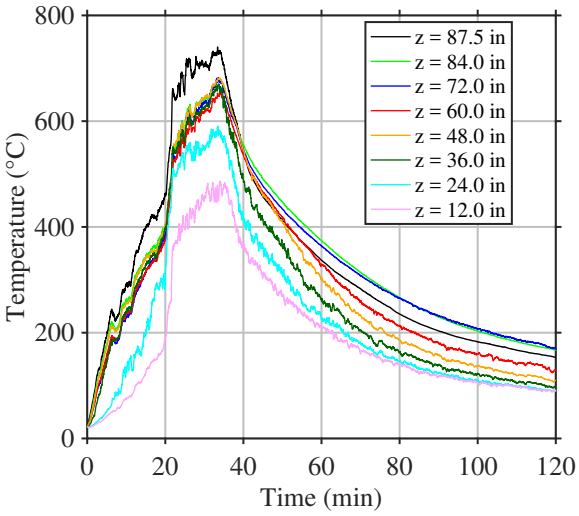


Figure 7.9: Test #1, fire gas temperatures, slice average.

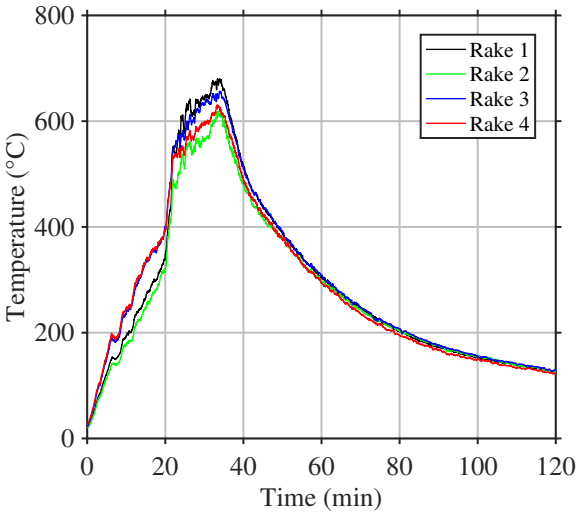


Figure 7.10: Test #1, fire gas temperatures, rake average.

were conditioned for 2 weeks following the final steel wall test, reducing their moisture content, resulting in an average mass of 14.24 kg. Lower moisture content means that less heat is required for the evaporation of water from the cellular wood, leading to a greater propensity for ignition and flame spread, and ultimately resulting in a greater mass burning rate of the fuel and greater rate of fire growth. These results highlight the importance of consistency and proper conditioning of the fuel load in this type of experiment.

From Figure 7.10 it is apparent that the rake averages were very close, indicating that slice averages should also be a good representation of the stratified gas temperatures in the compartment (far from the fire plume). In the early stages of the test, gas temperature at rakes 3 and 4 were greater than those at rakes 1 and 2, which makes sense given that the fire started at the front of the compartment. Interestingly temperatures at rakes 1 and 3, which are located on the left side of the compartment, were about 30°C greater than those at rakes 2 and 4 during the steady burning period. This might be attributed to asymmetric ventilation into the compartment, which is consistent with visual observations — Figures 7.11 and 7.12 show the state of the wall after 66.1 min and 79.5 min, respectively, as recorded by the fire-side camera. Deep cracking occurred over the entire wall, but gypsum board falloff occurred only in the hotter upper-left region of the wall. It is desirable to have symmetric ventilation in these experiments as asymmetry in flows is more difficult to represent accurately in a fire model. In future

work, an assessment of flow symmetry is recommended, and perhaps the inclusion of wind baffles at the compartment opening to promote more symmetric flows.


Figure 7.11: Real wall test #1, fire-side camera, 66.1 min.


Figure 7.12: Real wall test #1, fire-side camera, 79.5 min.

Figure 7.13 shows the average temperatures in each stud cavity on the back of the fire-side gypsum board. Measured temperatures were similar in all cavities for the first 50 min of the test, indicating that the exposure was uniform in the horizontal dimension for the first part of the test. Beyond this time, temperatures measured in cavities 3 and 4 (the right side of the wall) were greater than those measured in cavities 1 and 2 (the left side of the wall). While falloff did not occur on the left side until 66 min, deep cracking was present prior to this, allowing hot gases trapped between the gypsum board and the insulation to escape, and thus measured temperatures to decrease. This occurred preferentially on the hotter left side of the wall, explaining the differences noted above.

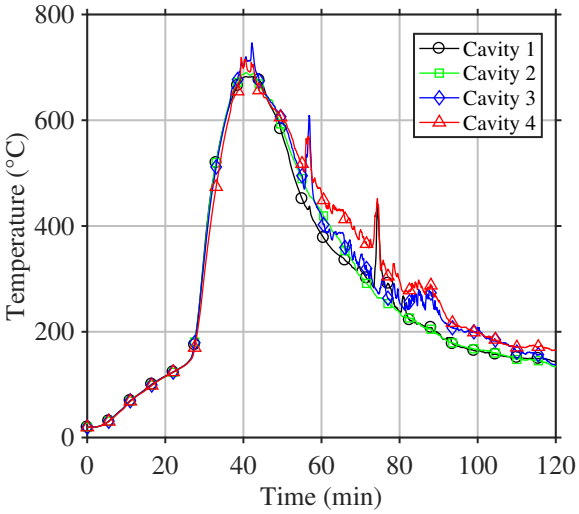


Figure 7.13: Test #1, main wall temperatures, cavity averages.

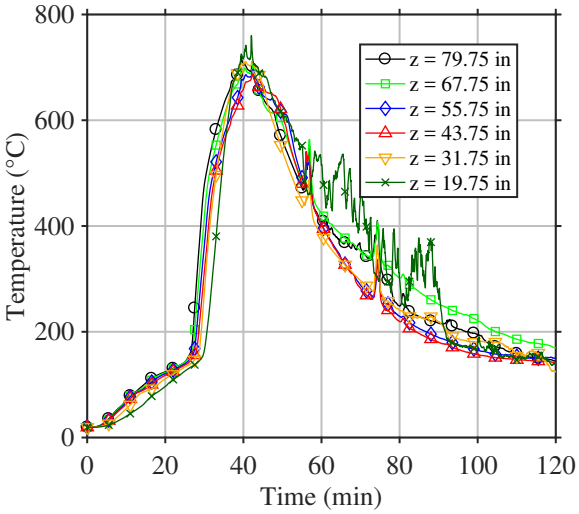


Figure 7.14: Test #1, main wall temperatures, height averages.

Figure 7.14 shows the averaged temperatures at each thermocouple height on the back of the fire-side gypsum board. For the first 35 min of the test, the temperatures followed the predictable trend of being greater near the top of the wall and lesser near the bottom. For example, at $t = 20$ min (before the fuel became fully-involved), the measured temperature ranged from 92°C to 125°C bottom-to-top. A sharp increase in temperature occurred after 27 min, at which time the back of the fire-side gypsum board was at approximately 140°C. This transition in heating rate is consistent with transitions that occurred in the preliminary experiments (Figure 3.13) and in small-scale mockup experiments of the same construction assembly [56]. In those cases the temperature at which the transition occurred was closer to 120°C. In the present case it must also be considered that the fire exposure was also rapidly increasing at this time, causing a

rapid increase in temperature due to heat conduction into the wall. While this transition certainly reflects the onset of the first stage of calcination (Section 2.2.3), the rapid increase in fire exposure resulted in elevated temperature measurements at this time.

The back of the fire-side gypsum board reached a peak temperature of about 720°C before decreasing as the fire decayed. Up to this time temperatures in the upper region of the wall (the black and light green traces in Figure 7.14) were greater than those in the middle and lower regions. By approximately 40 min into the test, however, the temperature at the bottom of the wall increased and began to fluctuate significantly. When examined further, this behaviour was in fact found to be a response to an issue with the experimental procedure, as explained below.

Figures 7.15 and 7.16 show the cavity and height averages of temperatures measured on the back of the cool-side gypsum board. For the first 60 minutes or so, temperatures were similar across all four cavities, eventually reaching slightly greater values on the right side of the wall. Similarly the upper region was hotter than the lower region, although this behaviour did not persist beyond approximately 50 min. This is also the time at which the fire-side gypsum board temperature increased at the bottom of the wall, and is also an artifact of the aforementioned experimental error, which is discussed below.

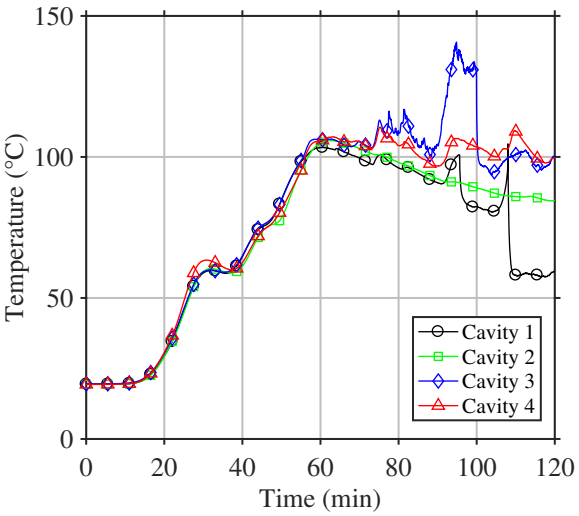


Figure 7.15: Test #1, back wall temperatures, cavity averages.

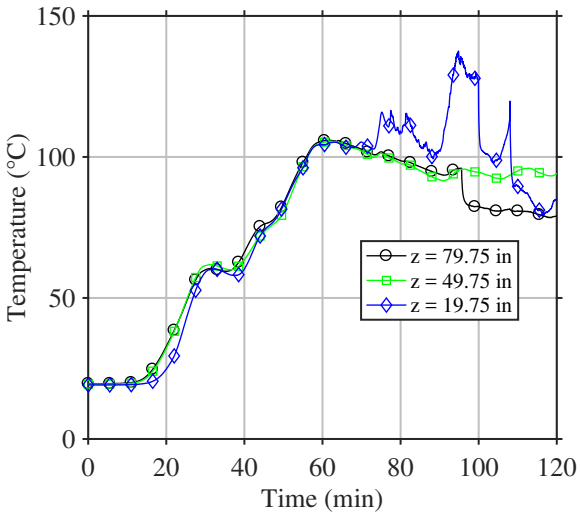


Figure 7.16: Test #1, back wall temperatures, height averages.

Both sides of the nominally 6×6 ft (183×183 cm) wall can almost completely be covered using three 4×8 ft (122×244 cm) sheets of gypsum board. However, bcause the gypsum board must extend to cover the studs on the edges of the wall, a small gap is

left at the bottom of the unexposed side (Figure 7.7). Figure 7.17 shows the unexposed side of the wall at the end of the test (>2 hours). The lack of covering allowed fresh air to enter the wall at the bottom, facilitating combustion of the wood, and exhausting of hot gases to the unexposed side of the wall — this is readily apparent from the burn patterns seen on the gypsum board. As a result, the transition section of the apparatus filled with hot gases, affecting the temperatures measured on the unexposed side of the wall. This oversight was rectified in subsequent tests by filling the gap.

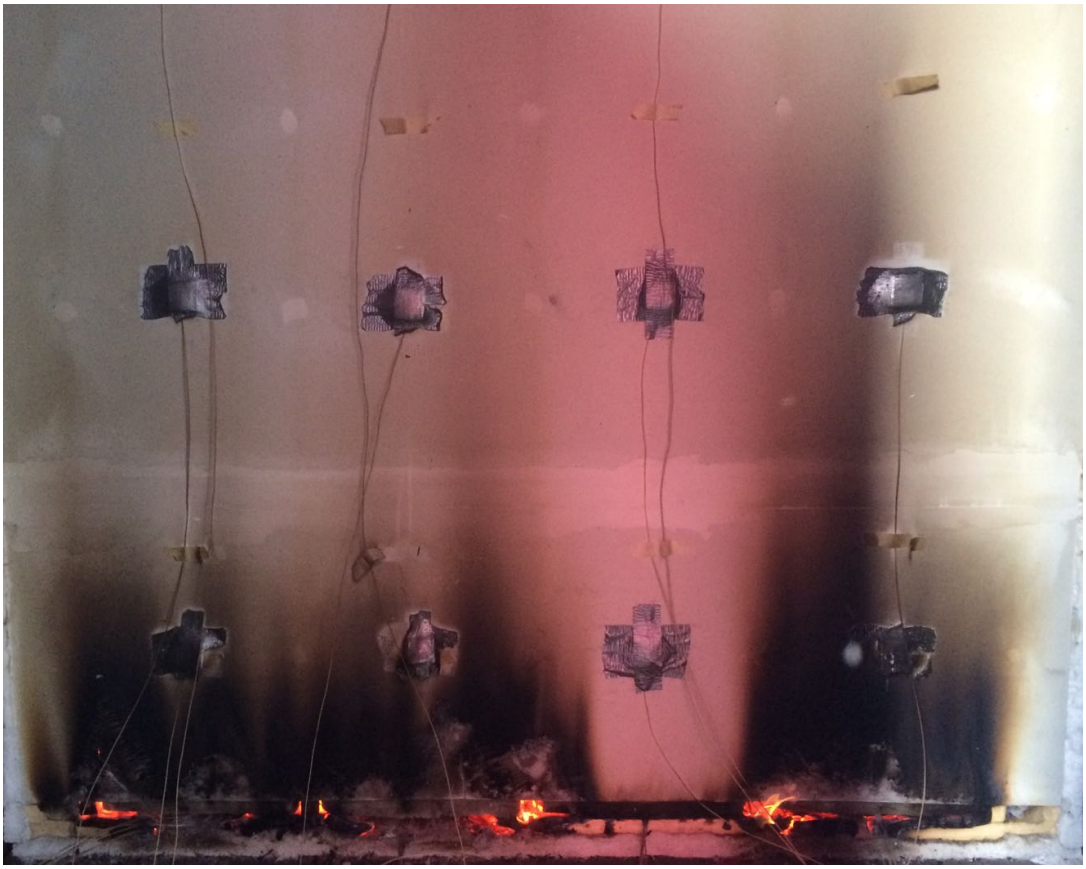

Figure 7.17: Real wall test #1, unexposed side of the wall, inadequate wallcovering.

Despite this issue, the the results still give meaningful insight into the temperature rise of the cool-side gypsum board. An initial temperature plateau of 60°C was reached after 27 min, as the insulation absorbed thermal energy and the gypsum board reached an unsteady equilibrium with the cool-side surroundings. As the fire exposure increased rapidly at 21 min, heat propagated through the wall, eventually instigating a secondary increase in temperature of the cool-side gypsum board. Fire gas temperatures began to decrease after 37 min, while the fire-side gypsum board temperatures began to decrease

after 41 min, and the cool-side gypsum board temperatures began to decrease after 59 min. Heat retention in the materials meant that thermal degradation continued long after the fuel had been consumed by the fire. Given this, it was decided to collect data for a duration of three hours in all subsequent tests.

### 7.3.2 Test #2 – Fibreglass Insulation

Test #2 used a similar wall as test #1, except with fibreglass instead of stone wool insulation. New wood was purchased one week prior to the start of this test for fabrication of the wood cribs. Cribs were built and conditioned for three days prior to the test per the standard methodology; despite this, the average mass of the four cribs was 16.62 kg compared to the design fire cribs with mass of $N(15.05, 0.46)$ kg. Clearly three days conditioning time for green wood was not sufficient to reduce the moisture content of the wood to levels of previous tests. Fire gas temperatures are plotted in Figures 7.18 and 7.19, for slice and rake averages, respectively.

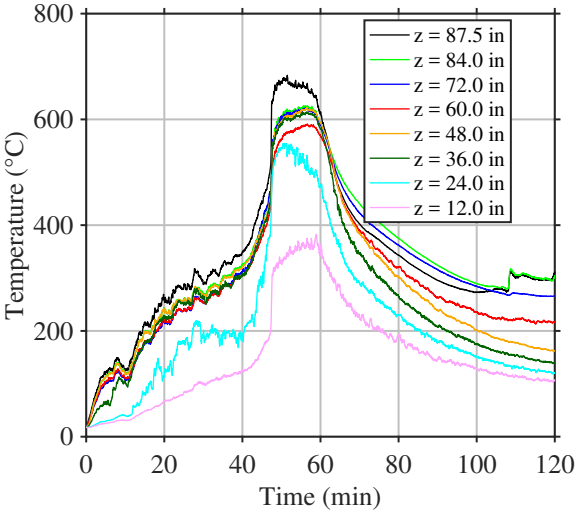


Figure 7.18: Test #2, fire gas temperatures, slice average.

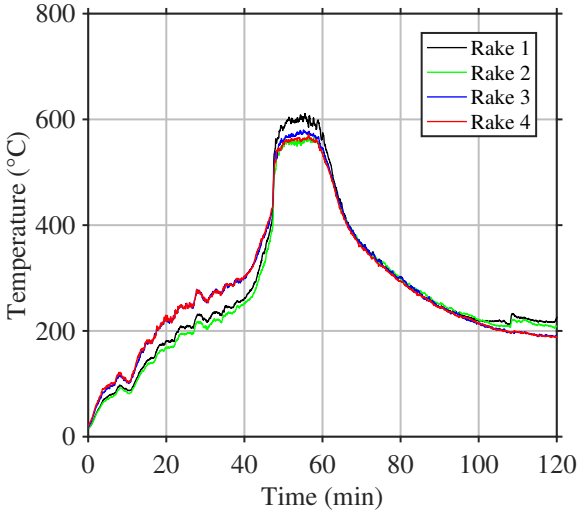


Figure 7.19: Test #2, fire gas temperatures, rake average.

The fire growth in test #2 was significantly slower than that of the design fire. The slow growth continued for the first 40 min, followed by a gradual transition to steady burning at 46 min (with an upper layer temperature of 665°C), followed by decay after 58 min. Compared to the design fire, the transition to steady burning was delayed by 15 min, in part a consequence of the high moisture content and low propensity for ignition

and flame spread of the fuel. Despite the slow growth, peak upper layer temperatures and duration of steady burning were consistent with those of the design fire. Based on the temperature profile of the fire-side gases, the intensity of the fire exposure to the wall in this test was consistent with that of the design fire, although delayed in time by about 15 min. Rake temperatures were consistent in the early stages of the fire, and 25°C greater near the left side of the wall during the period of steady burning.

Temperatures of the fire-side gypsum board are shown in Figures 7.20 and 7.21 for cavity and height averages, respectively. The exposed side of the gypsum board increased in temperature slowly at first, and then rapidly after 47 min, corresponding to the 120°C temperature threshold identified previously. Fire-side gypsum board temperatures varied by about 30°C from the bottom to the top in the early stages of the fire, with a more pronounced difference apparent as the exposure rapidly increased and more heat was transferred into the wall. Peak temperatures were achieved after 60 min, at which time the greatest temperatures were measured at the top and bottom two height positions. This is a consequence of the proximity of the fire to the wall, and reflects perfectly the exposure pattern identified in Chapter 6.

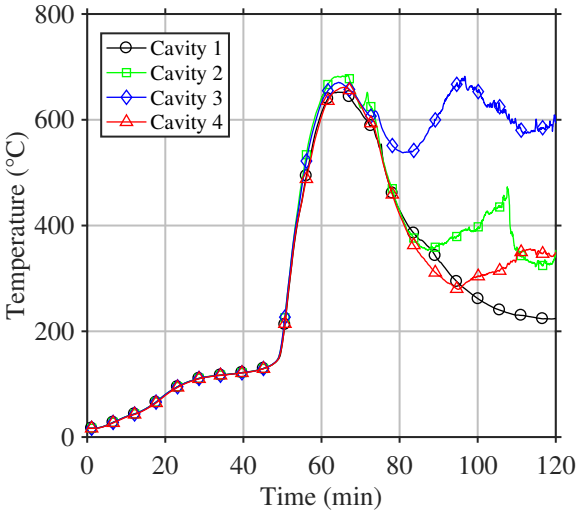


Figure 7.20: Test #2, main wall temperatures, cavity averages.

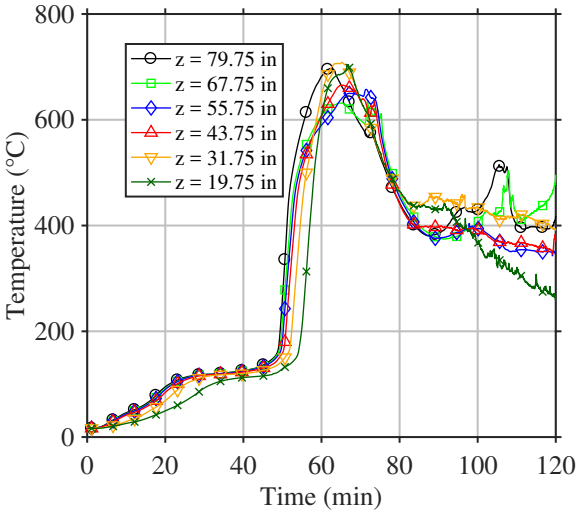


Figure 7.21: Test #2, main wall temperatures, height averages.

Cavity temperatures were very similar across the wall for the first 73 min, with temperatures in the middle cavities being about 10°C greater than the side cavities starting from 60 min; this is expected based on the exposure symmetry. After 73 min, the fire-side gypsum board temperature in cavity 3 began to increase significantly; the

same can be said for cavity 2 after 89 min and cavity 4 after 94 min. At these times the fire was well into its decay stage, and it was determined that these temperature increases were a result of the fibreglass insulation burning under the remains of the fire-side gypsum board. Figure 7.22 shows the state of the wall after 62.1 min, where deep cracking can be observed over the exposed side of the wall, predominantly in the upper-central region. By 110.3 min the fuel had been completely consumed, yet the wall temperatures continued to increase as the fibreglass insulation and wood frame burned (Figure 7.23). This is clear evidence that combustible construction can be susceptible to catastrophic failure even in the event of a fuel limited fire that does not reach flashover.


Figure 7.22: Real wall test #2, fire-side camera, 62.1 min.

The cavity and height averaged temperatures on the back of the cool-side gypsum board are shown in Figures 7.24 and 7.25, respectively. Temperatures across cavities were virtually identical for the first 60 min, after which time temperatures in cavity 2 began to increase more rapidly. By 100 min into the test, the temperatures over the four cavities differed by 34°C. These differences were driven by the burning of the fibreglass insulation, which tended to occur more in the middle cavities than in the edge cavities. The differences in temperature with height were consistent with the expected outcome, with the bottom temperature being 64°C, the middle temperature 91°C, and the top temperature in excess of 120°C after 2 hours of exposure.


Figure 7.23: Real wall test #2, fire-side camera, 110.3 min.

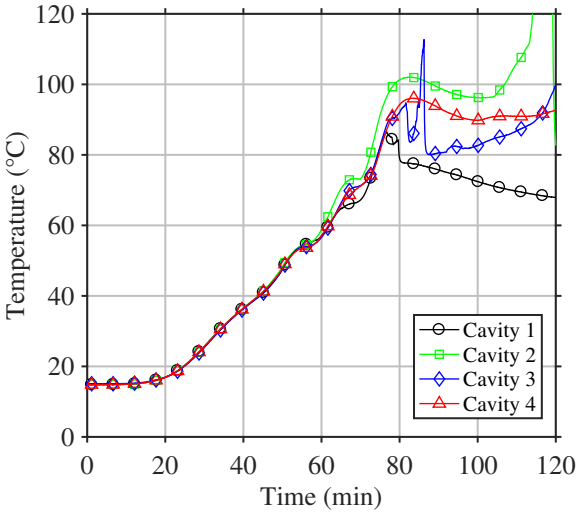


Figure 7.24: Test #2, back wall temperatures, cavity averages.

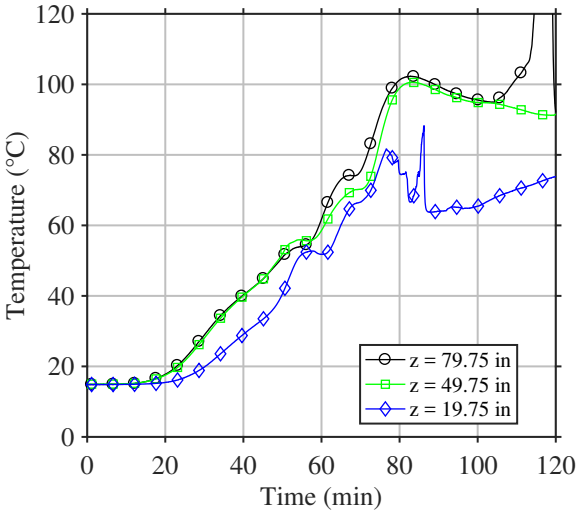


Figure 7.25: Test #2, back wall temperatures, height averages.

### 7.3.3 Test #3 – No Insulation

For the third test, a W1d wall was selected, which consists of non-insulated stud cavities and 5/8 in (15.9 mm) firecode gypsum board on both sides of the wall. This test was conducted in late October of 2016, and by this time the outdoor temperature had begun to drop; the ambient temperature at the time of the test was only 8.6°C compared to the typical temperatures of around 20°C in previous tests. Figures 7.26 and 7.27 show that

the fire grew to its peak after 37.5 min, and burned steadily to 42.5 min at an average upper layer temperature of 685°C. Compared to the design fire, the fire in test #3 took about 6 minutes longer to reach the steady burning period, which is consistent with a delay associated with cooler initial conditions and inlet air. As in the previous tests, slice averages exhibited the expected vertical stratification with hotter gases near the ceiling, and rake averages were consistent in all four locations.

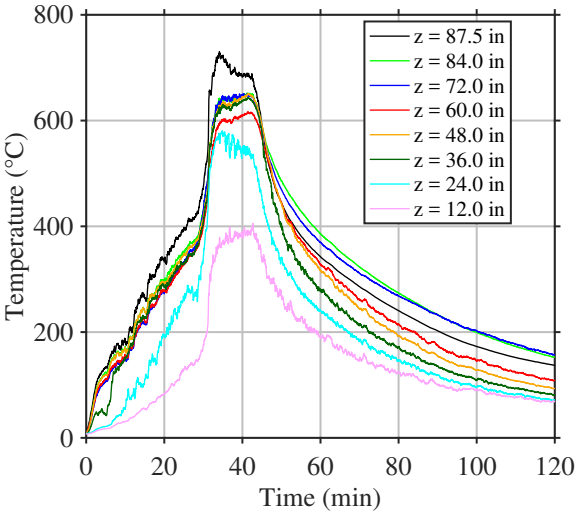


Figure 7.26: Test #3, fire gas temperatures, slice average.

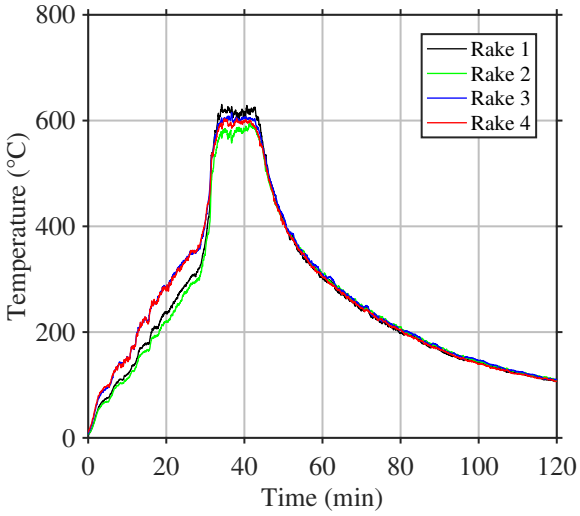


Figure 7.27: Test #3, fire gas temperatures, rake average.

Comparatively little damage of the wall was visible in this test. Figure 7.28 shows that, by the end of the test (after three hours of exposure) the only damage visible to the fire-side gypsum board was paper burnoff, tape falloff at the horizontal joint, and expansion of the horizontal joint; no cracking was visible. The cool-side side did not appear to have undergone any notable decomposition, as is apparent from Figure 7.29.

Temperatures measured on the back of the fire-side gypsum board increased gradually to approximately 120°C after 39.5 min, at which time significant spikes in temperature occurred in all four cavities (Figure 7.30) and at all six heights (Figure 7.31). Certainly this can be partially explained by the calcination reaction described previously; related to this thermochemical change, however, is the physical reduction in size of the panels, referred to as "shrinkage". Joint opening was a direct consequence of shrinkage, and as the joint opened the wall cavity filled with hot gases. By this time the fire was in its decay stage, but the effect is still strongly represented in the measurements at the bottom two height positions, which increased as hot gases entered the wall cavity near the bottom


Figure 7.28: Real wall test #3, fire-side camera, end-of-test.

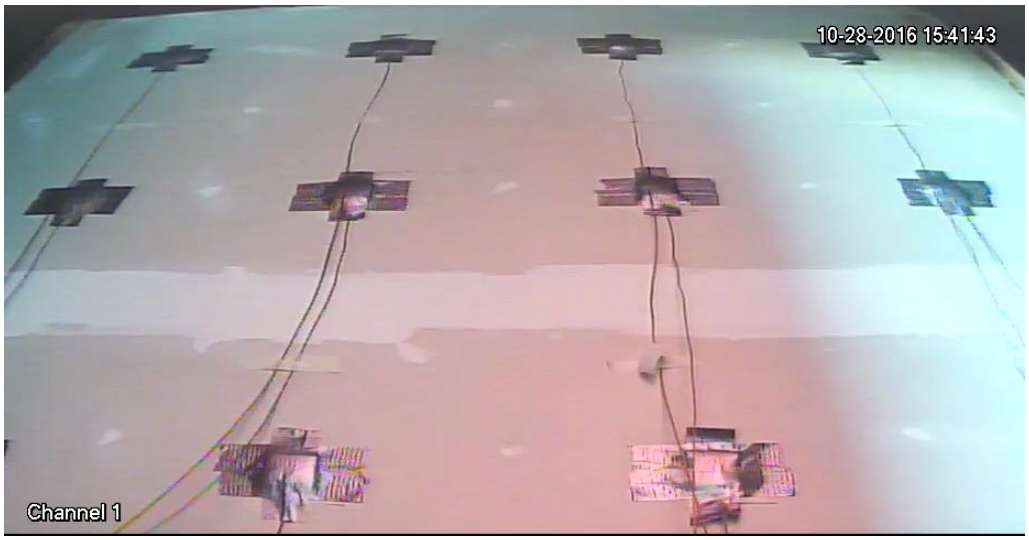


Figure 7.29: Real wall test #3, cool-side camera, end-of-test.

of the wall, at the joint location. While joint opening certainly occurred in previous the tests, as evidenced by video stills, gas propagation to the thermocouples on the back of the fire-side gypsum board was inhibited by the insulation, which was pressed firmly against the gypsum board. In test #3, the hot gases flowed unobstructed through the cavities, causing the observed increase in temperature measured by the thermocouples on the back of the gypsum board.

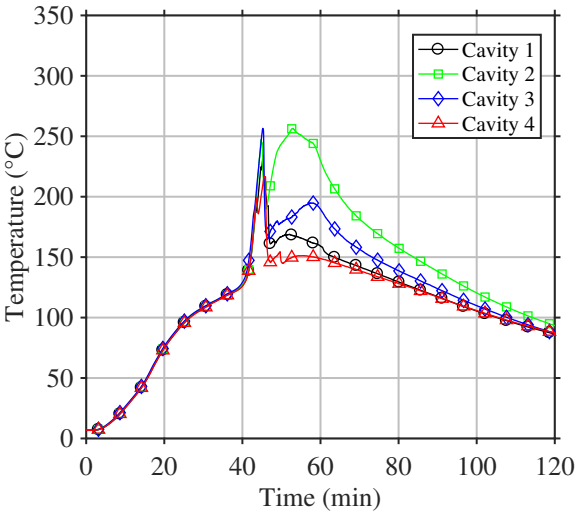


Figure 7.30: Test #3, main wall temperatures, cavity averages.

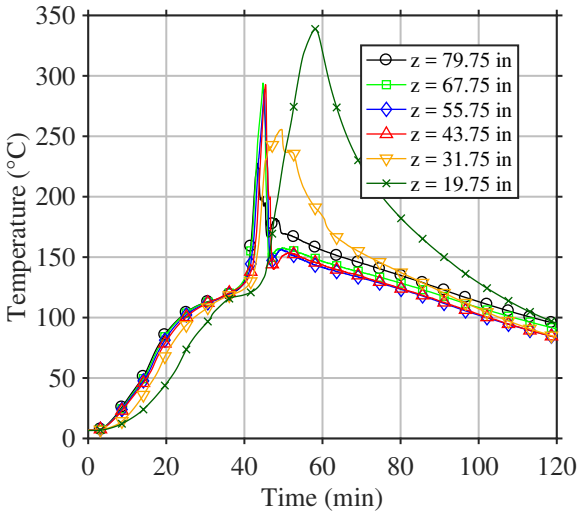


Figure 7.31: Test #3, main wall temperatures, height averages.

Prior to the joint opening (<40 min), a strong vertical temperature gradient had developed from top-to-bottom of the fire-side gypsum board, with virtually no variation across the cavities. This agrees with expectations based on the calculated design fire thermal exposure. After joint opening, temperatures in the middle two cavities were greater than in the side cavities, which can be attributed to the proximity of the fire and remaining fuel to the centre of the wall.

On the unexposed side of the wall, the gypsum board temperature increased to peak values of 90°C after 65–70 min. In the same vein as the fire-side gypsum board, the variation in cool-side gypsum board temperature across the cavities was negligible, while the variation from bottom-to-top was quite discernible. Since the wall did not reach the transition temperature, differences in thermal degradation would not have been realized; the temperature gradients that developed were simply a function of heat transport within the wall cavity. Temperatures measured on the cool-side gypsum board are shown in Figures 7.32 and 7.33.

These results demonstrate that, in fact, the uninsulated wall with firecode gypsum board was able to provide a level of fire protection similar to that of the previously tested insulated walls with standard gypsum board wallcoverings for the fire conditions used here. Compared to the previous two tests, thermal penetration to the unexposed side was actually less (sub-100°C) in the case of the uninsulated wall, although the cooler initial conditions may well have contributed to this observed difference as well.

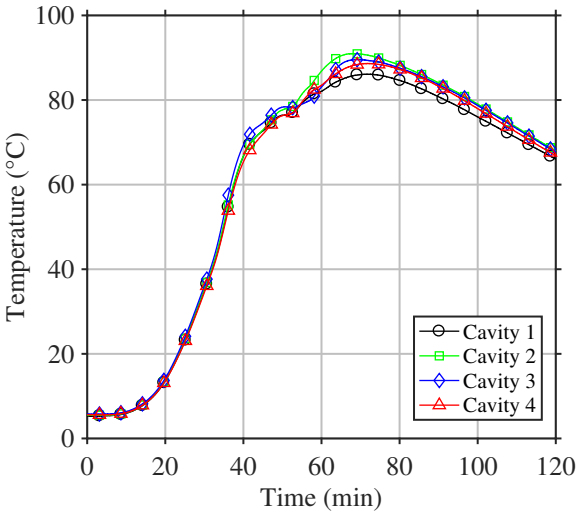


Figure 7.32: Test #3, back wall temperatures, cavity averages.

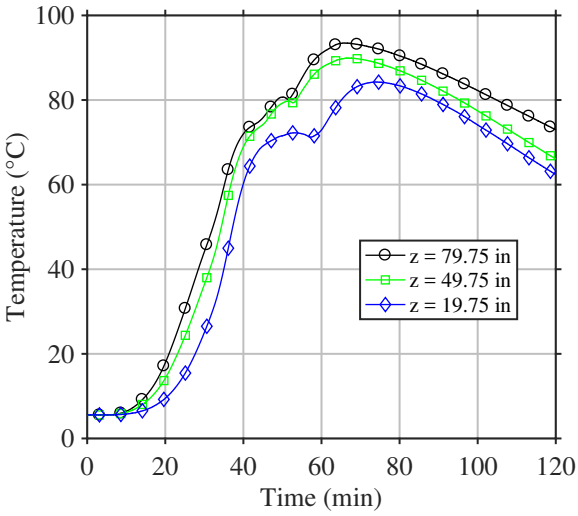


Figure 7.33: Test #3, back wall temperatures, height averages.

### 7.3.4 Test #4 – Stone Wool and Fibreglass Split

The fourth real wall test was a hybrid configuration of the first and second tests — a W1c wall with fibreglass insulation in cavities 1 and 2 (on the left) and stone wool insulation in cavities 3 and 4 (on the right). This test was intended to provide a direct comparison between the response of the two insulation types under conditions encountered during a realistic fire exposure, a topic of practical relevance in the industry [87].

The ambient temperature was quite suitable for this test at 18.5°C. Fire gas temperatures increased to an average value of 700°C near the ceiling during the steady burning period from 27–40 min, a result in reasonable agreement with the design fire. Again, temperature measurements from rakes 1 and 3 were slightly greater than those from rakes 2 and 4 during the steady burning period, a consistent behaviour that can be attributed to the typical ventilation conditions typical for the apparatus given its outdoor location. Slice and rake temperatures are given in Figures 7.34 and 7.35 below.

Figure 7.36 shows the state of the wall after 55.6 min of exposure, at which time the fuel had been mostly consumed and the upper layer gas temperature had reduced to about 420°C. Deep cracking can be observed over the fire-side gypsum board, predominantly in the upper region, though also present in the lower region. Of importance, the wall can be seen to be burning in cavities 1 and 2 (the side with the fibreglass insulation), which is not the case on the stone wool side of the wall. By 107.8 min (Figure 7.37) gypsum

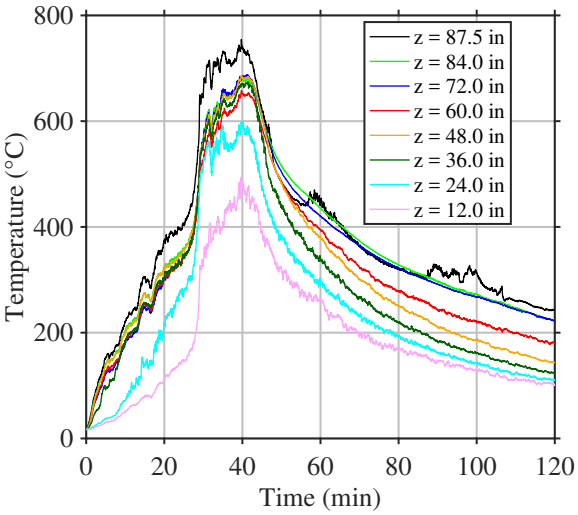


Figure 7.34: Test #4, fire gas temperatures, slice average.

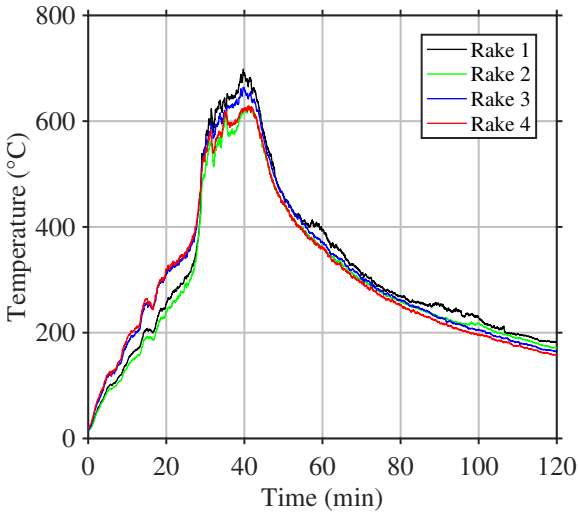


Figure 7.35: Test #4, fire gas temperatures, rake average.

board falloff had occurred at the central cavities (2 and 3) and the fibreglass side of the wall continued to burn even as the fire environment continued to cool. By the end of the test (three hours), almost the entire upper gypsum board panel had fallen off, and significant burning of the exposed fibreglass insulation was apparent. As shown in 7.38 even the studs on the fibreglass side of the wall were more significantly burned than those on the stone wool side.


Figure 7.36: Real wall test #4, fire-side camera, 55.6 min.


Figure 7.37: Real wall test #4, cool-side camera, 107.8 min.

Figure 7.38: Real wall test #4, cool-side camera, end-of-test.

Temperatures on the back of the fire-side gypsum board are plotted in Figures 7.39 and 7.40. For the first 47 min of the test the temperature rise was virtually identical across all four cavities, reaching peak values of 710°C. As the fire decayed and temperatures decreased, cracking of the fire-side gypsum board occurred and the studs and insulation on the left side of the wall (cavities 1 and 2) began to burn; consequently, measured temperatures in these cavities increased above those of the right side. The expected vertical gradient in measured fire-side gypsum board temperatures was also present and clearly defined for a large portion of the test.

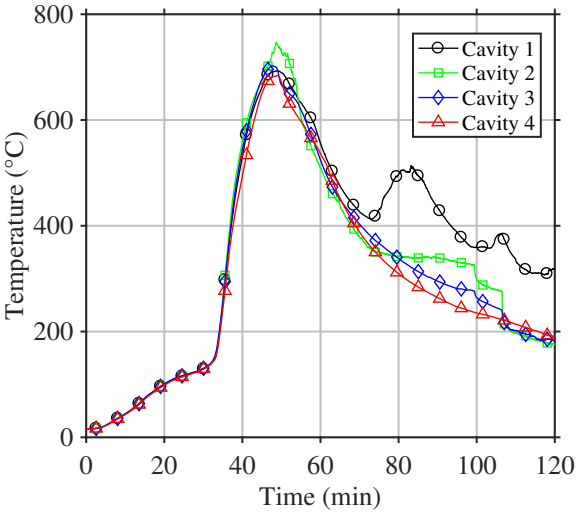


Figure 7.39: Test #4, main wall temperatures, cavity averages.

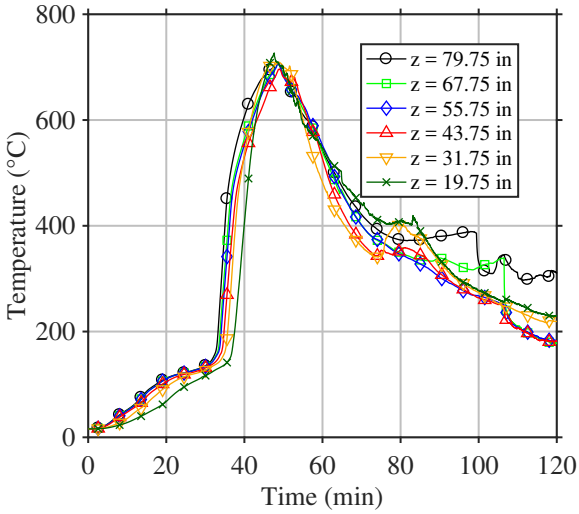


Figure 7.40: Test #4, main wall temperatures, height averages.

On the cool-side gypsum board, temperatures increased above 100°C after 60 min of exposure, at which time temperatures on the left side of the wall increased above those on the right side of the wall; this can be attributed to the burning insulation in these cavities. The temperature-time trace for cavity 1 exhibits a discontinuity at 93 min, which is a result of one of the cool-side thermocouples becoming detached from the surface of the gypsum board. Comparison of Figures 7.41 and 7.42 shows that this was in fact the bottom thermocouple in cavity 1. Before the thermocouple became detached from the wall, the temperature at this location increased dramatically. The suggested cause for this was that a localized region of the fibreglass insulation near this thermocouple location burned atypically, possibly due to non-uniformity of the material (e.g. a concentrated region of binder). Aside from this particular measurement, the trend of hotter temperatures occurring near the top of the wall remained in tact.

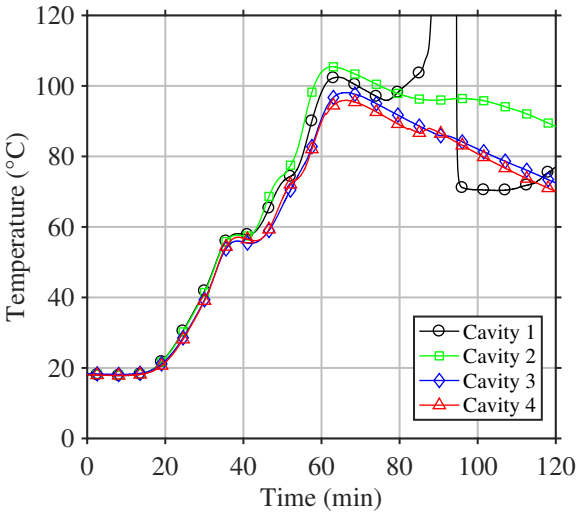


Figure 7.41: Test #4, back wall temperatures, cavity averages.

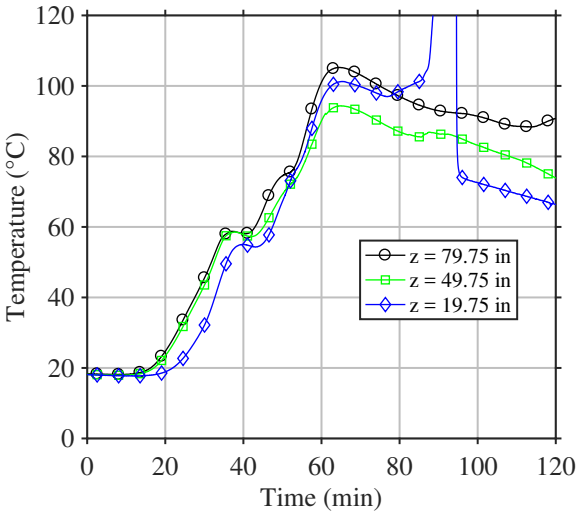


Figure 7.42: Test #4, back wall temperatures, height averages.

### 7.3.5 Test #5 – Stone Wool and Slag Wool Split

The fifth and final test was another hybrid, in this case a W1c wall with slag wool insulation in cavities 1 and 2 (on the left) and stone wool insulation in cavities 3 and 4 (on the right). The slag wool insulation has an R15 rating compared to the R14 of the stone wool, so ostensibly will provide a greater resistance to thermal penetration. Given that both insulations are non-combustible, it was of interest to evaluate whether there would be any difference in the response of the materials to this realistic fire exposure.

Test #5 was conducted in November of 2016, when the ambient temperature was only 7.2°C. It was decided for this test to remove the obstruction panel so that additional video and infrared thermography equipment could be used to assess the state of the degrading wall from the perspective of the compartment doorway. Initially the fire was consistent with test #4, reaching a steady burning period after 26 min and an average gas temperature of 700°C near the ceiling. The duration of the steady burning period was only 10 min compared to the 14 min of test #4, and the compartment upper layer cooled to 160°C after 2 hours compared to 240°C in test #4, so the fire exposure was certainly less severe than in the previous test. As before, rake temperatures were slightly greater on the left side of the compartment. Fire gas temperatures are shown in Figures 7.43 and 7.44 below.

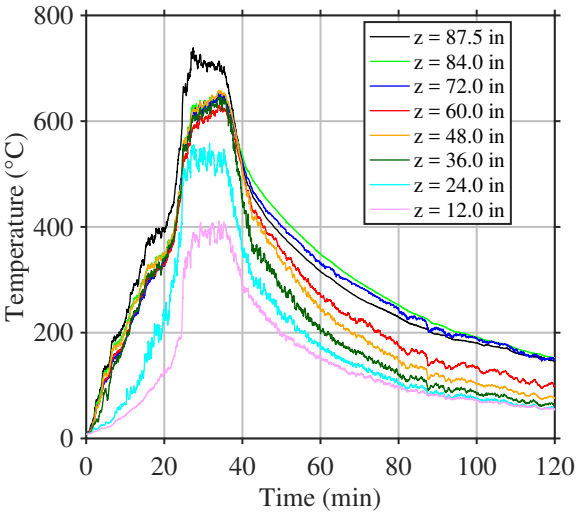


Figure 7.43: Test #5, fire gas temperatures, slice average.

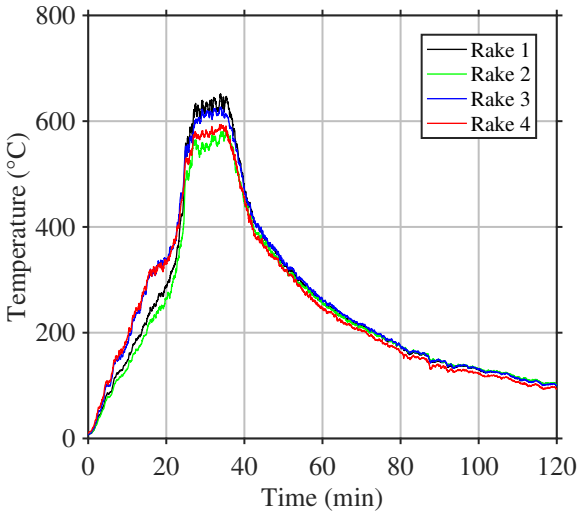


Figure 7.44: Test #5, fire gas temperatures, rake average.

With the obstruction panel removed, the front video camera was placed at the bottom of the doorway and directed upward to cause the entire wall to be in frame. Figure 7.45 shows an interior view of the fire compartment after 27.1 min, at which time the fire was growing rapidly and approaching the transition to steady burning. From this shot the condition of the wall is visible to the sides of the fire plume, and paper burnoff can be discerned.


Figure 7.45: Real wall test #5, fire-side camera, 27.1 min.

Figure 7.46 shows the state of the wall after 68.2 min, by which time the fuel had been almost completely burned. Deep cracking is apparent over the entire wall. By the end of the test, as the fire-side gypsum board and the underlying wood stud frame continued to degrade, a large portion of the fire-side gypsum board fell off. Falloff appeared to be more significant on the right side of the wall (stone wool) compared to the left side of the wall (slag wool), and a stud in the lower-right corner of the wall was actively burning at the end of the test (Figure 7.47). It would appear that the differences in damage observed between the two sides of the wall may be attributable to the different insulations used. One possible explanation is that the slag wool has a lower thermal diffusivity than the stone wool (it is much more dense), meaning that the rate of heat transfer through the insulation was slower in the slag wool, and accordingly less of the binder material was burned. This hypothesis that would require material testing (e.g. differential scanning calorimetry) to confirm. Another possible explanation is that differences in binder agent caused the stone wool insulation to produce more gases than the slag wool insulation as the binder burned off, which would cause greater pressures to develop within cavities, and consequently pushing against the brittle gypsum board. This could be confirmed by study of the mass loss at elevated temperatures (e.g. thermogravimetric analysis).


Figure 7.46: Real wall test #5, fire-side camera, 68.2 min.

To gain an improved insight into the thermal degradation of the wall, an infrared camera was used for this test. It was positioned at the front of the apparatus, so that the test wall was in frame. Unfortunately the device was not capable of capturing the temperature of the wall during the steady burning phase of the fire, due to the intensity


Figure 7.47: Real wall test #5, fire-side camera, end-of-test.

of the flames saturating the camera, but relevant IR images were recorded during the decay phase. The two images shown below correspond to 40 min (Figure 7.48) and 60 min (Figure 7.49) after ignition, respectively. The IR camera proved to be very useful for identifying cracks in the gypsum board. Furthermore, the camera was able to capture the burning of the underlying stud wall frame even as the gypsum board cooled in the decay-phase fire environment.

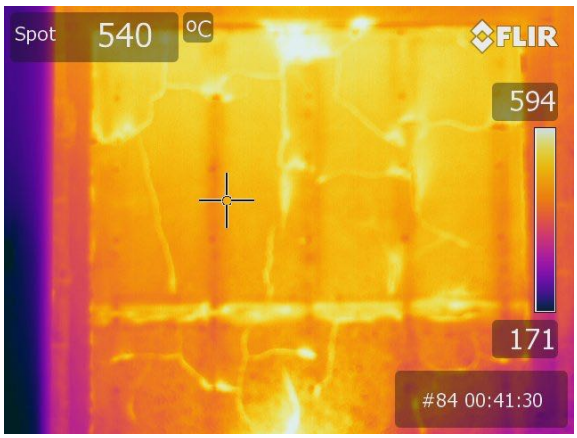


Figure 7.48: Test #5, wall temperatures, infrared camera, 40.0 min.

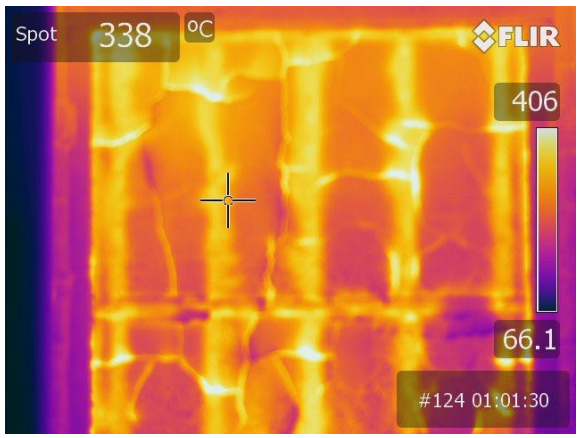


Figure 7.49: Test #5, fire gas temperatures, infrared camera, 60.0 min.

Temperatures on the back of the fire-side gypsum board were consistent across all four cavities for the first 40 min of the test, after which time gypsum board temperatures

were greater in cavities 1 and 2 than in cavities 3 and 4 through to 75 minutes, and finally cavities 3 and 4 were at a greater temperature through to 120 min (Figure 7.50). Greater temperatures in cavities 1 and 2 during the decay phase of the fire is reasonable considering the lesser thermal diffusivity of the slag wool insulation in those cavities. It is not entirely clear why the temperatures on the stone wool side increased at around 75 min, though certainly this could be attributed to crack formation. In consideration of the height-varied results (Figure 7.51), it appears that a crack may have formed near the bottom of the wall at around this time, causing hot gases to enter the wall at this location and consequently the measured temperature to increase.

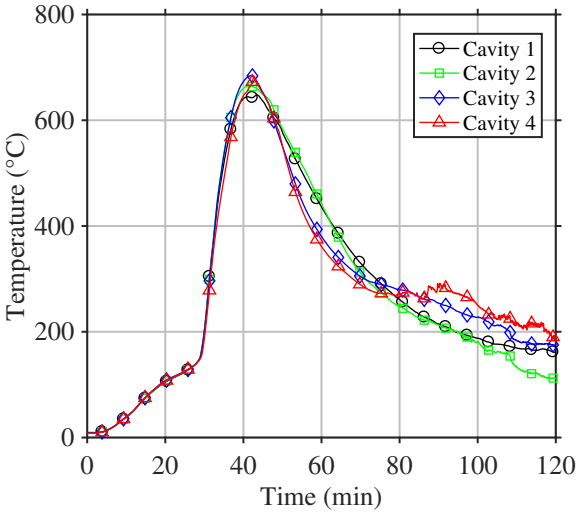


Figure 7.50: Test #5, main wall temperatures, cavity averages.

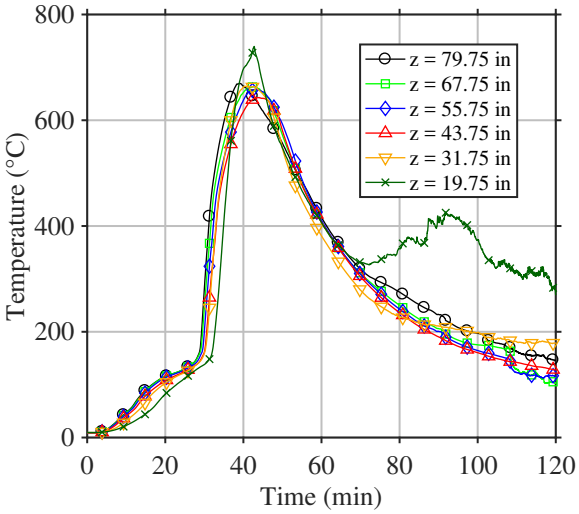


Figure 7.51: Test #5, main wall temperatures, height averages.

On the cool-side of the wall (Figures 7.53 and 7.53), temperatures of cavities 1 and 2 were notably less than those of cavities 3 and 4, with the thermal penetration being delayed by about 10 min at both the 44°C plateau and the 90°C plateau. From these results it is demonstrated that the greater thermal resistance and density of the slag wool did, in fact, delay and even reduce the thermal penetration to the unexposed side of the wall, effectively increasing the fire resistance of the construction assembly. Furthermore, the material appears to have held up better to direct fire attack, given that more of the fire-side gypsum board remained in place in cavities 1 and 2 than in cavities 3 and 4.

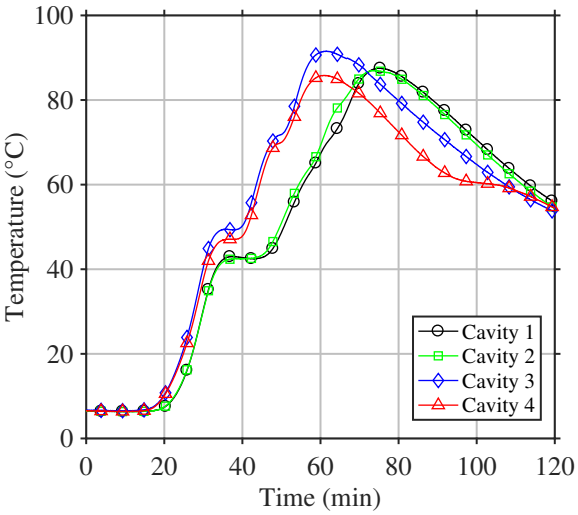


Figure 7.52: Test #5, back wall temperatures, cavity averages.

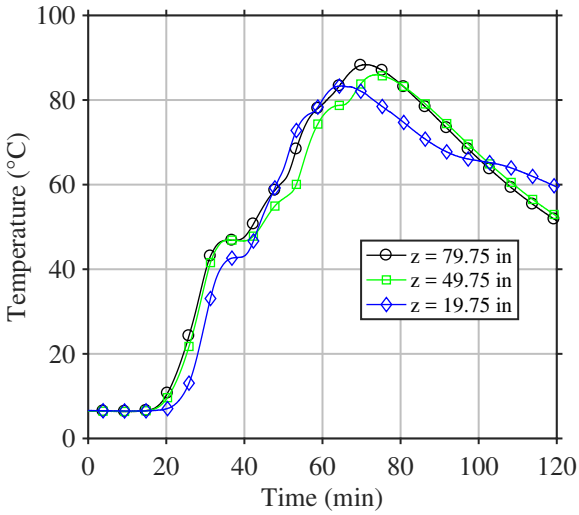


Figure 7.53: Test #5, back wall temperatures, height averages.

### 7.3.6 Summary

The results presented here are a refined subset of the experimental data, which are most useful for classification of the fire environment and identification of thermal degradation phenomena for a wall subject to a realistic fire exposure. For example, slice temperatures of fire gases can be used as direct validation in a fire dynamics model, and the uniformity of rake temperatures demonstrates that, on the whole, compartment gases were evenly stratified. Temperatures of the various wall components may be used not only to identify the impact of damage phenomena on the wall, as was done here, but also to validate the predictions of temperature rise and the occurrence of damage events future models of thermal degradation. The algorithms developed for the generation of this refined subset of data is given in Appendix E, and is of direct utility in the conduct of future tests and in the interpretation of the corresponding data.

Temperature measurements of the unexposed-side gases, surroundings, and frame were also assessed for each test, and generation of these refined data is also included in the aforementioned code. These results were not presented here as they are not conducive to the present analysis and discussion. The main use for these data is in the specification of the edge and unexposed-side boundary conditions in a heat transfer model, as demonstrated in Chapters 5 and 6 for the case of the steel wall, and consequently also in a more complex model of thermal degradation. The complete dataset is available in Appendix D.

Five tests were conducted on walls representative of typical residential construction assemblies, using various combinations of insulation and wallcoverings, as outlined in this section. For each test, thermal degradation phenomena were observed and assessed relative to temperatures measured in the degrading walls, as well as the temperatures measured in the fire compartment, which describe the fire exposure. Some observations of import include:

- the occurrence of gypsum board paper burnoff may be identified by visual and IR cameras, presuming smoke and flame obscuration does not preclude this;
- the occurrence of gypsum board cracking may be identified in a similar manner, and was observed to originate from fixture locations, eventually leading to falloff once chunks of the barrier were no longer mechanically retained;
- it is possible to identify thermal degradation phenomena unique to a particular wall construction, as evidenced by tests #4 and #5, in which portions of the wall containing different types of insulation experienced different temperature increases and damage;
- it is possible to identify the occurrence of known decomposition phenomena (e.g. the burning of insulation binder and the onset of gypsum board calcination) by measurement of temperatures within the wall; and
- the occurrence of gypsum board cracking led to measurable increases in temperatures near the locations of cracks, indicating that mass transport of hot gases at these locations is an important phenomena to be studied in the future.

From these findings, the utility of this new approach in the experimental study of thermal degradation of construction assemblies subject to realistic fire exposure was demonstrated. This new experimental approach may be used, moving forward, to develop a better understanding of large-scale thermal degradation phenomena.

Finally, it is interesting to compare the results present here, for a realistic fire, to those of a traditional furnace test. Such a comparison was made in previous work [69], in which a CAN/ULC S101 fire resistance test was conducted on a similar wall to the W1c, the "EW1". While the W1c partition wall has gypsum board on the unexposed face, the EW1 exterior wall has OSB sheathing and vinyl siding on its unexposed face; stone wool insulation is mandated for such a wall, rather than fibreglass, in order to achieve a 1-hour fire resistance rating. Despite this difference, the exposed-side degradation experienced by the two wall types is expected to be comparable, presuming a consistent fire exposure.

The fire resistance test subjected the wall to a much more severe fire exposure than that of the present work — for example, gas temperatures of 850°C compared to 700°C after 30 min, and 910°C compared to 420°C after 60 min. Accordingly, a greater degree of thermal degradation should be expected in the fire resistance test. Figure 7.36 above shows the exposed side of the W1c in the present work after one hour of exposure, while Figure 7.54 below shows the condition of the exposed side of the EW1 wall at the end of the fire resistance test (one hour).

Figure 7.54: Condition of the EW1 wall in the furnace test after 60 min of exposure.

Perhaps the most striking difference between the two conditions is that the gypsum board had fallen off in the middle region of the wall in the furnace test, and the underlying studs were actively flaming. In comparison, no falloff had occurred in the present work after 60 min, although the central region was heavily cracked, and burning studs were apparent behind the gypsum board. An important observation is that in the furnace test, cracking and falloff occurred uniformly (from the top-to-bottom of the wall) in the central region, and uniformly in the side regions (with minimal cracking). In contrast, in the present work cracking was observed not only in the central region, but also to the

wall extents in the upper region, where it was exposed to the developed hot gas layer. These results reaffirm the finding that thermal degradation in realistic fires, and thus per the methodology outlined in the present work, is very much unique from that of a furnace test. Furthermore, it is apparent that thermal degradation which occurred in the pre-flashover conditions of the present work was significant enough to allow for the investigation of several phenomena of import, despite the lesser severity in comparison to a fire resistance test.

# Chapter 8

# Closure

While the current understanding of the thermal degradation of construction assemblies has evolved sufficiently to support the predictive modelling of the fire resistance of some types of construction assemblies, these capabilities cannot reliably be extended to situations beyond the standard fire resistance furnace exposure. Presently, the most significant limitation in this regard is an inadequate understanding of large-scale thermal degradation phenomena, and how best to represent these phenomena in a predictive capacity. This shortcoming is restrictive to performance-based fire safety engineering analyses, which in many cases would benefit from more advanced models of thermal degradation of construction assemblies in real fires. Development of the next generation of thermal degradation models requires that the phenomena of interest be studied in a controlled setting, representative of a real fire scenario; a compartment fire experiment satisfies this requirement. This thesis presents the development and implementation of such an experiment, as well as a demonstration of its utility in the context of fire resisting compartment partitions exposed to realistic fires.

## 8.1 Conclusions

*1. A selection of relevant experimental techniques for investigating thermal degradation phenomena at the large scale were evaluated.*

A preliminary compartment fire experiment was conducted in order to gain insight into the thermal degradation that a wall would undergo in a realistic building fire, and to develop a set of experimental techniques relevant to the study of large-scale thermal

degradation phenomena. In the experiment, a large-scale wall was exposed to a pre-flashover compartment fire environment. The wall degraded preferentially in the upper region and in regions within close proximity to the fire, where temperatures and heat flux were greatest. This response is expected of a wall in a real building fire (pre-flashover), and is distinct from the response of a wall in a fire resistance test. It was found that the limited number of heat flux sensors used (three, distributed vertically) did not provide an adequate measure of the complex non-uniform fire exposure — an alternative approach was needed. The temperatures of gases near the wall were found to vary predominantly from floor-to-ceiling, despite the proximity to the fuel bed in the central region. This means that a one-dimensional temperature field is suitable for representation of the gas temperatures near the wall, which can be measured as compartment fire slice temperatures. Due to the orientation of the test wall in this experiment, it was not possible to record real-time observations of the degrading wall; while post-test observations are useful, the next phase of the research would incorporate a real-time observation component. The combination of compartment fire experiment with a well-instrumented wall as one of the boundaries of the compartment was demonstrated to be successful in satisfying the intent of facilitating the study of thermal degradation of a wall subject to realistic fire exposures.

*2. A novel apparatus and experimental methodology were developed for studying thermal degradation of fire resisting compartment partitions in realistic fire scenarios.*

Based on the findings of the preliminary work, a large-scale apparatus and test protocol, which are among the main deliverables of the present research, were developed. The apparatus accommodates a large test wall measuring 6 ft by 6 ft (1.83 m by 1.83 m), and has an insulated fire compartment with interior dimensions of 138 in (3.51 m) long, 90 in (2.29 m) wide, and 90 in (2.29 m) high. Ventilation is controlled at the primary compartment doorway, which is located opposite the test wall, affording multiple options for real-time observation. The apparatus was instrumented with 84 thermocouples in order to monitor temperatures of the degrading wall at various positions, temperatures in the compartment fire environment, temperatures around the edges of the wall, and temperatures on the unexposed side of the wall. The data acquisition system used is flexible and can accommodate a large number of additional sensors. The video recording system used can accommodate up to eight high definition cameras simultaneously; two were used here.

*3. A novel experimental method was developed for characterizing the heat exposure over a large area in a compartment fire.*

A fire was designed which involved four wood cribs oriented in-line and ignited on the end furthest from the test wall, such that the fire would grow toward the wall over time. The two-dimensional exposure to the wall from the design fire was evaluated by means of a series of characterization experiments. A custom sensor, a so-called "steel wall", was designed for this purpose, and a heat transfer model incorporating Kalman filtering optimization was developed and used to deduce the exposure conditions. A series of five repeat tests was conducted in order to characterize the fire exposure. On average, the upper layer gas temperatures were found to increase to approximately 635°C after 30 min, at which time the incident heat flux to the centre of the wall was approximately 55 $kW \cdot m^{-2}$. The distribution of heat flux over the wall varied significantly over time, predominantly in the vertical dimension at the beginning of the test, and becoming very non-uniform as the fire approached the wall. Thus, the experiment satisfies the stated objective of producing a realistic fire exposure.

*4. A series of tests were conducted on as-built fire resisting compartment partitions, and the utility of this novel experiment in facilitating the detailed study of large-scale thermal degradation phenomena was demonstrated.*

Five experiments were conducted on various residential wall construction assemblies. The materials used included wood studs, two types of gypsum board (lightweight and firecode), and three types of insulation (fibreglass, stone wool, and slag wool). Procedures for mounting and construction of the walls, installation of temperature probes, and conduct of the experiments are documented; the methodology is reproducible and may be adopted in future work. Temperature measurements within the wall cavities reflected the expected behaviour of the constituent materials as they thermally degraded. Video was recorded in each experiment, and the occurrence of large-scale thermal degradation phenomena of interest was captured in each test. Infrared thermography was also utilized, and found to be helpful in identifying phenomena such as paper burn-off and crack formation that may not be visible to the naked eye at first; a shortcoming, however, is that the fire can obstruct the camera's line of sight, saturating the sensor. The results presented demonstrate the utility of this new experimental approach in facilitating the study of thermal degradation of construction assemblies subject to realistic fire exposures, thereby achieving a positive outcome with respect to the stated objective of this research. This new approach may be used to develop a better understanding

of the large-scale phenomena of relevance to the thermal degradation of construction assemblies. Furthermore, a large set of experimental data from experiments involving real construction assemblies has been generated and made available for use in comparison to, or for validation of, thermal degradation models. These data may be obtained by accessing the digital version of this dissertation.

## 8.2 Recommendations

*1. Utilize the data measured in these experiments to support development and validation of the next generation of fire models.*

Future research will work toward the development of a comprehensive model of compartment fire dynamics and thermal degradation of compartment boundaries. Three levels of validation data are required in support of this work:

- data from thermal decomposition experiments, e.g. thermophysical properties;
- data from compartment fire experiments, e.g. gas temperatures and heat flux to the compartment boundaries; and
- data from thermal degradation experiments, e.g. fire gas temperatures, temperatures within a thermally degrading compartment boundary, and the onset of damage phenomena.

The first level of validation data can be satisfied in-part by the present collection of pertinent literature, and is an active area of research (e.g. pyrolysis modelling). The "steel wall" test data from the present work, for which the compartment boundaries were non-degrading, is suitable for use in the validation of temperature and heat flux predictions of a compartment fire model. Furthermore, the data from the five "real wall" tests in the present work is suitable for validation of thermal degradation models for compartment boundaries. It is recommended that such next-generation models first establish a good treatment of compartment fire dynamics coupled with 1D (in-depth) thermal degradation (e.g. the middle of a wall cavity).

*2. Conduct a calorimetric assessment of the fuel source for input into fire models.*

The fuel source used in the present work, wood cribs, was previously evaluated using an oxygen consumption calorimeter to measure the heat release rate and effective heat of combustion of a typical crib. Using this information, the mass of each crib involved, and

event tables, it is trivial to produce an effective heat release rate curve which describes the overall heat generation in a fire test over time, however these curves would require validation. It is recommended to validate the heat content of the fires in the present work by conducting calorimeter tests on cribs in the same configuration as used here — since the fire was fuel-controlled, the calorimeter should give a good measure of the total heat release rate in the compartment fire. If a different fuel source were to be used, in particular one that causes the compartment to become underventilated, an alternative method for calorimetric assessment would have to be adopted. One method would be to install load cells within the compartment to measure the rate of mass loss of the fuels over time. These devices must not be allowed to heat significantly, so intense fires (in particular those of long duration) would necessitate some form of cooling as well.

*3. Conduct additional experiments which utilize different fuel types and configurations.*

While the pre-flashover fires used in the present work were of sufficient size to produce thermal degradation phenomena of interest, it can be argued that, despite the lower probability of the occurrence of post-flashover building fires, the post-flashover fire is of great importance from a fire safety perspective. The experiment can easily be modified to incorporate fires of greater intensity by modifying the fuel load. It was shown in the present work that control of fuel package configuration allows for control of fire growth rates — this same concept can be applied to achieve fires of greater intensity and longer duration. Furthermore, it might be reasonable to adopt different fuel types, such as plastics and textiles as would commonly be found in structures. Regardless of the fuel type, it is strongly recommended that tight control of the moisture content of the fuel source should be ensured in order to improve test-to-test consistency.

*4. Refine the ventilation procedure and implement flow measurement.*

The procedure of ventilation control adopted in the present work involved blocking the compartment opening in such a manner that the flow symmetry would not be impacted (any more than would be the case in the absence of the device). A consequence of this style of flow restriction was that the exposed-side camera's view of the wall became obstructed. Also, the presence of the device blocked the doorway such that a symmetric configuration of bi-directional probes (for measurement of gas velocity entering and exiting the compartment) was not possible. These are very useful measurements, so it is recommended that alternative means of ventilation control and instrumentation at the compartment opening be adopted in the future. Furthermore, it is recommended that baffles be installed at the compartment opening to minimize the impact of crosswinds.

*5. Investigate in detail the phenomenon of gypsum board crack formation.*

Of the phenomena identified in the present work, gypsum board crack formation occurred consistently in all tests by propagation from fixture locations. Being the primary form of protection of the wall from the fire, it is critical to understand what drives this phenomenon, as well as the impact on heat and mass transport into the wall. Therefore it is recommended that crack formation be the first damage phenomena to be studied in detail, with the goal of ultimately developing a predictive model for the process. This can begin with the mechanically constrained unloaded scenario (as in the present work), and eventually work toward loaded scenarios as well.

# References


[1] Dougal Drysdale. *An Introduction to Fire Dynamics*. John Wiley & Sons, Chichester, West Sussex, England, 3rd edition, 2011.

[2] Björn Karlsson and James G. Quintiere. *Enclosure Fire Dynamics*. CRC Press LLC, Boca Raton, Florida, 1999.

[3] *National Building Code of Canada 2010 (NBC)*. National Research Council Canada, Ottawa, ON, 2010.

[4] CAN/ULC-S114-05 Standard Method of Test for Determination of Non-Combustibility in Building Materials. Underwriters Laboratories of Canada, Ottawa, ON, 2005.

[5] ASTM E119-16a Standard Test Methods for Fire Tests of Building Construction and Materials. ASTM International, West Conshohocken, PA, 2016.

[6] CAN/ULC-S101-07 Standard Methods of Fire Endurance Tests of Building Construction and Materials. Underwriters Laboratories of Canada, Ottawa, ON, 2007.

[7] J. P. Hidalgo, Stephen Welch, and J. L. Torero. Performance criteria for the fire safe use of thermal insulation in buildings. *Construction and Building Materials*, 100: 285–297, 2015. doi: 10.1016/j.conbuildmat.2015.10.014.

[8] ASTM E90-09 Standard Test Method for Laboratory Measurement of Airborne Sound Transmission Loss of Building Partitions and Elements. ASTM International, West Conshohocken, PA, 2009.

[9] ASTM E413-10 Classification for Rating Sound Insulation. ASTM International, West Conshohocken, PA, 2010.

[10] *Ontario Building Code, Supplementary Standard SB-12 Energy Efficiency for Housing, March 15, 2013 update*. Government of Ontario, Ministry of Municipal Affairs and Housing, Building and Development Branch, Ottawa, ON, 2006.

[11] V. K. R. Kodur and T. Z. Harmathy. Properties of building materials. In *SFPE Handbook of Fire Protection Engineering*, Chapter 1-10, pages 167–195. National Fire Protection Association, Quincy, MA, 4th edition, 2008.

[12] M. A. Dietenberger and L. E. Hasburgh. Wood products: Thermal degradation and fire. *Reference Module in Materials Science and Materials Engineering*, 2016. doi: 10.1016/B978-0-12-803581-8.03338-5.

[13] M. A. Sultan, G. D. Lougheed, R. C. Monette, J. W. MacLaurin, and E. M. Denham. Temperature Measurements in Full-Scale Insulated Gypsum Board-Protected Wall Assemblies with Resilient Channels. Report 676, National Research Council of Canada, Ottawa, ON, 1994.

[14] M. A. Sultan, G. D. Lougheed, J. W. MacLaurin, and E. M. Denham. Temperature Measurements in Fire Resistance Tests on Insulated and Non-Insulated Small-Scale Wall Assemblies Protected by Type X Gypsum Board. Report 677, National Research Council of Canada, Ottawa, ON, 1994.

[15] Keith D. Calder. The Historical Development of the Building Size Limits in the National Building Code of Canada. Technical Report 912046, Sereca Consulting Inc., Richmond, BC, 2015.

[16] A. A. Stec and T. R. Hull. Assessment of the fire toxicity of building insulation materials. *Energy and Buildings*, 43(2–3):498–506, 2011. doi: 10.1016/j.enbuild.2010.10.015.

[17] Stefan Kowatsch. Mineral Wool Insulation Binders. In *Phenolic Resins: A Century of Progress*, pages 209–242. Springer Berlin Heidelberg, Berlin, Heidelberg, 2010. doi: 10.1007/978-3-642-04714-5_10.

[18] ASTM E136-16a Standard Test Method for Behavior of Materials in a Vertical Tube Furnace at 750°C. ASTM International, West Conshohocken, PA, 2016.

[19] ASTM E84-16 Standard Test Method for Surface Burning Characteristics of Building Materials. ASTM International, West Conshohocken, PA, 2016.

[20] An assessment of thermal insulation materials and systems for building applications. Technical Report BNL-50862, UC-95d, Brookhaven National Laboratory, 1978.

[21] BS EN 13501-1:2007 Fire classification of construction products and building elements – Classification using data from reaction to fire tests. British Standards Institution, London, UK, 2007.

[22] P. Keerthan and M. Mahendran. Thermal performance of composite panels under fire conditions using numerical studies: Plasterboards, rockwool, glass fibre and cellulose insulations. *Fire Technology*, 49(2):329–356, 2012. doi: 10.1007/s10694-012-0269-6.

[23] Nicole Nagy, Matthew J. DiDomizio, Elizabeth J. Weckman, and Richard Roos. Determination of thermochemical properties of stone wool insulation materials. In *Fire and Materials 2017 – 15th International Conference*, pages 491–502, London, UK, 2017. Interscience Communications Limited.

[24] Benedikt Weber. Heat transfer mechanisms and models for a gypsum board exposed to fire. *International Journal of Heat and Mass Transfer*, 55(5-6):1661–1678, 2012. doi: 10.1016/j.ijheatmasstransfer.2011.11.022.

[25] L. Andersson and B. Jansson. Analytical Fire Design with Gypsum – A Theoretical and Experimental Study. Technical report, Institute of Fire Safety Design, Lund, Sweden, 1987.

[26] A. W. Groves. Gypsum and Anhydrite, Overseas Geological Surveys. Technical report, Mineral Resources Division, Her Majesty's Stationary Office, London, UK, 1958.

[27] M. A. Sultan. A model for predicting heat transfer through noninsulated unloaded steel-stud gypsum board wall assemblies exposed to fire. *Fire Technology*, 32(3): 239–259, 1996. doi: 10.1007/BF01040217.

[28] EN 1993-1-2:2005 Eurocode 3 – Design of steel structures. Part 1-2: General rules – Structural fire design. European Committee for Standardization, 2005.

[29] Seul-Hyun Park, Samuel L. Manzello, Dale P. Bentz, and Tensei Mizukami. Determining thermal properties of gypsum board at elevated temperatures. *Fire and Materials*, 34(5):237–250, 2009. doi: 10.1002/fam.1017.

[30] N. Bénichou and M. A. Sultan. Thermal properties of lightweight-framed construction components at elevated temperatures. *Fire and Materials*, 29(3):165–179, 2005. doi: 10.1002/fam.880.

[31] N. Bénichou and M. A. Sultan. Fire resistance performance of lightweight wood-framed assemblies. Nrcc-43382, National Research Council of Canada, 2000.

[32] Hisa Takeda and J. R. Mehaffey. WALL2D: A model for predicting heat transfer through wood-stud walls exposed to fire. *Fire and Materials*, 22(4):133–140, 1998. doi: 10.1002/(SICI)1099-1018(1998070)22:4⟨133::AID-FAM642⟩3.0.CO;2-L.

[33] Samuel L. Manzello, Richard G. Gann, Scott R. Kukuck, Kuldeep Prasad, and Walter W. Jones. Performance of a non-load-bearing steel stud gypsum board wall assembly : Experiments and modelling. *Fire and Materials*, 31(5):297–310, 2007. doi: 10.1002/fam.939.

[34] Nicolas Bal and Guillermo Rein. On the effect of inverse modelling and compensation effects in computational pyrolysis for fire scenarios. *Fire Safety Journal*, 72:68–76, 2015. doi: 10.1016/j.firesaf.2015.02.012.

[35] C F Fischl. Heat conduction through dry walls. *Fire Research Notes*, 131, 1955.

[36] Lie Tiam Tjoan. Heat conduction through walls during fire. *Journal of Heat Transfer*, 83(4):508–510, 1961. doi: 10.1115/1.3683680.

[37] Kazunori Harada and Toshio Terai. Heat and mass transfer in the walls subjected to fire. *International Journal for Fire Science and Technology*, 17(1):70–77, 1997. doi: 10.3210/fst.17.70.

[38] E. C. Y. Lin and J. R. Mehaffey. Modeling the fire resistance of wood-frame office buildings. *Journal of Fire & Flammability*, 15(4):308–338, 1997. doi: 10.1177/073490419701500403.

[39] R. D. Peacock, P. A. Reneke, and G. P. Forney. CFAST – Consolidated Model of Fire Growth and Smoke Transport (Version 6) User's Guide. NIST Special Publication, National Institute of Standards and Technology, Gaithersburg, MD, 2013.

[40] R. D. Peacock, G. P. Forney, and P. A. Reneke. CFAST – Consolidated Model of Fire Growth and Smoke Transport (Version 6) Technical Reference Guide. NIST

Special Publication, National Institute of Standards and Technology, Gaithersburg, MD, 2013.

[41] James G. Quintiere. Fundamentals of enclosure fire "zone" models. *Journal of Fire Protection Engineering*, 1(3):99–119, 1989. doi: 10.1177/104239158900100302.

[42] P Clancy. Advances in modelling heat transfer through wood framed walls in fire. *Fire and Materials*, 25(6):241–254, 2001. doi: 10.1002/fam.773.

[43] Marc L. Janssens. Modeling of the thermal degradation of structural wood members exposed to fire. *Fire and Materials*, 28(2–4):199–207, 2004. doi: 10.1002/fam.848.

[44] Hisa Takeda and F. Kahsay. The effects of insulation on the fire resistance of wood-stud walls. In *World Conference on Timber Engineering 2000*, Whistler, BC, 2000. University of British Columbia.

[45] Hisa Takeda. A model to predict fire resistance of non-load bearing wood-stud walls. *Fire and Materials*, 27(1):19–39, 2003. doi: 10.1002/fam.816.

[46] Hisa Takeda. Fire resistance of wood-framed exterior walls: The effect of an external air cavity and external insulation. In *Fire Safety Science 7*, pages 1123–1134. International Association for Fire Safety Science, 2003. doi: 10.3801/IAFSS.FSS.7-1123.

[47] Hisa Takeda. Fire Resistance Of Exterior Walls: Model And Full-scale Test. In *Fire Safety Science 8*, pages 291–302. International Association for Fire Safety Science, 2005. doi: 10.3801/IAFSS.FSS.8-291.

[48] Hisa Takeda and Leslie R. Richardson. Fire Resistance of Wood-Framed Exterior Walls: Model and Full-Scale Test. In *World Conference on Timber Engineering 2004*, pages 347–352, Lahti, Finland, 2004. University of Ljubljana.

[49] P Clancy and S A Young. Full scale experiments for evaluating theoretical fire wall models. *Fire and Materials*, 28(6):431–458, 2004. doi: 10.1002/fam.862.

[50] Samuel L Manzello, Richard G Gann, Scott R Kukuck, Kuldeep Prasad, and Walter W Jones. Real fire performance of partition assemblies. *Fire and Materials*, 29(6):351–366, 2005. doi: 10.1002/fam.892.

[51] Scott R Kukuck. Heat and Mass Transfer Through Gypsum Partitions Subjected to Fire Exposures. NISTIR 7461, National Institute of Standards and Technology, Gaithersburg, MD, 2009.

[52] S. T. Craft, B. Isgor, J. Mehaffey, and G. Hadjisophocleous. Modelling Heat And Mass Transfer In Wood-Frame Floor Assemblies Exposed To Fire. In *Fire Safety Science 9*, pages 1303–1314. International Association For Fire Safety Science, 2008. doi: 10.3801/IAFSS.FSS.9-1303.

[53] S. T. Craft. *CUWoodFrame – A Heat and Mass Transfer Model for Light-frame Wood Floors Exposed to Fire*. PhD thesis, Carleton University, Ottawa, ON, 2009.

[54] S. T. Craft, B. Isgor, G. Hadjisophocleous, and J. R. Mehaffey. Predicting the thermal response of gypsum board subjected to a constant heat flux. *Fire and Materials*, 32(6):333–355, 2008. doi: 10.1002/fam.971.

[55] Sheeba Vilakkathu Saidu. Fire Performance of Materials – Wood , Gypsum Board , Limestone , Concrete and Steel. Master's thesis, Carleton University, Ottawa, ON, 2011.

[56] Charles T. Aire. Experimental and numerical modeling of heat transfer in wall assemblies. Master's thesis, University of Saskatchewan, Saskatoon, SA, 2014.

[57] Charles T. Aire, Matthew J. DiDomizio, David A. Torvi, Elizabeth J. Weckman, and Richard Roos. Heat transfer in small-scale models of exterior wall designs. In *Fire and Materials 2015 – 14th International Conference*, pages 652–666, London, UK, 2015. Interscience Communications Limited.

[58] Ling Lu, O. B. Isgor, and George Hadjisophocleous. A computer model for light-frame wood floor assemblies under fire attack. In *World Conference on Timber Engineering 2010*, pages 2831–2839, Riva del Garda, Italy, 2010.

[59] O. A. Ezekoye. Applications of heat transfer fundamentals to fire modeling. *Journal of Thermal Science and Engineering Applications*, 5(2):021009–021009–11, 2013. doi: 10.1115/1.4024015.

[60] Amanda J. Klinck. An Experimental Investigation of the Fire Characteristics of the University of Waterloo Burn House Structure. Master's thesis, University of Waterloo, Waterloo, ON, 2006.

[61] Fiberfrax Blanket and Mat Products. Unifrax I LLC, `http://www.unifrax.com/products/blankets/fiberfrax-ceramic-fiber-blanket/`, 2010. Online; accessed 2014-06-29.

[62] Ethernet/Serial Interfaces for Compact FieldPoint. National Instruments, http://www.ni.com/pdf/products/us/2005_6072_161_101_d.pdf, 2006. Online; accessed 2017-02-02.

[63] Thermocouple and RTD Modules for Compact FieldPoint. National Instruments, http://www.ni.com/pdf/products/us/cat_cfp_fp_thermocouple_rtd.pdf, 2009. Online; accessed 2017-02-02.

[64] Analog Input Modules for Compact FieldPoint and FieldPoint. National Instruments, http://www.ni.com/pdf/products/us/cpf_fp_ai.pdf, 2003. Online; accessed 2017-02-02.

[65] Matthew R Obach. *Effects of initial fire attack suppression tactics on the firefighter and compartment environment*. PhD thesis, University of Waterloo, 2011.

[66] Charles T. Aire, David A. Torvi, and Elizabeth J. Weckman. Heat transfer in cone calorimeter tests of generic wall assemblies. In *ASME 2013 International Mechanical Engineering Congress and Exposition*, volume 8A, page V08AT09A019, San Diego, CA, 2013. ASME. doi: 10.1115/IMECE2013-63981.

[67] Charles T. Aire, David A. Torvi, and Elizabeth J. Weckman. Finite difference model of heat transfer in small-scale models of generic wall assemblies. In *Combustion Institute Canadian Section Spring 2014 Technical Meeting*, Windsor, ON, 2014. Combustion Institute.

[68] James G. Quintiere. Compartment fire modelling. In *SFPE Handbook of Fire Protection Engineering*, Chapter 3-5, pages 195–203. National Fire Protection Association, Quincy, MA, 4th edition, 2008.

[69] Matthew J. DiDomizio, Elizabeth J. Weckman, and Richard Roos. Experimental evaluation of damage and thermal penetration in residential walls under realistic fire loads. In *Proceedings of Combustion Institute – Canadian Section Spring Technical Meeting*, pages FS24–FS29, University of Saskatchewan, 2015.

[70] J. B. Fang. Repeatability of large-scale room fire tests. *Fire Technology*, 17(1):5–16, 1981. doi: 10.1007/BF03377280.

[71] ISO 9705-1:2016 Reaction to fire tests – Room corner test for wall and ceiling lining products – Part 1: Test method for a small room configuration. International Organization for Standardization, Geneva, Switzerland, 2016.

[72] Ronald D. Lucier. Understanding the challenges of surface temperature measurement using thermocouples. Technical report, FLIR Systems, Inc., 2011. URL: http://www.flir.com/science/blog/details/?ID=75018.

[73] N. R. Keltner and J. L. Moya. Defining the thermal environment in fire tests. *Fire and Materials*, 14(4), 1989. doi: 10.1002/fam.810140403.

[74] ASTM E457-08 Standard Test Method for Measuring Heat-Transfer Rate Using a Thermal Capacitance (Slug) Calorimeter. ASTM International, West Conshohocken, PA, 2015.

[75] ASTM E459-05 Standard Test Method for Measuring Heat Transfer Rate Using a Thin-Skin Calorimeter. ASTM International, West Conshohocken, PA, 2016.

[76] J. Zhang and Michael A Delichatsios. Determination of the convective heat transfer coefficient in three-dimensional inverse heat conduction problems. *Fire Safety Journal*, 44(5):681–690, 2009. doi: 10.1016/j.firesaf.2009.01.004.

[77] Frank P. Incropera, David P. DeWitt, Theodore L. Bergman, and Adrienne S. Lavine. *Fundamentals of Heat and Mass Transfer*. John Wiley & Sons, 6 edition, 2006.

[78] Solid Silicone Sheet – THT High Temperature Sheeting. Silex Silicone, http://www.silex.co.uk/media/29226/Solid-sheet-THT-40-70-spec-2013.pdf, 2015. Online; accessed 2017-04-07.

[79] Fiberfrax Durablanket S: Technical Data Sheet A1-004. Insulcon, http://www.insulcon.com/products/fibre-products/blankets/, 2009. Online; accessed 2016-09-09.

[80] Matthew Redmond and A. J. Mastropietro. Thermophysical and optical properties of materials considered for use on the ldsd test vehicle. In *ICES 2015 - Proceedings of the 45th International Conference on Environmental Systems*, Bellevue, WA, 2015. Texas Tech University.

[81] Michael F. Modest. *Radiative Heat Transfer*. Academic Press, Oxford, UK, 3rd edition, 2013.

[82] N. A. Kotey, J. L. Wright, and M. R. Collins. Determining longwave radiative properties of flat shading materials. In *33rd Annual SESCI Conference*, Fredericton, NB, 2008. Solar Energy Society of Canada.

[83] Mohinder S. Grewal and Angus P. Andrews. *Kalman Filtering: Theory and Practice Using MATLAB®*. John Wiley & Sons, Inc., Hoboken, NJ, 4th edition, 2014. doi: 10.1002/9781118984987.

[84] ASTM E3057-16 Standard Test Method for Measuring Heat Flux Using Directional Flame Thermometers with Advanced Data Analysis Techniques. ASTM International, West Conshohocken, PA, 2016.

[85] Roger A. Horn and Charles R. Johnson. *Matrix Analysis*. Cambridge University Press, 2nd edition, 2012. ISBN 978-0521548236.

[86] Ron A. Wallis. *The thermal performance of an ultra high power (UHP) electrical furnace for the reheating of steel slabs*. PhD thesis, Cranfield Institute of Technology, Cranfield, UK, 1989.

[87] Matthew J. DiDomizio, Elizabeth J. Weckman, and Richard Roos. Decomposition of large-scale multicomponent construction assemblies exposed to real fires. In *Fire and Materials 2017 – 15th International Conference*, pages 528–542, London, UK, 2017. Interscience Communications Limited.

[88] Dougal Drysdale. Thermochemistry. In *SFPE Handbook of Fire Protection Engineering*, Chapter 1-5, pages 91–100. National Fire Protection Association, Quincy, MA, 4th edition, 2008.

[89] P. H. Thomas. Testing products and materials for their contribution to flashover in rooms. *Fire and Materials*, 5(3):103–111, 1981. doi: 10.1002/fam.810050305.

[90] Daniel T. Gottuk and Brian Y. Lattimer. Effect of combustion conditions on species production. In *SFPE Handbook of Fire Protection Engineering*, Chapter 2-5, pages 67–95. National Fire Protection Association, Quincy, MA, 4th edition, 2008.

# Appendix A

# Construction Drawings

This appendix contains Portable Document Format (PDF) files of the construction drawings for the fire test apparatus (`dwg-fire-test-apparatus.pdf`) and for the steel wall sensor (`dwg-steel-wall-sensor.pdf`). The drawings were created using Autodesk Inventor 2016, and exported to the PDF format. The page size is ANSI C landscape (22 in $\times$ 17 in).

If you accessed this thesis from a source other than the University of Waterloo, you may not have access to these files. You may access them by searching for this thesis on `https://uwspace.uwaterloo.ca/UWSpace`.

# Appendix B

# Instrumentation

## B.1 Real Wall Thermal Degradation Experiments

Table B.1 lists and provides descriptions of all data acquisition channels used in the fire test apparatus for the real wall thermal degradation experiments. Headers in the raw data files are consistent with the naming convention used here.

Figure B.1 shows a top-view schematic of sensor locations through the entire apparatus. Additional details are provided in Figures B.2 (sensors within the stud cavities) and B.3 (sensors on the unexposed side of the wall). DAQ references in these figures correspond to those given in Table B.1.

Figure B.4 shows a top-view schematic of the fire test apparatus with global dimensions indicated. The height of the fire compartment is 90 in (brick floor to insulated ceiling), while the height of the transition room is 93.5 in (brick floor to steel ceiling).

Figure B.5 shows the instrumentation cable routing used in the fire test apparatus. Red lines represent thermocouple cables connecting to the DAQ1 data acquisition board, green lines represent thermocouple cables connecting to the DAQ2 data acquisition board and blue lines represent video cables.

Figure B.6 shows the locations of sensors installed in the fire test apparatus, including dimensions. Red circles represent thermocouple locations, and blue circles represent video camera locations. Height dimensions relative to the compartment floor are provided in Tables B.1–B.4.

Figure B.7 shows the locations of sensors on the wall (4-cavity stud wall), including

dimensions. In the figure, red circles represent thermocouples installed within stud cavities, and green triangles represent thermocouples installed on the unexposed side of the wall. Height dimensions relative to the compartment floor are provided in Table B.5.

| DAQ | MODULE | CHANNEL | DESCRIPTION |
|---|---|---|---|
| 1 | 1 | 0 | Fire compartment, TC rake 1, TC0 (top). |
| 1 | 1 | 1 | Fire compartment, TC rake 1, TC1. |
| 1 | 1 | 2 | Fire compartment, TC rake 1, TC2. |
| 1 | 1 | 3 | Fire compartment, TC rake 1, TC3. |
| 1 | 1 | 4 | Fire compartment, TC rake 1, TC4. |
| 1 | 1 | 5 | Fire compartment, TC rake 1, TC5. |
| 1 | 1 | 6 | Fire compartment, TC rake 1, TC6. |
| 1 | 1 | 7 | Fire compartment, TC rake 1, TC7 (bottom). |
| 1 | 2 | 0 | Fire compartment, TC rake 2, TC0 (top). |
| 1 | 2 | 1 | Fire compartment, TC rake 2, TC1. |
| 1 | 2 | 2 | Fire compartment, TC rake 2, TC2. |
| 1 | 2 | 3 | Fire compartment, TC rake 2, TC3. |
| 1 | 2 | 4 | Fire compartment, TC rake 2, TC4. |
| 1 | 2 | 5 | Fire compartment, TC rake 2, TC5. |
| 1 | 2 | 6 | Fire compartment, TC rake 2, TC6. |
| 1 | 2 | 7 | Fire compartment, TC rake 2, TC7 (bottom). |
| 1 | 3 | 0 | Fire compartment, TC rake 3, TC0 (top). |
| 1 | 3 | 1 | Fire compartment, TC rake 3, TC1. |
| 1 | 3 | 2 | Fire compartment, TC rake 3, TC2. |
| 1 | 3 | 3 | Fire compartment, TC rake 3, TC3. |
| 1 | 3 | 4 | Fire compartment, TC rake 3, TC4. |
| 1 | 3 | 5 | Fire compartment, TC rake 3, TC5. |
| 1 | 3 | 6 | Fire compartment, TC rake 3, TC6. |
| 1 | 3 | 7 | Fire compartment, TC rake 3, TC7 (bottom). |
| 1 | 4 | 0 | Fire compartment, TC rake 4, TC0 (top). |
| 1 | 4 | 1 | Fire compartment, TC rake 4, TC1. |
| 1 | 4 | 2 | Fire compartment, TC rake 4, TC2. |
| 1 | 4 | 3 | Fire compartment, TC rake 4, TC3. |
| 1 | 4 | 4 | Fire compartment, TC rake 4, TC4. |
| 1 | 4 | 5 | Fire compartment, TC rake 4, TC5. |
| 1 | 4 | 6 | Fire compartment, TC rake 4, TC6. |

| | | | |
|---|---|---|---|
| 1 | 4 | 7 | Fire compartment, TC rake 4, TC7 (bottom). |
| 1 | 5 | 0 | Fire compartment, open. |
| 1 | 5 | 1 | Fire compartment, open. |
| 1 | 5 | 2 | Fire compartment, open. |
| 1 | 5 | 3 | Fire compartment, open. |
| 1 | 5 | 4 | Fire compartment, open. |
| 1 | 5 | 5 | Fire compartment, open. |
| 1 | 5 | 6 | Fire compartment, open. |
| 1 | 5 | 7 | Fire compartment, open. |
| 1 | 6 | 0 | Back room, wall frame, TC0 (top-right). |
| 1 | 6 | 1 | Back room, wall frame, TC1 (right-top). |
| 1 | 6 | 2 | Back room, wall frame, TC2 (right-bottom). |
| 1 | 6 | 3 | Back room, wall frame, TC3 (bottom-right). |
| 1 | 6 | 4 | Back room, rake 1 (right), TC4 (top). |
| 1 | 6 | 5 | Back room, rake 1 (right), TC5 (middle). |
| 1 | 6 | 6 | Back room, rake 1 (right), TC6 (bottom). |
| 1 | 6 | 7 | Back room, back wall (right), TC7. |
| 1 | 7 | 0 | Back room, wall frame, TC0 (top-left). |
| 1 | 7 | 1 | Back room, wall frame, TC1 (left-top). |
| 1 | 7 | 2 | Back room, wall frame, TC2 (left-bottom). |
| 1 | 7 | 3 | Back room, wall frame, TC3 (bottom-left). |
| 1 | 7 | 4 | Back room, rake 2 (left), TC4 (top). |
| 1 | 7 | 5 | Back room, rake 2 (left), TC5 (middle). |
| 1 | 7 | 6 | Back room, rake 2 (left), TC6 (bottom). |
| 1 | 7 | 7 | Back room, back wall (left), TC7. |
| 2 | 1 | 0 | Stud wall, cavity 4, TC1. |
| 2 | 1 | 1 | Stud wall, cavity 4, TC2. |
| 2 | 1 | 2 | Stud wall, cavity 4, TC3. |
| 2 | 1 | 3 | Stud wall, cavity 4, TC4. |
| 2 | 1 | 4 | Stud wall, cavity 4, TC5. |
| 2 | 1 | 5 | Stud wall, cavity 4, TC6. |
| 2 | 1 | 6 | Stud wall, cavity 3, TC5. |
| 2 | 1 | 7 | Stud wall, cavity 3, TC6. |
| 2 | 2 | 0 | Stud wall, cavity 3, TC1. |
| 2 | 2 | 1 | Stud wall, cavity 3, TC2. |
| 2 | 2 | 2 | Stud wall, cavity 3, TC3. |

| | | | |
|---|---|---|---|
| 2 | 2 | 3 | Stud wall, cavity 3, TC4. |
| 2 | 2 | 4 | Stud wall, cavity 2, TC3. |
| 2 | 2 | 5 | Stud wall, cavity 2, TC4. |
| 2 | 2 | 6 | Stud wall, cavity 2, TC6. |
| 2 | 2 | 7 | Stud wall, cavity 2, TC5. |
| 2 | 3 | 0 | Stud wall, cavity 2, TC1. |
| 2 | 3 | 1 | Stud wall, cavity 2, TC2. |
| 2 | 3 | 2 | Stud wall, cavity 1, TC1. |
| 2 | 3 | 3 | Stud wall, cavity 1, TC2. |
| 2 | 3 | 4 | Stud wall, cavity 1, TC3. |
| 2 | 3 | 5 | Stud wall, cavity 1, TC4. |
| 2 | 3 | 6 | Stud wall, cavity 1, TC5. |
| 2 | 3 | 7 | Stud wall, cavity 1, TC6. |
| 2 | 4 | 0 | Stud wall, unexposed, cavity 4, TC1 |
| 2 | 4 | 1 | Stud wall, unexposed, cavity 4, TC2 |
| 2 | 4 | 2 | Stud wall, unexposed, cavity 4, TC3 |
| 2 | 4 | 3 | Stud wall, unexposed, cavity 3, TC1 |
| 2 | 4 | 4 | Stud wall, unexposed, cavity 3, TC2 |
| 2 | 4 | 5 | Stud wall, unexposed, cavity 3, TC3 |
| 2 | 4 | 6 | Stud wall, Open. |
| 2 | 4 | 7 | Stud wall, Open. |
| 2 | 5 | 0 | Stud wall, unexposed, cavity 2, TC1 |
| 2 | 5 | 1 | Stud wall, unexposed, cavity 2, TC2 |
| 2 | 5 | 2 | Stud wall, unexposed, cavity 2, TC3 |
| 2 | 5 | 3 | Stud wall, unexposed, cavity 1, TC1 |
| 2 | 5 | 4 | Stud wall, unexposed, cavity 1, TC2 |
| 2 | 5 | 5 | Stud wall, unexposed, cavity 1, TC3 |
| 2 | 5 | 6 | Stud wall, Open. |
| 2 | 5 | 7 | Stud wall, Open. |
| 2 | 6 | 0 | Stud wall, Open. |
| 2 | 6 | 1 | Stud wall, Open. |
| 2 | 6 | 2 | Stud wall, Open. |
| 2 | 6 | 3 | Stud wall, Open. |
| 2 | 6 | 4 | Stud wall, Open. |
| 2 | 6 | 5 | Stud wall, Open. |
| 2 | 6 | 6 | Stud wall, Open. |

| | | | |
|---|---|---|---|
| 2 | 6 | 7 | Stud wall, Open. |

Table B.1: Instrumentation overview for the fire test apparatus.

| LABEL | POSITION | HEIGHT FROM COMPARTMENT FLOOR |
|---|---|---|
| T1/T2/T3/T4 | 0 | 87.5 in (2.5 in below fire-side ceiling). |
| T1/T2/T3/T4 | 1 | 84 in (6 in below fire-side ceiling). |
| T1/T2/T3/T4 | 2 | 72 in (18 in below fire-side ceiling). |
| T1/T2/T3/T4 | 3 | 60 in (30 in below fire-side ceiling). |
| T1/T2/T3/T4 | 4 | 48 in (42 in below fire-side ceiling). |
| T1/T2/T3/T4 | 5 | 36 in (54 in below fire-side ceiling). |
| T1/T2/T3/T4 | 6 | 24 in (66 in below fire-side ceiling). |
| T1/T2/T3/T4 | 7 | 12 in (78 in below fire-side ceiling). |

Table B.1: Sensor height positions — fire compartment thermocouple rakes.

| LABEL | POSITION | HEIGHT FROM COMPARTMENT FLOOR |
|---|---|---|
| TR | 4 | 87.5 in (6 in below cool-side ceiling). |
| TR | 5 | 49.75 in (43.75 in below cool-side ceiling). |
| TR | 6 | 12 in (81.5 in below cool-side ceiling). |
| TL | 4 | 87.5 in (6 in below cool-side ceiling). |
| TL | 5 | 49.75 in (43.75 in below cool-side ceiling). |
| TL | 6 | 12 in (81.5 in below cool-side ceiling). |

Table B.2: Sensor height positions — transition room thermocouple rakes.

| LABEL | POSITION | HEIGHT FROM COMPARTMENT FLOOR |
|---|---|---|
| BR | 7 | 49.75 in (43.75 in below cool-side ceiling). |
| BL | 7 | 49.75 in (43.75 in below cool-side ceiling). |

Table B.3: Sensor height positions — back side of the transition room.

| LABEL | POSITION | HEIGHT FROM COMPARTMENT FLOOR |
|---|---|---|
| FR | 0 | 87.5 in (6 in below cool-side ceiling). |
| FR | 1 | 62.5 in (31 in below cool-side ceiling). |
| FR | 2 | 37 in (56.5 in below cool-side ceiling). |
| FR | 3 | 12 in (81.5 in below cool-side ceiling). |
| FL | 0 | 87.5 in (6 in below cool-side ceiling). |
| FL | 1 | 62.5 in (31 in below cool-side ceiling). |
| FL | 2 | 37 in (56.5 in below cool-side ceiling). |
| FL | 3 | 12 in (81.5 in below cool-side ceiling). |

Table B.4: Sensor height positions — wall frame.

| LABEL | POSITION | HEIGHT FROM COMPARTMENT FLOOR |
|---|---|---|
| C1/C2/C3/C4 | 0 (main) | 79.75 in (67.75 in from bottom of wall frame). |
| C1/C2/C3/C4 | 1 (main) | 67.75 in (55.75 in from bottom of wall frame). |
| C1/C2/C3/C4 | 2 (main) | 55.75 in (43.75 in from bottom of wall frame). |
| C1/C2/C3/C4 | 3 (main) | 43.75 in (31.75 in from bottom of wall frame). |
| C1/C2/C3/C4 | 4 (main) | 31.75 in (19.75 in from bottom of wall frame). |
| C1/C2/C3/C4 | 5 (main) | 19.75 in (7.75 in from bottom of wall frame). |
| C1/C2/C3/C4 | 0 (back) | 79.75 in (67.75 in from bottom of wall frame). |
| C1/C2/C3/C4 | 2/3 (back) | 49.75 in (37.75 in from bottom of wall frame). |
| C1/C2/C3/C4 | 5 (back) | 19.75 in (7.75 in from bottom of wall frame). |

Table B.5: Sensor height positions — real wall (4-cavity stud wall).

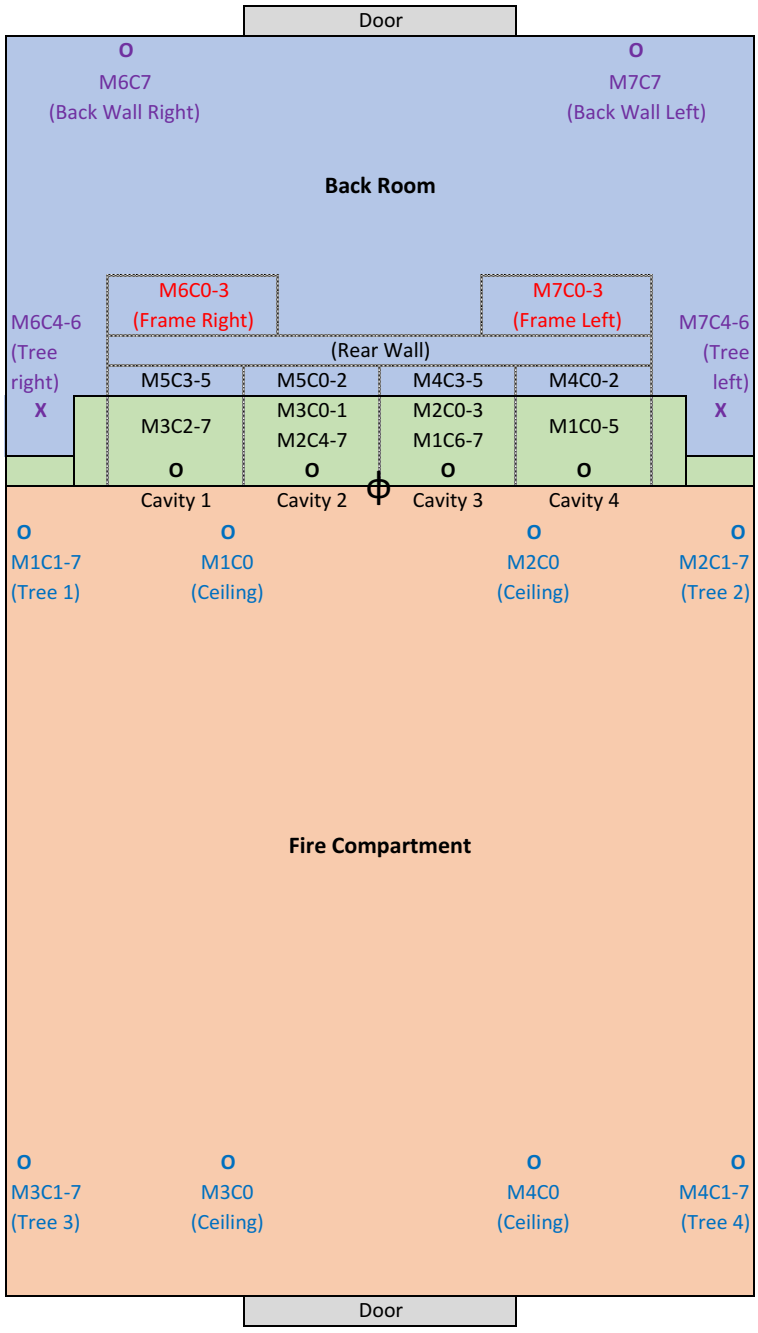


Figure B.1: Instrumentation schematic for the fire test apparatus.

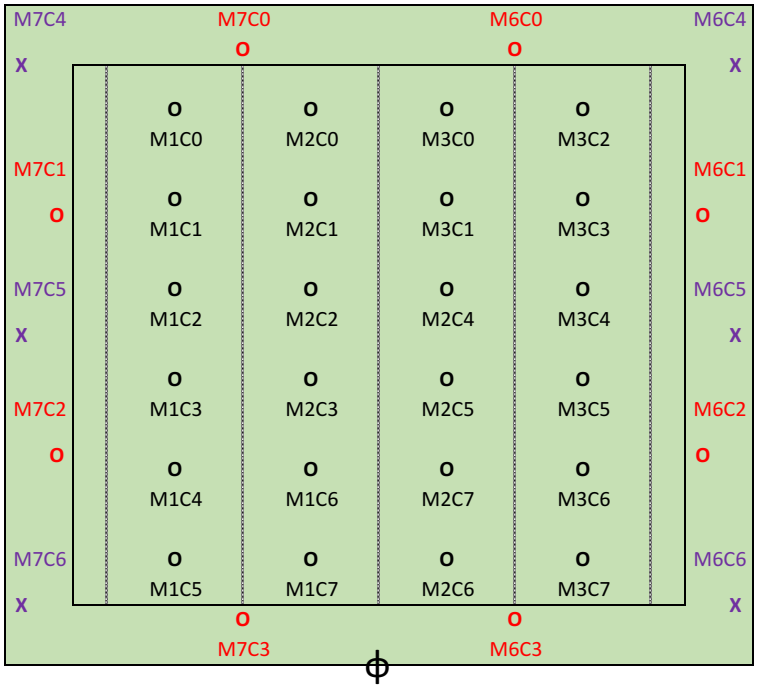


Figure B.2: Instrumentation schematic for the fire test apparatus, from the perspective of the unexposed side of the wall, sensors located within stud cavities.

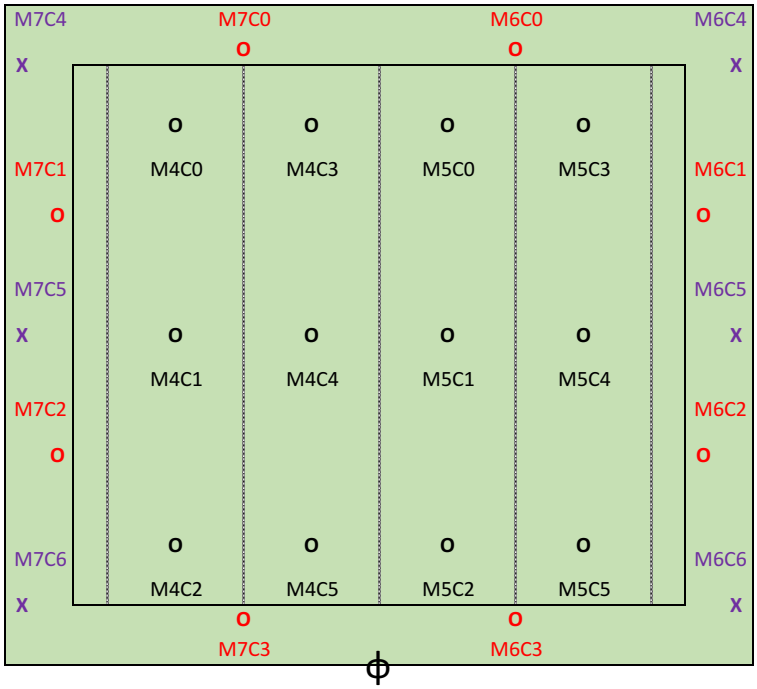


Figure B.3: Instrumentation schematic for the fire test apparatus, from the perspective of the unexposed side of the wall, sensors located on the unexposed side of the wall.

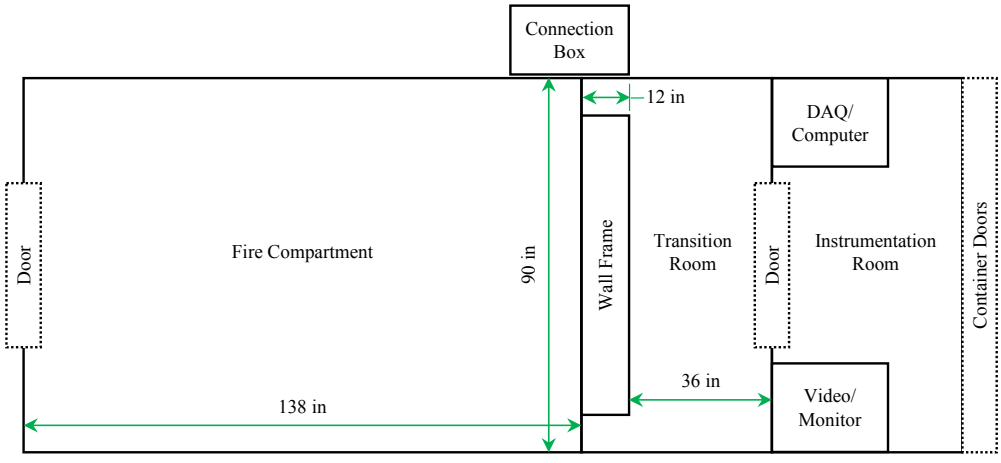


Figure B.4: Global dimensions in the fire test apparatus.

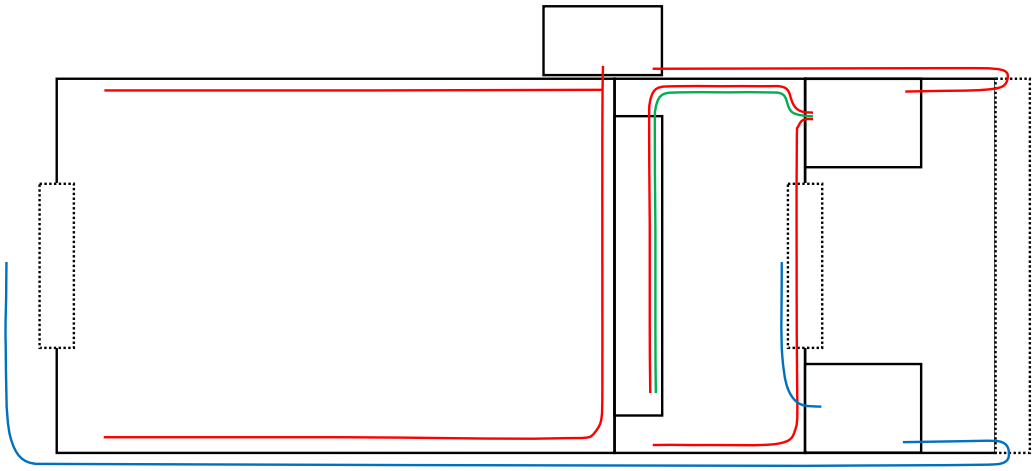

Figure B.5: Cable routing for instrumentation in the fire test apparatus.

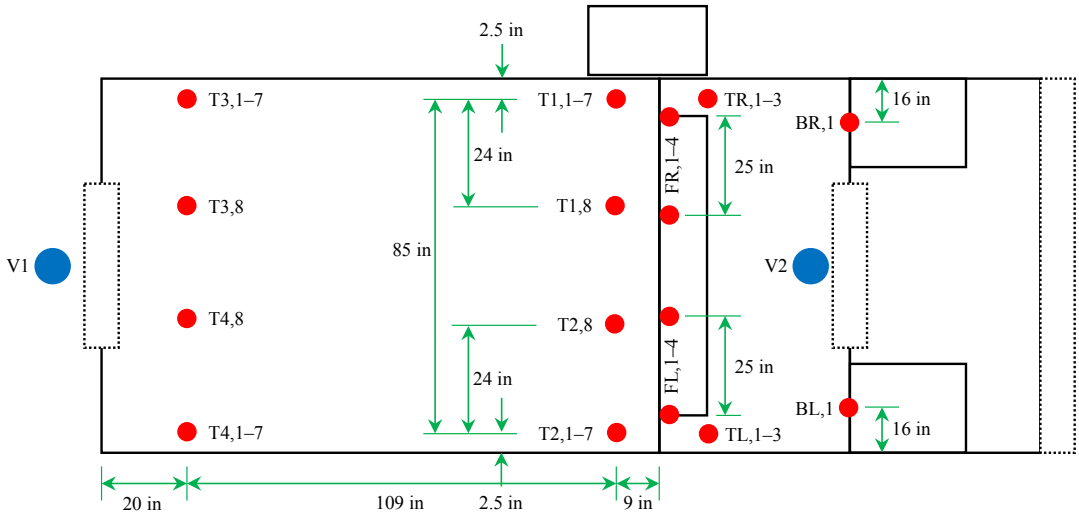


Figure B.6: Sensor locations in the fire test apparatus.

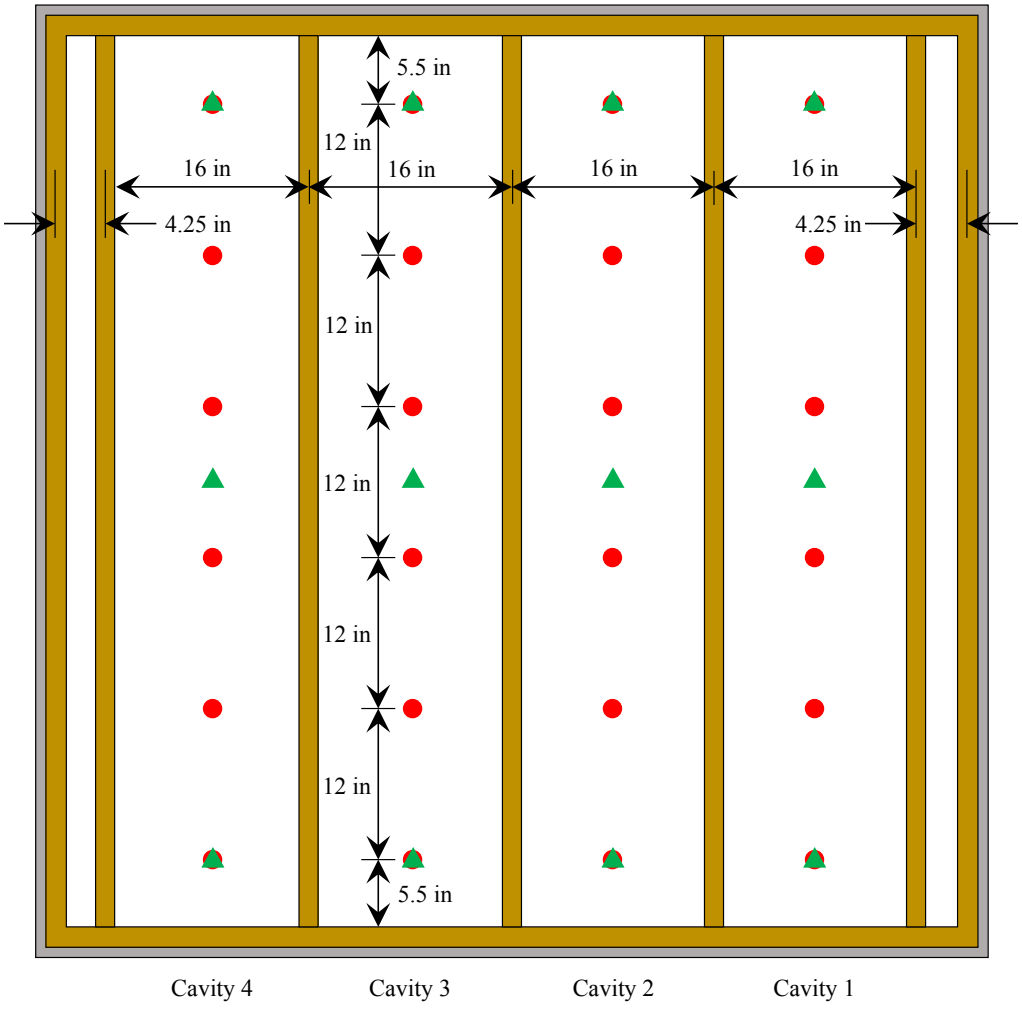


Figure B.7: Sensor locations for a real wall test.

## B.2 Steel Wall Characterization Experiments

Table B.2 lists and provides descriptions of all data acquisition channels used in the fire test apparatus for the steel wall characterization experiments. Headers in the raw data files are consistent with the naming convention used here.

Figure B.8 shows a top-view schematic of sensor locations through the entire apparatus. Additional details are provided in Figure B.9. DAQ references in these figures correspond to those given in Table B.1.

Figure B.10 shows the locations of sensors on the steel wall, including dimensions. In the figure, red circles represent thermocouples welded to the unexposed side of the wall. Height dimensions relative to the compartment floor are provided in Table B.6.

| DAQ | MODULE | CHANNEL | DESCRIPTION |
|---|---|---|---|
| 1 | 1 | 0 | Fire compartment, TC rake 1, TC0 (top). |
| 1 | 1 | 1 | Fire compartment, TC rake 1, TC1. |
| 1 | 1 | 2 | Fire compartment, TC rake 1, TC2. |
| 1 | 1 | 3 | Fire compartment, TC rake 1, TC3. |
| 1 | 1 | 4 | Fire compartment, TC rake 1, TC4. |
| 1 | 1 | 5 | Fire compartment, TC rake 1, TC5. |
| 1 | 1 | 6 | Fire compartment, TC rake 1, TC6. |
| 1 | 1 | 7 | Fire compartment, TC rake 1, TC7 (bottom). |
| 1 | 2 | 0 | Fire compartment, TC rake 2, TC0 (top). |
| 1 | 2 | 1 | Fire compartment, TC rake 2, TC1. |
| 1 | 2 | 2 | Fire compartment, TC rake 2, TC2. |
| 1 | 2 | 3 | Fire compartment, TC rake 2, TC3. |
| 1 | 2 | 4 | Fire compartment, TC rake 2, TC4. |
| 1 | 2 | 5 | Fire compartment, TC rake 2, TC5. |
| 1 | 2 | 6 | Fire compartment, TC rake 2, TC6. |
| 1 | 2 | 7 | Fire compartment, TC rake 2, TC7 (bottom). |
| 1 | 3 | 0 | Fire compartment, TC rake 3, TC0 (top). |
| 1 | 3 | 1 | Fire compartment, TC rake 3, TC1. |
| 1 | 3 | 2 | Fire compartment, TC rake 3, TC2. |
| 1 | 3 | 3 | Fire compartment, TC rake 3, TC3. |
| 1 | 3 | 4 | Fire compartment, TC rake 3, TC4. |
| 1 | 3 | 5 | Fire compartment, TC rake 3, TC5. |
| 1 | 3 | 6 | Fire compartment, TC rake 3, TC6. |

| | | | |
|---|---|---|---|
| 1 | 3 | 7 | Fire compartment, TC rake 3, TC7 (bottom). |
| 1 | 4 | 0 | Fire compartment, TC rake 4, TC0 (top). |
| 1 | 4 | 1 | Fire compartment, TC rake 4, TC1. |
| 1 | 4 | 2 | Fire compartment, TC rake 4, TC2. |
| 1 | 4 | 3 | Fire compartment, TC rake 4, TC3. |
| 1 | 4 | 4 | Fire compartment, TC rake 4, TC4. |
| 1 | 4 | 5 | Fire compartment, TC rake 4, TC5. |
| 1 | 4 | 6 | Fire compartment, TC rake 4, TC6. |
| 1 | 4 | 7 | Fire compartment, TC rake 4, TC7 (bottom). |
| 1 | 5 | 0 | Fire compartment, open. |
| 1 | 5 | 1 | Fire compartment, open. |
| 1 | 5 | 2 | Fire compartment, open. |
| 1 | 5 | 3 | Fire compartment, open. |
| 1 | 5 | 4 | Fire compartment, open. |
| 1 | 5 | 5 | Fire compartment, open. |
| 1 | 5 | 6 | Fire compartment, open. |
| 1 | 5 | 7 | Fire compartment, open. |
| 1 | 6 | 0 | Back room, wall frame, TC0 (top-right). |
| 1 | 6 | 1 | Back room, wall frame, TC1 (right-top). |
| 1 | 6 | 2 | Back room, wall frame, TC2 (right-bottom). |
| 1 | 6 | 3 | Back room, wall frame, TC3 (bottom-right). |
| 1 | 6 | 4 | Back room, rake 1 (right), TC4 (top). |
| 1 | 6 | 5 | Back room, rake 1 (right), TC5 (middle). |
| 1 | 6 | 6 | Back room, rake 1 (right), TC6 (bottom). |
| 1 | 6 | 7 | Back room, back wall (right), TC7. |
| 1 | 7 | 0 | Back room, wall frame, TC0 (top-left). |
| 1 | 7 | 1 | Back room, wall frame, TC1 (left-top). |
| 1 | 7 | 2 | Back room, wall frame, TC2 (left-bottom). |
| 1 | 7 | 3 | Back room, wall frame, TC3 (bottom-left). |
| 1 | 7 | 4 | Back room, rake 2 (left), TC4 (top). |
| 1 | 7 | 5 | Back room, rake 2 (left), TC5 (middle). |
| 1 | 7 | 6 | Back room, rake 2 (left), TC6 (bottom). |
| 1 | 7 | 7 | Back room, back wall (left), TC7. |
| 2 | 1 | 0 | Steel wall, panel 1, TC0 (top). |
| 2 | 1 | 1 | Steel wall, panel 1, TC1. |
| 2 | 1 | 2 | Steel wall, panel 1, TC2. |

| | | | |
|---|---|---|---|
| 2 | 1 | 3 | Steel wall, panel 1, TC3. |
| 2 | 1 | 4 | Steel wall, panel 1, TC4. |
| 2 | 1 | 5 | Steel wall, panel 1, TC5. |
| 2 | 1 | 6 | Steel wall, panel 1, TC6. |
| 2 | 1 | 7 | Steel wall, panel 1, TC7 (bottom). |
| 2 | 2 | 0 | Steel wall, panel 2, TC0 (top). |
| 2 | 2 | 1 | Steel wall, panel 2, TC1. |
| 2 | 2 | 2 | Steel wall, panel 2, TC2. |
| 2 | 2 | 3 | Steel wall, panel 2, TC3. |
| 2 | 2 | 4 | Steel wall, panel 2, TC4. |
| 2 | 2 | 5 | Steel wall, panel 2, TC5. |
| 2 | 2 | 6 | Steel wall, panel 2, TC6. |
| 2 | 2 | 7 | Steel wall, panel 2, TC7 (bottom). |
| 2 | 3 | 0 | Steel wall, panel 3, TC0 (top). |
| 2 | 3 | 1 | Steel wall, panel 3, TC1. |
| 2 | 3 | 2 | Steel wall, panel 3, TC2. |
| 2 | 3 | 3 | Steel wall, panel 3, TC3. |
| 2 | 3 | 4 | Steel wall, panel 3, TC4. |
| 2 | 3 | 5 | Steel wall, panel 3, TC5. |
| 2 | 3 | 6 | Steel wall, panel 3, TC6. |
| 2 | 3 | 7 | Steel wall, panel 3, TC7 (bottom). |

Table B.2: Instrumentation overview for the characterization experiments.

| LABEL | POSITION | HEIGHT FROM COMPARTMENT FLOOR |
|---|---|---|
| P1/P2/P3 | 0 | 82.5625 in (70.5625 in from bottom of wall frame). |
| P1/P2/P3 | 1 | 73.1875 in (61.1875 in from bottom of wall frame). |
| P1/P2/P3 | 2 | 63.8125 in (51.8125 in from bottom of wall frame). |
| P1/P2/P3 | 3 | 54.4375 in (42.4375 in from bottom of wall frame). |
| P1/P2/P3 | 4 | 45.0625 in (33.0625 in from bottom of wall frame). |
| P1/P2/P3 | 5 | 35.6875 in (23.6875 in from bottom of wall frame). |
| P1/P2/P3 | 6 | 26.3125 in (14.3125 in from bottom of wall frame). |
| P1/P2/P3 | 7 | 16.9375 in (4.9375 in from bottom of wall frame). |

Table B.6: Sensor height positions — steel wall.

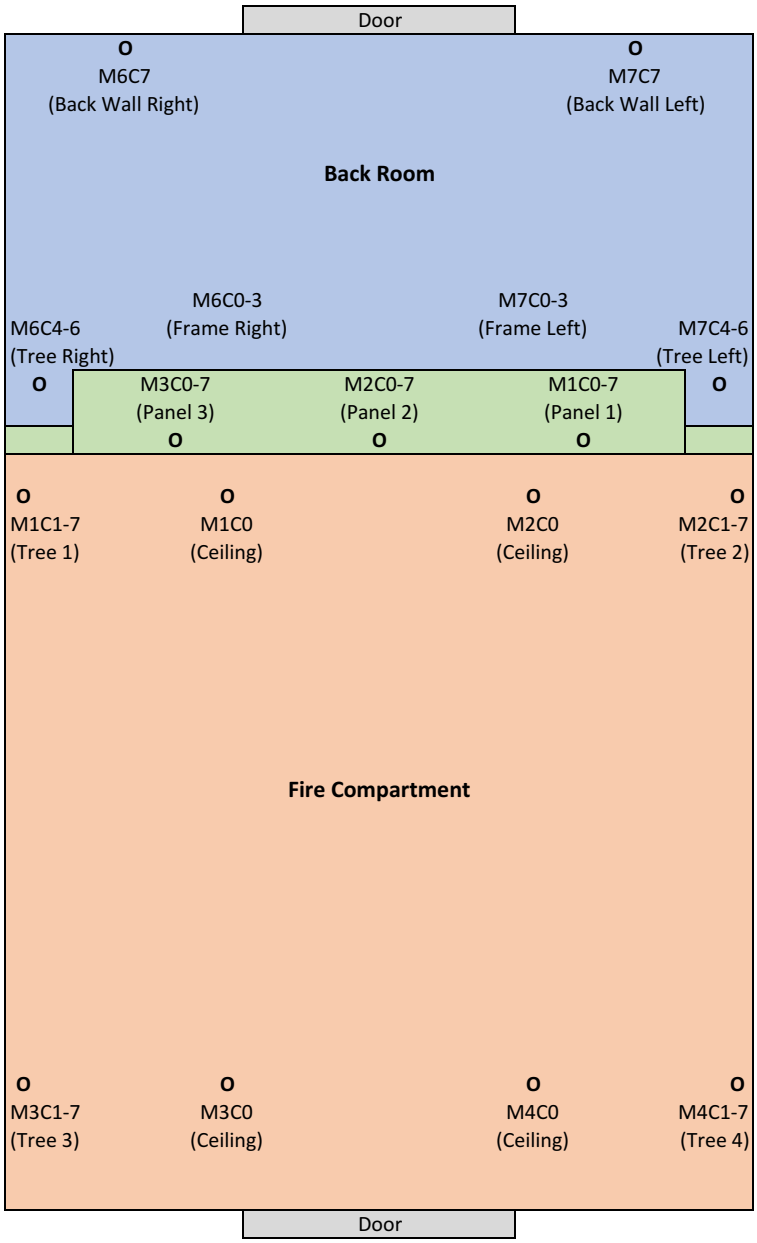


Figure B.8: Instrumentation schematic for the characterization experiments.

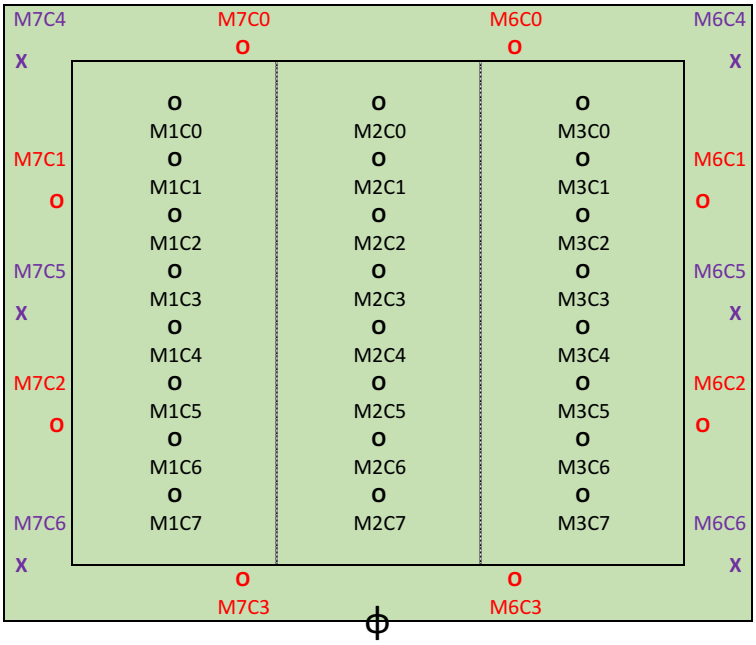


Figure B.9: Instrumentation schematic for the characterization experiments, from the perspective of the unexposed side of the wall.

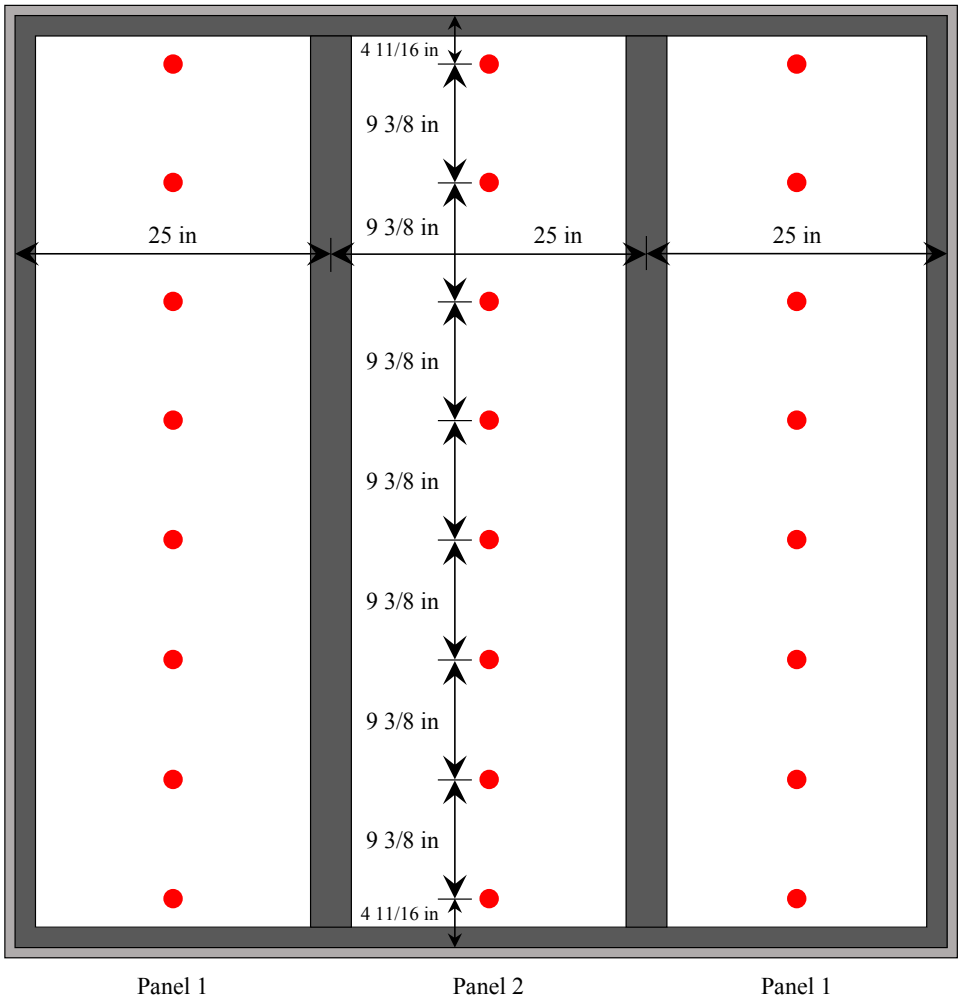


Figure B.10: Sensor locations for a steel wall test.

# Appendix C

# Fuel Configurations

## C.1 Real Wall Thermal Degradation Experiments

Figures C.1–C.5 detail the fuel configurations used for the five real wall thermal degradation experiments.

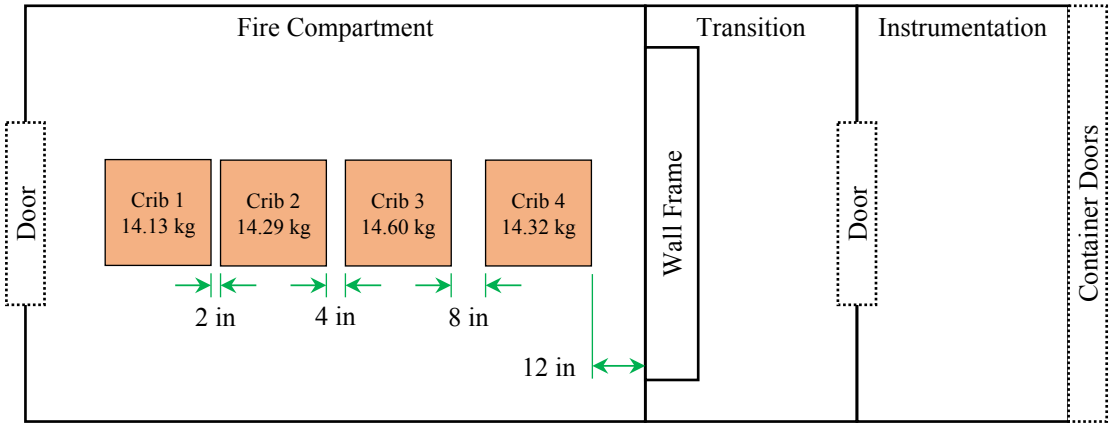


Figure C.1: Fuel configuration used for thermal degradation test #1.

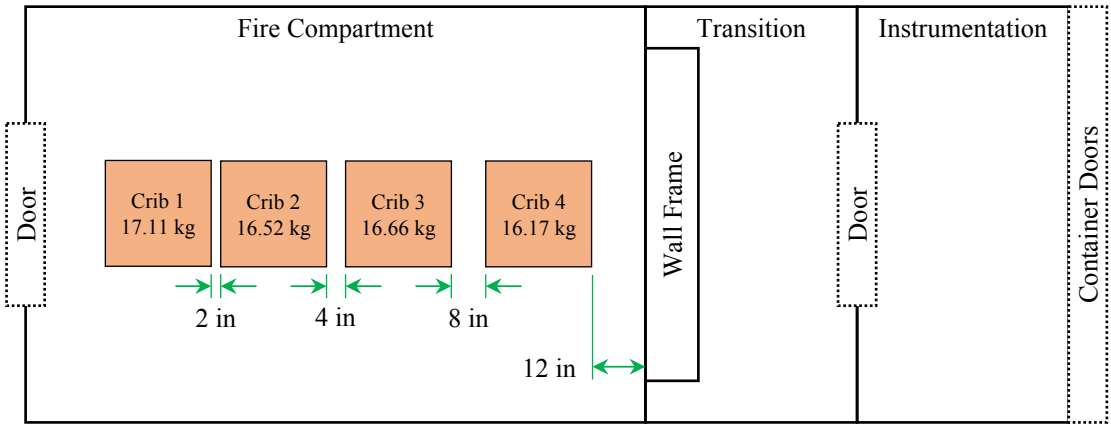


Figure C.2: Fuel configuration used for thermal degradation test #2.

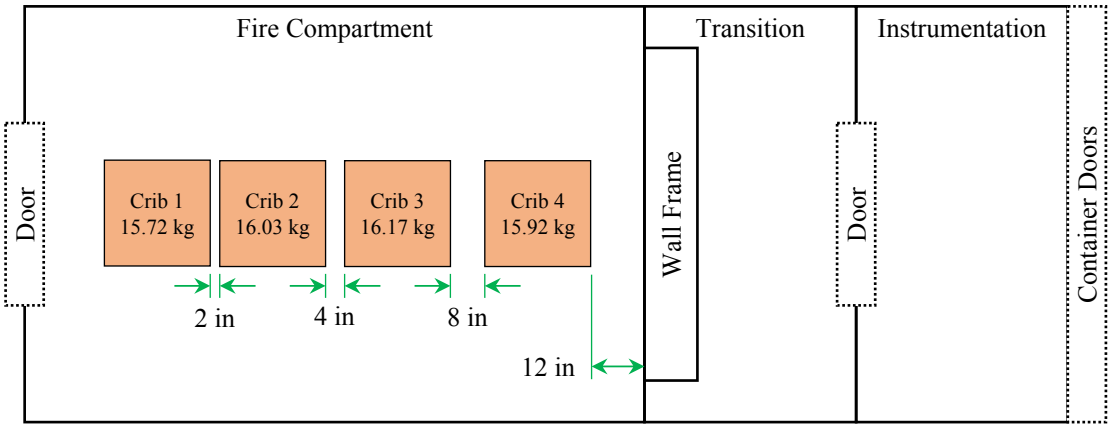


Figure C.3: Fuel configuration used for thermal degradation test #3.

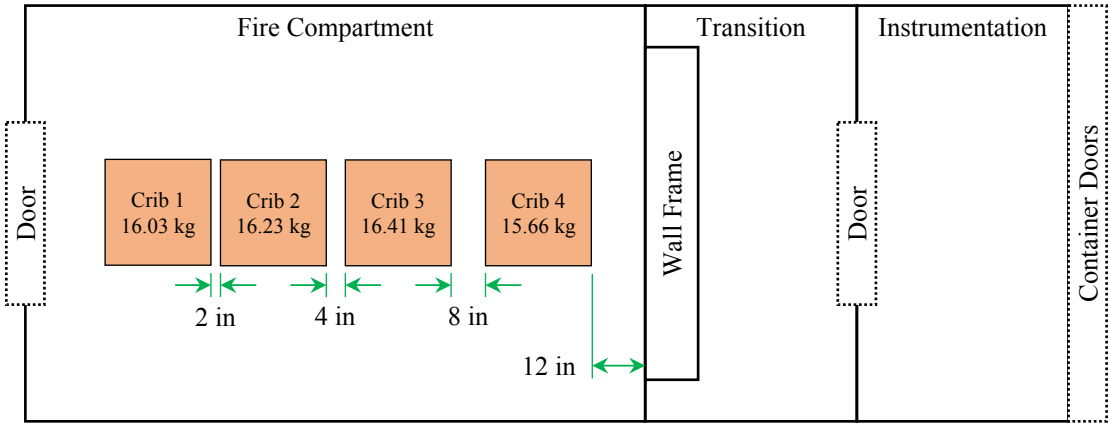


Figure C.4: Fuel configuration used for thermal degradation test #4.

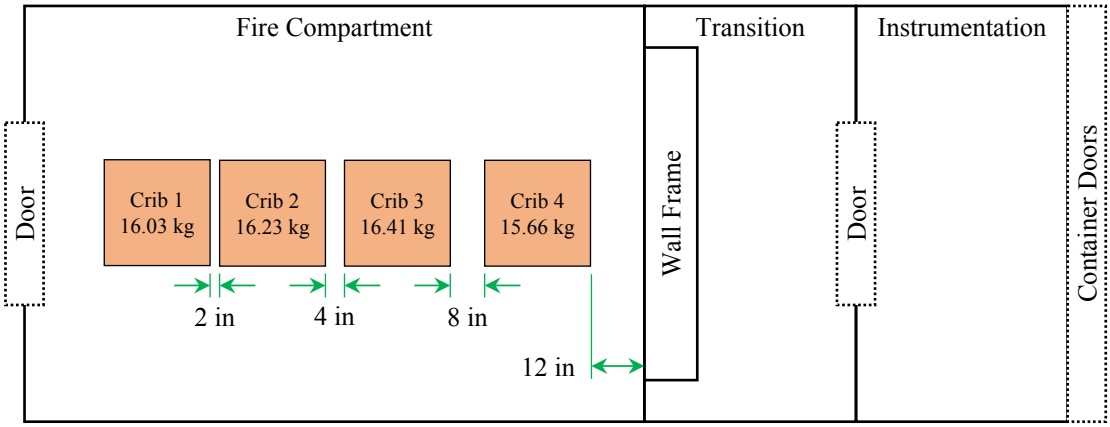


Figure C.5: Fuel configuration used for thermal degradation test #5.

## C.2 Steel Wall Characterization Experiments

Figures C.6–C.18 detail the fuel configurations used for the 12 steel wall characterization tests.

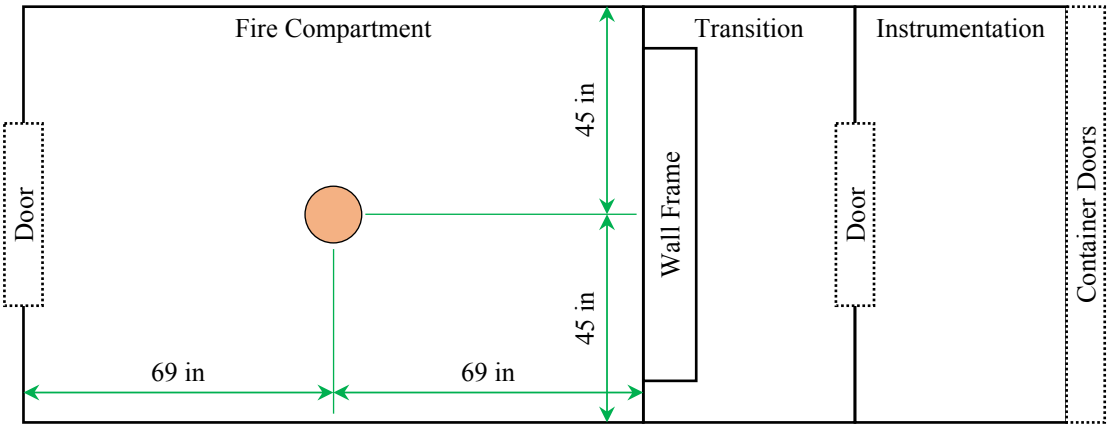


Figure C.6: Fuel configuration used for characterization test #1.

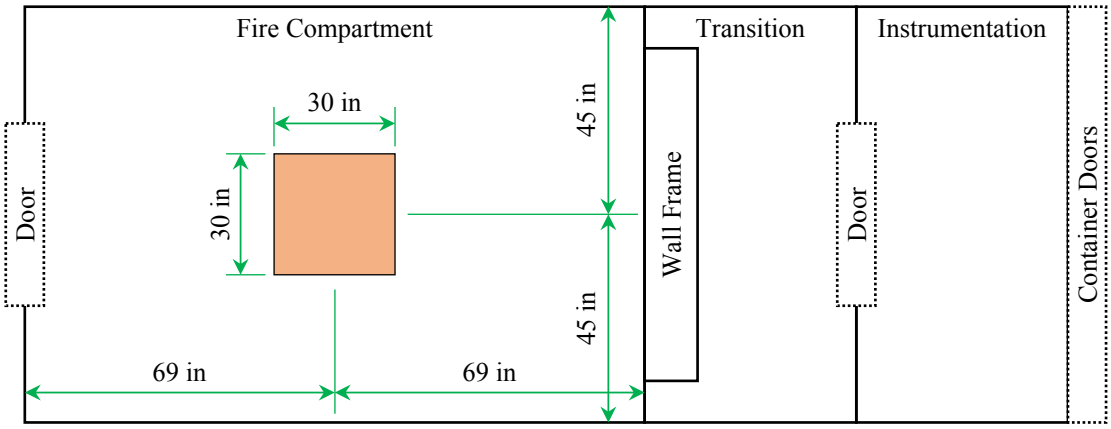


Figure C.7: Fuel configuration used for characterization test #2.

Figure C.8: Fuel contents for characterization test #2.

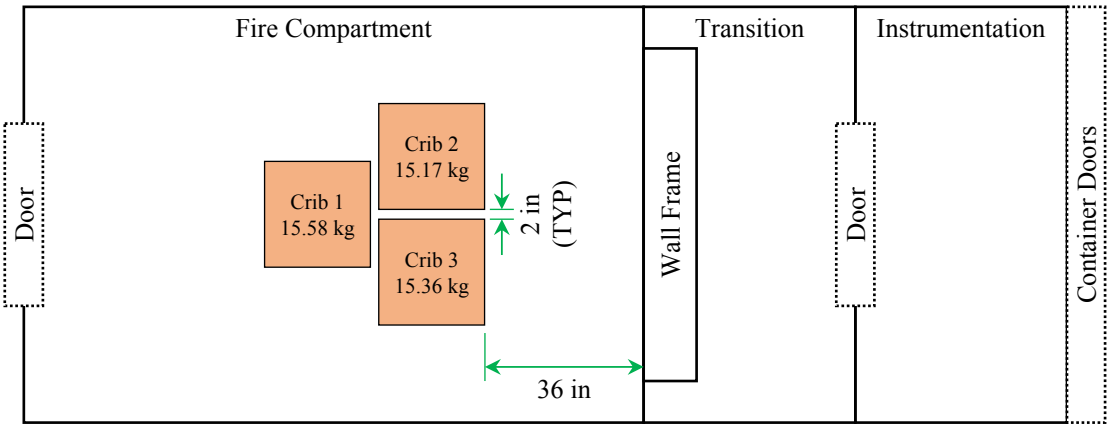


Figure C.9: Fuel configuration used for characterization test #3.

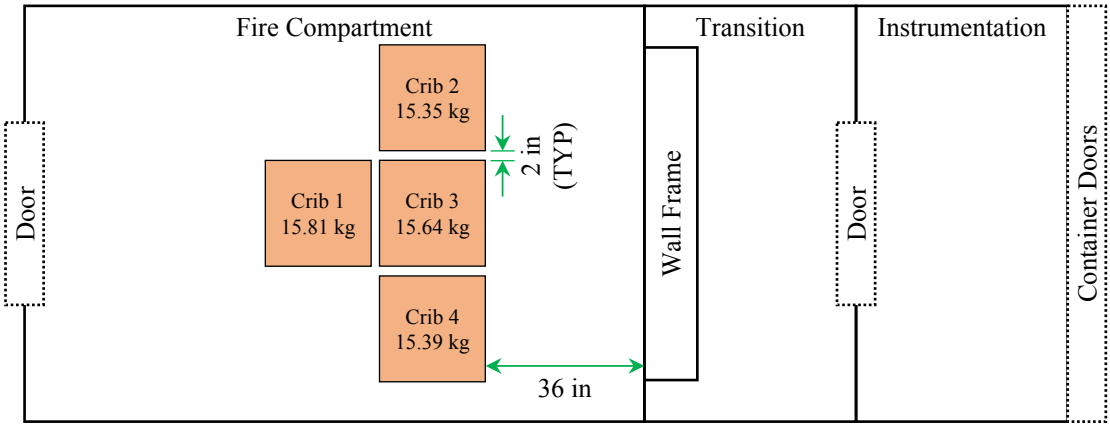


Figure C.10: Fuel configuration used for characterization test #4.

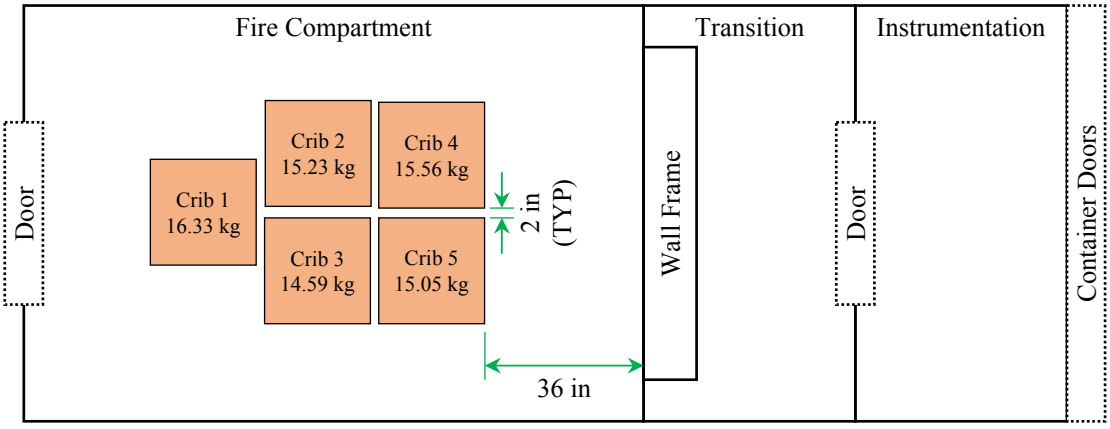


Figure C.11: Fuel configuration used for characterization test #5.

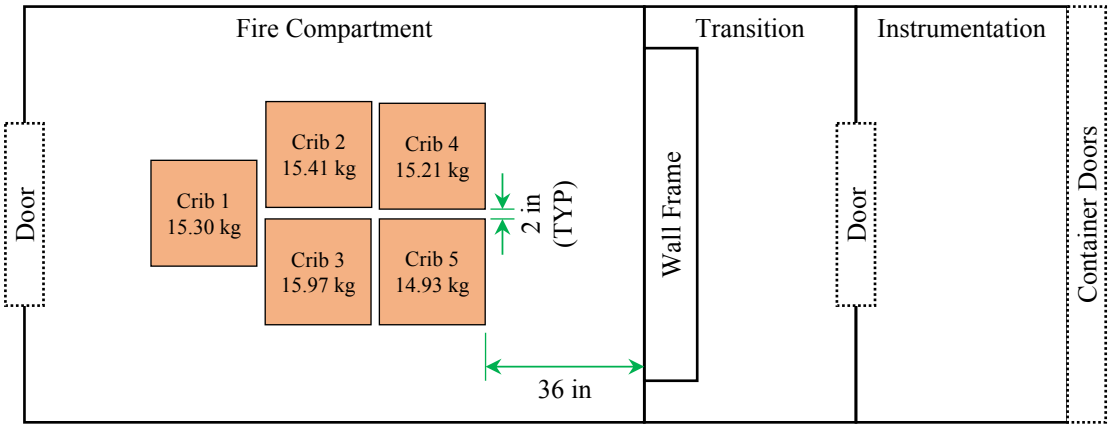


Figure C.12: Fuel configuration used for characterization test #6.

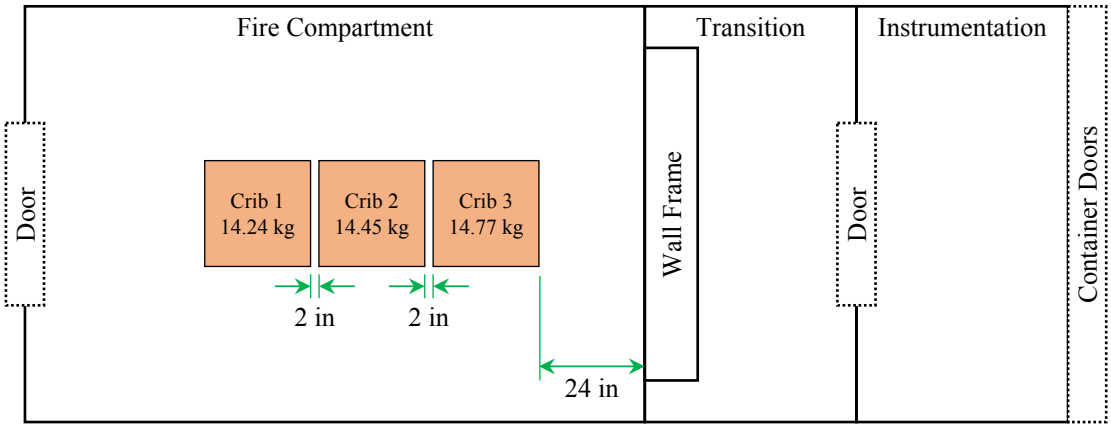


Figure C.13: Fuel configuration used for characterization test #7.

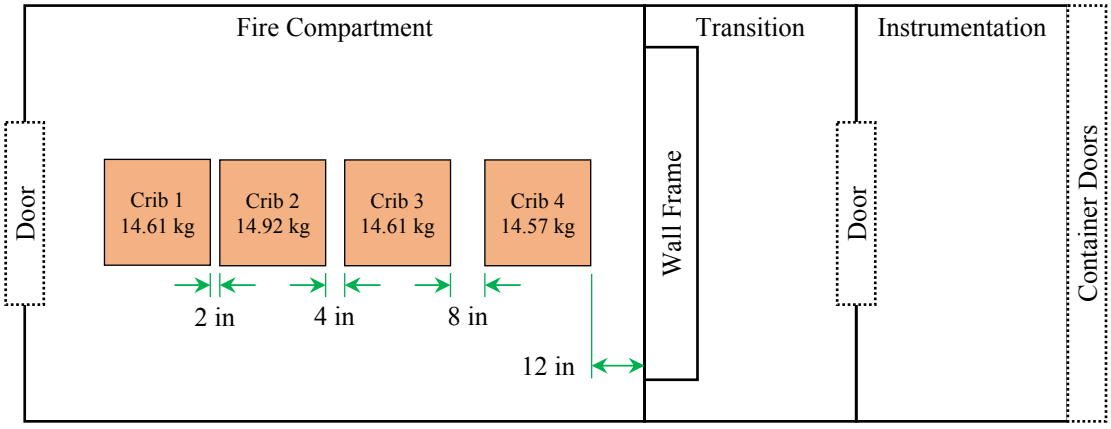


Figure C.14: Fuel configuration used for characterization test #8.

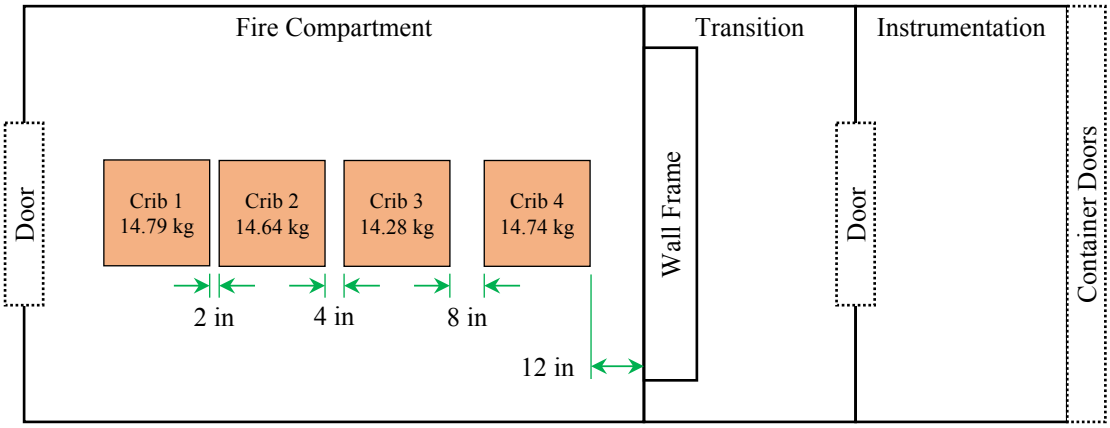


Figure C.15: Fuel configuration used for characterization test #9.

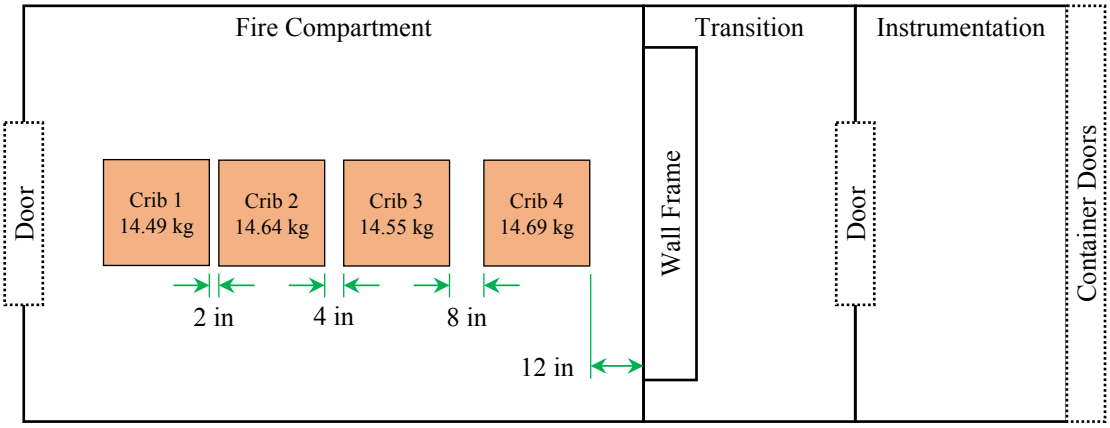


Figure C.16: Fuel configuration used for characterization test #10.

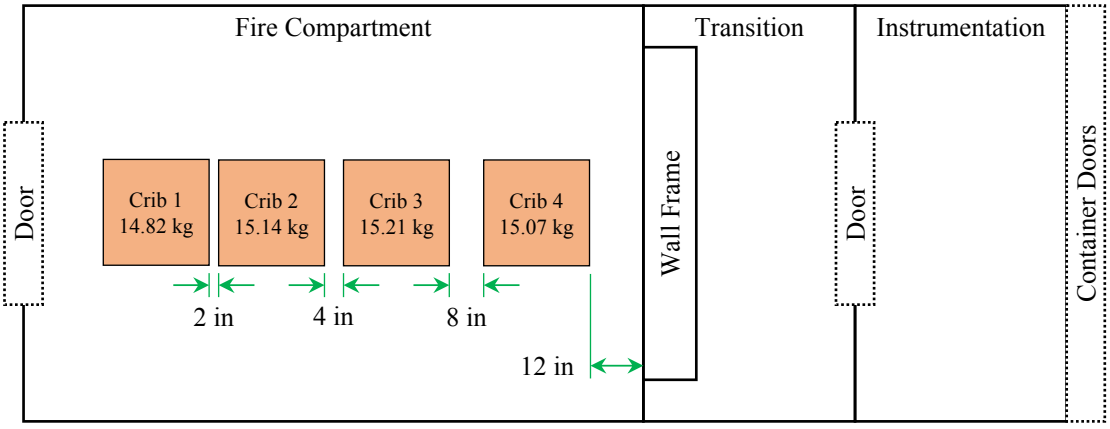


Figure C.17: Fuel configuration used for characterization test #11.

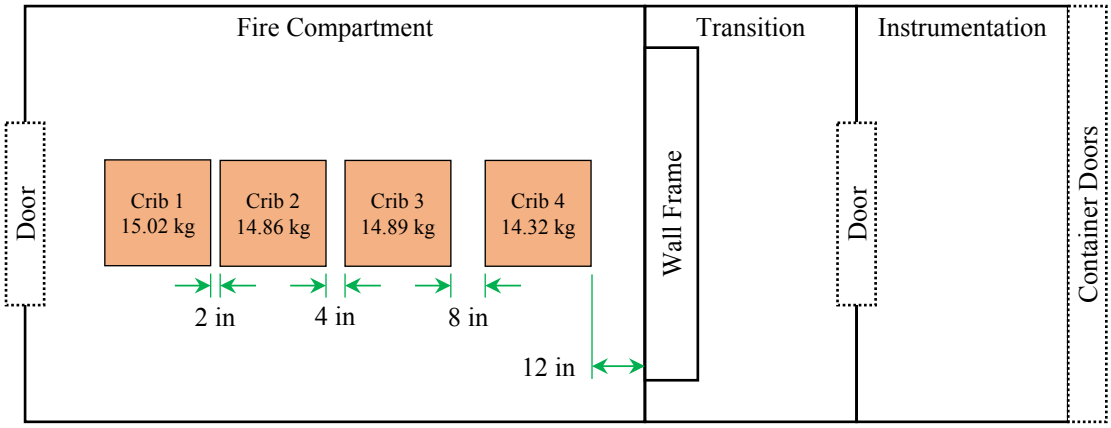


Figure C.18: Fuel configuration used for characterization test #12.

# Appendix D

# Raw Test Data

This appendix contains raw data files in the Comma Separated Values (CSV) format for the experiments conducted in the present work, as detailed below:

| | |
|---|---|
| Steel wall characterization test #1 | `steel-wall-test-01-2016-08-15.csv` |
| Steel wall characterization test #2 | `steel-wall-test-02-2016-08-15.csv` |
| Steel wall characterization test #3 | `steel-wall-test-03-2016-08-17.csv` |
| Steel wall characterization test #4 | `steel-wall-test-04-2016-08-18.csv` |
| Steel wall characterization test #5 | `steel-wall-test-05-2016-08-26.csv` |
| Steel wall characterization test #6 | `steel-wall-test-06-2016-08-29.csv` |
| Steel wall characterization test #7 | `steel-wall-test-07-2016-09-14.csv` |
| Steel wall characterization test #8 | `steel-wall-test-08-2016-09-18.csv` |
| Steel wall characterization test #9 | `steel-wall-test-09-2016-09-19.csv` |
| Steel wall characterization test #10 | `steel-wall-test-10-2016-09-20.csv` |
| Steel wall characterization test #11 | `steel-wall-test-11-2016-09-21.csv` |
| Steel wall characterization test #12 | `steel-wall-test-12-2016-09-23.csv` |
| Real wall thermal degradation test #1 | `real-wall-test-01-2016-10-05.csv` |
| Real wall thermal degradation test #2 | `real-wall-test-02-2016-10-19.csv` |
| Real wall thermal degradation test #3 | `real-wall-test-03-2016-10-28.csv` |
| Real wall thermal degradation test #4 | `real-wall-test-04-2016-11-01.csv` |
| Real wall thermal degradation test #5 | `real-wall-test-05-2016-11-09.csv` |

If you accessed this thesis from a source other than the University of Waterloo, you may not have access to these files. You may access them by searching for this thesis on `https://uwspace.uwaterloo.ca/UWSpace`.

# Appendix E

# Raw Test Data Import Procedures — Code Listings

## E.1 Real Wall Thermal Degradation Experiments

s_import_raw_data_real_wall.m

```
% ============================================================
% Script: s_import_raw_data_real_wall
% ============================================================

%% SECTION 1: INITIALIZE SCRIPT

% Initialize script.
clear; clc;
SCRIPTNAME = 's_import_raw_data_real_wall';
SCRIPTVER = 2.0;
disp('============================================================');
fprintf(['Running script: ' SCRIPTNAME ' (version ' ...
        '%.2f) \n'], SCRIPTVER);
fileID = fopen('l_data_import.txt','w');
fprintf(fileID, ['...\n' 'Script name: ' SCRIPTNAME ' (version ' ...
        '%.2f) \n' 'Script initialized: ' datestr(now) '\n' ], SCRIPTVER);
fclose(fileID);

% Determine whether to import raw CSV data or MATLAB data.
tempvar1 = input('Import from CSV data file (y/n)? ','s');
if strcmp(tempvar1,'N') || strcmp(tempvar1,'n')
  tempvar2 = input('Import from MATLAB data file (y/n)? ','s');
  if strcmp(tempvar2,'N') || strcmp(tempvar2,'n')
```

```
24      disp('No file selected. Script aborted.');
25      disp('=======================================================');
26      fileID = fopen('l_data_import.txt','a');
27      fprintf(fileID, ['No file selected. \n' 'Script aborted: '...
28              datestr(now) '\n...\n'] );
29      fclose(fileID);
30      clearvars SCRIPTNAME SCRIPTVER filename tempvar1 tempvar2 fileID ans
31      return
32    else
33      filename = uigetfile('*.mat','Select a MATLAB data file');
34      if filename == 0
35        disp('No file selected. Script aborted.');
36        disp('=======================================================');
37        fileID = fopen('l_data_import.txt','a');
38        fprintf(fileID, ['No file selected. \n' 'Script aborted: '...
39                datestr(now) '\n...\n'] );
40        fclose(fileID);
41        clearvars SCRIPTNAME SCRIPTVER filename tempvar1 tempvar2 fileID ans
42          return
43      end
44      load(filename);
45      disp(['MATLAB data was imported from: "' filename '"']);
46      if EXP_SCRIPTVER < SCRIPTVER
47        disp('Warning: Data version is less than script version!');
48      elseif EXP_SCRIPTVER > SCRIPTVER
49        disp('Warning: Script version is less than data version!');
50      end
51      disp('Script completed.');
52      disp('=======================================================');
53      fileID = fopen('l_data_import.txt','a');
54      fprintf(fileID, ['MATLAB data was imported from: "' filename ...
55              '" \n' 'Script completed: ' datestr(now) '\n...\n'] );
56      fclose(fileID);
57      clearvars SCRIPTNAME SCRIPTVER filename tempvar1 tempvar2 fileID ans
58      return
59    end
60  else
61    disp('Select a raw data file in CSV format.');
62    disp('Ensure that multiple data files have been concatenated!');
63    pause(1);
64    filename = uigetfile('*.csv','Select a CSV data file');
65    if filename == 0
66      disp('No file selected. Script aborted.');
67      disp('=======================================================');
68      fileID = fopen('l_data_import.txt','a');
69      fprintf(fileID, ['No file selected. \n' 'Script aborted: '...
70              datestr(now) '\n...\n'] );
71      fclose(fileID);
72      clearvars SCRIPTNAME SCRIPTVER filename tempvar1 tempvar2 fileID ans
73      return
74    end
75  end
76
```

```
% Labels for user-defined parameters.
EXP_CRIB_MASS_LABEL = cellstr(['Mass of crib #1'
                               'Mass of crib #2'
                               'Mass of crib #3'
                               'Mass of crib #4']);
EXP_EVENT_LABEL = cellstr(['DAQ started           '
                           'DAQ time step         '
                           'Ignition              '
                           'Fire spread to crib #2'
                           'Fire spread to crib #3'
                           'Fire spread to crib #4'
                           'End of test           ']);
% Values for user-defined parameters.
tempvar1 = input('Enter user-defined test parameters (y/n)? ','s');
if strcmp(tempvar1,'N') || strcmp(tempvar1,'n')
  EXP_CRIB_MASS = 15*[1 1 1 1];
  EXP_EVENT = [0 1.1 0 0 0 0 3600];
  disp('Default values for user-defined parameters.');
  fileID = fopen('l_data_import.txt','a');
  fprintf(fileID, ['Default values for user-defined parameters. \n'] );
  fclose(fileID);
else
  for i = 1:4
    EXP_CRIB_MASS(i)=input([char(EXP_CRIB_MASS_LABEL(i)) ' (kg): ']);
  end
  EXP_EVENT(1)=input([char(EXP_EVENT_LABEL(1)) ' (s): ']);
  for i = 2:7
    EXP_EVENT(i)=input([char(EXP_EVENT_LABEL(i)) ' (s): '])-EXP_EVENT(1);
  end
end

% Import data from CSV data file
delimiter = ',';
startRow = 2;
formatSpec = '%q%f%f%f%f%f%f%f%f%f%f%f%f%f%f%f%f%f%f%f%f%f%f%f%f%f%f%f%f%f...
              %f%f%f%f%f%f%f%f%f%f%f%f%f%f%f%f%f%f%f%f%f%f%f%f%f%f%f%f%f%f...
              %f%f%f%f%f%f%f%f%f%f%f%f%f%f%f%f%f%f%f%f%f%f%f%f%f%f%f%f%f%f...
              %f%f%f%f%f%f%f%f%f%f%f%f%f%f%[^\n\r]';
fileID = fopen(filename,'r');
dataArray = textscan(fileID, formatSpec, 'Delimiter', delimiter, ...
                     'EmptyValue' ,NaN,'HeaderLines' ,startRow-1, ...
                     'ReturnOnError', false, 'EndOfLine', '\r\n');
fclose(fileID);

%% SECTION 2: REDUCE DATA

% Time (ref time and ignition).
EXP_TIME(:,1) = dataArray{:,2};
EXP_TIME(:,2) = EXP_TIME(:,1) - EXP_TIME(1,1);
EXP_TIME(:,3) = EXP_TIME(:,2) - EXP_EVENT(3);
EXP_TIME_DT = EXP_EVENT(2);
EXP_TIME_IGN = EXP_EVENT(3);
EXP_TIME_TOTAL = max(EXP_TIME(:,3));
```

```
130
131 % Gas temperatures in the fire compartment.
132 EXP_FIRE_GAS(:,:,1) = [dataArray{:,3},dataArray{:,4},dataArray{:,5},...
133                        dataArray{:,6},dataArray{:,7},dataArray{:,8},...
134                        dataArray{:,9},dataArray{:,10}] - 273.15;
135 EXP_FIRE_GAS(:,:,2) = [dataArray{:,11},dataArray{:,12},dataArray{:,13},...
136                        dataArray{:,14},dataArray{:,15},dataArray{:,16},...
137                        dataArray{:,17},dataArray{:,18}] - 273.15;
138 EXP_FIRE_GAS(:,:,3) = [dataArray{:,19},dataArray{:,20},dataArray{:,21},...
139                        dataArray{:,22},dataArray{:,23},dataArray{:,24},...
140                        dataArray{:,25},dataArray{:,26}] - 273.15;
141 EXP_FIRE_GAS(:,:,4) = [dataArray{:,27},dataArray{:,28},dataArray{:,29},...
142                        dataArray{:,30},dataArray{:,31},dataArray{:,32},...
143                        dataArray{:,33},dataArray{:,34}] - 273.15;
144
145 % Wall frame temperatures.
146 EXP_FRAME = [dataArray{:,35},dataArray{:,36},dataArray{:,37},...
147              dataArray{:,38},dataArray{:,43},dataArray{:,44},...
148              dataArray{:,45},dataArray{:,46}] - 273.15;
149
150 % Back compartment gas temperatures.
151 EXP_BACK_GAS = [dataArray{:,39},dataArray{:,40},dataArray{:,41},...
152                 dataArray{:,47},dataArray{:,48},dataArray{:,49}] - 273.15;
153
154 % Back compartment surroundings temperatures.
155 EXP_BACK_SURR = [dataArray{:,42},dataArray{:,50}] - 273.15;
156
157 % Wall temperatures (main).
158 EXP_WALL_MAIN(:,:,1) = [dataArray{:,69},dataArray{:,70},...
159                         dataArray{:,71},dataArray{:,72},...
160                         dataArray{:,73},dataArray{:,74}] - 273.15;
161 EXP_WALL_MAIN(:,:,2) = [dataArray{:,67},dataArray{:,68},...
162                         dataArray{:,63},dataArray{:,64},...
163                         dataArray{:,66},dataArray{:,65}] - 273.15;
164 EXP_WALL_MAIN(:,:,3) = [dataArray{:,59},dataArray{:,60},...
165                         dataArray{:,61},dataArray{:,62},...
166                         dataArray{:,57},dataArray{:,58}] - 273.15;
167 EXP_WALL_MAIN(:,:,4) = [dataArray{:,51},dataArray{:,52},...
168                         dataArray{:,53},dataArray{:,54},...
169                         dataArray{:,55},dataArray{:,56}] - 273.15;
170
171 % Wall temperatures (unexposed).
172 EXP_WALL_REAR(:,:,1) = [dataArray{:,86},dataArray{:,87},...
173                         dataArray{:,88}] - 273.15;
174 EXP_WALL_REAR(:,:,2) = [dataArray{:,83},dataArray{:,84},...
175                         dataArray{:,85}] - 273.15;
176 EXP_WALL_REAR(:,:,3) = [dataArray{:,78},dataArray{:,79},...
177                         dataArray{:,80}] - 273.15;
178 EXP_WALL_REAR(:,:,4) = [dataArray{:,75},dataArray{:,76},...
179                         dataArray{:,77}] - 273.15;
180
181 %% SECTION 3: COMPLETE SCRIPT
182
```

```
EXP_SCRIPTVER = SCRIPTVER;
EXP_FILENAME = filename;
disp(['CSV data was imported from: "' filename '"']);
disp('Script completed.');
disp('===========================================================');
fileID = fopen('1_data_import.txt','a');
fprintf(fileID, ['CSV data was imported from: "' filename '" \n'...
                 'Script completed: ' datestr(now) '\n...\n' ] );
fclose(fileID);
clearvars SCRIPTNAME SCRIPTVER filename tempvar1 tempvar2 delimiter...
          startRow formatSpec fileID dataArray i ans;
save(replace(EXP_FILENAME,'.csv','.mat'));
```

## E.2 Steel Wall Characterization Experiments

### s_import_raw_data_steel_wall.m

```
% =============================================================
% Script: s_import_raw_data_steel_wall
% =============================================================

%% INITIALIZE SCRIPT

% Select a CSV data file
clear;clc
disp('=============================================================');
disp('Script to import raw data from a steel wall test.');
filename = uigetfile('*.csv','Select a CSV data file (raw test data)');
if filename == 0
  disp('No file selected. Script aborted.');
  disp('=============================================================');
  clearvars filename ans
  return
end
EXP_TIME_IGN = input('Ignition time (default 0 s): ');
EXP_TIME_DT = input('Time step (default 1.1 s): ');
EXP_TIME_TOTAL = input('Test duration (default 5400 s): ');

% Import data from CSV data file
delimiter = ',';
startRow = 2;
formatSpec = '%f%f%f%f%f%f%f%f%f%f%f%f%f%f%f%f%f%f%f%f%f%f%f%f%f%f%f%f...
              %f%f%f%f%f%f%f%f%f%f%f%f%f%f%f%f%f%f%f%f%f%f%f%f%f%f%f%f...
              %f%f%f%f%f%f%f%f%f%f%f%f%f%f%f%f%f%f%[^\n\r]';
fileID = fopen(filename,'r');
dataArray = textscan(fileID, formatSpec, 'Delimiter', delimiter,...
'EmptyValue' ,NaN,'HeaderLines' ,startRow-1, 'ReturnOnError', false);
```

```
fclose(fileID);


%% REDUCE DATA

% File name
EXP_FILENAME = strrep(filename,'.csv','');

% Time (ref time, not ignition)
tempvar = dataArray{:,2};
EXP_TIME = tempvar - tempvar(1);
clearvars tempvar

% Fire gas temperature (horizontal slice average)
tempvar(:,:,1) = [dataArray{:,3},dataArray{:,4},dataArray{:,5},...
                  dataArray{:,6},dataArray{:,7},dataArray{:,8},...
                  dataArray{:,9},dataArray{:,10}];
tempvar(:,:,2) = [dataArray{:,11},dataArray{:,12},dataArray{:,13},...
                  dataArray{:,14},dataArray{:,15},dataArray{:,16},...
                  dataArray{:,17},dataArray{:,18}];
tempvar(:,:,3) = [dataArray{:,19},dataArray{:,20},dataArray{:,21},...
                  dataArray{:,22},dataArray{:,23},dataArray{:,24},...
                  dataArray{:,25},dataArray{:,26}];
tempvar(:,:,4) = [dataArray{:,27},dataArray{:,28},dataArray{:,29},...
                  dataArray{:,30},dataArray{:,31},dataArray{:,32},...
                  dataArray{:,33},dataArray{:,34}];
for i = 1:8
    EXP_FIRE_GAS(:,i) = mean([tempvar(:,i,1),tempvar(:,i,2),...
                              tempvar(:,i,3),tempvar(:,i,4)],2);
end
clearvars tempvar i

% Steel wall temperature (each location)
tempvar(:,:,1) = [dataArray{:,67},dataArray{:,68},dataArray{:,69},...
                  dataArray{:,70},dataArray{:,71},dataArray{:,72},...
                  dataArray{:,73},dataArray{:,74}];
tempvar(:,:,2) = [dataArray{:,59},dataArray{:,60},dataArray{:,61},...
                  dataArray{:,62},dataArray{:,63},dataArray{:,64},...
                  dataArray{:,65},dataArray{:,66}];
tempvar(:,:,3) = [dataArray{:,51},dataArray{:,52},dataArray{:,53},...
                  dataArray{:,54},dataArray{:,55},dataArray{:,56},...
                  dataArray{:,57},dataArray{:,58}];
EXP_WALL = tempvar;
clearvars tempvar

% Wall frame temperature (top, sides, bot)
tempvar = [dataArray{:,35},dataArray{:,36},dataArray{:,37},...
           dataArray{:,38},dataArray{:,43},dataArray{:,44},...
           dataArray{:,45},dataArray{:,46}];
EXP_FRAME(:,1) = mean([tempvar(:,1),tempvar(:,5)],2);
EXP_FRAME(:,2) = mean([tempvar(:,2),tempvar(:,3),...
                       tempvar(:,6),tempvar(:,7)],2);
EXP_FRAME(:,3) = mean([tempvar(:,4),tempvar(:,8)],2);
```

```
clearvars tempvar

% Back compartment gas temperature (average)
tempvar = [dataArray{:,39},dataArray{:,40},dataArray{:,41},...
           dataArray{:,47},dataArray{:,48},dataArray{:,49}];
EXP_BACK_GAS = mean(tempvar,2);
clearvars tempvar

% Back compartment surroundings temperature (average)
tempvar = [dataArray{:,42},dataArray{:,50}];
EXP_BACK_SURR = mean(tempvar,2);
clearvars tempvar

%% COMPLETE SCRIPT

disp(['Raw data was imported from: "' filename '"']);
disp('Script completed.');
disp('=============================================================');
save(strrep(filename,'.csv','.mat'),'EXP_BACK_GAS','EXP_BACK_SURR',...
     'EXP_FILENAME','EXP_FIRE_GAS','EXP_FRAME','EXP_TIME',...
     'EXP_TIME_DT','EXP_TIME_IGN','EXP_TIME_TOTAL','EXP_WALL');
clear;
```

# Appendix F

# Computation of Incident Heat Flux — Code Listings

## F.1 Generalized Thermal Capacitance Model

s_general_model.m

```
% ------------------------------------------------------------------------
% Name: s_general_model.m
% Desc: This script calculates the forward and inverse solution for a
%       generalized thermal capacitance model.
% ------------------------------------------------------------------------

%% PREAMBLE

% Start Model
clear;clc;
disp('------------------------------------------------------------');
disp('Generalized Thermal Capacitance Model');
disp('------------------------------------------------------------');
plot_results = true;
save_results = true;
filename = 'fig-general-model';

% Geometry (sphere)
D = 1/100;
A = 4*pi*(D/2)^2;
V = 4/3*pi*(D/2)^3;

% Properties
```

```
spheat = 600;
density = 7850;
em = 0.9;
sbconst = 5.67e-8;
h_c = 10;

% Timing
dt = 5;
t_max = 600;
time = 0:dt:t_max;
n_count = t_max/dt+1;

% Input conditions - temperature
T = zeros(1,n_count);
T(1) = 300;
T_inf = T(1);

% Input conditions - heat flux
q_i = zeros(1,n_count);
q_i_initial = 0;
q_i_max = 50*1000;
q_i_rate = (q_i_max - q_i_initial)/t_max^2;
for k = 1:n_count
  t = (k-1)*dt;
  q_i(k) = q_i_rate*t^2 + q_i_initial;
end
q_i_inv = zeros(1,n_count);

% Convergeance criteria
threshold = 0.1;
max_iterations = 1000;
ht_count_max = 0;
ht_count_sum = 0;

%% MAIN

% Forward solution
disp('Computing forward solution...');
for k = 2:n_count
  % Setup state variable
  T_old = T(k-1);
  T_calc = T_old;
  ht_count = 1;
  while true
    % Calculate heat transfer coefficients
    h_r = em*sbconst*T_calc^3;
    beta = (A/(density*V*spheat))*(h_r+h_c);
    alpha = (A/(density*V*spheat))*(em*q_i(k)+h_c*T_inf);
    gamma = 1/(1+beta*dt);
    % Calculate temperature
    T_new = gamma*T_old + dt*gamma*alpha;
    % Check heat transfer coefficients
    h_r_new = em*sbconst*T_new^3;
```

```
77      if f_param_check(h_r,h_r_new,threshold); break; end;
78      T_calc = T_new;
79      ht_count = ht_count+1;
80      if ht_count > max_iterations
81        disp(['Abort: Failed to converge on step ' num2str(k) ' of ' ...
82        num2str(n_count) '.']);
83        disp('------------------------------------------------------------');
84        return;
85      end
86    end
87    % Store new temperature
88    T(k) = T_new;
89    % Calculate performance stats
90    if ht_count > ht_count_max; ht_count_max = ht_count; end;
91    ht_count_sum = ht_count_sum + ht_count;
92  end
93
94  % Inverse solution
95  disp('Computing inverse solution...');
96  for k = 2:n_count
97      h_r = em*sbconst*T(k)^3;
98      beta = (A/(density*V*spheat))*(h_r+h_c);
99      alpha = (beta+1/dt)*T(k) - (1/dt)*T(k-1);
100     q_i_inv(k) = (density*V*spheat)/(A*em)*alpha - h_c/em*T_inf;
101 end
102
103 %% POST-PROCESSING
104
105 % Plot results
106 if plot_results
107
108   % Plot settings
109   disp('Plotting results...');
110   plot_width = 3.2;
111   plot_height = 2.8;
112   plot_scale = 2;
113   range_start = 1;
114   range_end = k;
115   x_data = time(range_start:range_end)/60;
116   degC = [sprintf('%c', char(176)) 'C'];
117
118   % Plot Temperature and heat flux
119   clear y_data
120   y_data(1,:) = q_i(range_start:range_end)/1000;
121   y_data(2,:) = T(range_start:range_end)-273.15;
122   y_data(3,:) = q_i_inv(range_start:range_end)/1000;
123   f = figure(1); clf;
124   hold on;
125   yyaxis right
126   p(1) = plot(x_data,y_data(1,:),'k-','LineWidth',1.5*plot_scale);
127   yyaxis left
128   p(2) = plot(x_data,y_data(2,:),'b:','LineWidth',4*plot_scale);
129   yyaxis right
```

```
130   p(3) = plot(x_data,y_data(3,:),'r:','LineWidth',4*plot_scale);
131   h = legend(p,'Forward model input (q^{\prime\prime}_{r,i})',...
132               'Forward model result (T)',...
133               'Inverse model result (q^{\prime\prime}_{r,i})');
134   xlabel('Time (min)');
135   xlim([0,t_max/60]);
136   yyaxis left; ylim([0,600]); set(gca,'ycolor','k')
137   ylabel(['Temperature (' degC ')']);
138   yyaxis right; ylim([0,60]); set(gca,'ycolor','k')
139   ylabel('Heat Flux (kW/m^2)');
140   s_plot_settings;
141   set(h,'Location','Northwest');
142   hold off
143 %   if save_results; print([filename '.png'],'-dpng','-r300'); end;
144   if save_results; saveas(gcf,filename,'epsc'); end;
145   clear f p h
146 
147 end
148 
149 % Save results
150 if save_results; save([filename '.mat'],'time','T','q_i','q_i_inv'); end;
151 
152 % Complete script
153 disp('Script completed!');
154 disp(['Total number of steps: ' num2str(k)]);
155 disp(['Total number of iterations: ' num2str(ht_count_sum)]);
156 disp(['Average iterations per step: ' num2str(round(ht_count_sum/k,2))]);
157 disp(['Maximum iterations per step: ' num2str(ht_count_max)]);
158 disp('------------------------------------------------------------');
159 clear;
```

## f_param_check.m

```
1  % ---------------------------------------------------------------------
2  % Name: f_param_check.m
3  % Desc: This function calculates the percent difference between two values
4  %       and returns a pass/fail based on the specified % threshold.
5  % ---------------------------------------------------------------------
6  function [pass] = f_param_check(prior,posterior,threshold_percent)
7  
8  % Calculate the percent difference between the prior and posterior
9  p_diff = abs(posterior-prior)./mean([posterior,prior],2)*100;
10 if p_diff < threshold_percent
11   pass = true;
12 else
13   pass = false;
14 end
15 
16 end
```

s_plot_settings.m

```
% ------------------------------------------------------------------------
% Name: s_plot_settings.m
% Desc: This script sets various plot settings for visual appearance.
% ------------------------------------------------------------------------

grid on;
box on
set(gca,'LineWidth',0.75*plot_scale);
set(gca,'TickDir','out');
set(gca,'GridAlpha',0.25);
set(gca,'GridLineStyle','-');
set(gca,'GridColor',[0 0 0]);
set(f,'PaperUnits','inches');
set(f,'PaperPosition',[0 0 plot_scale*plot_width plot_scale*plot_height]);
set(findall(f,'-property','FontName'), 'FontName', 'Times New Roman');
set(findall(f,'-property','FontSize'), 'FontSize', 10*plot_scale);
set(h,'FontSize',8*plot_scale);
set(h,'Location','Best');
```

## F.2 Steel Wall Thermal Capacitance Model (0D)

s_steel_wall_model_0D.m

```
% ------------------------------------------------------------------------
% Name: s_steel_wall_model.m
% Desc: This script generates some dummy data for a steel wall test.
% ------------------------------------------------------------------------

%% PREAMBLE

% Start Model
clear;clc;
disp('------------------------------------------------------------');
disp('Thermal capacitance model for steel wall sensor (0D).');
disp('------------------------------------------------------------');
disp('Initializing...');

% Script options
tempvar = input('Plot results (y/n)? ','s');
if tempvar == 'y'; plot_results = true; else; plot_results = false; end;
tempvar = input('Save results (y/n)? ','s');
if tempvar == 'y'; save_results = true; else; save_results = false; end;
tempvar = input('Add noise (y/n)? ','s');
if tempvar == 'y'
```

```
  filename = 'steel-wall-model-noisy';
  noise_fire = 10;
  noise_wall = 0.5;
else
  filename = 'steel-wall-model';
  noise_fire = 0;
  noise_wall = 0;
end

% Compartment and wall geometry
D = 0.0045;
L = (75.0*25.4)/1000;
A = L^2;
V = A*D;
A_c = (94.0*92.5+2*94.00*36.0+2*92.5*36.00)*0.0254^2;
A_f = (88.5*89.5+2*136.5*89.5+2*88.0*136.5)*0.0254^2;
D_l = 6.35/1000;
A_l = 4*L*D;

% Thermophysical properties
dens = 7850;
spheat = 600;
thcond_s = 42;
thcond_l = 0.24;
em = 0.98;
em_c = 0.75;
em_f = 0.75;

% Heat transfer parameters
sbconst = 5.6704e-8;
r_c = 1/em + A/A_c*(1/em_c - 1);
r_f = 1/em + A/A_f*(1/em_f - 1);

% Timing
dt = 5;
t_max = 600;
time = 0:dt:t_max;
n_count = t_max/dt+1;

% Baseline temperatures
T_proc = zeros(1,n_count);
T_proc(1) = 25+273.15;
T_meas = T_proc;
T_inf_c = T_proc(1);
T_sur_c = T_proc(1);
T_l = T_proc(1);

% Fire temperatures
T_inf_f = zeros(1,n_count);
T_i = T_proc(1);
T_f_max = 550+273.15;
T_rate = (T_f_max - T_i)/(t_max)^2;
for k = 1:n_count
```

```
  t = (k-1)*dt;
  T_inf_f(k) = T_rate*t^2 + T_i + randn()*noise_fire;
end
T_sur_f = T_inf_f;

% Heat flux
q_f_proc = zeros(1,n_count);
h_cf = f_chtc(T_inf_f(1),T_proc(1));
q_f_proc(1) = -1/em*0 + sbconst*T_proc(1)^4 + ...
              h_cf/em*(T_proc(1) - T_inf_f(1));
q_f_meas = q_f_proc;

% Convergeance criteria
threshold = 0.1;
max_iterations = 100;
ht_count_max = 0;
ht_count_sum = 0;

%% MAIN

% Process model
disp('Computing solution using process model...');

% Forward solution
for k = 2:n_count
  % Setup state variable
  T_old = T_proc(k-1);
  T_calc = T_old;
  ht_count = 1;
  while true
    % Calculate heat transfer coefficients
    h_l = A_l/A*thcond_l/D_l;
    h_cf = f_chtc(T_inf_f(k),T_calc);
    h_rf = sbconst/r_f*(T_calc+T_sur_f(k))*(T_calc^2+T_sur_f(k)^2);
    h_cc = f_chtc(T_inf_c,T_calc);
    h_rc = sbconst/r_c*(T_calc+T_sur_c)*(T_calc^2+T_sur_c^2);
    beta  = (A/(dens*V*spheat))*(h_rf + h_cf + h_rc + h_cc + h_l);
    alpha = (A/(dens*V*spheat))*(h_rf*T_sur_f(k) + ...
            h_cf*T_inf_f(k) + h_rc*T_sur_c + h_cc*T_inf_c + h_l*T_l);
    gamma = 1/(1+beta*dt);
    % Calculate temperature
    T_new = gamma*T_old + dt*gamma*alpha;
    % Check heat transfer coefficients
    h_l = A_l/A*thcond_l/D_l;
    h_cf = f_chtc(T_inf_f(k),T_new);
    h_rf = sbconst/r_f*(T_new+T_sur_f(k))*(T_new^2+T_sur_f(k)^2);
    h_cc = f_chtc(T_inf_c,T_new);
    h_rc = sbconst/r_c*(T_new+T_sur_c)*(T_new^2+T_sur_c^2);
    beta  = (A/(dens*V*spheat))*(h_rf + h_cf + h_rc + h_cc + h_l);
    alpha_new = (A/(dens*V*spheat))*(h_rf*T_sur_f(k) + ...
                h_cf*T_inf_f(k) + h_rc*T_sur_c + h_cc*T_inf_c + h_l*T_l);
    if f_param_check(alpha,alpha_new,threshold); break; end;
    T_calc = T_new;
```

```
    ht_count = ht_count+1;
    if ht_count > max_iterations
      disp(['Abort: Failed to converge on step ' num2str(k) ' of ' ...
           num2str(n_count) '.']);
      disp('------------------------------------------------------------');
      return;
    end
  end
  % Store new temperature
  T_proc(k) = T_new;
  % Calculate performance stats
  if ht_count > ht_count_max; ht_count_max = ht_count; end;
  ht_count_sum = ht_count_sum + ht_count;
end

% Inverse solution
for k = 2:n_count
  h_l = A_l/A*thcond_l/D_l;
  h_cf = f_chtc(T_inf_f(k),T_proc(k));
  h_cc = f_chtc(T_inf_c,T_proc(k));
  h_rc = sbconst/r_c*(T_proc(k)+T_sur_c)*(T_proc(k)^2+T_sur_c^2);
  beta  = (A/(dens*V*spheat))*(h_rc + h_cc + h_l);
  alpha = (beta+1/dt)*T_proc(k) - (1/dt)*T_proc(k-1);
  q_net = -alpha*((dens*V*spheat)/A) + h_rc*T_sur_c + ...
          h_cc*T_inf_c + h_l*T_l;
  q_f_proc(k) = -1/em*q_net + sbconst*T_proc(k)^4 + ...
                h_cf/em*(T_proc(k) - T_inf_f(k));
end

% Measurement model
disp('Computing solution using measurement model...');

% Generate dummy data
T_meas = zeros(1,n_count);
T_meas_max = T_proc(n_count);
T_rate = (T_meas_max - T_i)/(t_max)^2;
for k = 1:n_count
  t = (k-1)*dt;
  T_meas(k) = T_rate*t^2 + T_i + randn()*noise_wall;
end

% Inverse solution
for k = 2:n_count
  h_l = A_l/A*thcond_l/D_l;
  h_cf = f_chtc(T_inf_f(k),T_meas(k));
  h_cc = f_chtc(T_inf_c,T_meas(k));
  h_rc = sbconst/r_c*(T_meas(k)+T_sur_c)*(T_meas(k)^2+T_sur_c^2);
  beta  = (A/(dens*V*spheat))*(h_rc + h_cc + h_l);
  alpha = (beta+1/dt)*T_meas(k) - (1/dt)*T_meas(k-1);
  q_net = -alpha*((dens*V*spheat)/A) + h_rc*T_sur_c + ...
          h_cc*T_inf_c + h_l*T_l;
  q_f_meas(k) = -1/em*q_net + sbconst*T_meas(k)^4 + ...
                h_cf/em*(T_meas(k)-T_inf_f(k));
```

```
end


%% POST-PROCESSING

% Plot results
if plot_results

  % Plot settings
  disp('Plotting results...');
  plot_width = 3.2;
  plot_height = 2.8;
  plot_scale = 2;
  range_start = 1;
  range_end = k;
  x_data = time(range_start:range_end)/60;
  degC = [sprintf('%c', char(176)) 'C'];

  % Plot temperature
  clear y_data
  y_data(1,:) = T_inf_f(range_start:range_end)-273.15;
  y_data(2,:) = T_proc(range_start:range_end)-273.15;
  y_data(3,:) = T_meas(range_start:range_end)-273.15;
  f = figure(1); clf;
  hold on;
  p(1) = plot(x_data,y_data(1,:),'k:','LineWidth',1.0*plot_scale);
  p(2) = plot(x_data,y_data(2,:),'b-','LineWidth',1.0*plot_scale);
  p(3) = plot(x_data,y_data(3,:),'r-','LineWidth',1.0*plot_scale);
  h = legend(p,'Fire gas',...
             'Process model)',...
             'Measurements');
  xlabel('Time (min)'); xlim([0,t_max/60]);
  ylabel(['Temperature (' degC ')']); ylim([0,600]);
  s_plot_settings;
  hold off
  if save_results; saveas(gcf,['fig-' filename '-T'],'epsc'); end;
  clear f p h

  % Plot heat flux
  clear y_data
  y_data(1,:) = q_f_proc(range_start:range_end)/1000;
  y_data(2,:) = q_f_meas(range_start:range_end)/1000;
  f = figure(2); clf;
  hold on;
  p(1) = plot(x_data,y_data(1,:),'b-','LineWidth',1.0*plot_scale);
  p(2) = plot(x_data,y_data(2,:),'r-','LineWidth',1.0*plot_scale);
  h = legend(p,'Process model)',...
             'Measurements');
  xlabel('Time (min)'); xlim([0,t_max/60]);
  ylabel('Incident Heat Flux (kW/m^2)'); ylim([0,30]);
  s_plot_settings;
  hold off
  if save_results; saveas(gcf,['fig-' filename '-HF'],'epsc'); end;
```

```
234     clear f p h
235
236   end
237
238   % Complete script
239   disp('Script completed!');
240   if save_results
241     % Vectorize constant temperatures
242     T_inf_c(1,1:n_count) = T_inf_c;
243     T_sur_c(1,1:n_count) = T_sur_c;
244     T_l(1,1:n_count) = T_l;
245     % Save data to standard format for reduced datafile
246     EXP_BACK_GAS = T_inf_c.';
247     EXP_BACK_SURR = T_sur_c.';
248     EXP_FILENAME = filename;
249     EXP_FIRE_GAS = [T_inf_f;T_inf_f;T_inf_f;T_inf_f;...
250                     T_inf_f;T_inf_f;T_inf_f;T_inf_f].';
251     EXP_FRAME = [T_l;T_l;T_l].';
252     EXP_TIME = time.';
253     EXP_TIME_DT = dt;
254     EXP_TIME_IGN = 0;
255     EXP_TIME_TOTAL = t_max;
256     EXP_WALL(:,1:8,1) = [T_meas;T_meas;T_meas;T_meas;...
257                          T_meas;T_meas;T_meas;T_meas].';
258     EXP_WALL(:,1:8,2) = [T_meas;T_meas;T_meas;T_meas;...
259                          T_meas;T_meas;T_meas;T_meas].';
260     EXP_WALL(:,1:8,3) = [T_meas;T_meas;T_meas;T_meas;...
261                          T_meas;T_meas;T_meas;T_meas].';
262     EXP_HF = q_f_meas.';
263     PROC_WALL(:,1:8,1) = [T_proc;T_proc;T_proc;T_proc;...
264                           T_proc;T_proc;T_proc;T_proc].';
265     PROC_WALL(:,1:8,2) = [T_proc;T_proc;T_proc;T_proc;...
266                           T_proc;T_proc;T_proc;T_proc].';
267     PROC_WALL(:,1:8,3) = [T_proc;T_proc;T_proc;T_proc;...
268                           T_proc;T_proc;T_proc;T_proc].';
269     PROC_HF = q_f_proc.';
270     save([filename '.mat'],'EXP_BACK_GAS','EXP_BACK_SURR','EXP_FILENAME',...
271                            'EXP_FIRE_GAS','EXP_FRAME','EXP_TIME',...
272                            'EXP_TIME_DT','EXP_TIME_IGN','EXP_TIME_TOTAL',...
273                            'EXP_WALL','EXP_HF','PROC_WALL','PROC_HF');
274     disp(['Results saved to: ' filename '.mat']);
275   end
276   disp('------------------------------------------------------------');
277   disp(['Total number of steps: ' num2str(k)]);
278   disp(['Total number of iterations: ' num2str(ht_count_sum)]);
279   disp(['Avg iterations per step: ' num2str(round(ht_count_sum/k,2))]);
280   disp(['Max iterations per step: ' num2str(ht_count_max)]);
281   disp('------------------------------------------------------------');
```

## f_chtc.m

```
% ------------------------------------------------------------------------
% Name: f_chtc.m
% Desc: This function calculates the convection heat transfer coefficient
%       on a wall in a compartment fire using a correlation:
%       <http://jfs.sagepub.com/content/31/5/410.full.pdf+html>.
% ------------------------------------------------------------------------
function result = f_chtc(T_gas,T_surface)

% % Generalized method (Equation 15 of the paper)
% T_ratio = (T_gas-T_surface)/T_gas;
% if T_ratio < 0.2
%   h_star = (2e-3);
% else
%   h_star = (16e-3)*T_ratio;
% end
% cp = 1000; % J/kgK
% rho = 1.2; % kg/m^3
% g = 9.81; % m/s^2
% l = 89.5*0.0254; % m
% result = h_star*rho*cp*(g*l)^(1/2); % W/m^2K

% Curve fit method (basically the same, but smoother at the transition)
result = 0.0583*abs(T_gas-T_surface) + 13.3;

end
```

## f_param_check.m

```
% ------------------------------------------------------------------------
% Name: f_param_check.m
% Desc: This function calculates the percent difference between two values
%       and returns a pass/fail based on the specified % threshold.
% ------------------------------------------------------------------------
function [pass] = f_param_check(prior,posterior,threshold_percent)

% Calculate the percent difference between the prior and posterior
p_diff = abs(posterior-prior)./mean([posterior,prior],2)*100;
if p_diff < threshold_percent
  pass = true;
else
  pass = false;
end

end
```

## s_plot_settings.m

```
% ------------------------------------------------------------------------
% Name: s_plot_settings.m
% Desc: This script sets various plot settings for visual appearance.
% ------------------------------------------------------------------------

grid on;
box on
set(gca,'LineWidth',0.75*plot_scale);
set(gca,'TickDir','out');
set(gca,'GridAlpha',0.25);
set(gca,'GridLineStyle','-');
set(gca,'GridColor',[0 0 0]);
set(f,'PaperUnits','inches');
set(f,'PaperPosition',[0 0 plot_scale*plot_width plot_scale*plot_height]);
set(findall(f,'-property','FontName'), 'FontName', 'Times New Roman');
set(findall(f,'-property','FontSize'), 'FontSize', 10*plot_scale);
set(h,'FontSize',8*plot_scale);
set(h,'Location','Best');
```

## F.3 Steel Wall Kalman Filter (0D)

### f_chtc.m

```
% ------------------------------------------------------------------------
% Name: f_chtc.m
% Desc: This function calculates the convection heat transfer coefficient
%       on a wall in a compartment fire using a correlation:
%       <http://jfs.sagepub.com/content/31/5/410.full.pdf+html>.
% ------------------------------------------------------------------------
function result = f_chtc(T_gas,T_surface)

% % Generalized method (Equation 15 of the paper)
% T_ratio = (T_gas-T_surface)/T_gas;
% if T_ratio < 0.2
%   h_star = (2e-3);
% else
%   h_star = (16e-3)*T_ratio;
% end
% cp = 1000; % J/kgK
% rho = 1.2; % kg/m^3
% g = 9.81; % m/s^2
% l = 89.5*0.0254; % m
% result = h_star*rho*cp*(g*l)^(1/2); % W/m^2K

% Curve fit method (approximation of the same curve, but with a smoother
% transition and less computational cost)
```

```
result = 0.0583*abs(T_gas-T_surface) + 13.3;

end
```

## f_ht_calc_fwd.m

```
% ------------------------------------------------------------------------
% Name: f_ht_calc_fwd.m
% Desc: This function calculates the heat transfer coefficients used in
%       the forward computation step of the 0D Kalman filter model.
% ------------------------------------------------------------------------
function [alpha,gamma] = f_ht_calc_fwd(dt,x,T_inf_f,T_sur_f,T_inf_c,...
                         T_sur_c,T_l)

% Load geometry and thermophysical properties
load('properties.mat');

% Calculate heat transfer coefficients
h_l = A_l/A*thcond_l/D_l;
h_cf = f_chtc(T_inf_f,x);
h_rf = sbconst/r_f*(x+T_sur_f).*(x.^2+T_sur_f.^2);
h_cc = f_chtc(T_inf_c,x);
h_rc = sbconst/r_c*(x+T_sur_c).*(x.^2+T_sur_c.^2);
beta  = (A/(dens*V*spheat))*(h_rf + h_cf + h_rc + h_cc + h_l);
gamma = (1+beta*dt).^(-1);
alpha = (A/(dens*V*spheat))*(h_rf.*T_sur_f + h_cf.*T_inf_f + ...
                             h_rc.*T_sur_c + h_cc.*T_inf_c + h_l.*T_l);

end
```

## f_ht_calc_inv.m

```
% ------------------------------------------------------------------------
% Name: f_ht_calc_fwd.m
% Desc: This function calculates the heat transfer coefficients used in
%       the inverse computation step of the 0D Kalman filter model.
% ------------------------------------------------------------------------
function [q_inc_m,q_inc_s] = f_ht_calc_inv(dt,x_new,x_old,P_new,...
                             T_inf_f,T_inf_c,T_sur_c,T_l,std_pro)

% Load geometry and thermophysical properties
load('properties.mat');

% Calculate state stdev from covariance
s_new = sqrt(diag(P_new));

% Calculate heat transfer coefficients
h_l = A_l/A*thcond_l/D_l;
```

```
h_cf = f_chtc(T_inf_f,x_new);
h_cc = f_chtc(T_inf_c,x_new);
h_rc = sbconst/r_c*(x_new+T_sur_c).*(x_new.^2+T_sur_c.^2);
beta  = (A/(dens*V*spheat))*(h_rc + h_cc + h_l);
alpha_m = (beta+1/dt).*x_new - (1/dt).*x_old;

% Calculate variance on alpha
gamma = (1+dt*beta).^(-1);
G = diag(dt*gamma);
S = std_pro*std_pro.'; % diag(std_pro.^2);
Q = G*S*G.';
alpha_s = sqrt(diag(Q))/(gamma*dt);

% Calculate net heat flux and variance
q_net_m = -alpha_m.*((dens*V*spheat)/A) + h_rc.*T_sur_c + ...
          h_cc.*T_inf_c + h_l.*T_l;
q_net_s = alpha_s.*((dens*V*spheat)/A);

% Calculate incident heat flux and variance
q_inc_m = -1/em*q_net_m + sbconst.*x_new.^4 + ...
          1/em*h_cf.*(x_new - T_inf_f);
q_inc_s = 1/em*q_net_s + sbconst.*s_new.^4 + 1/em*h_cf.*(s_new);

end
```

## f_initial.m

```
% -------------------------------------------------------------------------
% Name: f_initial.m
% Desc: This function calculates the initial state, covariance, and heat
%       flux for input to the 0D Kalman filter model.
% -------------------------------------------------------------------------
function [x,P,std_pro,q_inc_m,q_inc_s] = f_initial(dt,n,T_i,...
         T_inf_f,T_inf_c,T_sur_c,T_l,phi)

% State
x = ones(n,1)*T_i;

% Heat transfer parameters and process variance
load('properties.mat');
h_l = A_l/A*thcond_l/D_l;
h_cc = f_chtc(T_inf_c,x);
h_rc = sbconst/r_c*(x+T_sur_c).*(x.^2+T_sur_c.^2);
beta = (A/(dens*V*spheat))*(h_rc + h_cc + h_l);
alpha = beta.*x;
std_pro = phi*alpha;

% State variance
P = diag((std_pro(:,1)*dt).^2);

% Heat flux
```

```
25 [q_inc_m,q_inc_s] = f_ht_calc_inv(dt,x,x,P,T_inf_f,T_inf_c,T_sur_c,...
26                                   T_l,std_pro);
27
28 end
```

## f_kf_predict.m

```
1  % ---------------------------------------------------------------------
2  % Name: f_kf_update.m
3  % Desc: This function calculates the mean and variance for the predict
4  %       step of the Kalman filter.
5  % ---------------------------------------------------------------------
6  function [x_new,P_new] = f_kf_predict(x,P,F,Q,varargin)
7
8  % Resolve the optional control input function (B and U)
9  numvarargs = length(varargin);
10 if numvarargs > 2
11     error('Error: f_predict requires either 4 or 6 inputs');
12 end
13 optargs = {0 0};
14 optargs(1:numvarargs) = varargin;
15 [B,u] = optargs{:};
16
17 % Calculate the new prior
18 x_new = F*x + B*u;
19 P_new = F*P*F.' + Q;
20
21 end
```

## f_kf_setup.m

```
1  % ---------------------------------------------------------------------
2  % Name: f_kf_setup.m
3  % Desc: This function sets up the various inputs to the Kalman filter.
4  % ---------------------------------------------------------------------
5  function [F,B,u,Q,R,H] = f_kf_setup(dt,alpha,gamma,std_pro,std_sen)
6
7  % State transition function
8  F = diag(gamma);
9
10 % Control input function
11 B = diag(dt*gamma);
12
13 % Control input
14 u = alpha;
15
16 % Process covariance
17 G = B;
```

```
S = std_pro*std_pro.'; % diag(std_pro.^2);
Q = G*S*G.';

% Measurement covariance
R = std_sen*std_sen.'; % diag(std_sen.^2);

% Measurement transformation
H = eye(length(std_sen));

end
```

## f_kf_update.m

```
% -------------------------------------------------------------------------
% Name: f_kf_update.m
% Desc: This function calculates the mean and variance for the update
%       step of the Kalman filter.
% -------------------------------------------------------------------------
function [x_new,P_new] = f_kf_update(x,P,z,R,varargin)

% Resolve the optional measurement function (B and U)
numvarargs = length(varargin);
if numvarargs > 1
    error('Error: f_update requires either 4 or 5 inputs');
end
optargs = {0};
optargs(1:numvarargs) = varargin;
[H] = optargs{:};

% Calculate the system uncertainty, Kalman gain, and residual
S = H*P*H.' + R;
K = (P*H.')/S;
y = z - H*x;

% Calculate the new posterior
x_new = x + K*y;
P_new = (eye(size(x,1)) - K*H)*P;

end
```

## f_param_check.m

```
% -------------------------------------------------------------------------
% Name: f_param_check.m
% Desc: This function calculates the percent difference between two values
%       and returns a pass/fail based on the specified % threshold.
% -------------------------------------------------------------------------
function [pass] = f_param_check(prior,posterior,threshold_percent)
```

```
7
8  p_diff = abs(posterior-prior)./mean([posterior,prior],2)*100;
9  if p_diff < threshold_percent
10   pass = true;
11 else
12   pass = false;
13 end
14
15 end
```

## s_import_data_0D_KF.m

```
1  % ------------------------------------------------------------------------
2  % Name: s_import_data_0D_KF.m
3  % Desc: This script imports reduced datafiles from a steel wall test to
4  %       be used with the 0D Kalman filter model. The user can also select
5  %       a "dummy" datafile, created by "s_steel_wall_model_0D.m".
6  % ------------------------------------------------------------------------
7
8  %% MAIN
9
10 % Import test data
11 filename = uigetfile('*.mat','Select a steel wall test data file (MAT).');
12 if filename == 0
13   clear filename
14   return
15 else
16     load(filename);
17 end
18 tempvar = input('Is this a dummy data file (y/n)? ','s');
19 if tempvar == 'y'
20   dummy = true;
21 else
22   dummy = false;
23 end
24
25 % State references
26 n = 1;
27 m = 1;
28
29 % Timing
30 dt = EXP_TIME_DT;
31 n_offset = round(EXP_TIME_IGN/EXP_TIME_DT,0)+1;
32 n_steps = round(EXP_TIME_TOTAL/EXP_TIME_DT,0)+1;
33 time_range = n_offset:n_steps+n_offset-1;
34 t_tot = (n_steps-1)*dt;
35 time = 0:dt:t_tot;
36
37 % Fire-side gases and surroundings
38 T_inf_f = EXP_FIRE_GAS(time_range,:).';
39 T_inf_f = mean(T_inf_f,1);
```

```
T_sur_f = T_inf_f;

% Cool-side gases and surroundings
T_inf_c = EXP_BACK_GAS(time_range).';
T_sur_c = EXP_BACK_SURR(time_range).';

% Wall frame
T_l_left = EXP_FRAME(time_range,2).'; % Left
T_l_right = EXP_FRAME(time_range,2).'; % Right
T_l_top = EXP_FRAME(time_range,1).'; % Top
T_l_bot = EXP_FRAME(time_range,3).'; % Bot
T_l = [T_l_left; T_l_right; T_l_top; T_l_bot];
T_l = mean(T_l,1);
clear T_l_left T_l_right T_l_top T_l_bot

% Steel wall (meas)
T_w_left = EXP_WALL(time_range,1:8,1).';
T_w_mid = EXP_WALL(time_range,1:8,2).';
T_w_right = EXP_WALL(time_range,1:8,3).';
T_w_meas = [T_w_left; T_w_mid; T_w_right];
T_w_meas = mean(T_w_meas,1);
clear T_w_left T_w_mid T_w_right

% Steel wall (proc) -- dummy data only
if dummy
  T_w_left = PROC_WALL(time_range,1:8,1).';
  T_w_mid = PROC_WALL(time_range,1:8,2).';
  T_w_right = PROC_WALL(time_range,1:8,3).';
  T_w_proc = [T_w_left; T_w_mid; T_w_right];
  T_w_proc = mean(T_w_proc,1);
  clear T_w_left T_w_mid T_w_right
end

% Heat flux -- dummy data only
if dummy
  q_f_proc = PROC_HF.';
  q_f_meas = EXP_HF.';
end
```

## s_plot_settings.m

```
% --------------------------------------------------------------------------
% Name: s_plot_settings.m
% Desc: This script sets various plot settings for visual appearance.
% --------------------------------------------------------------------------

grid on;
box on
set(gca,'LineWidth',0.75*plot_scale);
set(gca,'TickDir','out');
set(gca,'GridAlpha',0.25);
```

```
set(gca,'GridLineStyle','-');
set(gca,'GridColor',[0 0 0]);
set(f,'PaperUnits','inches');
set(f,'PaperPosition',[0 0 plot_scale*plot_width plot_scale*plot_height]);
set(findall(f,'-property','FontName'), 'FontName', 'Times New Roman');
set(findall(f,'-property','FontSize'), 'FontSize', 10*plot_scale);
set(h,'FontSize',8*plot_scale);
set(h,'Location','Best');
```

## s_properties.m

```
% ------------------------------------------------------------------------
% Name: s_properties.m
% Desc: This script imports the geometry and thermophysical properties
%       for use in the 0D Kalman filter model.
% ------------------------------------------------------------------------

% Start
clear

% Compartment and wall geometry
D = 0.0045;
L = (75.0*25.4)/1000;
A = L^2;
V = A*D;
A_c = (94.0*92.5+2*94.00*36.0+2*92.5*36.00)*0.0254^2;
A_f = (88.5*89.5+2*136.5*89.5+2*88.0*136.5)*0.0254^2;
D_l = 6.35/1000;
A_l = 4*L*D;

% Thermophysical properties
dens = 7850;
spheat = 600;
thcond_s = 42;
thcond_l = 0.24;
em = 0.98;
em_c = 0.75;
em_f = 0.75;

% Heat transfer parameters
sbconst = 5.6704e-8;
r_c = 1/em + A/A_c*(1/em_c - 1);
r_f = 1/em + A/A_f*(1/em_f - 1);

% End
save('properties.mat');
clear
```

## s_steel_wall_model_0D_KF.m

```
% ------------------------------------------------------------------------
% Name: s_steel_wall_model_0D_KF.m
% Desc: This script calculates the temperature of the steel wall sensor
%       and heat flux to the steel wall sensor during a fire exposure
%       using the 0D kalman filter model.
% Note: Increase the process gain to make the filter favour measurements
%       over process estimates, but decrease certainty in the predictions.
% ------------------------------------------------------------------------

%% PREAMBLE

% Initialize script
clear;clc;
disp('-------------------------------------------------------------');
disp('Thermal capacitance model for steel wall sensor (0D KF).');
disp('-------------------------------------------------------------');
disp('Initializing...');
s_import_data_0D_KF;
if not(exist('filename','var'))
  disp('No file selected. Script aborted.');
  disp('-------------------------------------------------------------');
  return
end
disp(['Datafile selected: ' filename]);
filename = replace(filename,'.mat','');

% Script options
tempvar = input('Plot results (y/n)? ','s');
if tempvar == 'y'; plot_results = true; else; plot_results = false; end;
tempvar = input('Save results (y/n)? ','s');
if tempvar == 'y'; save_results = true; else; save_results = false; end;

% Process and sensor variance
phi = 0.05;
std_pro = zeros(n,n_steps);
std_sen = ones(n,1)*2.0;

% Convergeance criteria
threshold = 0.1;
max_iterations = 100;
ht_count_max = 1;
ht_count_sum = 1;

% Pre-allocate variables
x = zeros(n,n_steps);
P = zeros(n,n,n_steps);
q_inc_m = zeros(n,n_steps);
q_inc_s = zeros(n,n_steps);

% Initial Conditions
T_i = T_w_meas(1);
[x(:,1),P(:,:,1),std_pro(:,1),q_inc_m(:,1),q_inc_s(:,1)] = ...
f_initial(dt,n,T_i,T_inf_f(:,1),T_inf_c(:,1),T_sur_c(:,1),T_l(:,1),phi);
```

```
54
55 %% MAIN
56
57 % Run the Kalman Filter
58 progress = 0;
59 n_update = 1;
60 for k = 2:n_steps
61   % Progress / housekeeping
62   if mod(k-1,n_update) == 0
63     fprintf(1, repmat('\b',1,progress));
64     progress = fprintf('Running Kalman filter... %d of %d',k-1,n_steps);
65   end
66   ht_count = 1;
67   % Prior state and covariance
68   x_old = x(:,k-1);
69   x_calc = x_old;
70   P_old = P(:,:,k-1);
71   P_calc = P_old;
72   % Current measurements
73   z = T_w_meas(:,k);
74   % State calculations
75   while true
76     % Heat transfer coefficients
77     [alpha,gamma] = f_ht_calc_fwd(dt,x_calc,T_inf_f(:,k),T_sur_f(k),...
78                     T_inf_c(k),T_sur_c(k),T_l(:,k));
79     % Process error
80     std_pro(:,k) = phi*alpha;
81     % Setup Kalman filter matrices
82     [F,B,u,Q,R,H] = f_kf_setup(dt,alpha,gamma,std_pro(:,k),std_sen);
83     % Predict state
84     [x_new,P_new] = f_kf_predict(x_old,P_old,F,Q,B,u);
85     % Update state
86     [x_new,P_new] = f_kf_update(x_new,P_new,z,R,H);
87     % Update parameters
88     [alpha_new,gamma_new] = f_ht_calc_fwd(dt,x_new,T_inf_f(:,k),...
89                             T_sur_f(k),T_inf_c(k),T_sur_c(k),T_l(:,k));
90     % Check parameters
91     if f_param_check(alpha,alpha_new,threshold); break; end;
92     x_calc = x_new;
93     P_calc = P_new;
94     ht_count = ht_count+1;
95     if ht_count > max_iterations
96       fprintf(1, repmat('\b',1,progress));
97       progress = fprintf('Iteration step did not converge.\n');
98       disp(['Aborted on step ' num2str(k) ' of ' num2str(n_steps) '.']);
99       disp('------------------------------------------------------------');
100      return;
101    end
102  end
103  % Output posterior state and parameters
104  x(:,k) = x_new;
105  P(:,:,k) = P_new;
106  % Calculate heat flux (inverse solution)
```

```
  [q_inc_m(:,k),q_inc_s(:,k)] = f_ht_calc_inv(dt,x_new,x_old,...
                                P_new,T_inf_f(:,k),T_inf_c(k),...
                                T_sur_c(k),T_l(:,k),std_pro(:,k));
  % Calculate performance stats
  if ht_count > ht_count_max; ht_count_max = ht_count; end;
  ht_count_sum = ht_count_sum + ht_count;
end

% Update progress
fprintf(1, repmat('\b',1,progress));
progress = fprintf('Running Kalman filter...\n');

%% POST-PROCESSING

% Plot results
if plot_results

  % Plot settings
  disp('Plotting results...');
  plot_width = 3.2;
  plot_height = 2.8;
  plot_scale = 2;
  range_start = 1;
  range_end = k;
  x_data = time(range_start:range_end)/60;
  degC = [sprintf('%c', char(176)) 'C'];

  % Plot temperature
  f = figure(1); clf;
  clear y_data
  hold on;
  if dummy
    y_data(1,:) = T_inf_f(1,range_start:range_end)-273.15;
    y_data(2,:) = x(1,range_start:range_end)-273.15;
    y_data(3,:) = T_w_meas(1,range_start:range_end)-273.15;
    y_data(4,:) = T_w_proc(1,range_start:range_end)-273.15;
    p(1) = plot(x_data,y_data(1,:),'k-','LineWidth',0.5*plot_scale);
    p(2) = plot(x_data,y_data(2,:),'k-','LineWidth',1.0*plot_scale);
    p(3) = plot(x_data,y_data(3,:),'r:','LineWidth',1.0*plot_scale);
    p(4) = plot(x_data,y_data(4,:),'b:','LineWidth',1.0*plot_scale);
    h = legend(p,'Fire gas','Kalman filter',...
                 'Measurements','Process model');
  else
    y_data(1,:) = T_inf_f(1,range_start:range_end)-273.15;
    y_data(2,:) = x(1,range_start:range_end)-273.15;
    y_data(3,:) = T_w_meas(1,range_start:range_end)-273.15;
    p(1) = plot(x_data,y_data(1,:),'r-','LineWidth',0.5*plot_scale);
    p(2) = plot(x_data,y_data(2,:),'k-','LineWidth',1.0*plot_scale);
    p(3) = plot(x_data,y_data(3,:),'k:','LineWidth',2.0*plot_scale);
    h = legend(p,'Fire gas','Kalman filter','Measurements');
  end
  xlabel('Time (min)'); xlim([0,round(t_tot/60,0)]);
                        xticks(0:round(t_tot/60,0)/5:round(t_tot/60,0));
```

```
  ylabel(['Temperature (' degC ')']); ylim([0,600]); yticks(0:100:600);
  s_plot_settings;
  hold off
  if save_results; saveas(gcf,['fig-' filename '-T'],'epsc'); end;
  clear f p h

  % Plot heat flux
  f = figure(2); clf;
  clear y_data
  hold on;
  if dummy
    y_data(1,:) = q_inc_m(1,range_start:range_end)/1000;
    y_data(2,:) = y_data(1,:) + q_inc_s(1,range_start:range_end)/1000;
    y_data(3,:) = y_data(1,:) - q_inc_s(1,range_start:range_end)/1000;
    y_data(4,:) = q_f_meas(1,range_start:range_end)/1000;
    y_data(5,:) = q_f_proc(1,range_start:range_end)/1000;
    p(1) = plot(x_data,y_data(1,:),'k-','LineWidth',1.0*plot_scale);
    p(2) = plot(x_data,y_data(2,:),'k-','LineWidth',0.5*plot_scale);
    p(3) = plot(x_data,y_data(3,:),'k-','LineWidth',0.5*plot_scale);
    p(4) = plot(x_data,y_data(4,:),'r:','LineWidth',1.0*plot_scale);
    p(5) = plot(x_data,y_data(5,:),'b:','LineWidth',1.0*plot_scale);
    h = legend([p(1) p(2) p(4) p(5)],'Kalman Filter (\mu)',...
                                     'Kalman Filter (\mu\pm\sigma)',...
                                     'Measurements',...
                                     'Process model');
  else
    y_data(1,:) = q_inc_m(1,range_start:range_end)/1000;
    y_data(2,:) = y_data(1,:) + q_inc_s(1,range_start:range_end)/1000;
    y_data(3,:) = y_data(1,:) - q_inc_s(1,range_start:range_end)/1000;
    p(1) = plot(x_data,y_data(1,:),'k-','LineWidth',1.0*plot_scale);
    p(2) = plot(x_data,y_data(2,:),'r-','LineWidth',0.5*plot_scale);
    p(3) = plot(x_data,y_data(3,:),'b-','LineWidth',0.5*plot_scale);
    h = legend([p(1) p(2) p(3)],'Kalman Filter (\mu)',...
                                'Kalman Filter (\mu+\sigma)',...
                                'Kalman Filter (\mu-\sigma)');
  end
  xlabel('Time (min)'); xlim([0,round(t_tot/60,0)]);
                        xticks(0:round(t_tot/60,0)/5:round(t_tot/60,0));
  ylabel('Incident Heat Flux (kW/m^2)'); ylim([0,25]); yticks(0:5:25);
  s_plot_settings;
  hold off
  if save_results; saveas(gcf,['fig-' filename '-HF'],'epsc'); end;
  clear f p h

end

% Complete script
disp('Script completed!');
if save_results
  save(['results-' filename '.mat'],'time','x','T_w_meas','T_inf_f',...
                                    'q_inc_m','q_inc_s','std_pro');
  disp(['Results saved to: results-' filename '.mat']);
end
```

```
213 disp('------------------------------------------------------------');
214 disp(['Total number of steps: ' num2str(k)]);
215 disp(['Total number of iterations: ' num2str(ht_count_sum)]);
216 disp(['Avg iterations per step: ' num2str(round(ht_count_sum/k,2))]);
217 disp(['Max iterations per step: ' num2str(ht_count_max)]);
218 disp('------------------------------------------------------------');
```

## F.4 Steel Wall Kalman Filter (2D)

### f_chtc.m

```
1  % ---------------------------------------------------------------------
2  % Name: f_chtc.m
3  % Desc: This function calculates the convection heat transfer coefficient
4  %       on a wall in a compartment fire using a correlation:
5  %       <http://jfs.sagepub.com/content/31/5/410.full.pdf+html>.
6  % ---------------------------------------------------------------------
7  function result = f_chtc(T_gas,T_surface)
8
9  % % Generalized method (Equation 15 of the paper)
10 % T_ratio = (T_gas-T_surface)/T_gas;
11 % if T_ratio < 0.2
12 %   h_star = (2e-3);
13 % else
14 %   h_star = (16e-3)*T_ratio;
15 % end
16 % cp = 1000; % J/kgK
17 % rho = 1.2; % kg/m^3
18 % g = 9.81; % m/s^2
19 % l = 89.5*0.0254; % m
20 % result = h_star*rho*cp*(g*l)^(1/2); % W/m^2K
21
22 % Curve fit method (approximation of the same curve, but with a smoother
23 % transition and less computational cost)
24 result = 0.0583*abs(T_gas-T_surface) + 13.3;
25
26 end
```

### f_ht_calc_fwd.m

```
1  % ---------------------------------------------------------------------
2  % Name: f_ht_calc_fwd.m
3  % Desc: This function calculates the heat transfer coefficients used in
4  %       the forward computation step of the 2D Kalman filter model.
```

```
% ------------------------------------------------------------------------
function [alpha,beta] = f_ht_calc_fwd(dt,a,b,x,T_inf_f,...
                                      T_sur_f,T_inf_c,T_sur_c)

% Heat transfer coefficients
h_cf = f_chtc(T_inf_f,x);
h_rf = (x+T_sur_f).*(x.^2+T_sur_f.^2);
h_cc = f_chtc(T_inf_c,x);
h_rc = (x+T_sur_c).*(x.^2+T_sur_c.^2);

% Beta
beta_tot = b(:,1) + b(:,2) + b(:,3) + b(:,4) + ...
               b(:,5).*h_rf + b(:,6).*h_cf + b(:,7).*h_rc + b(:,8).*h_cc;
beta(:,:) = [(1/dt-beta_tot),b(:,1),b(:,2),b(:,3),b(:,4)];

% Alpha
alpha_c = a(:,3).*h_rc.*T_sur_c +  a(:,1).*h_cc.*T_inf_c;
alpha_f = a(:,2).*h_rf.*T_sur_f +  a(:,1).*h_cf.*T_inf_f;
alpha = alpha_f + alpha_c;

end
```

## f_ht_calc_inv.m

```
% ------------------------------------------------------------------------
% Name: f_ht_calc_fwd.m
% Desc: This function calculates the heat transfer coefficients used in
%       the inverse computation step of the 2D Kalman filter model.
% ------------------------------------------------------------------------
function [q_inc_m,q_inc_s] = f_ht_calc_inv(dt,n,n_ref,a,b,x_new,x_old,...
                             P_new,T_inf_f,T_inf_c,T_sur_c,std_pro)

% Heat transfer coefficients
h_cf = f_chtc(T_inf_f,x_new);
h_cc = f_chtc(T_inf_c,x_new);
h_rc = (x_new+T_sur_c).*(x_new.^2+T_sur_c.^2);

% Beta
beta_tot = b(:,1) + b(:,2) + b(:,3) + b(:,4) + ...
               b(:,7).*h_rc + b(:,8).*h_cc;
beta(:,:) = [(1/dt-beta_tot),b(:,1),b(:,2),b(:,3),b(:,4)];

% Inverse state transition function
F = zeros(n,n);
for i = 1:n
  ref = n_ref(i,:);
  for j = 1:5
    F(i,ref(j)) = dt*beta(i,j);
  end
end

```

```
% Alpha
alpha_c = a(:,3).*h_rc.*T_sur_c + a(:,1).*h_cc.*T_inf_c;
alpha_m = 1/dt*(x_new - F*x_old);

% Variance on alpha
G = eye(n)*dt;
S = diag(std_pro.^2);
% S = phi*(eye(n)*std_pro^2);
Q = G*S*G.';
alpha_s = sqrt(diag(Q))/(dt);

% Calculate net heat flux and variance
q_net_m = -a(:,1).^(-1).*(alpha_m - alpha_c);
q_net_s = a(:,1).^(-1).*(alpha_s);
q_net_v = q_net_s*q_net_s.';

% Calculate incident heat flux and variance
sbconst = 5.6704e-8;
em = 0.98;
q_inc_m = -1/em*q_net_m + sbconst*x_new.^4 + 1/em*h_cf.*(x_new - T_inf_f);
q_inc_v = 1/em*q_net_v + sbconst*(P_new.^4) + 1/em*h_cf.*(P_new);
q_inc_s = sqrt(diag(q_inc_v));

end
```

## f_import_state_refs.m

```
% ------------------------------------------------------------------------
% Name: f_import_state_refs.m
% Desc: This function imports all state reference and heat transfer
%       coefficient data for a given model formulation from CSV files.
% ------------------------------------------------------------------------
function [n,n_hid,n_var,n_wall,n_wall_r,n_wall_c,n_ref,n_T_f_ref,a,b] ...
         = f_import_state_refs(filename)

% Import data
delimiter = ',';
startRow = 2;
formatSpec = '%s%s%s%s%s%s%s%s%s%s%s%s%s%s%s%s%s%s%s%s%s%s%s%[^\n\r]';
fileID = fopen(filename,'r');
dataArray = textscan(fileID,formatSpec,'Delimiter',delimiter,...
            'HeaderLines',startRow-1, 'ReturnOnError', false,...
             'EndOfLine', '\r\n');
fclose(fileID);
raw = repmat({''},length(dataArray{1}),length(dataArray)-1);
for col=1:length(dataArray)-1
  raw(1:length(dataArray{col}),col) = dataArray{col};
end
numericData = NaN(size(dataArray{1},1),size(dataArray,2));
for col=[1,2,3,4,5,6,7,8,9,10,11,12,13,14,15,16,17,18,19,20,21,22,23]
  rawData = dataArray{col};
```

```
  for row=1:size(rawData, 1);
    regexstr = '(?<prefix>.*?)(?<numbers>([-]*(\d+[\,]*)+[\.]{0,1}\d*...
                [eEdD]{0,1}[-+]*\d*[i]{0,1})|([-]*(\d+[\,]*)*[\.]{1,1}...
                \d+[eEdD]{0,1}[-+]*\d*[i]{0,1}))(?<suffix>.*)';
    try
      result = regexp(rawData{row}, regexstr, 'names');
      numbers = result.numbers;
      invalidThousandsSeparator = false;
      if any(numbers==',');
        thousandsRegExp = '^\d+?(\,\d{3})*\.{0,1}\d*$';
        if isempty(regexp(numbers, thousandsRegExp, 'once'));
          numbers = NaN;
          invalidThousandsSeparator = true;
        end
      end
      if ¬invalidThousandsSeparator;
        numbers = textscan(strrep(numbers, ',', ''), '%f');
        numericData(row, col) = numbers{1};
        raw{row, col} = numbers{1};
      end
    catch me
    end
  end
end

% Wall configuration
n = cell2mat(raw(1, 18));
n_hid = cell2mat(raw(1, 19));
n_var = cell2mat(raw(1, 20));
n_wall = cell2mat(raw(1, 21));
n_wall_r = cell2mat(raw(1, 22));
n_wall_c = cell2mat(raw(1, 23));

% State references
state = cell2mat(raw(:, 1));
state_x1 = cell2mat(raw(:, 2));
state_x2 = cell2mat(raw(:, 3));
state_y1 = cell2mat(raw(:, 4));
state_y2 = cell2mat(raw(:, 5));
n_ref = [state,state_x1,state_x2,state_y1,state_y2];
n_T_f_ref = cell2mat(raw(:, 6));

% Beta
b_x1 = cell2mat(raw(:, 7));
b_x2 = cell2mat(raw(:, 8));
b_y1 = cell2mat(raw(:, 9));
b_y2 = cell2mat(raw(:, 10));
b_rf = cell2mat(raw(:, 11));
b_cf = cell2mat(raw(:, 12));
b_rc = cell2mat(raw(:, 13));
b_cc = cell2mat(raw(:, 14));
b = [b_x1,b_x2,b_y1,b_y2,b_rf,b_cf,b_rc,b_cc];

```

```
78 % Alpha
79 a = cell2mat(raw(:, 15));
80 a_rf = cell2mat(raw(:, 16));
81 a_rc = cell2mat(raw(:, 17));
82 a = [a,a_rf,a_rc];
83
84 end
```

## f_initial.m

```
1  % -------------------------------------------------------------------------
2  % Name: f_initial.m
3  % Desc: This function calculates the initial state, covariance, and heat
4  %       flux for input to the 0D Kalman filter model.
5  % -------------------------------------------------------------------------
6  function [x,P,std_pro,q_inc_m,q_inc_s] = f_initial(dt,n,n_ref,a,b,T_i,...
7           T_inf_f,T_inf_c,T_sur_c,phi)
8
9  % State
10 x = ones(n,1)*T_i;
11
12 % Heat transfer coefficients
13 h_cc = f_chtc(T_inf_c,x);
14 h_rc = (x+T_sur_c).*(x.^2+T_sur_c.^2);
15
16 % Beta
17 beta_tot = b(:,1) + b(:,2) + b(:,3) + b(:,4) + ...
18                b(:,7).*h_rc + b(:,8).*h_cc;
19 beta(:,:) = [(1/dt-beta_tot),b(:,1),b(:,2),b(:,3),b(:,4)];
20
21 % Inverse state transition function
22 F = zeros(n,n);
23 for i = 1:n
24   ref = n_ref(i,:);
25   for j = 1:5
26     F(i,ref(j)) = dt*beta(i,j);
27   end
28 end
29
30 % Alpha
31 alpha_m = 1/dt*(x - F*x);
32
33 % Process variance
34 std_pro = phi*alpha_m;
35
36 % State variance
37 P = diag((std_pro(:,1)*dt).^2);
38
39 % Heat flux
40 [q_inc_m,q_inc_s] = f_ht_calc_inv(dt,n,n_ref,a,b,x,x,P,...
41                                   T_inf_f,T_inf_c,T_sur_c,std_pro);
```

```
42
43 end
```

## f_kf_H.m

```
1  % ------------------------------------------------------------------------
2  % Name: f_kf_H.m
3  % Desc: This function calculates the transformation matrix based on the
4  %       user-selected number of sensors and states.
5  % ------------------------------------------------------------------------
6  function [ H ] = f_kf_H(m,n,n_hid)
7
8  % Transformation matrix for n states and m sensors (m = n, interpolated)
9  H = zeros(m+n_hid,n);
10 for i = 1:m
11   H(i,i) = 1;
12 end
13 for i = 1:n_hid
14   H(m+i,(n-n_hid)+i) = 1;
15 end
16
17 end
```

## f_kf_predict.m

```
1  % ------------------------------------------------------------------------
2  % Name: f_kf_update.m
3  % Desc: This function calculates the mean and variance for the predict
4  %       step of the Kalman filter.
5  % ------------------------------------------------------------------------
6  function [x_new,P_new] = f_kf_predict(x,P,F,Q,varargin)
7
8  % Resolve the optional control input function (B and U)
9  numvarargs = length(varargin);
10 if numvarargs > 2
11     error('Error: f_predict requires either 4 or 6 inputs');
12 end
13 optargs = {0 0};
14 optargs(1:numvarargs) = varargin;
15 [B,u] = optargs{:};
16
17 % Calculate the new prior
18 x_new = F*x + B*u;
19 P_new = F*P*F.' + Q;
20
21 end
```

## f_kf_setup.m

```
% ------------------------------------------------------------------------
% Name: f_kf_setup.m
% Desc: This function sets up the various inputs to the Kalman filter.
% ------------------------------------------------------------------------
function [F,B,u,Q,R,H] = f_kf_setup(dt,n,n_hid,m,n_ref,alpha,beta,...
                         std_pro,std_sen)

% State transition function
F = zeros(n,n);
for i = 1:n
  for j = 1:5
    F(i,n_ref(i,j)) = dt*beta(i,j);
  end
end

% Control input function
B = eye(n)*dt;

% Control input
u = alpha;

% Process covariance
G = B;
S = diag(std_pro.^2);
Q = G*S*G.';

% Measurement covariance
R = diag(std_sen.^2);

% Measurement transformation
H = f_kf_H(m,n,n_hid);

end
```

## f_kf_update.m

```
% ------------------------------------------------------------------------
% Name: f_kf_update.m
% Desc: This function calculates the mean and variance for the update
%       step of the Kalman filter.
% ------------------------------------------------------------------------
function [x_new,P_new,K] = f_kf_update(x,P,z,R,varargin)

% Resolve the optional measurement function (B and U)
numvarargs = length(varargin);
if numvarargs > 1
    error('Error: f_update requires either 4 or 5 inputs');
```

```
end
optargs = {0};
optargs(1:numvarargs) = varargin;
[H] = optargs{:};

% Calculate the system uncertainty, Kalman gain, and residual
S = H*P*H.' + R;
K = (P*H.')/S;
y = z - H*x;

% Calculate the new posterior
x_new = x + K*y;
P_new = (eye(size(x,1)) - K*H)*P;

end
```

## f_param_check.m

```
% ------------------------------------------------------------------------
% Name: f_param_check.m
% Desc: This function calculates the percent difference between two values
%       and returns a pass/fail based on the specified % threshold.
% ------------------------------------------------------------------------
function [pass] = f_param_check(prior,posterior,threshold_percent)

p_diff = abs(posterior-prior)./mean([posterior,prior],2)*100;
if p_diff < threshold_percent
  pass = true;
else
  pass = false;
end

end
```

## s_import_data_2D_KF.m

```
% ------------------------------------------------------------------------
% Name: s_import_data_2D_KF.m
% Desc: This script imports reduced datafiles from a steel wall test to
%       be used with the 2D Kalman filter model. The user can also select
%       a "dummy" datafile, created by "s_steel_wall_model_0D.m".
% ------------------------------------------------------------------------

%% MAIN

% Import test data
filename = uigetfile('*.mat','Select a steel wall test data file (MAT).');
if filename == 0
```

```
  clear filename
  return
else
  load(filename);
end
if exist('PROC_WALL','var')
  disp('Dummy data file selected, proc variables ignored.');
end

% Import state references
staterefs = uigetfile('*.csv','Select a state references file (CSV).');
if staterefs == 0
  clear staterefs
  return
end
[n,n_hid,n_var,n_wall,n_wall_r,n_wall_c,n_ref,n_T_f_ref,a,b] = ...
f_import_state_refs(staterefs);

% Timing
dt = EXP_TIME_DT;
n_offset = round(EXP_TIME_IGN/EXP_TIME_DT,0)+1;
n_steps = round(EXP_TIME_TOTAL/EXP_TIME_DT,0)+1;
time_range = n_offset:n_steps+n_offset-1;
t_tot = (n_steps-1)*dt;
time = 0:dt:t_tot;

% Fire-side gases and surroundings
T_inf_ff = EXP_FIRE_GAS(time_range,:).';
T_sur_f = mean(T_inf_ff,1);
T_inf_f = zeros(n,n_steps);
for i = 1:n
  T_inf_f(i,:) = T_inf_ff(n_T_f_ref(i),:);
end

% Cool-side gases and surroundings
T_inf_c = EXP_BACK_GAS(time_range).';
T_sur_c = EXP_BACK_SURR(time_range).';

% Wall frame
T_l_left = EXP_FRAME(time_range,2).';
T_l_right = EXP_FRAME(time_range,2).';
T_l_top = EXP_FRAME(time_range,1).';
T_l_bot = EXP_FRAME(time_range,3).';
T_l = [T_l_left; T_l_right; T_l_top; T_l_bot];
clear T_l_left T_l_right T_l_top T_l_bot

% Steel wall (meas)
T_w_left = EXP_WALL(time_range,1:8,1).';
T_w_mid = EXP_WALL(time_range,1:8,2).';
T_w_right = EXP_WALL(time_range,1:8,3).';
T_w = [T_w_left; T_w_mid; T_w_right];
clear T_w_left T_w_mid T_w_right

```

```
% Interpolate measured data over the modelling grid
T_w = f_meas_interp(T_w,n_wall_r,n_wall_c,n_steps,false);
m = size(T_w,1);
```

## s_plot_contours.m

```
% -------------------------------------------------------------------------
% Name: s_plot_contours_quick.m
% Desc: This script builds contour plots for incident heat flux and
%       temperature at a particular time.
% -------------------------------------------------------------------------

%% PREAMBLE

% Contour details
contour_plot_time = 40;
T_min = 0;
T_max = 600;
HF_min = 0;
HF_max = 60;
contour_divs = 15;
contour_lines = 'none'; % change to 'black' to add contour lines

% Plot settings
plot_width = 3.2;
plot_height = 2.6;
plot_scale = 2;
save_vector = true;
save_raster = false;

%% TEMPERATURE PLOTS

% Wall geometry
W_tot = (75)*25.4/1000;
H_tot = (75)*25.4/1000;
W = W_tot/n_wall_c;
H = H_tot/n_wall_r;

% Assemble contour array (repeat each row/column twice)
plot_var = zeros(2*n_wall_r,2*n_wall_c,n_steps);
for k = 1:n_steps
  for j = 1:n_wall_c
    for i = 1:n_wall_r
      tempvar = x(i+n_wall_r*(j-1),k)-273.15;
      plot_var(2*i-1,2*j-1,k) = tempvar; % Top-left
      plot_var(2*i-0,2*j-1,k) = tempvar; % Bot-left
      plot_var(2*i-1,2*j-0,k) = tempvar; % Top-right
      plot_var(2*i-0,2*j-0,k) = tempvar; % Bot-right
    end
  end
end
```

```
46
47 % Contour spacing, horizontal
48 sx = W/2-0.001;
49 X(1,1) = 0;
50 for i = 2:2*n_wall_c-1
51   if mod(i/2,1)==0
52     X(1,i) = floor(i/2)*W-sx;
53   else
54     X(1,i) = floor(i/2)*W+sx;
55   end
56 end
57 X(1,2*n_wall_c) = n_wall_c*W;
58
59 % Contour spacing, veritcal
60 sy = H/2-0.001;
61 Y(1,1) = 0;
62 for i = 2:2*n_wall_r-1
63   if mod(i/2,1)==0
64     Y(1,i) = floor(i/2)*H-sy;
65   else
66     Y(1,i) = floor(i/2)*H+sy;
67   end
68 end
69 Y(1,2*n_wall_r) = n_wall_r*H;
70
71 % Universal Plot Settings
72 X_scale = 0:W_tot/6:W_tot;
73 Y_scale = 0:H_tot/6:H_tot;
74 Z_min = T_min;
75 Z_max = T_max;
76 Z_scale = 10;
77 degC = [sprintf('%c', char(176)) 'C'];
78
79 % Contour plot
80 contour_time = contour_plot_time;
81 contour_data = flip(plot_var(:,:,round(contour_time*60/dt,0)+1),1);
82 f = figure(1);clf;
83 contourf(X,Y,contour_data,contour_divs,'ShowText','off',...
84          'LineColor',contour_lines);
85 colormap(parula(Z_scale*contour_divs));
86 xlabel('Horizontal Position (m)');
87 ylabel('Vertical Position (m)');
88 box on;
89 caxis([Z_min,Z_max]); axis([0,W_tot,0,H_tot]);
90 set(gca,'XTick',X_scale);set(gca,'XTickLabel',sprintf('%1.2f\n',X_scale));
91 set(gca,'XTickLabelRotation',0);
92 set(gca,'YTick',Y_scale);set(gca,'YTickLabel',sprintf('%1.2f\n',Y_scale));
93 set(gca,'linewidth',0.75*plot_scale); set(gca,'TickDir','out');
94 set(gca,'GridAlpha',0.25); set(gca,'GridLineStyle','-');
95 set(gca,'GridColor',[0 0 0]);
96 c = colorbar; c.Label.String = ['Temperature (' degC ')'];
97 set(f,'PaperUnits','inches');
98 set(f,'PaperPosition',[0 0 plot_scale*plot_width plot_scale*plot_height]);
```

```
set(findall(f,'-property','FontName'), 'FontName', 'Times New Roman');
set(findall(f,'-property','FontSize'), 'FontSize', 10*plot_scale);
if save_raster
  print(['fig-' filename '-' num2str(n_wall) '-contour-T-' ...
        num2str(contour_time) '.png'],'-dpng','-r300');
end
if save_vector
  saveas(gcf,['fig-' filename '-' num2str(n_wall)...
                  '-contour-T-' num2str(contour_time)],'epsc');
end

%% HEAT FLUX PLOTS

% Wall geometry
W_tot = (75)*25.4/1000;
H_tot = (75)*25.4/1000;
W = W_tot/n_wall_c;
H = H_tot/n_wall_r;

% Contour array (repeat each row/column twice)
plot_var = zeros(2*n_wall_r,2*n_wall_c,n_steps);
for k = 1:n_steps
  for j = 1:n_wall_c
    for i = 1:n_wall_r
      tempvar = q_inc_m(i+n_wall_r*(j-1),k)/1000;
      plot_var(2*i-1,2*j-1,k) = tempvar; % Top-left
      plot_var(2*i-0,2*j-1,k) = tempvar; % Bot-left
      plot_var(2*i-1,2*j-0,k) = tempvar; % Top-right
      plot_var(2*i-0,2*j-0,k) = tempvar; % Bot-right
    end
  end
end

% Contour spacing, horizontal
sx = W/2-0.001;
X(1,1) = 0;
for i = 2:2*n_wall_c-1
  if mod(i/2,1)==0
    X(1,i) = floor(i/2)*W-sx;
  else
    X(1,i) = floor(i/2)*W+sx;
  end
end
X(1,2*n_wall_c) = n_wall_c*W;

% Contour spacing, veritcal
sy = H/2-0.001;
Y(1,1) = 0;
for i = 2:2*n_wall_r-1
  if mod(i/2,1)==0
    Y(1,i) = floor(i/2)*H-sy;
  else
    Y(1,i) = floor(i/2)*H+sy;
```

```
  end
end
Y(1,2*n_wall_r) = n_wall_r*H;

% Universal Plot Settings
X_scale = 0:W_tot/6:W_tot;
Y_scale = 0:H_tot/6:H_tot;
Z_min = HF_min;
Z_max = HF_max;
Z_scale = 10;

% Contour plot
contour_time = contour_plot_time;
contour_data = flip(plot_var(:,:,round(contour_time*60/dt,0)+1),1);
f = figure(2);clf;
contourf(X,Y,contour_data,contour_divs,'ShowText','off',...
         'LineColor',contour_lines);
colormap(parula(Z_scale*contour_divs));
xlabel('Horizontal Position (m)');
ylabel('Vertical Position (m)');
box on;
caxis([Z_min,Z_max]); axis([0,W_tot,0,H_tot]);
set(gca,'XTick',X_scale);set(gca,'XTickLabel',sprintf('%1.2f\n',X_scale));
set(gca,'XTickLabelRotation',0);
set(gca,'YTick',Y_scale);set(gca,'YTickLabel',sprintf('%1.2f\n',Y_scale));
set(gca,'linewidth',0.75*plot_scale); set(gca,'TickDir','out');
set(gca,'GridAlpha',0.25); set(gca,'GridLineStyle','-');
set(gca,'GridColor',[0 0 0]);
c = colorbar; c.Label.String = 'Incident Heat Flux (kW/m^2)';
set(f,'PaperUnits','inches');
set(f,'PaperPosition',[0 0 plot_scale*plot_width plot_scale*plot_height]);
set(findall(f,'-property','FontName'), 'FontName', 'Times New Roman');
set(findall(f,'-property','FontSize'), 'FontSize', 10*plot_scale);
if save_raster
  print(['fig-' filename '-' num2str(n_wall) '-contour-HF-' ...
        num2str(contour_time) '.png'],'-dpng','-r300');
end
if save_vector
  saveas(gcf,['fig-' filename '-' num2str(n_wall)...
                '-contour-HF-' num2str(contour_time)],'epsc');
end
```

## s_plot_settings.m

```
% ------------------------------------------------------------------------
% Name: s_plot_settings.m
% Desc: This script sets various plot settings for visual appearance.
% ------------------------------------------------------------------------

grid on;
box on;
```

```
set(gca,'LineWidth',0.75*plot_scale);
set(gca,'TickDir','out');
set(gca,'GridAlpha',0.25);
set(gca,'GridLineStyle','-');
set(gca,'GridColor',[0 0 0]);
set(f,'PaperUnits','inches');
set(f,'PaperPosition',[0 0 plot_scale*plot_width plot_scale*plot_height]);
set(findall(f,'-property','FontName'), 'FontName', 'Times New Roman');
set(findall(f,'-property','FontSize'), 'FontSize', 10*plot_scale);
set(h,'FontSize',8*plot_scale);
set(h,'Location','Best');
```

## s_steel_wall_model_2D_KF.m

```
% ------------------------------------------------------------------------
% Name: s_steel_wall_model_2D_KF.m
% Desc: This script calculates the temperature of the steel wall sensor
%       and heat flux to the steel wall sensor during a fire exposure
%       using the 2D kalman filter model.
% Note: Increase the process gain to make the filter favour measurements
%       over process estimates, but decrease certainty in the predictions.
% ------------------------------------------------------------------------

%% PREAMBLE

% Initialize script
clear;clc;
disp('------------------------------------------------------------');
disp('Kalman Filter solution for a steel wall test (2D model)');
disp('------------------------------------------------------------');
disp('Initializing...');
s_import_data_2D_KF;
if or(not(exist('filename','var')),not(exist('staterefs','var')))
  disp('No file selected. Script aborted.');
  disp('------------------------------------------------------------');
  return
end
disp(['Datafile selected: ' filename]);
disp(['State references file selected: ' staterefs]);
filename = replace(filename,'.mat','');
staterefs = replace(staterefs,'.csv','');

% Script options
tempvar = input('Plot results (y/n)? ','s');
if tempvar == 'y'; plot_results = true; else; plot_results = false; end;
tempvar = input('Save results (y/n)? ','s');
if tempvar == 'y'; save_results = true; else; save_results = false; end;

% Process and sensor variance
phi = 0.05;
std_pro = zeros(n,n_steps);
```

```
38 std_sen = ones(m+n_hid,1)*2.0;
39
40 % Convergeance criteria
41 threshold = 0.1;
42 max_iterations = 100;
43 ht_count_max = 1;
44 ht_count_sum = 1;
45
46 % Pre-allocate variables
47 x = zeros(n,n_steps);
48 P = zeros(n,n,n_steps);
49 K = zeros(n,m+n_hid,n_steps);
50 q_inc_m = zeros(n,n_steps);
51 q_inc_s = zeros(n,n_steps);
52
53 % Initial conditions
54 T_i = mean(T_w(:,1),1);
55 [x(:,1),P(:,:,1),std_pro(:,1),q_inc_m(:,1),q_inc_s(:,1)] = ...
56 f_initial(dt,n,n_ref,a,b,T_i,T_inf_f(:,1),T_inf_c(1),T_sur_c(1),phi);
57
58 %% MAIN
59
60 % Run the Kalman Filter
61 progress = 0;
62 n_update = 1;
63 for k = 2:n_steps
64   % Progress / housekeeping
65   if mod(k-1,n_update) == 0
66     fprintf(1, repmat('\b',1,progress));
67     progress = fprintf('Running Kalman filter... %d of %d',k-1,n_steps);
68   end
69   ht_count = 1;
70   % Prior state and covariance
71   x_old = x(:,k-1);
72   x_calc = x_old;
73   P_old = P(:,:,k-1);
74   P_calc = P_old;
75   % Measurements
76   z(1:m,1) = T_w(:,k);
77   z(m+1:m+n_hid,1) = T_l(:,k);
78   % State calculations
79   while true
80     % Calculate heat transfer coefficients
81     [alpha,beta] = f_ht_calc_fwd(dt,a,b,x_calc,T_inf_f(:,k),...
82                    T_sur_f(k),T_inf_c(k),T_sur_c(k));
83     % Process error
84     std_pro(:,k) = phi*alpha;
85     % Setup Kalman filter matrices
86     [F,B,u,Q,R,H] = f_kf_setup(dt,n,n_hid,m,n_ref,alpha,beta,...
87                     std_pro(:,k),std_sen);
88     % Predict state
89     [x_new,P_new] = f_kf_predict(x_old,P_old,F,Q,B,u);
90     % Update state
```

```
91      [x_new,P_new,K_new] = f_kf_update(x_new,P_new,z,R,H);
92      % Update parameters
93      [alpha_new,beta_new] = f_ht_calc_fwd(dt,a,b,x_new,T_inf_f(:,k),...
94                              T_sur_f(k),T_inf_c(k),T_sur_c(k));
95      % Check parameters
96      if f_param_check(alpha(1:n_var),alpha_new(1:n_var),threshold)
97        break;
98      end
99      x_calc = x_new;
100     P_calc = P_new;
101     ht_count = ht_count+1;
102     if ht_count > max_iterations
103       fprintf(1, repmat('\b',1,progress));
104       progress = fprintf('Iteration step did not converge.\n');
105       disp(['Aborted on step ' num2str(k) ' of ' num2str(n_steps) '.']);
106       disp('------------------------------------------------------------');
107       return;
108     end
109   end
110   % Output posterior state and parameters
111   x(:,k) = x_new;
112   P(:,:,k) = P_new;
113   K(:,:,k) = K_new;
114   % Calculate heat flux (inverse solution)
115   [q_inc_m(:,k),q_inc_s(:,k)] = f_ht_calc_inv(dt,n,n_ref,a,b,x_new,...
116                                 x_old,P_new,T_inf_f(:,k),T_inf_c(k),...
117                                 T_sur_c(k),std_pro(:,k));
118   % Calculate performance stats
119   if ht_count > ht_count_max; ht_count_max = ht_count; end;
120   ht_count_sum = ht_count_sum + ht_count;
121 end
122
123 % Update progress
124 fprintf(1, repmat('\b',1,progress));
125 progress = fprintf('Running Kalman filter...\n');
126
127 %% POST-PROCESSING
128
129 % Plot results
130 if plot_results
131
132   % Plot settings
133   disp('Plotting results...');
134   plot_width = 3.2;
135   plot_height = 2.8;
136   plot_scale = 2;
137   range_start = 1;
138   range_end = k;
139   x_data = time(range_start:range_end)/60;
140   degC = [sprintf('%c', char(176)) 'C'];
141
142   % Plot temperature
143   f = figure(1); clf;
```

```
144     clear y_data
145     hold on;
146     y_data(1,:) = T_inf_f(1,range_start:range_end)-273.15;
147     y_data(2,:) = T_inf_f(8,range_start:range_end)-273.15;
148     y_data(3,:) = x(round(n_wall/2,0),range_start:range_end)-273.15;
149     y_data(4,:) = T_w(round(m/2,0),range_start:range_end)-273.15;
150     p(1) = plot(x_data,y_data(1,:),'r-','LineWidth',0.5*plot_scale);
151     p(2) = plot(x_data,y_data(2,:),'b-','LineWidth',0.5*plot_scale);
152     p(3) = plot(x_data,y_data(3,:),'k-','LineWidth',1.0*plot_scale);
153     p(4) = plot(x_data,y_data(4,:),'k:','LineWidth',2.0*plot_scale);
154     h = legend([p(1) p(2) p(3) p(4)],'Fire gas (top)',...
155                                      'Fire gas (bottom)',...
156                                      'Kalman filter (centre)',...
157                                      'Measurements (centre)');
158     xlabel('Time (min)'); xlim([0,round(t_tot/60,0)]);
159                           xticks(0:round(t_tot/60,0)/6:round(t_tot/60,0));
160     ylabel(['Temperature (' degC ')']); ylim([0,700]); yticks(0:100:700);
161     s_plot_settings;
162     hold off
163     if save_results
164       saveas(gcf,['fig-' filename '-' num2str(n_wall) '-T'],'epsc')
165     end
166     clear f p h
167
168     % Plot heat Flux
169     f = figure(2); clf;
170     clear y_data
171     hold on;
172     y_data(1,:) = q_inc_m(round(n_wall/2,0),range_start:range_end)/1000;
173     y_data(2,:) = y_data(1,:) + ...
174                   q_inc_s(round(n_wall/2,0),range_start:range_end)/1000;
175     y_data(3,:) = y_data(1,:) - ...
176                   q_inc_s(round(n_wall/2,0),range_start:range_end)/1000;
177     p(1) = plot(x_data,y_data(1,:),'k-','LineWidth',1.0*plot_scale);
178     p(2) = plot(x_data,y_data(2,:),'r-','LineWidth',0.5*plot_scale);
179     p(3) = plot(x_data,y_data(3,:),'b-','LineWidth',0.5*plot_scale);
180       h = legend([p(1) p(2) p(3)],'Kalman Filter (\mu)',...
181                                   'Kalman Filter (\mu+\sigma)',...
182                                   'Kalman Filter (\mu-\sigma)');
183     xlabel('Time (min)'); xlim([0,round(t_tot/60,0)]);
184                           xticks(0:round(t_tot/60,0)/6:round(t_tot/60,0));
185     ylabel('Incident Heat Flux (kW/m^2)'); ylim([0,70]); yticks(0:10:70);
186     s_plot_settings;
187     hold off
188     if save_results
189       saveas(gcf,['fig-' filename '-' num2str(n_wall) '-HF'],'epsc')
190     end
191     clear f p h
192
193   end
194
195   % Complete script
196   disp('Script completed!');
```

```
197 if save_results
198   save(['results-' filename '.mat'],'time','x','K','T_w','T_inf_f',...
199                                     'q_inc_m','q_inc_s','std_pro');
200   disp(['Results saved to: results-' filename '.mat']);
201 end
202 disp('------------------------------------------------------------');
203 disp(['Total number of steps: ' num2str(k)]);
204 disp(['Total number of iterations: ' num2str(ht_count_sum)]);
205 disp(['Average iterations per step: ' num2str(round(ht_count_sum/k,2))]);
206 disp(['Maximum iterations per step: ' num2str(ht_count_max)]);
207 disp('------------------------------------------------------------');
```

# Appendix G

# State Reference Data for the Heat Flux Model

This appendix contains a Portable Document Format (PDF) file of the state reference data for use with the 2D Steel Wall Kalman filter (`data-state-refs.pdf`). The data files were created in Excel 2017 and exported to PDF. The page size is ANSI A portrait (8.5 in $\times$ 11 in).

If you accessed this thesis from a source other than the University of Waterloo, you may not have access to this file. You may access it by searching for this thesis on `https://uwspace.uwaterloo.ca/UWSpace`.